

UNIVERSITÄT
BAYREUTH

Spectroscopic Analysis and
Materials Engineering
for Passive Radiative Cooling

Dissertation

to be awarded the degree of
Doctor of Natural Sciences (Dr. rer. nat)
at the Faculty of Biology, Chemistry & Earth Sciences

submitted by

Tobias Lauster

born in Kirchheim unter Teck

Die Vorliegende Arbeit wurde in der Zeit von Juli 2018 bis Mai 2023 in Bayreuth am Lehrstuhl Physikalische Chemie I unter Betreuung von Herr Prof. Dr. Markus Retsch angefertigt.

Vollständiger Abdruck der von der Fakultät für Biologie, Chemie und Geowissenschaften der Universität Bayreuth genehmigten Dissertation zur Erlangung des akademischen Grades eines Doktors der Naturwissenschaften (Dr. rer. nat.).

Art der Dissertation: Kumulative Dissertation

Dissertation eingereicht am: 07.06.2023

Zulassung durch die Promotionskommission: 22.06.2023

Wissenschaftliches Kolloquium: 11.12.2023

Amtierender Dekan: Prof. Dr. Cyrus Samimi

Prüfungsausschuss:

Prof. Dr. Markus Retsch (Gutachter)

Prof. Dr. Anna Schenk (Gutachterin)

Prof. Dr. Mukundan Thelakkat (Vorsitz)

Prof. Dr. Jürgen Senker



List of Publications

This thesis is written as a cumulative dissertation. The thesis is based on the following publications in peer-reviewed journals:

[1] Marius Schöttle, Tobias Lauster, Lukas J. Roemling, Nicolas Vogel, and Markus Retsch*, A Continuous Gradient Colloidal Glass, *Advanced Materials*, **2022**, 2208745.

[2] Kai Herrmann[‡], Tobias Lauster[‡], Qimeng Song*, and Markus Retsch*, „Homogeneous Polymer Films for Passive Radiative Daytime Cooling: Optimized Thickness for Maximized Cooling Performance”, *Advanced Energy and Sustainability Research*, **2022**, 3, 2100166.

[‡] These authors contributed equally.

[3] Tobias Lauster, Anika Mauer, Kai Herrmann, Qimeng Song, Jürgen Senker, and Markus Retsch*, „From Chitosan to Chitin: Bioinspired Thin Films for Passive Daytime Radiative Cooling”, *Advanced Science*, **2023**, 2206616.

[4] Qimeng Song, Thomas Tran, Kai Herrmann, Tobias Lauster, Maximilian Breitenbach, and Markus Retsch*, „A Tailored Indoor Setup for Reproducible Passive Radiative Cooling Characterization”, *Cell Reports Physical Science*, **2022**, 3, 100986.

[5] Qiang Gao, Tobias Lauster, Bernd A. F. Kopera, Markus Retsch*, Seema Agarwal*, and Andreas Greiner*, „Breathable and Flexible Dual-Sided Nonwovens with Adjustable Infrared Optical Performances for Smart Textile“, *Advanced Functional Materials*, **2022**, 32, 2108808.

The following publications were also published in the time period of this thesis:

[6] Nelson W. Pech-May*, Tobias Lauster, and Markus Retsch*, “Design of Multimodal Absorption in the Mid-IR: A Metal Dielectric Metal Approach”, *ACS Applied Materials and Interfaces*, **2021**, 13, 1921-1929.

[7] Anna M. Neuhöfer, Kai Herrmann, Flora Lebeda, Tobias Lauster, Christoph Kathmann, Svend-Age Biehs*, and Markus Retsch*, „High-Temperature Thermal Transport in Porous Silica Materials: Direct Observation of a Switch from conduction to Radiation”, *Advanced Functional Materials*, **2021**, 32, 2108370.

[8] Moritz B. Heindl, Nicholas Kirkwood, Tobias Lauster, Julia A. Lang, Markus Retsch, Paul Mulvaney, and Georg Herink*, „Ultrafast imaging of terahertz electric waveforms using quantum dots”, *Light: Science & Applications*, **2022**, 11, 5.

List of Contributions

[1] Tobias Lauster, Tanja Feller, Kishin Matsumori, Nelson W. Pech-May, and Markus Retsch, “Optical Broadband Characterisation of Silica Particles in Chitosan Thin Films”, Poster presentation, 15th Zsigmondy Colloquium **2019**, Dresden, Germany.

[3] Tobias Lauster, Tanja Feller, Kishin Matsumori, Nelson W. Pech-May, and Markus Retsch, „Chitosan/Silica Composite Materials for Radiative Daytime Cooling: Broadband Optical Characterisation”, Poster presentation, Macromolecular Colloquium **2020**, Freiburg im Breisgau, Germany.

[2] Tobias Lauster, and Markus Retsch, “Material Design Strategies for Passive Radiative Daytime cooling”, Oral Presentation, 16th Zsigmondy Colloquium **2020**, Düsseldorf, Germany.

[4] Tobias Lauster, Kishin Matsumori, and Markus Retsch, „Bioinspired Structured Chitosan/Silica Composites for Passive Radiative Daytime Cooling”, Poster Presentation, MRS Spring Meeting **2022**, Honolulu, USA.

[5] Kai Herrmann, Tobias Lauster, Qimeng Song, and Markus Retsch, “Homogenous Polymer Films for Passive Daytime Cooling: Optimized Thickness for Maximized Cooling Performance”, Oral Presentation, MRS Spring Meeting **2022**, Honolulu, USA.

List of Abbreviations

AgNW	silver nanowires
AM	air mass
CrEEP	controlled emulsion extraction process
FTIR	Fourier-transform infrared (spectroscopy)
IR	infrared
NIR	near Infrared
NMR	nuclear magnetic resonance
PDMS	polydimethylsiloxane
PE	polyethylene
PI	polyimide
PMMA	poly(methyl methacrylate)
PMP	polymethylpentene
PVDF	polyvinylidene fluoride
PVDF-HFP	polyvinylidene fluoride-co-hexafluoropentene
PVF	polyvinyl fluoride
SBW	spectral bandwidth
SEM	scanning electron microscope
UV	ultraviolet
Vis	visible
XPS	expanded polystyrene



Abstract

Radiative transport processes are omnipresent in everyday life but mostly invisible since the human eye is only sensitive to a small fraction of wavelengths. However, through our skin, we can feel radiation as heating or cooling. After intensely researching radiative transport, I perceive the world differently. For example, when walking home through a clear night sky, I know now that the chilly feeling from above is outer space trying to kill me. Sometimes I wish for a blanket of clouds that protects my body from radiating body heat through the atmosphere into outer space. Or when I sit at a campfire in summer and observe the colors and feel the warmth, I inevitably think about Planck's law now.

The central theme of this thesis revolves around a special application of radiative heat transfer: Passive radiative daytime cooling. All contributions within this thesis have direct or indirect connections to this field of research. The aim is to utilize the radiative heat transport pathway to cool objects. By specifically tailoring the optical properties, materials can spontaneously cool below ambient temperatures without external energy input, even with direct sunlight illumination. With climate change as the biggest challenge of this century, improving cooling technologies seemed highly important to me.

Different material aspects are crucial for passive radiative daytime cooling. The thermal emission must be optimized as the primary channel to dissipate energy. Other factors are loss contributions that reduce the cooling effect. The biggest potential loss for passive daytime cooling is the power input by solar irradiation. Absorbed solar energy can quickly diminish the cooling effect. Therefore, solar management strategies are required. The first contribution within this thesis presents one potential strategy to prevent solar absorption by strongly reflecting sunlight. A colloidal glass is assembled from particles with gradually increasing size. When assembled as a gradient material, this colloidal assembly shows broadband solar reflectance based on scattering for the entire visible wavelength range.

The second contribution in this thesis presents an approach to maximize the thermal emission and optimizes the layer thickness of different polymeric materials. In this work, my colleagues and I show how the thermal emission and the different loss contributions depend on the material thickness. With theoretical calculations based on the optical properties of the materials, an optimum layer thickness is revealed. To validate our calculations, simple radiative coolers with different emitter thicknesses are prepared, spectroscopically characterized, and tested in a field test on the rooftop. The optimization strategy is directly transferable to other materials if the optical properties are known and thus can help other researchers to improve their designs.

Besides optimizing widely applied materials also, new materials are introduced for passive radiative daytime cooling. Within the third contribution, I studied the biomaterials Chitosan and Chitin and whether they are suitable for passive radiative daytime cooling. With a solid-state conversion reaction, the water-soluble polymer Chitosan can be converted to Chitin. We reveal that both materials show below-ambient passive radiative daytime cooling through extensive optical characterization and calculation of the cooling behavior. The use of bio-compatible and abundant biomaterials is a clear advantage of the introduced system, and the work diversifies the pool of available materials.

The last two contributions within this thesis extend the available characterization methods for passive radiative daytime cooling and radiative heat transport. One big challenge in the research area is to compare materials and their performance. The state-of-the-art is a field test to measure the performance, but a direct comparison of the results is impossible due to fluctuations in atmospheric conditions. To overcome this problem, an indoor test setup to study passive radiative daytime cooling materials is introduced in this thesis. The indoor setup aims to emulate outside conditions like outer space and the sun with a liquid nitrogen-cooled aluminum dome and a solar simulator, respectively. In our work, we even show how atmospheric selectivity can be included by the addition of a selective filter.

The introduced aluminum dome of the indoor test setup can also be used to address other questions regarding radiative heat transfer. In the last contribution of this thesis, a dual-sided nonwoven material is introduced for advanced personal thermal management. The nonwoven consists of a polymeric- and metallic-side. With the dome at room temperature and a feedback-controlled heater system for the sample, the radiative transfer between the human body and the surrounding can be emulated. With the adjusted setup, we show that if the metallic side is facing the surroundings, radiative energy loss is suppressed. With the presented material design, new functional clothes for personal thermal management can be imagined.

Zusammenfassung

Strahlungstransportprozesse sind im täglichen Leben allgegenwärtig, aber meist unsichtbar, da das menschliche Auge nur für einen kleinen Teil der Wellenlängen empfindlich ist. Über unsere Haut können wir jedoch Strahlung als Erwärmen oder Abkühlen spüren. Nachdem ich mich intensiv mit dem Strahlungstransport beschäftigt habe, nehme ich die Welt anders wahr. Wenn ich zum Beispiel bei klarem Nachthimmel nach Hause gehe, weiß ich jetzt, dass das kühle Gefühl von oben das Weltall ist, das mich umbringen will. Manchmal wünsche ich mir eine Wolkendecke, die meinen Körper vor der Abstrahlung von Körperwärme durch die Atmosphäre ins Weltall schützt. Oder wenn ich im Sommer an einem Lagerfeuer sitze und die Farben betrachte und die Wärme spüre, denke ich jetzt unweigerlich an das Plancksche Gesetz.

Das zentrale Thema dieser Arbeit dreht sich um eine spezielle Anwendung der Wärmeübertragung durch Strahlung: Der passiven strahlungsbasierten Kühlung am Tag. Alle Beiträge dieser Arbeit haben direkt oder indirekt einen Bezug zu diesem Forschungsgebiet. Ziel ist es, den Strahlungstransportweg von Wärme zur Kühlung von Objekten zu nutzen. Durch gezielte Anpassung der optischen Eigenschaften können Materialien spontan unter die Umgebungstemperatur abkühlen, ohne dass Energie von außen zugeführt wird, selbst bei direkter Sonneneinstrahlung. Da der Klimawandel die größte Herausforderung dieses Jahrhunderts darstellt, erschien mir die Verbesserung von Kühltechnologien sehr wichtig.

Für die passive strahlungsbasierte Kühlung am Tag sind verschiedene Materialaspekte entscheidend. Die Wärmeabgabe muss als primärer Kanal für die Energieableitung optimiert werden. Andere Faktoren sind Verlustbeiträge, die die Kühlwirkung verringern. Der größte potenzielle Verlust bei der passiven Kühlung am Tag ist der Energieeintrag durch Sonneneinstrahlung. Die absorbierte Sonnenenergie kann den Kühleffekt schnell vermindern. Daher sind Strategien zum Umgang mit Sonneneinstrahlung erforderlich. Der erste Beitrag dieser Arbeit stellt eine mögliche Strategie zur Verhinderung der Absorption von Sonnenlicht durch starke Reflexion vor. Ein kolloidales Glas wird aus Partikeln mit allmählich zunehmender Größe hergestellt. Wenn es als Gradientenmaterial zusammengesetzt ist, zeigt diese kolloidale Anordnung eine breitbandige Sonnenreflexion auf der Grundlage von Streuung für den gesamten sichtbaren Wellenlängenbereich.

Der zweite Beitrag in dieser Arbeit stellt einen Ansatz zur Maximierung der Wärmeabstrahlung und zur Optimierung der Schichtdicke verschiedener polymerer Materialien vor. In dieser Arbeit zeigen meine Kollegen und ich, wie die thermische Emission und die verschiedenen Verlustbeiträge von der Materialdicke abhängen. Mit theoretischen Berechnungen, die auf den optischen Eigenschaften der Materialien basieren, wird eine optimale Schichtdicke ermittelt.

Um unsere Berechnungen zu validieren, werden einfache strahlungsbasierte Kühler mit unterschiedlichen Strahlerdicken hergestellt, spektroskopisch untersucht und in einem Feldversuch auf dem Dach getestet. Die Optimierungsstrategie ist direkt auf andere Materialien übertragbar, wenn die optischen Eigenschaften bekannt sind, und kann somit anderen Forschern helfen, ihre Designs zu verbessern.

Neben der Optimierung von weit verbreiteten Materialien werden auch neue Materialien für die passive strahlungsbasierte Kühlung am Tag vorgestellt. Im dritten Beitrag habe ich die Biomaterialien Chitosan und Chitin untersucht und geprüft, ob sie für die passive strahlungsbasierte Kühlung am Tag geeignet sind. Mit einer Festkörperumwandlungsreaktion kann das wasserlösliche Polymer Chitosan in Chitin umgewandelt werden. Durch umfangreiche optische Untersuchung und Berechnung des Kühlverhaltens zeigen wir, dass beide Materialien eine passive strahlungsbasierte Kühlung bei Tageslicht unterhalb der Umgebungstemperatur aufweisen. Die Verwendung von biokompatiblen und reichlich vorhandenen Biomaterialien ist ein klarer Vorteil des vorgestellten Systems, und die Arbeit erweitert das Angebot der verfügbaren Materialien.

Die letzten beiden Beiträge dieser Arbeit erweitern die verfügbaren Charakterisierungsmethoden für passive strahlungsbasierte Kühlung am Tag und strahlungsbasierten Wärmetransport. Eine große Herausforderung in diesem Forschungsbereich ist der Vergleich von Materialien und ihrer Leistung. Der Stand der Technik ist ein Feldtest, um die Leistung zu messen, aber ein direkter Vergleich der Ergebnisse ist aufgrund von Schwankungen der atmosphärischen Bedingungen unmöglich. Um dieses Problem zu überwinden, wird in dieser Arbeit ein Testaufbau für Innenräume zur Untersuchung von Materialien für die passive strahlungsbasierte Kühlung bei Tageslicht vorgestellt. Mit einer mit flüssigem Stickstoff gekühlten Aluminiumkuppel und einem Sonnensimulator sollen die Außenbedingungen wie im Weltraum und Einstrahlung der Sonne simuliert werden. In unserer Arbeit zeigen wir sogar, wie die atmosphärische Selektivität durch Hinzufügen eines selektiven Filters einbezogen werden kann.

Die eingeführte Aluminiumkuppel des Indoor-Testaufbaus kann auch zur Untersuchung anderer Fragen der strahlungsbasierten Wärmeübertragung verwendet werden. Im letzten Beitrag dieser Arbeit wird ein doppelseitiges Vliesmaterial für persönliches Wärmemanagement vorgestellt. Der Vliesstoff besteht aus einer Polymer- und einer Metallseite. Mit der Kuppel bei Raumtemperatur und einem rückkopplungsgesteuerten Heizsystem für die Probe kann der Strahlungstransfer zwischen dem menschlichen Körper und der Umgebung nachgestellt werden. Mit dem angepassten Aufbau zeigen wir, dass, wenn die metallische Seite der Umgebung zugewandt ist, der Strahlungsverlust unterdrückt wird. Mit dem vorgestellten Materialdesign ist Funktionskleidung für das Wärmemanagement denkbar.

Table of Contents

1. Introduction.....	1
Light-Matter Interaction	2
Optical Properties of Materials	4
Passive Radiative Cooling	6
State of the Art.....	12
2. Method Section	21
Rooftop Experiment	21
Indoor Experiment.....	23
Characterization Techniques for Optical Properties	23
3. Thesis Outline	29
3.1 Synopsis	29
3.2 Individual Contributions to Joint Publications.....	45
4. References.....	49
5. A Continuous Gradient Colloidal Glass.....	55
6. Homogeneous Polymer Films for Passive Daytime Cooling: Optimized Thickness for Maximized Cooling	89
7. From Chitosan to Chitin: Bio-Inspired Thin Films for Passive Daytime Radiative Cooling	107
8. A tailored indoor setup for reproducible passive daytime cooling characterization	121
9. Breathable and Flexible Dual-Sided Nonwovens with Adjustable Infrared Optical Performance for Smart Textile	145
Acknowledgements	167



1. Introduction

The radiative heat transfer pathway is essential for the energy exchange between the planet and outer space. The absorbed power irradiated by the sun on the heating side and the thermal emission on the cooling side are the basis of this thermodynamic equilibrium. The resulting surface temperature is the consequence of an overall complex energy balance between the sun, air, land, and oceans.¹ However, human activities like the burning of fossil fuels to generate energy lead to an imbalance of the equilibrium and causes a warming of the planet.² This climate crisis is expected to have drastic consequences for the planet's ecosystems and will significantly affect humanity. The transformation to net zero emissions to stop the planet's warming is the biggest challenge of this century. Therefore, reducing the energy demand is an important goal for developing future technologies and materials. One large fraction of the current energy demand is used for temperature management.³ To reduce the demand in this sector and to develop new technologies, it is fundamental to understand how heat is transported. The contributions in this thesis revolve around the radiative energy transfer pathway, but also conduction and convection need to be considered in many applications.

Heat transfer is present in everyday life. An example can be found in heat management in buildings.⁴ At low outside temperatures, heating raises the indoor temperature. Insulation is applied to walls and roofing to reduce conductive and convective transport and to prevent heat loss to the outside. For window systems, a gap (gas or vacuum) can act as insulation between multiple layers of glass, but also a low emissivity coating can help to decrease heat loss by suppressing the radiative heat transfer pathway.⁵ In contrast, when the interior temperature is uncomfortably high, air conditioning systems are used for cooling. Commonly used (active) systems use electricity to displace the heat from the inside to the outside of the building. The excess heat remains in close vicinity and causes a heat up of the direct surrounding. This situation is especially problematic in urban areas, with a high concentration of air conditioning units and reduced convection caused by taller buildings. The example of heat management in buildings shows how interconnected the heat transport pathways are.

With the prospects of global warming, the demand for air conditioning is increasing, which will exacerbate the described urban heat island effect and electricity demand for active cooling systems.⁶ A technology that can contribute to a solution for this problem is passive radiative cooling. The fundamental idea is to use the natural cooling mechanism of the planet and design surfaces such that they efficiently emit energy. This passive cooling strategy has the advantage that no electricity is needed to drive the cooling process, and the displaced energy is transported over larger distances. In fact, the radiative energy transfer pathway can be used to dissipate heat to outer space, the ultimate heat sink.

The concept of passive radiative cooling was already applied more than 2000 years ago. Ice pits were constructed in desert areas that operate with a combination of radiative and evaporative cooling to freeze water.⁷ In shallow water lagoons, a temperature drop below freezing was achieved with radiative energy loss during night-time. Additionally, mud walls were built on the southern, eastern, and western sides to prevent sunshine. This example from the past shows the potential of passive radiative cooling. In the modern world, a multitude of application scenarios for passive radiative cooling technology can be imagined and are already tested. Systems that have paint-like applicability or are producible in a scalable fashion have a clear advantage compared to highly optimized and complex materials.⁸ Besides the direct application as paint, panels that exchange the cooling power to a liquid are proposed and tested to harvest the cooling power.⁹ The cooled fluid is then integrated into air conditioning systems and thus, reducing energy consumption.¹⁰ Another highly researched area is the integration of passive radiative cooling in photovoltaic cells.^{11, 12} The reduction of temperature has the potential to increase the efficiency of the cells.¹³ Another application is constructing dew harvesting systems, including passively cooled surfaces to promote water condensation.¹⁴ The condensed water is collected from the surfaces and can supply arid regions with drinking water, or the systems can be used for the desalination of saltwater.¹⁵

Besides those technical examples, passive radiative cooling can also be included for personal thermal management.¹⁶ The human body temperature is above ambient temperature in many scenarios. Clothing is applied (among other reasons) to preserve energy otherwise lost to the surrounding. In case of exercise or higher ambient temperatures, the natural cooling mechanism relies on the evaporation of water.¹⁷ Therefore, novel textile materials with improved radiative heat management strategies are of great interest.^{18, 19}

The mentioned examples show how impactful passive radiative cooling strategies can be. Especially for applications and processes that involve higher temperatures, the radiative heat transfer pathway becomes more important. To understand why and to develop new materials and solutions or to improve existing systems, it is essential to understand the fundamentals of radiative heat transfer. Following, the relevant principles for light-matter interaction and the concept of radiative cooling will be briefly introduced.

Light-Matter Interaction

The fundamentals of understanding the interaction of light and matter root in the Maxwell Equations. Light is treated as an electromagnetic wave with an electric and magnetic field that oscillates spatially over time. For the application in the field of radiative cooling, mostly dielectric materials are used. Therefore, the origin of their properties will be outlined here.

Except otherwise cited, the introduction mainly follows the descriptions in the book of M. Modest.²⁰

In free space, electromagnetic waves travel with the maximum speed, known as the speed of light c . In contrast, the speed of the electromagnetic wave c_m is reduced within a medium. This ratio of propagation speed is known as refractive index n with

$$n = \frac{c}{c_m} \quad (1)$$

The speed of the wave is reduced due to the interaction of the electric field with the medium. For simplicity, dielectric media are considered nonmagnetic (permeability $\mu = 1$). The strength of the interaction can be related to how well the medium can be polarized and is expressed with the electrical permittivity ϵ_m . For free space $\epsilon = 1$, and it follows:

$$c_m = \frac{c}{\sqrt{\mu\epsilon}} = c \quad (2)$$

For dielectric materials, the electrical permittivity is larger than for free space. Hence the propagation speed is reduced, and $n > 1$. Similar to the description of the refractive index for a medium, the relative permittivity ϵ_p is introduced:

$$\epsilon_p = \frac{\epsilon}{\epsilon_m} \quad (3)$$

The relative permittivity of a material is a function of frequency ν , and the frequency relates to the wavelength λ with:

$$\lambda = \frac{c}{\nu} \quad (4)$$

Therefore, the refractive index is also a function of wavelength $n(\lambda)$, which is commonly known as dispersion. It is customary to introduce the refractive index as a complex quantity with

$$\tilde{n} = n - ik \quad (5)$$

Where n describes the propagation of the wave and the imaginary part k is used to describe the loss (absorption). With the introduction of the complex refractive index, the electrical permittivity of a medium also becomes a complex quantity that is related to the complex refractive index with:

$$\epsilon_p = \epsilon' - i\epsilon'' = \tilde{n}^2 \quad (6)$$

This expression is known as the complex dielectric function, which Lorentz described with a series of harmonic oscillators.²¹ The series of oscillators is used to model the absorption characteristics of dielectric materials. If a material's complex dielectric function or the complex refractive index is known, optical properties like reflection or absorption characteristics can even be calculated.

Optical Properties of Materials

If electromagnetic radiation is incident on a material, several phenomena can occur, depending on the optical properties of the material.

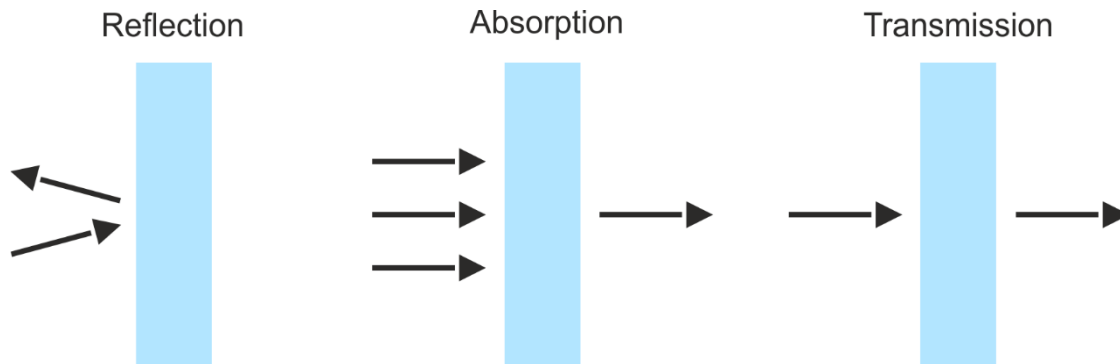


Figure 1.1: Schematic illustration of light-matter interaction processes.

At the surface of the material, parts of the electromagnetic radiation will be reflected. This part is described by the reflectivity ρ of the sample as the fraction of reflected intensity $I_{\text{reflected}}$ to total intensity I_{total} with

$$\rho = \frac{I_{\text{reflected}}}{I_{\text{total}}} \quad (7)$$

The non-reflected part of the electromagnetic radiation will enter the material and propagate there. Within the material, a fraction of the electromagnetic wave can be attenuated, which is described by the absorptivity α and the fraction of absorbed intensity I_{absorbed}

$$\alpha = \frac{I_{\text{absorbed}}}{I_{\text{total}}} \quad (8)$$

If the material has a finite thickness, a fraction of the incident electromagnetic radiation can be transmitted I_{trans} through the material. This fraction with respect to the total incident intensity is the transmissivity τ and is defined as

$$\tau = \frac{I_{\text{trans}}}{I_{\text{total}}} \quad (9)$$

The respective processes are schematically shown in Figure 1.1. For the event, energy conservation must be fulfilled and therefore:

$$\rho + \tau + \alpha = 1 \quad (10)$$

If a material is sufficiently absorbing (opaque), transmission can be neglected, and equation (10) is simplified to

$$\rho + \alpha = 1 \quad (11)$$

Note that for real materials, typically, the surface exhibits a certain roughness. Depending on the wavelength range of interest, this can have severe consequences for the penetration

behavior of the electromagnetic wave. The reflection properties at the interface can be enhanced or attenuated, and consequently, the fractions of absorbed or transmitted radiation are also affected. For real materials, the terminology of reflectance, absorptance, and transmittance will be used, describing the properties of the actual material. In contrast, reflectivity, absorptivity, and transmissivity will be used to describe an idealized material's general mechanisms and behavior.

For the fundamental description of light-matter interaction, the medium was considered to be homogeneous, and the interface was perfectly smooth. Within the material, fluctuations of electron density result in local refractive index variations. At the interface, structural differences like surface roughness affect the refractive index. This heterogeneity of the material can change the trajectory of incident radiation, a process typically known as scattering.²²

For the description of scattering for a perfectly spherical object, Gustav Mie solved the Maxwell equations for different particle radius r to wavelength ratios. This analytical solution extended the theory of lord Rayleigh from the 19th century for the scattering of very small spherical particles with a more general solution of the scattering problem. The calculations of Mie showed that for perfectly spherical individual particles, the scattering properties could be fully described. However, based on the radius of the particle to wavelength ratio, simplified equations are used. Conventionally, three different regimes are distinguished. Particles much smaller than the wavelength ($r \ll \lambda$) are within the so-called Rayleigh regime. For particles with sizes in the order of the wavelength ($r \approx \lambda$), the Mie theory is applied. The scattering properties of larger particles ($r \gg \lambda$) can be described with ray optics.

In real materials, multiple scattering centers are present, and with increasing material thickness, multi-scattering becomes dominant. For materials with high symmetry, the multi-scattering problem simplifies and follows Bragg's law for highly ordered systems like photonic crystals.²³ For unordered systems like paints, statistical considerations, and assumptions are applied, and light transport can be described as a diffusive process. Within the field of radiative cooling, scattering processes can be highly effective as a solar management strategy, a topic that will be discussed in a later chapter.

The parameters introduced so far describe the processes for incident radiation on a material. However, the quantity most relevant for the radiative heat transfer is the electromagnetic radiation emitted by the material. The material parameter related to the emission is called emissivity ε (emittance) and describes the radiant intensity of a material I_{material} compared to that of a perfect emitter (blackbody) $I_{\text{blackbody}}$ with

$$\varepsilon = \frac{I_{\text{material}}}{I_{\text{blackbody}}} \quad (12)$$

In thermal equilibrium, the emissivity of a material is equal to the absorptivity as described by Kirchhoff's law of radiation

$$\varepsilon = \alpha \tag{13}$$

This implies that if the absorption properties of a material are characterized, the emission properties of that material are also known. Experimentally, the absorption properties are much easier to access. Thus, Kirchhoff's law of radiation is widely applied to assess radiative cooling materials.

Passive Radiative Cooling

Within the field of radiative cooling, researchers aim to utilize the radiative heat transfer pathway to cool objects. In this section, the fundamentals of radiative heat transfer will be briefly introduced.

An ideal object (so-called blackbody) at a given temperature T emits electromagnetic radiation randomly in all directions. The emitted energy E_{bb} is a function of temperature and wavelength and is described by Planck's law²⁰

$$E_{bb} = \frac{2hc^2}{\lambda^5} \frac{1}{e^{hc/k_b T \lambda} - 1} \tag{14}$$

Where h is the Planck constant, and k_b is the Boltzmann constant.

The emission profiles for perfect blackbody emitters at different (ambient) temperatures in Figure 1.2 reveal that the emission is mainly located in the near- to mid-infrared wavelength region. The maximum of the emission shifts to smaller wavelengths with increasing temperature while the overall emitted intensity is increasing.

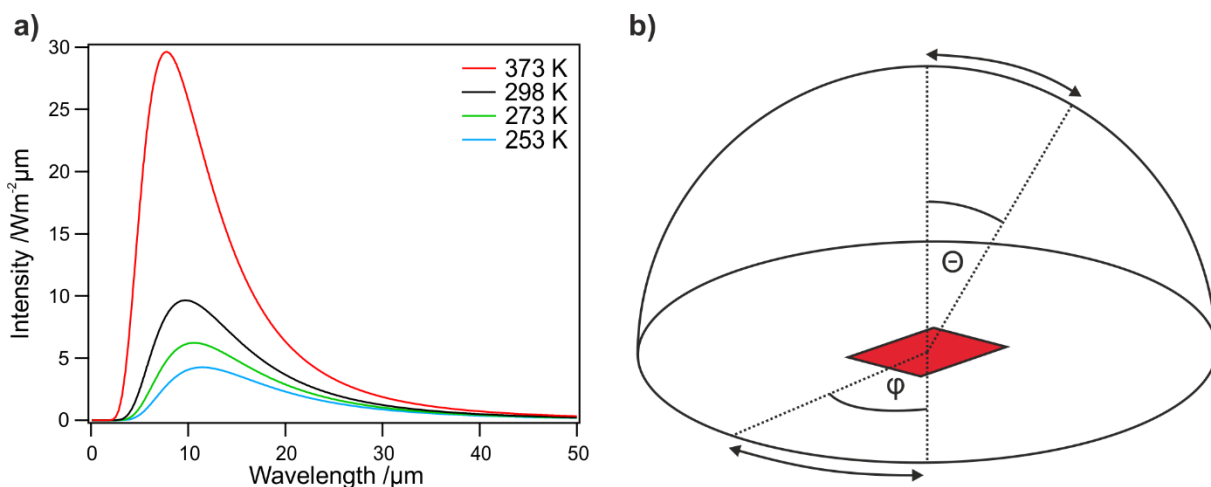


Figure 1.2: a) Blackbody intensity as a function of wavelength calculated with Planck's law for different emitter temperatures. For typical ambient temperatures, the emission is mainly located at infrared wavelengths. b) Schematic of an emitter in a hemispherical enclosure with the polar angle θ and the azimuthal angle φ .

The total emitted power P_{bb} is received after spectral integration over all frequencies and angular integration over the hemisphere above the emitter. Figure 1.2b shows an emitter in a hemispherical enclosure. For the description, a polar coordinate system is used with the polar angle θ as the angle with respect to the surface normal and the azimuthal angle φ . For the total emitted power, angular integration is performed between 0 and 90° ($\pi/2$) for θ and between 0 and 360° (2π) in azimuthal direction for the entire hemisphere:

$$P_{bb} = \int_0^{\infty} E_{bb} d\lambda \int_0^{2\pi} \int_0^{\frac{\pi}{2}} \sin \theta \cos \theta d\theta d\varphi \quad (15)$$

And leads to the Stefan-Boltzmann law²⁰ with the Stefan-Boltzmann constant σ :

$$P_{bb} = \sigma T^4 \quad (16)$$

Therefore, the emitted power of a perfect emitter scales with T^4 . This connection implies that radiative coolers at higher ambient temperatures potentially emit more energy than coolers at lower ambient temperatures.

Planck's law describes a perfect black body that emits (and consequently absorbs) radiation of all frequencies. However, typically objects are non-perfect emitters and emit radiation depending on their optical properties. The emitted power of a non-perfect emitter (grey body) can be obtained by multiplication of the materials emissivity $\varepsilon(\lambda)$ with the intensity of the blackbody.

$$P_{mat} = P_{bb} \cdot \varepsilon(\lambda) \quad (17)$$

Examples of thermal emission profiles at room temperature (298 K) for real samples with different emittances are shown in Figure 1.3. The example material with distinct emission peaks (Figure 1.3a) has an overall reduced emission intensity compared to the blackbody. The example also reveals that even with high emittance, the emitted intensity is still low for regions with overall low blackbody intensity at the given temperatures. In the example case, towards Near infrared (NIR) and Visible (Vis) wavelengths. In contrast, the second example material (Figure 1.3b) exhibits high emittance for most Infrared (IR) wavelengths and, therefore, nearly blackbody intensity.

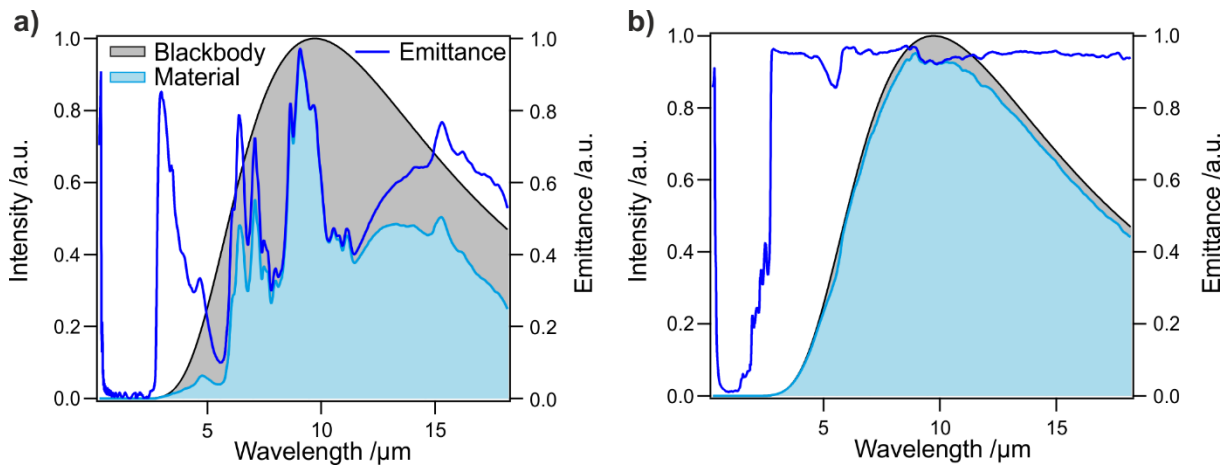


Figure 1.3: Comparison of relative radiation intensity for two real samples with a) distinct emittance and b) broadband emittance. The Ideal blackbody spectrum is displayed in the background, and the calculated sample emission is presented as a blue area, respectively.

To receive the total emitted power of a real material, the angle dependence of the emissivity needs to be reviewed. While the emissivity of a blackbody and a grey body is, per definition, angle independent (Lambert surface), the emissivity of a real material depends on the polar angle and decreases for higher angles. An example of the angle dependence extracted from the work of Rüdissler et al.²⁴ is presented for a Soda-Lime glass in Figure 1.4. The radiant intensity follows the Lambert cosine law, and the actual radiant intensity is in close agreement with the prediction for a Lambert surface.

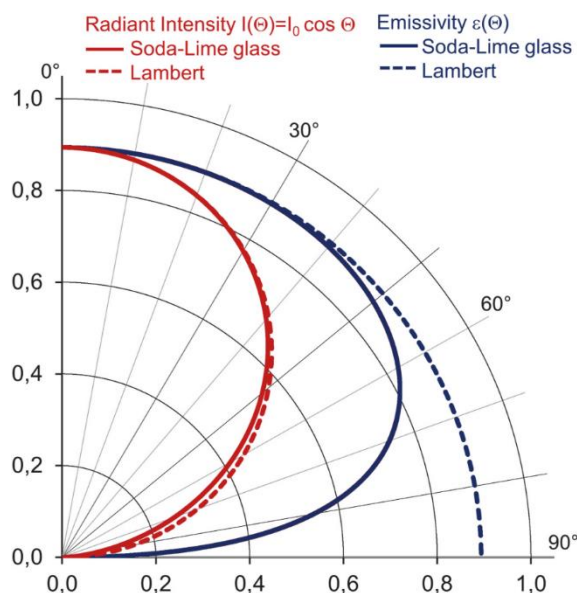


Figure 1.4: Angle dependence (polar angle θ) of the emissivity for a Soda-Lime glass compared to the emissivity of a Lambert emitter (angle independent). The figure is adapted from the original publication²⁴ and used according to the permission granted under the Creative Commons Attribution license (CC BY 4.0).

Assuming azimuthal independence of the emissivity, the total emitted power of a material is described by²⁵

$$P_{\text{mat}} = \int_0^{\infty} \int_0^{2\pi} \int_0^{\frac{\pi}{2}} \sin \theta \cos \theta \varepsilon(T, \lambda, \theta) \cdot I_{\text{bb}}(T, \lambda) d\theta d\varphi d\lambda \quad (18)$$

Within the field of passive radiative cooling, materials are designed that exhibit a positive net cooling power P_{cool} that leads to a temperature reduction in thermal equilibrium. This net cooling power is typically calculated by consideration of different contributions. The emittance of the material is the main mechanism exploited for the cooling effect. However, different loss mechanisms need to be considered. The equation for predicting the net cooling power is given by:

$$P_{\text{cool}} = P_{\text{mat}} - P_{\text{atm}} - P_{\text{sun}} - P_{\text{nonrad}} \quad (19)$$

It considers loss due to energy transfer with the atmosphere P_{atm} , the power input caused by solar absorption P_{sun} , and non-radiative contributions P_{nonrad} , affecting the energy balance due to conductive and convective heat transfer. A schematic overview of the contributions is presented in Figure 1.5. The following paragraph will discuss the origin, relationships, and magnitude of the loss contributions.

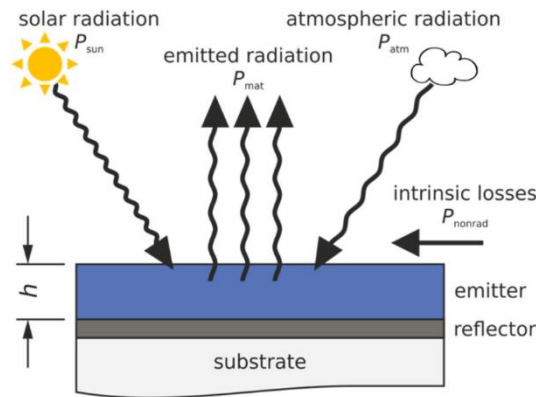


Figure 1.5: Schematic overview of the contributions to the net cooling power equation (19). The example shows an emitter film on a reflective substrate surface. The figure is adapted from the publication of Herrmann et al.²⁶ and used according to the permission granted under the Creative Commons Attribution license (CC BY 4.0).

For the energy exchange from the material to outer space, atmospheric transparency must be considered. Earth's atmosphere is a mixture of gases that partially absorb thermal wavelengths. Without this absorption and the resulting greenhouse effect, the planet would be significantly colder.²⁷ Gases like nitrogen and oxygen are the main constituents of the atmosphere but contribute very little to the overall absorption. The main contribution is from water, carbon dioxide, and ozone and, to a smaller extent, also nitrogen oxides or hydrocarbon compounds.²⁸ The resulting transmittance of the atmosphere²⁹ is used to model the angle-dependent emissivity $\varepsilon(\theta)$ with

$$\varepsilon(\theta) = \alpha = 1 - \tau^{1/\cos\theta} \quad (20)$$

This expression of the angle-dependent emissivity considers the atmosphere as a radiator and is an approximation with the Lambert cosine law.³⁰ With the emissivity of the atmosphere, the radiated power from the atmosphere can be calculated similarly to the material radiance. For the atmospheric power loss of the material also, the absorption properties of the material are taken into account, leading to

$$P_{\text{atm}} = 2\pi \int_0^{\frac{\pi}{2}} \sin\theta \cos\theta \int_0^{\infty} E_{\text{bb}}(\lambda, T_{\text{atm}}) \cdot \varepsilon_{\text{mat}}(\lambda) \cdot \varepsilon_{\text{atm}}(\lambda) d\lambda d\theta \quad (21)$$

To minimize P_{atm} , the material emissivity must be low in spectral regions where the atmosphere is not transparent. However, reduced emissivity implies reduced material emission. The delicate balance between emission and atmospheric loss leads to a complex relationship between overall cooling power as a function of temperature. A typical example is a selective emitter.²⁵ A selective emitter is a material designed to specifically emit radiation in the first atmospheric transparency window between wavelengths of 8-13 μm . The emissivity in this region is set to be 1, while for all other wavelengths, the emissivity is considered to be 0. The other extreme is the broadband emitter case which considers an ideal blackbody with an emissivity of 1 for all wavelengths relevant to emission at typical ambient temperatures ($>4 \mu\text{m}$). Ideal emissivity profiles of a selective and broadband emitter are displayed in Figure 1.6.

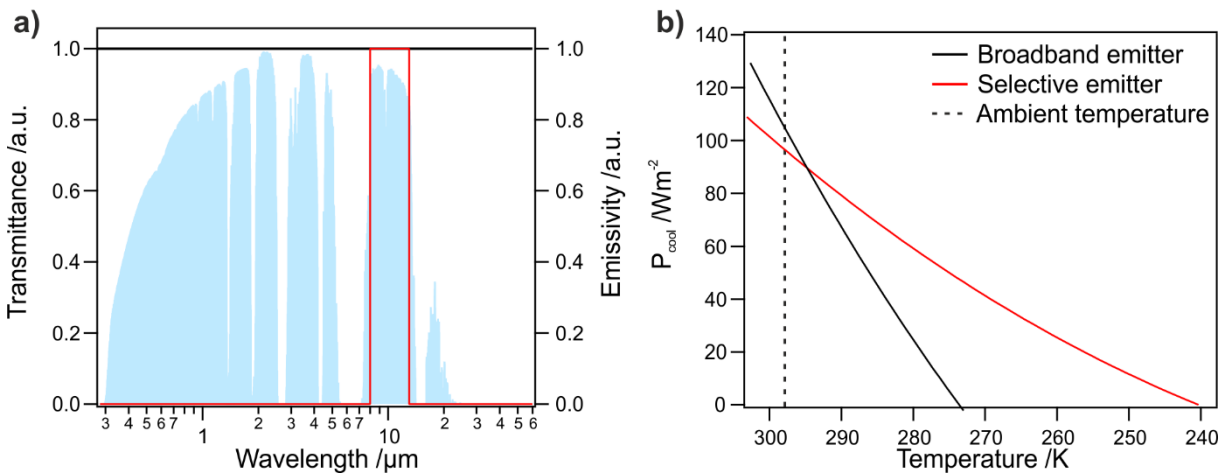


Figure 1.6: a) Comparison of the emissivity for a selective (red) and broadband emitter (black). The atmospheric transparency is displayed in the background.²⁹ b) Net cooling power for the two emitter cases as a function of temperature for an ambient temperature of 298 K. Losses by solar absorption or non-radiative contributions are excluded. The selective emitter has lower cooling power at ambient but reaches lower equilibrium temperatures.

Both contributions to the cooling power P_{mat} and P_{atm} are a function of temperature, and the equilibrium temperature is reached at $P_{\text{cool}} = 0$. For comparing the two emitter cases, the

cooling power is displayed as a function of material temperature in Figure 1.6b. Note that solar absorption and non-radiative losses are not considered for this example ($P_{\text{sun}} = 0$, $P_{\text{nonrad}} = 0$).

While the selective emitter provides lower cooling power at ambient temperatures, a positive cooling power remains for colder temperatures below ambient. Consequently, a potentially low equilibrium temperature of the emitter ($P_{\text{cool}} = 0$) can be reached. In contrast, broadband emitters have higher ambient and above ambient cooling power, but the reached equilibrium temperatures will be higher than the selective emitter case. Idealized emitters with more complex wavelength dependent emissivity were compared in the work of Li et al.³¹ For the full description of the system, the additional losses of solar irradiation and non-radiative processes need to be included. The origin and magnitude of these will be discussed in the following paragraph.

The sun's power input can potentially vanish the cooling effect completely. Early works on radiative cooling only considered the nighttime case, where solar irradiation is absent.^{30, 32} For calculating the passive cooling potential, a solar irradiance of 1000 Wm^{-2} is typically considered. This value is the integrated solar irradiance of an Air mass (AM) of 1.5. The AM is defined with $\text{AM} = l/l_0$, with l as the actual length of a light beam through the atmosphere and the shortest possible length at normal incidence l_0 . The actual solar irradiation can drastically change depending on the season, irradiation angle, and atmospheric conditions like cloud coverage.³³ For standardization, the American society for testing and materials recommends using the AM 1.5 solar spectrum (ASTM G-173-03).³⁴ A typical spectrum is shown in Figure 1.7 and can be described by a blackbody at a temperature of 5777 K. The spectrum considers losses to the atmosphere by scattering or absorption, and the sun is positioned at an angle of $\theta_{\text{sun}} = 41.8^\circ$ with respect to the surface normal. This aims to represent the year average for the mid-latitude sun position.

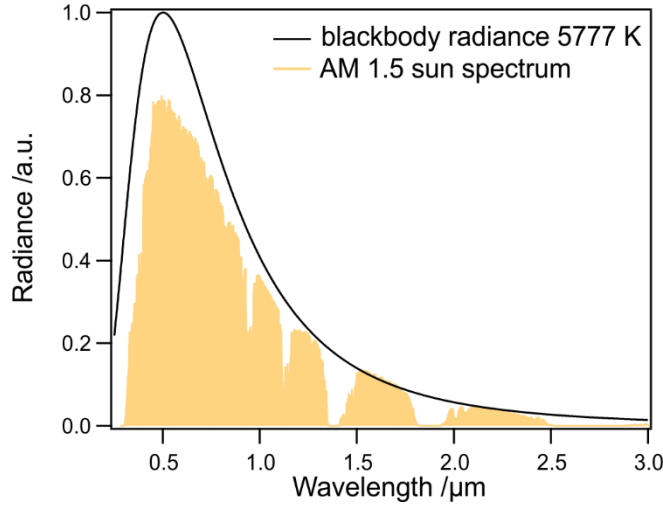


Figure 1.7: AM 1.5 solar spectrum (normalized) used as a standard for calculations.³⁴ The overall intensity distribution is represented by a blackbody with a temperature of 5777 K. Absorption in the atmosphere leads to reduced radiance for specific wavelengths.

To minimize solar absorption, the radiative cooler should not absorb any light in the wavelength range of solar irradiation. At the same time, the light should not be absorbed in the material below the cooler; therefore, high reflectance needs to be achieved. The loss contribution due to solar absorption P_{sun} can be calculated after integration, similar to the material emittance. Angular integration for the emissivity is not necessary as the sun position is fixed for the AM 1.5 solar spectrum, leading to:

$$P_{\text{sun}} = \int_0^{\infty} I_{\text{AM1.5}}(\lambda) \cdot \varepsilon_{\text{mat}}(\lambda, \theta_{\text{Sun}}) d\lambda \quad (22)$$

Besides radiative contributions also, non-radiative losses need to be considered. Convection from the surrounding gas phase and conductive losses via direct contact with the cooling material are conventionally combined into one term:

$$P_{\text{nonrad}} = h(T_{\text{amb}} - T_{\text{mat}}) \quad (23)$$

With h , the non-radiative heat transfer coefficient. The non-radiative power losses are a function of material temperature and have a stronger influence if the material temperature drops further below ambient. In actual applications of cooling materials, the non-radiative heat transport pathways could be target pathways to harness the generated cooling power and dissipate heat from a heat source. For the contributions in this thesis, typically, a value of $h = 4.4 \text{ Wm}^{-2}\text{K}^{-1}$ is used for calculations as an average value. Depending on the experimental system, the value can range from 0 (perfectly isolated) to $10 \text{ Wm}^{-2}\text{K}^{-1}$ (or more).³⁵

With the outlined concepts, researchers realized passive cooling properties within actual devices with many materials and advanced concepts. The following section will briefly summarize current state-of-the-art developments relevant to this thesis.

State of the Art

Different researchers already described the concept of cooling surfaces by utilizing selectively emitting materials decades ago.^{30, 32, 36-39} Back then, the idea was to find materials that selectively emit within the atmospheric transparency window between 8-13 μm to reach low temperatures during night-time. With the first demonstration of radiative cooling also during daytime by Raman et al.⁴⁰, the research attention in this field greatly increased. In the last decade, new materials, concepts, and strategies emerged to design radiative cooling materials.^{25, 35, 41, 42} In the following section, key design concepts and materials will be briefly introduced and summarized.

Tune emission properties

To create materials with the highest cooling power or that can reach the lowest equilibrium temperature, the emissivity of the material needs to be optimized. As thermal emission at typical ambient temperatures is located at infrared wavelengths, the optical properties in this wavelength regime are most important. Tuning the emission properties is achieved by selecting materials that intrinsically possess the desired properties or by optical engineering with a certain structure.

The intrinsic material properties in the infrared region originate from vibrational transitions within the material.⁴³ The molecular composition affects the frequency of the occurring transition, and therefore, with the presence of a certain molecular motive, the absorption/emission can be selected. Within the range of the atmospheric transparency window (8-13 μm or 770 – 1250 cm^{-1}), deformation vibrations are predominant. Many materials exhibit favorable absorptions from reoccurring molecular motives and their respective deformation vibrations. Synthetic polymeric materials that include functionalities with bonds of C-F, C-Cl, C-O, or C-N are possible candidates for passive radiative daytime cooling because the frequencies of the respective deformation vibrations are likely to be in the correct range.⁴⁴ The resulting flexibility is a clear advantage for selecting a suitable polymer. Researchers demonstrated passive cooling with Poly(methyl methacrylate) (PMMA)⁴⁴, Polyvinylidene fluoride (PVDF)⁴⁴, polymethylpentene (PMP)⁴⁵, clear epoxy⁴⁶, or Polyvinyl fluoride (PVF)⁴⁷. An example of a polymeric cooling material that consists of a porous copolymer of Polyvinylidene fluoride-co-hexafluoropentene (PVDF-HFP)⁴⁸ is presented in Figure 1.8a.

An important polymer that is heavily investigated because of its favorable absorptions is polydimethylsiloxane PDMS⁴⁹⁻⁵¹. The material consists of a Si-O connected polymer backbone with Si-C connected methyl groups. This combination of molecular motives leads to a strong and selective absorption within the atmospheric window. In combination with other properties like low solar absorption, and low cost, PDMS is a simple but highly effective material for

passive radiative cooling. The emissivity of PDMS can be further enhanced by the addition of structure.⁵²⁻⁵⁴ The structured surfaces exhibit lower reflectance in the emission regime, and therefore, higher emittance is achieved. The additional emittance gain of this approach is comparably low, as a plain PDMS surface already has an emittance > 90% in the atmospheric window.⁵⁰ However, this general strategy can be easily transferred to other polymers⁵⁵, offering a versatile approach to fine-tune the emission properties.

The example of PDMS shows that also vibrational modes found in inorganic materials are suitable for passive radiative cooling. Especially a variety of oxides like SiO₂³⁰, SiO₂⁵⁶, Al₂O₃⁵⁷, and Si₃N₄⁵⁶ were considered in previous works. Combining different inorganic materials in a layered fashion is a common approach to optimize the emission of these structures. Photonic materials with stacked layers of different oxides or nitrides can show exceptional selectivity.^{40, 58-60} However, proposed heavily optimized photonic structures can consist of more than 30 layers with complex geometrical architecture.⁶¹ An Example of a photonic structure made from alternating layers of SiO₂ and Si₃N₄ with different layer thicknesses from the work of Yao et al. is presented in Figure 1.8b.⁵⁹

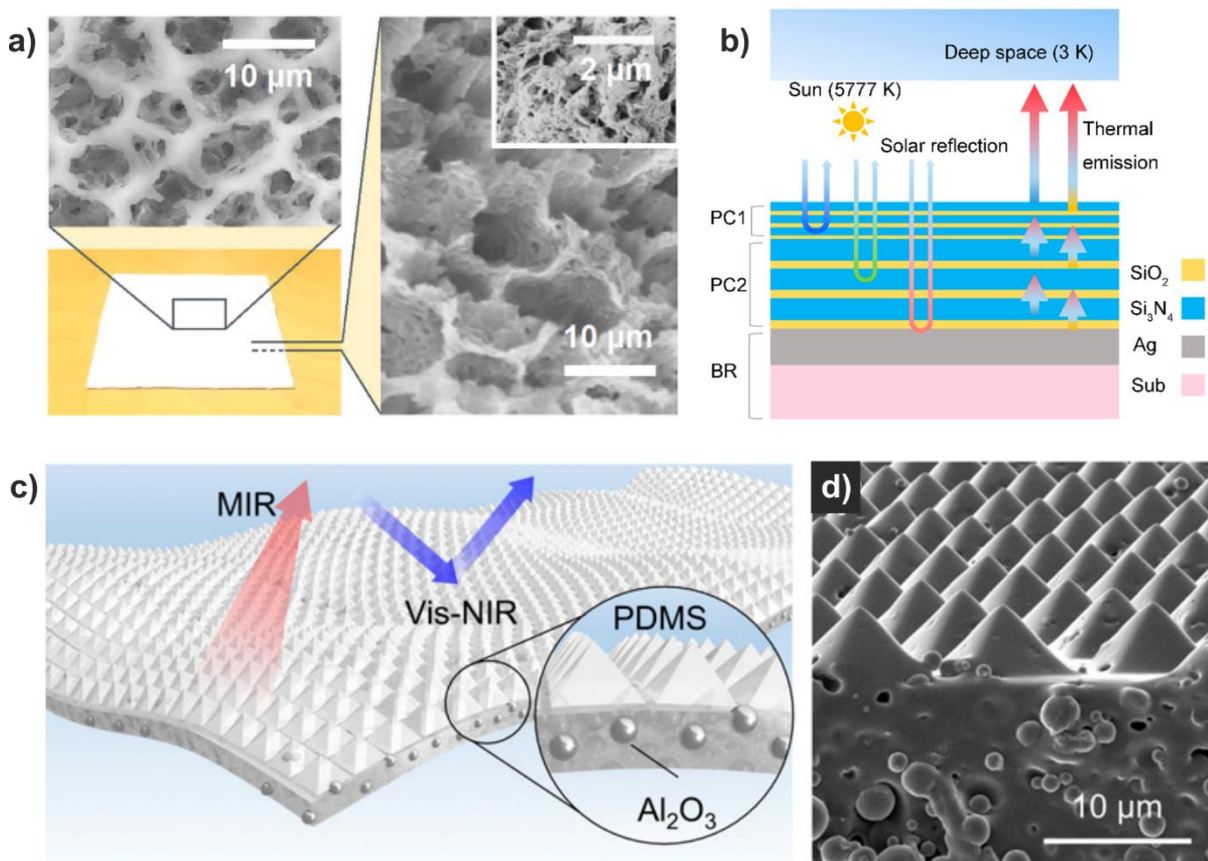


Figure 1.8: a) porous PVDF-HFP copolymer film adapted from the work of Mandal et al.⁴⁸ Reprinted with permission from AAAS. The inset shows the hierarchically porous microstructure of the film. b) Photonic structure build from alternating layers of SiO₂ and Si₃N₄ on a back reflector (BR). The design combines thermal emission and high solar reflectance. Adapted with permission from ref⁵⁹ Copyright © 2023 American Chemical Society. c)

Schematic presentation of the Bio radiative cooling film proposed by Zhang et al.⁶² The material consists of a composite of Al₂O₃ nanoparticles in a PDMS matrix. The surface of the material is structured with a pyramidal pattern to enhance the Vis-NIR reflectance. Permission to reproduce for non-commercial use is granted under the PNAS license.

Another approach for realizing specific emissions is the combination of inorganic particles in a polymer matrix. The theoretic potential of this approach was outlined by Gentle and Smith with the combination of SiO₂ and SiC nanoparticles in a Polyethylene (PE) matrix.⁶³ They showed that the particles strongly and selectively emit in parts of the atmospheric window, while the matrix material contributes little when the overall film thickness is small. The selective nature of the emission from Si-O and Si-C vibrations was later utilized within one material (PDMS), as outlined before. After the initial demonstration of daytime passive radiative cooling with a photonic structure⁴⁰, Zhai et al. prepared a composite material consisting of silica spheres in a PMP matrix.⁶⁴ This material achieved sub-ambient daytime cooling in combination with a silver reflector and has the advantage of being producible in a roll-to-roll fashion. In recent works, other matrix materials like fluorinated polyimide⁶⁵, PMMA⁶⁶, or Acrylic polymer systems^{67, 68} were proposed. Further, particle materials like Al₂O₃⁶⁷, TiO₂⁶⁹, or BaSO₄⁶⁸ gained increasing attention. One example material that combines Al₂O₃ nanoparticles with a PDMS matrix is presented in the work of Zhang et al.⁶² (Figure 1.8c). In general, the combination of particles and a matrix material as a composite offers high flexibility in the selection of materials and the resulting properties.

Besides the choice of materials, also particle size affects the optical response. In the theoretical description of Gentle and Smith, the particle diameter was small (50 nm) compared to the wavelength range of interest (8 – 13 μm), and the film was considered an effective medium.⁶³ In contrast, the composite material demonstrated by Zhai et al. used larger particles with 8 μm in diameter, leading to a broadband emitter.⁶⁴ Therefore, for the design of a composite material, the particle size must be chosen accordingly. Note that the particle size also significantly influences the material response to solar wavelengths. This interaction will be discussed in the following section about solar management.

Solar management

To realize passive radiative cooling below ambient during daytime, the absorption of sunlight needs to be mostly prevented. This is only achievable by high solar reflectance, as transmitted sunlight will be absorbed by underlying layers within the system eventually. For maximized cooling power, no sunlight absorption is the best case. How much solar absorption can be tolerated depends on the exact atmospheric conditions, the material emission properties, and the power and irradiation angle of the sunlight.

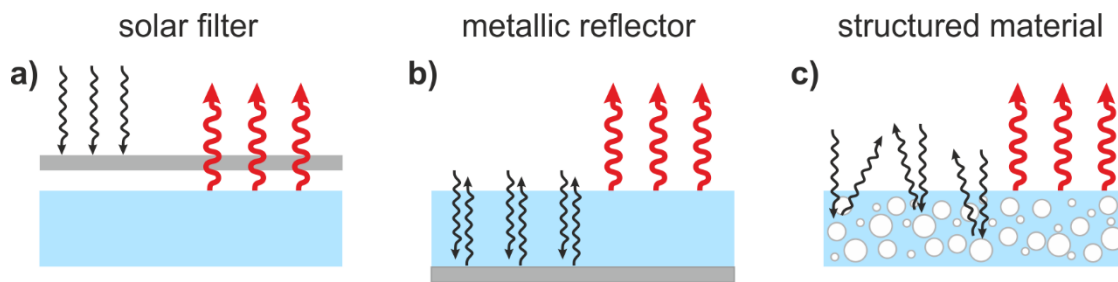


Figure 1.9: Schematic overview of solar management strategies. The solar filter (a) is introduced above the emitter and prevents solar absorption but is transparent for infrared emission. A metallic reflector (b) below the emitter reflects solar wavelengths. The emitter ideally absorbs no sunlight for this approach. c) within a structured emitter material, scattering of solar wavelengths leads to high overall reflectance, and no additional reflector is needed.

For high solar reflectance, three main concepts are currently used and discussed. The three concepts are schematically displayed in Figure 1.9. The solar filter approach Figure 1.9a utilizes the frequency differences between solar irradiation and thermal emission. A cover material is designed above the thermal emitter that is mostly transparent for thermal radiation but reflects sunlight. Early works proposed pigmented polymer foils^{70, 71} but failed to achieve the necessary reflectance to cool below ambient temperature. In more recent works, porosity was introduced to achieve a solar reflectance of 92 %⁷², and 95 % after further optimization.⁷³ While this approach offers more flexibility in the choice of the emitter material, the thickness required for the high reflectance has the drawback of reducing the transmittance within the atmospheric transparency window below 80 %.

The second concept is to use a solar reflector layer below the emitter material Figure 1.9b. This approach is widely adopted in recent works that demonstrate passive radiative daytime cooling.^{49-51, 74} Typically, metal layers like aluminum or silver are used, as they offer high solar reflectance and are easy to apply. While aluminum is cheaper, the lower solar reflectance of 86 to 91 % compared to silver with 92.5 to 95.5 % is not ideal for maximum cooling performance.⁷⁵

The third approach aims to design the emitter material such that it combines the properties of high emittance in the IR and high solar reflectance (Figure 1.9c). This was demonstrated by Mandal et al. in a recent work.⁴⁸ A dual solvent system was used to prepare a hierarchically porous PVDF-HFP film. A solar reflectance of 97 % could be demonstrated while the material strongly emits thermal radiation at the same time. The introduction of a scattering structure in the form of pores is the second widely used approach for solar management.⁷⁶⁻⁸⁴ With this strategy, the commonly used metallic reflection layer can be omitted, but the fabrication of porous structures can be a challenging task, depending on the target emitter material.

From the proposed approaches, the metallic reflectors are the easiest to realize, and substrates are commercially available. The use of reflector substrates, therefore, enables the

direct comparison of different emitter materials, and they can be used as simple reference material in field tests. Throughout this thesis, metallic reflectors are the main tool for solar management in chapters 6,7 and 8. However, chapter 5 presents an alternative approach that relies on the reflectance of a colloidal assembly.

To describe the optical response within assemblies of particles or pores, Mie theory is applied.⁴⁸ If particles are assembled in an ordered structure, additional optical effects can be achieved. For example, in colloidal crystals, a close-packed assembly of colloidal particles, certain wavelengths are strongly reflected.⁸⁵ This causes the assembly to exhibit iridescent (angle-dependent) structural colors that can be tuned by changing particle size.⁸⁶ The fabrication and properties of these materials were studied with great detail.⁸⁷ In contrast to highly ordered systems, also disordered assemblies are of great interest. Within these non-close packed systems, the light transport can be described as diffusive, and the coloration caused by individual Mie resonances and short-range order is angle independent.^{88, 89} For passive cooling, these systems are especially interesting because disordered systems can show remarkable scattering efficiency even for thin layers and low refractive index materials.^{90,}

91

Apart from synthetic materials, also naturally occurring systems can show passive radiative cooling. One example found in nature is the Saharan silver ant (Figure 1.10a). With the intricate structure of its chitin hairs (Figure 1.10b), the ant can maintain a below-critical body temperature, even with direct sunlight illumination in the Sahara desert. The study of the underlying mechanisms by Shi et al.⁹² revealed that the hair structure enhances the solar reflectance while simultaneously decreasing the reflectance for infrared wavelengths (thus enhancing the thermal emittance). Besides this example, other structures found in nature are of great interest for Bio-inspired photonic materials (also beyond the field of radiative cooling).^{93, 94} In nature, the evolutionarily developed photonic structures serve different functions, from thermal management to camouflage. To mimic these structures for passive cooling, different beetle species are especially interesting. A random network structure within *Cyphochilius* and *Lepidiota stigma* beetles showed exceptional scattering properties for comparable low thicknesses and refractive index of the material (Figure 1.10c and d).⁹⁵ Another example is the shell/hollow cylindrical structure found in the *Goliathus goliatus* beetle, which exhibits omnidirectional reflectance for solar wavelengths.⁹⁶

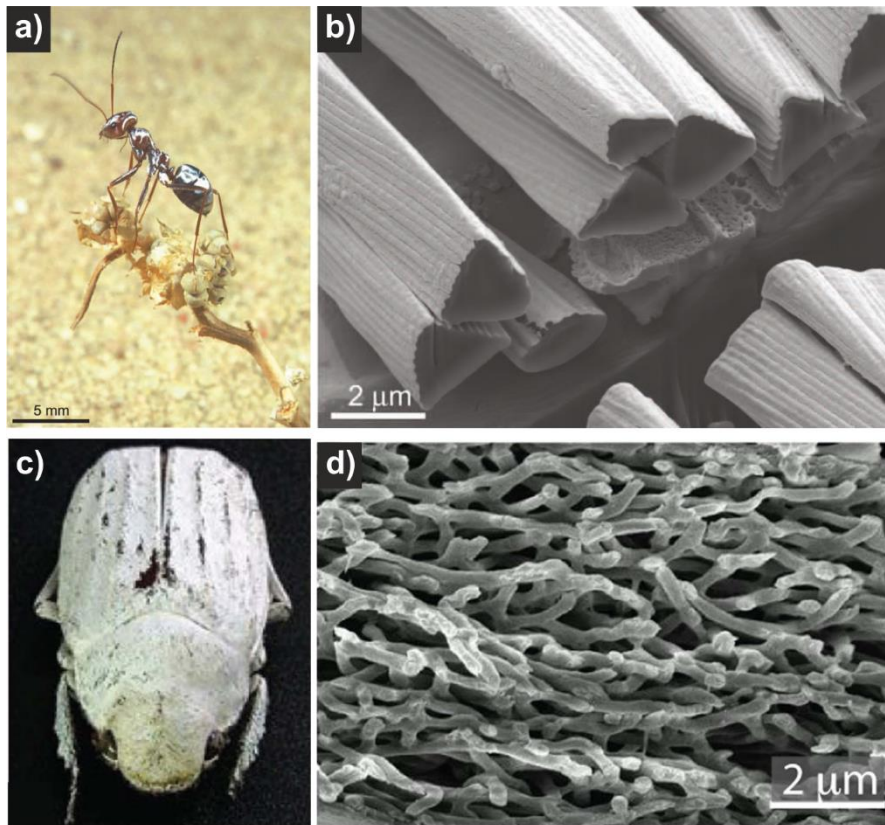


Figure 1.10: a) picture of a Saharan silver ant that displays the reflective appearance of the ant's body. The scale bar is 5 mm. b) A Scanning electron microscope (SEM) image with a cross-section of the ant's hairs reveals the hierarchical structure of the triangular hairs. The scale bar is 2 μm . The images are adapted from ref.⁹² Reprinted with permission from AAAS. c) A photograph of the *Cyphochilius* beetle shows the white appearance of its scales. d) SEM micrograph of the scale cross-section reveals an unorderd network structure. The scale bar is 2 μm . The figure is adapted from the original work⁹⁵ and used according to the permission granted under the Creative Commons Attribution license (CC BY 4.0).

Attempts to mimic biological structures with polymeric material is a common approach in recent literature.^{62, 91, 97-99} However, the actual material the structures are made of in nature (chitin) and its water-processable form (chitosan) received little attention in the field of passive radiative cooling (a detailed study of these materials is presented in Chapter 7). In contrast, cellulose, the chemically similar and most abundant polysaccharide on earth¹⁰⁰, was studied more comprehensively. In a recent publication, Li et al. presented passive daytime radiative cooling with a material that consists of aligned nano cellulose fibers extracted from wood.¹⁰¹ Other works used cellulose in combination with silica particles¹⁰² or prepared a material from cellulose acetate⁸⁴ for the purpose of passive radiative cooling.

Besides cellulose also, silk was investigated as a biomaterial for passive radiative cooling¹⁰³, and a silk-inspired system was presented.¹⁰⁴ Especially the high reflectance for visible wavelengths in natural silk is a clear advantage of the materials. The origin of this property was found to be rooted in the randomly distributed nanofibrils within the individual silk fibers.

This intricate structure hinders the free diffusion of light (Anderson localization), resulting in high reflectance.¹⁰⁵

The presented examples show that, in nature, the combination of material and structure leads to advantageous effective properties. For the application or transfer to passive radiative cooling systems especially, the light scattering mechanisms are interesting to improve solar management strategies. But also, the used materials are a source of inspiration for biocompatible and sustainable passive cooling systems.



2. Method Section

With the demonstration of below ambient passive daytime radiative cooling and the newly gained interest in the concept, also new characterization methods were developed to assess the material performance. In this section, a summary of the current state-of-the-art methods and technical challenges for optical characterization relevant to this thesis are described.

Rooftop Experiment

The actual demonstration of passive radiative (daytime) cooling is mainly done in a field test. The sample is exposed to the atmosphere and outer space for the radiative energy exchange to take place. To evaluate the overall cooling performance of a material, two strategies are widely adapted: The measurement of the equilibrium temperature in a steady state or the measurement of the cooling power with a feedback-controlled system to hold the temperature at a constant value.⁵⁵

Temperature measurement

The setup for the measurement of equilibrium temperature typically consists of a temperature sensor below the sample to track the sample temperature. The sample is placed in an isolating enclosure (foam) to minimize conductive losses. A thin PE cover foil is used to prevent convective losses, which prevents air exchange to the outside of the enclosure. At the same time, the cover is mostly transparent for infrared and solar radiation, not to strongly interfere with the radiative balance of the sample system. Below the sample, a highly thermally conducting metal plate can be used to ensure a homogeneous temperature distribution. An example setup as used by Li et al.¹⁰⁶ is shown in Figure 2.1a.

For the actual measurement, the setup is presented to the atmosphere under outside conditions. An elevated position is chosen (rooftop) to access the entire hemisphere and to avoid radiative thermal contact with other objects like buildings or vegetation. More advanced constructions can include a cover frame to change the accessed angle range of the emittance.⁵⁰ Another option is to block direct sunlight illumination during the daytime with a shading cover.¹⁰⁷

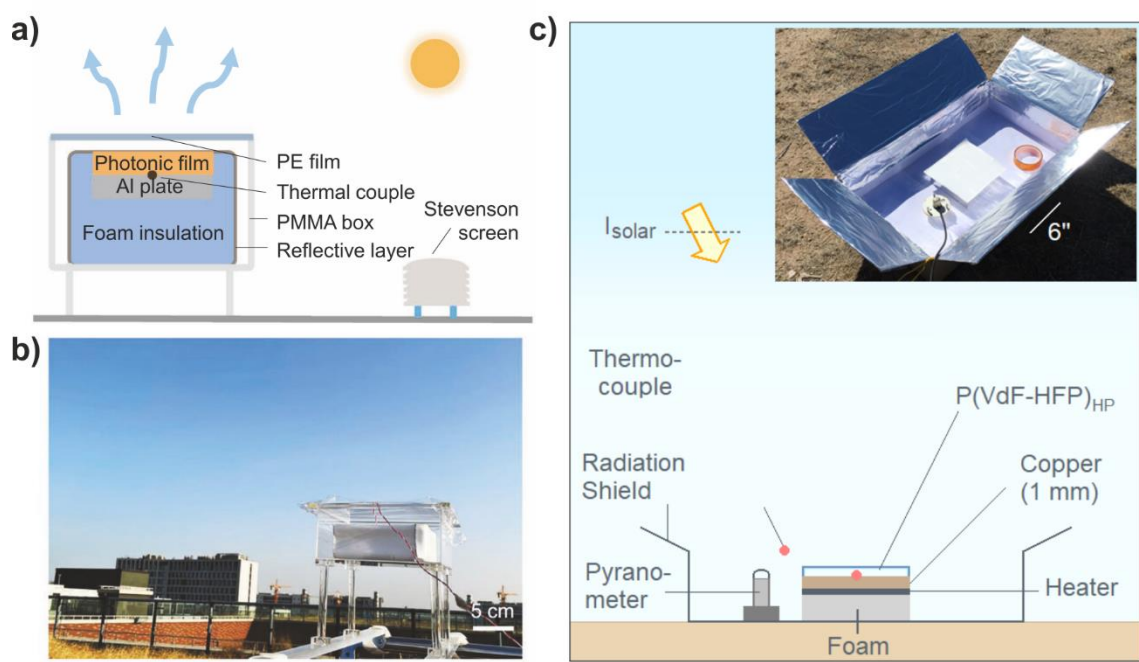


Figure 2.1: a) Typical Rooftop setup for measurement of the below ambient temperature as presented in the work of Li et al.¹⁰⁶ A thermocouple below the sample (photonic film) monitors the temperatures. Foam insulation is applied to prevent conductive losses, and a PE cover film reduces convective losses. For an even temperature distribution, this setup includes an aluminum plate. The ambient temperature is monitored next to the setup with a weather station (Stevenson screen). A picture of the actual setup is shown in panel b). Adapted with permission from ref¹⁰⁶ copyright © 2021 Wiley-VCH GmbH. b) From the work of Mandal et al.⁴⁸ Reprinted with permission from AAAS.

As the emitted power (and consequently, the equilibrium temperature with respect to ambient) is a function of ambient temperature, the surrounding temperature must be monitored. The ambient temperature measurement is equally important, as it marks the reference point for below-ambient cooling. Where this temperature is measured is ambiguous and, thus, reduces the comparability of results. Sometimes, the ambient temperature measurement is performed either next to the setup^{68, 108} or integrated into a weather station.^{74, 106} The reference temperature measurement within the sample box can result in thermal contact between the sample and reference and is consequently not ideal. A possible solution is presented in chapters 6 and 7 with the construction of multiple equally designed test boxes, where one is designed for the reference measurement.

Power Measurement

The second commonly applied option to evaluate the material performance aims to measure the cooling power of the sample.^{64, 109, 110} The overall approach and setup follow a similar design as the temperature measurement. However, in this approach, a feedback-controlled heater system below the sample holds the temperature constant. An example setup for this measurement approach is presented in Figure 2.1b. The power input to drive the heater is monitored and directly translates to the overall cooling power. If the system is held at ambient

temperature, the non-radiative losses are greatly suppressed and ideally vanish, as they are a function of temperature difference with respect to ambient. By setting different temperatures below and above ambient, the non-radiative heat loss coefficient of the setup can even be determined.⁷²

Indoor Experiment

One main challenge for all setups is the comparability of obtained results. The atmospheric conditions and solar irradiation fluctuate depending on the exact location and time with seasonal and daily changes. The temperature or power measurements for the samples are supplemented with additional measurements of the total solar irradiation, wind speed, and humidity. For these data, the standardized methods developed by meteorologists can be utilized, and instruments are commercially available. However, the direct comparison of two materials is only possible by measuring them simultaneously and in the same location with identical setups.

One way to become independent of atmospheric conditions would be to construct an artificial measurement setup. A first attempt was shown by Zhou et al. with a liquid nitrogen-cooled container, including an absorber as a heat sink.⁵⁰ In the work of Park et al., a similar setup is demonstrated that even includes a solar simulator to emulate solar irradiation during daytime.¹¹¹ One attempt is also presented in this thesis in chapter 8, but to mimic all aspects of the outside measurement (sun, atmospheric selectivity, and outer space) perfectly, remains a challenge.

Characterization Techniques for Optical Properties

The optical properties of a material are key to tailoring the radiative energy exchange of the material and its surrounding. For incoming radiation (loss), the absorption properties over the entire spectrum of electromagnetic radiation are relevant. In contrast, the energy radiated off by the material depends on the emission properties and the temperature of the material, as described by Planck's law. For the application as a passive radiative cooling material, the wavelength range of interest is localized between the UV-Vis region and the far-IR. Consequently, to predict the performance of passive cooling materials, the optical properties need to be known for this large wavelength range. In the following section, the technical aspects of measuring the broadband optical response of materials (as performed in this thesis) are briefly discussed.

Experimentally spectroscopic techniques are employed to measure the reflectance and transmittance of the sample material directly. The absorptance, and consequently, emittance, is then calculated considering energy conservation as introduced in equation (19). Because

the wavelength range of interest is large, typical instruments cannot probe the entire range of interest. However, with a UV-Vis and Fourier-transform infrared (FTIR) spectrometer (which are commercially available), most of the relevant wavelengths can be investigated. A typical setup includes a radiation source that illuminates the sample, and the transmitted/reflected intensity is detected. Wavelength discrimination is either achieved with an optical grid to select individual wavelengths (UV-Vis), or an ensemble signal is collected, and in combination with an interferometer, a spectrum is extracted with Fourier transform of the signal. With respect to a reference measurement, the quantity of interest is finally extracted.

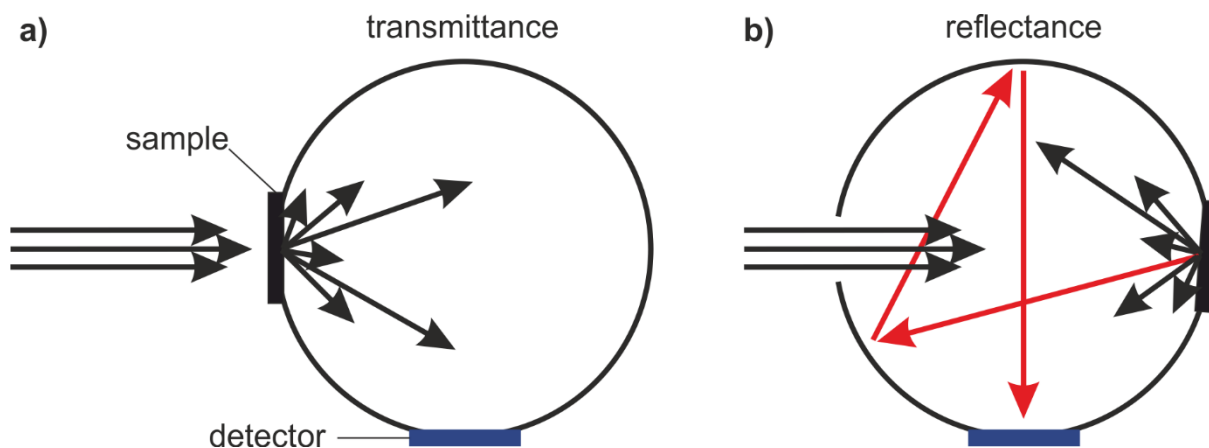


Figure 2.2: Illustration of the light propagation within an integrating sphere for transmittance a) and reflectance b) geometry, respectively. The reflected or transmitted light is diffusely distributed within the integrating sphere, and the detector (bottom of the sphere) measures an average illumination signal.

For samples that include inhomogeneities like structures or in composite materials, scattering of transmitted or reflected light needs to be considered. An integrating sphere is included in the measurement geometry to collect scattered light intensity.¹¹² The measurement geometry for transmittance and reflectance is schematically displayed in Figure 2.2. The sphere is made of a material that is highly reflecting in a diffuse manner. For the UV-Vis wavelength range, fluorinated polymers or BaSO₄ coatings are used, while for IR wavelengths, a diffuse gold coating is applied to the sphere surface. The sample is mounted at an opening of the sphere, and the transmitted or reflected light is diffusely distributed within the sphere. The measurement signal is the average illumination intensity of the sphere with respect to a reference sample. The signal is collected with a detector that is ideally placed such that specular reflected or transmitted light does not reach the detector directly (overestimation of average illumination). The quantity of interest is not measured with perfect accuracy, as the sphere needs to have an opening for the incident beam, and the sample needs to be mounted to cover parts of the sphere. A fraction of the light will, therefore, escape the sphere or is not contributing to the average illumination in an equal manner. In general, with a larger integrating sphere diameter, a smaller fraction of the sphere surface is needed for openings, and the

accuracy is higher. This is especially relevant if different instruments and spheres are used as required to investigate passive radiative cooling materials. Another challenge is the selection of a reference sample for the integrating sphere measurement. A mirror reference is recommended for mostly specularly reflecting surfaces, while for rough, structured, or composite samples, a diffuse standard is chosen.

An example measurement for a film that scatters light is presented in Figure 2.3. The transmittance measured for normal incidence and detection in the normal direction is below 80 % for the entire measurement range. However, a measurement with the integrating sphere that also collects scattered light reveals that the overall transmittance is even above 80 % for the entire wavelength range. Without the integrating sphere, the transmittance is underestimated, and therefore, the absorptance of the sample is overestimated.

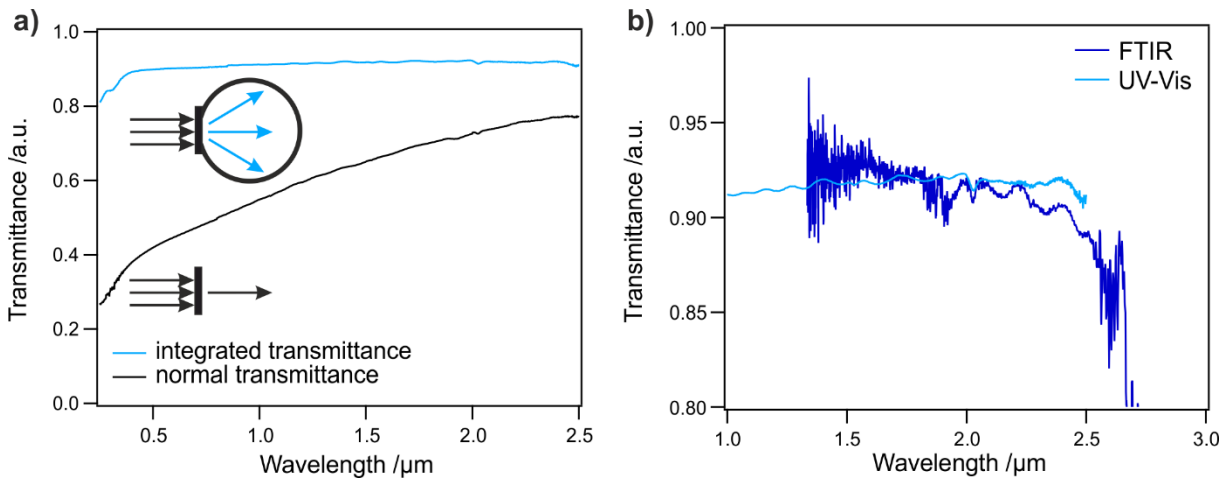


Figure 2.3: a) Comparison between normal and integrated transmittance for an example polymer composite film with scattering particles. The detected transmittance intensity is much higher if the scattered light is included. b) Changeover region between the UV-Vis and FTIR spectrometer with overlap of the traces between wavelengths of 1.3 μm - 2.5 μm . Quantitative agreement between the two measurements at the different instruments is found.

Besides the recognition of scattering contributions, another challenge for the experimental measurement of the optical properties is the large wavelength range of interest. To cover the wavelength range from UV to IR, different instruments are used with multiple light sources, detectors, and reference samples. The large number of components leads to multiple changeover points within the measurement, and following, the critical wavelength regions will be briefly introduced.

The most dominant changeover is between the UV-Vis and FTIR spectrometer. Two example spectra are presented in Figure 2.3b for transmittance measurements at the respective integrating spheres. The UV-Vis measurement range extends up to a wavelength of 2.5 μm while the FTIR spectrometer measurement starts at 1.3 μm . An overlap region is apparent, and very similar transmittance is found for the sample. To calculate the cooling performance

of materials, the spectra are combined by cutting both spectra at $2\ \mu\text{m}$ as the edges of the probed range show increased noise (especially for FTIR due to low light source intensity for these wavelengths). If a disagreement between the two instruments occurs, different factors can be the cause. The spot size between the instruments is different, and for inhomogeneous samples, the measured quantity can deviate. Other reasons for a disagreement could be the sphere size difference or the choice of reference material.

Other critical changeover points are located in the Vis region of the spectrum. To cover the entire measurement range ($0.25\ \mu\text{m} - 2.5\ \mu\text{m}$) within one instrument, two light sources, two grids, and two detectors are used. One difficulty for the detector changeover is the polarization dependence presented in Figure 2.4a. The example sample is measured in transmission geometry, and a polarizer is included within the measurement path. The two polarization directions are measured individually, and a step in transmission intensity can be observed at the detector changeover wavelength ($1.05\ \mu\text{m}$). After averaging the two measurements, the step vanishes. Polarization effects are most visible at the changeover points as the detector is polarization sensitive, and optical components like the grid for wavelength selection will partially polarize the incident beam.¹¹³ The step can be severe, especially for samples with a certain anisotropy. If no polarizer can be included in the beam path, two measurements can be averaged after rotating the sample by 90° , respectively. This technique can potentially reduce the step (for example, at the port of the integrating sphere).

Another reoccurring difficulty for samples investigated within this thesis is related to an interference effect visible for thin films. Figure 2.4b shows a transmittance experiment performed on a thin polymer film. An oscillating transmittance intensity is apparent that originates from the interference of the directly transmitted beam with the partially reflected beam at the interfaces of the film. The amplitude of the oscillations changes at a wavelength of $0.85\ \mu\text{m}$, the detector and grid changeover point for this experiment (dashed line). To elucidate the change in intensity, a series of experiments are presented in Figure 2.4c and d that were measured at the same sample with different spectrometer settings. The sample is a thin film on a reflective substrate, and the presented traces are vertically shifted for better comparison. The changing parameter is the set spectral bandwidth (SBW), a parameter that describes the width (full-width half maximum) of the incident wavelength distribution after the optical grid. The SBW is controlled with a slit opening after the grid within the spectrometer. With higher spectral bandwidth (slit open) overall, more light intensity is achieved, and the signal-to-noise ratio is improving. However, the wavelength resolution decreases, and the interference effect is less resolved. Thus, the amplitude of the oscillations decreases. This is also the case if the sample region is inhomogeneous, as the interference effect is sensitive to the sample thickness. Changing spectral bandwidth can lead to abrupt intensity fluctuation and

occurs at the grid and detector changeover point (Figure 2.4, dashed line). This challenge can be solved with fixed SBW, however, overall at the cost of wavelength resolution and reduced signal-to-noise ratio towards the infrared region.

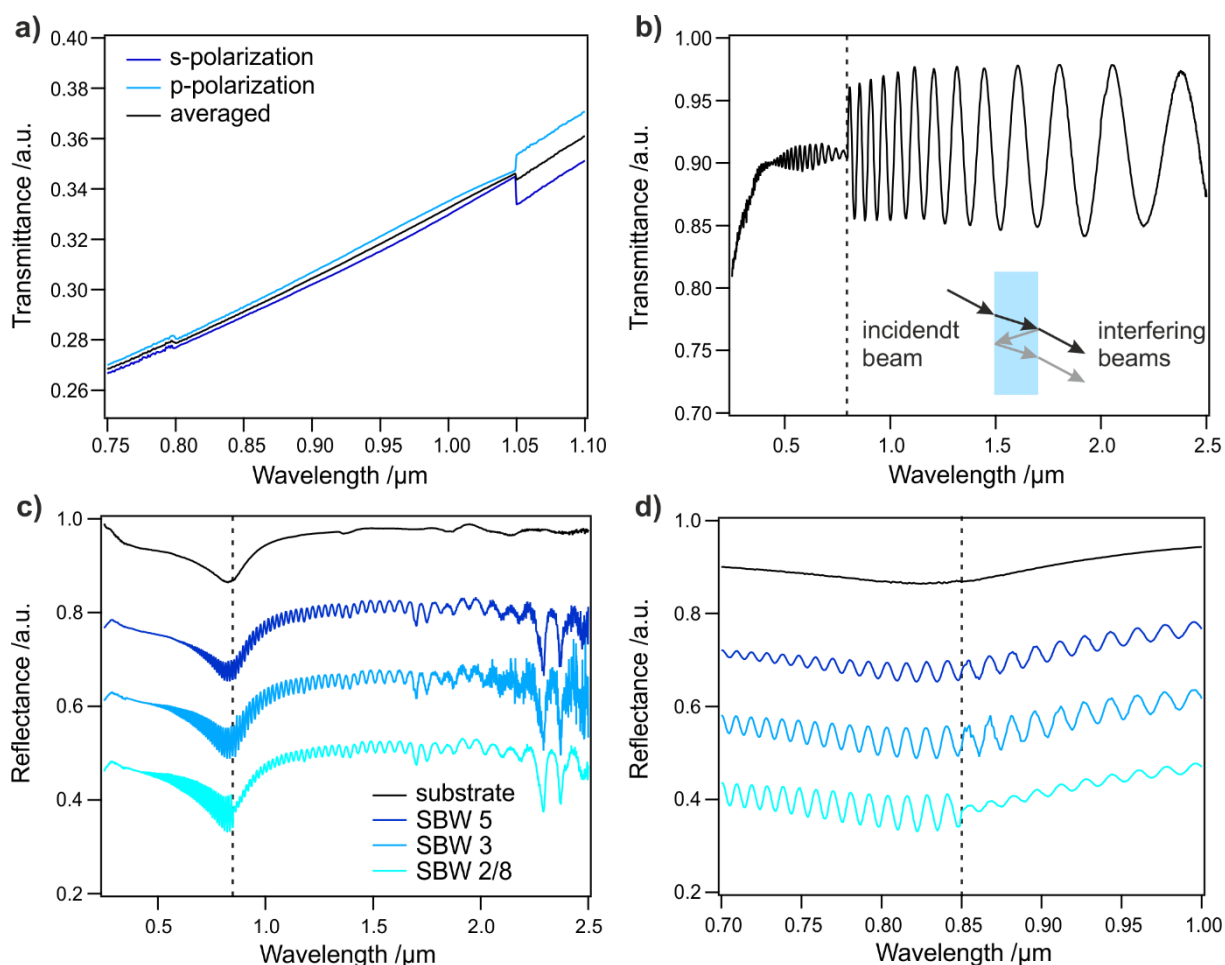


Figure 2.4: a) polarization-dependent transmittance measurement with detector changeover at 1.05 μm . The jump in transmittance intensity at the changeover point can be diminished by averaging both polarization directions. b) transmittance measurement of polymer thin film with periodically fluctuating intensity caused by interference of the primary beam with the double reflected beam. The dashed line marks the detector and grid changeover point for the measurement. c) reflectance measurement of polymer thin film on a reflecting substrate with different spectral bandwidth settings. The traces are shifted vertically for a better overview. With lower spectral bandwidth towards infrared wavelengths, the noise level increases. d) zoom-in around the detector and grid changeover point (dashed line) reveals a higher resolution of interference (increased amplitude of oscillation) for smaller spectral bandwidth. Different spectral bandwidths before and after the changeover lead to a jump in intensity.

Polymeric thin films are a common sample type throughout different contributions of this thesis, and investigating and solving the described challenges was an integral part of my work. However, the technical aspects of the measurements are of minor importance in the context of the individual contributions and will not be further discussed in the following chapters.



3. Thesis Outline

3.1 Synopsis

This thesis presents new design strategies, materials, and characterization methods for passive radiative cooling. Five individual contributions are included that treat different aspects of how optical properties influence radiative heat transfer. A schematic overview of the different contributions of this thesis is presented in Figure 3.1.

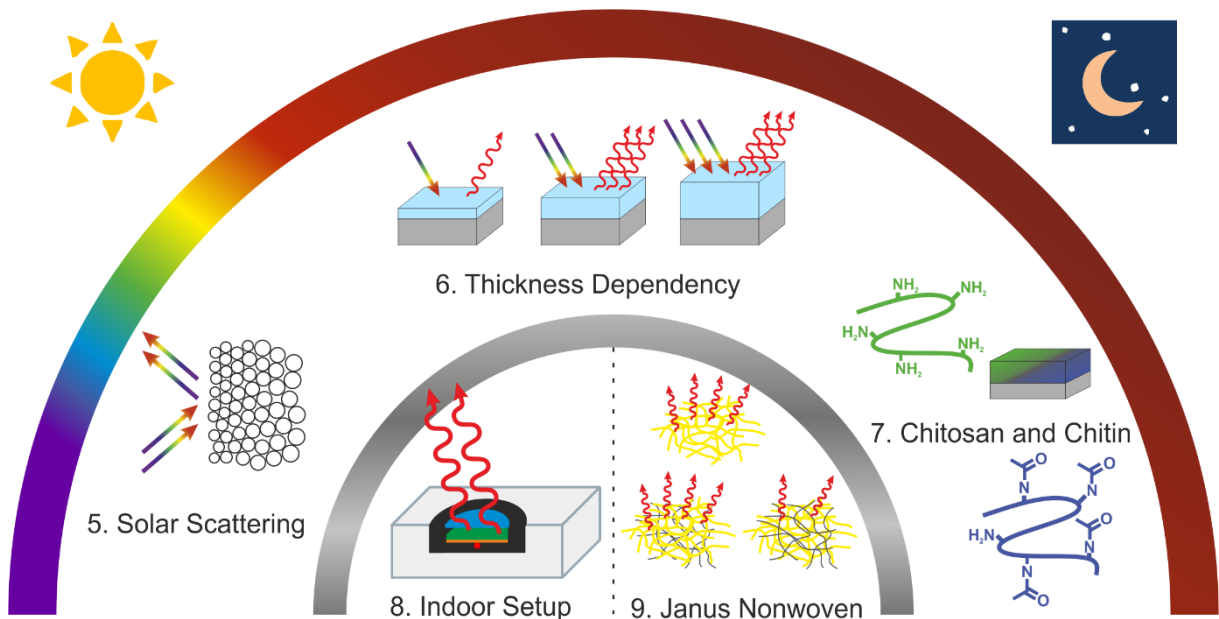


Figure 3.1: Schematic overview of the content presented within this thesis. Chapters 5 – 7 discuss different design aspects of Materials for passive radiative cooling. Chapters 8 and 9 present advancements in radiative heat transport characterization.

In the first part of the thesis (chapters 5 – 7), different material design aspects for passive cooling materials are investigated. Chapter 5 presents a novel synthesis method for colloidal polymer particles with gradually increasing size. The work of this contribution has been conducted in cooperation with Marius Schöttle. Individual fractions of particles were extracted, and their size and optical response in crystalline assemblies were analyzed. A colloidal glass was assembled from the individual fractions with a continuous size gradient from bottom to top, and the reflectance of these novel assemblies and suitable reference systems were studied with spectroscopy. The unique broadband reflectance of the gradient mesostructure is a feature that expands the toolbox of solar management strategies for passive radiative daytime cooling.

In chapter 6, the role of another material parameter of radiative daytime cooling materials is discussed: layer thickness. A theoretical framework enables the calculation of the material cooling performance solely based on complex refractive index data. The theoretical

calculations are verified by comparing samples with different layer thicknesses. This comparison includes extensive optical characterization over a broad wavelength range from UV-Vis to mid-IR. The study reveals an optimum thickness for both daytime and nighttime operation. In chapter 7, the cooling potential of films made from the Bio-derived materials Chitosan and Chitin are evaluated in detail. A transformation reaction between the two polymers is presented that can be performed in the solid state. To quantify the reaction process, solid-state nuclear magnetic resonance (NMR) spectroscopy is applied. The water processability of chitosan becomes a drawback in an outside application. Thus, the water stability of chitosan and chitin is assessed in a dissolution experiment. Additionally, the cooling performance is estimated based on the optical properties and confirmed in a field experiment.

The second part of the thesis revolves around methods developed to characterize the radiative heat transfer properties of materials. To quantify the radiative cooling performance, rooftop experiments are widely performed. Chapter 8 presents an indoor setup that aims to mimic typical outside conditions for field tests of radiative cooling materials, which has been developed in cooperation with my colleagues Qimeng Song and Thomas Tran. The setup enables reproducible characterization of the passive cooling properties independent of outside conditions. A hemispherical dome is used to resemble the radiative energy transfer problem of the earth's surface to outer space. With the addition of a mid-IR filter, even atmospheric selectivity is introduced to this artificial system. Finally, chapter 9 presents how the radiative energy transfer experiment of a sample in the hemispherical dome can be adapted to characterize textile materials. Specifically, it is investigated how the optical properties of a dual-sided textile fabricated by my collaborator Qiang Gao affect the radiative energy loss from the human body to the surrounding. Following, the results of the individual contributions to this thesis will be summarized.

The first contribution (Chapter 5) presents a synthesis method for colloidal polymer particles to obtain particles with gradually increasing size, which was developed by my colleague Marius Schöttle. Fractions of the synthesized particles can be stored in a tube with the introduced controlled emulsion extraction process (CrEEP). Each fraction contains a distinct particle size that increases in subsequent fractions with a longer reaction time.

The stored fractions were used to produce different colloidal glass assemblies to study their optical properties. One set of glasses consists of particles with uniform sizes but different diameters (Figure 3.2a and b). The optical properties of these assemblies were compared to a bilayer colloidal glass (Figure 3.2c) and a continuous gradient assemble. To prepare the continuous gradient, the fractions were gradually assembled with increasing size, resulting in a colloidal glass with continuously increasing particle size (Figure 3.2d).

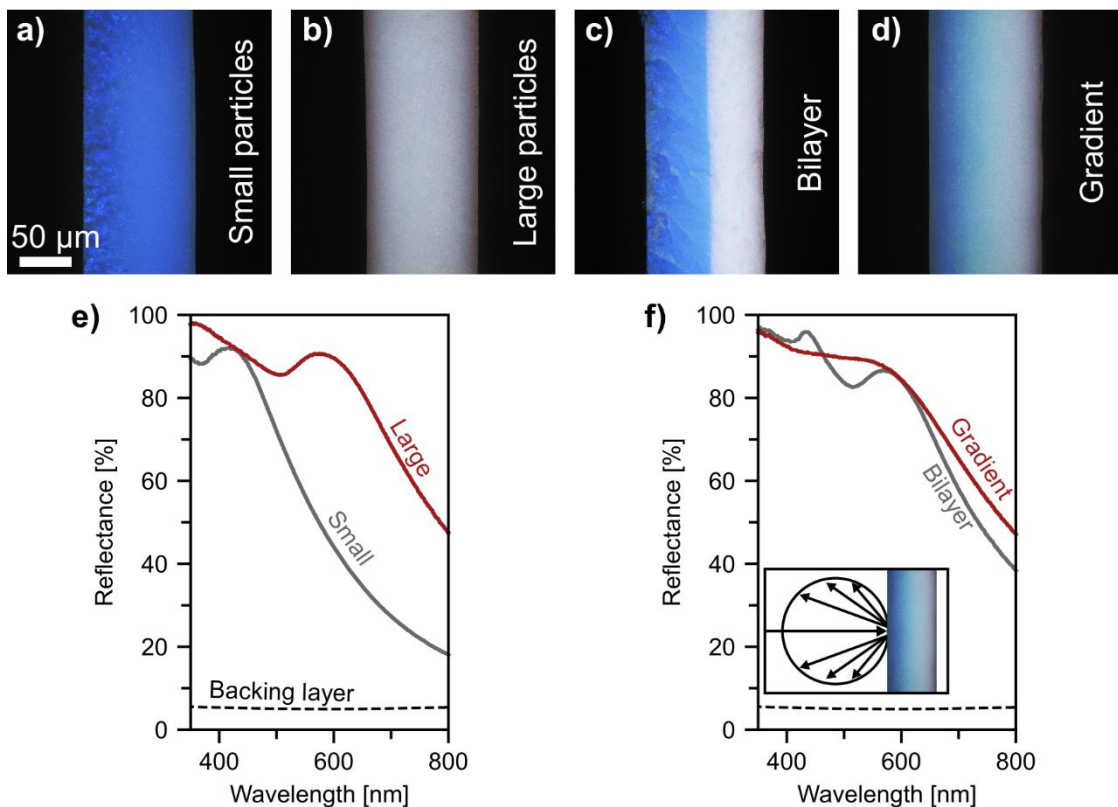


Figure 3.2: Optical microscopy images displaying cross-sections of different colloidal glass assemblies (a – d). The scale bar is 50 μm. e)-f) Respective UV-Vis reflectance spectra of the presented colloidal glass assemblies measured with an integrating sphere. The inset in f) shows the measurement geometry. The backing layer attaching the samples to a substrate has negligible reflectance (dashed line). The figure is adapted from the original publication¹¹⁴ and used according to the permission granted under the Creative Commons Attribution license (CC BY 4.0).

The reflectance of the respective assemblies was measured with a UV-Vis spectrometer at the reflectance port of an integrating sphere. With this measurement, the specular and diffuse reflected light is collected. The samples were mounted on supporting glass substrates with sticky carbon tape as an adhesive layer, as freestanding samples were not stable enough.

While ordered assemblies show distinct reflectance peaks due to the long-range order and fixed interparticle distance⁸⁶, the response of colloidal glasses is fundamentally different. In disordered systems, Mie resonances of the individual particles show angle-independent coloration obscured by diffuse light scattering. This optical response can be observed in the resulting reflectance spectra of the individual particle glasses Figure 3.2. Both assemblies exhibit a reflectance peak at different wavelengths (small at 420 nm, large at 580 nm) due to their respective Mie resonance. A contribution from the adhesive backing layer is minor compared to the overall reflectance of the assemblies.

In contrast, the gradient mixture exhibits a less pronounced reflectance peak at ~515 nm. With particles of different sizes, the respective Mie resonances are expected to overlap to one continuous reflectance response. The unexpected reflectance peak of the gradient mixture is not the response of formed crystallized particle clusters, as an SEM analysis revealed a statistical distribution of particle sizes. Analysis of simulated pair distribution functions reveals that a certain particle correlation (short-range order) persists for the gradient mixture. Therefore, we attribute the more pronounced reflectance of the gradient mixture to this correlation. In contrast, the continuous gradient assembly has broad reflectance for the entire wavelength range between the expected resonances of the particles.

This behavior is especially interesting for applications where broadband reflectance is required. With the variation of size range and particle type, the presented approach can be used to realize the strong reflectance of a target wavelength range. In the context of passive radiative cooling, broadband reflectance is required to prevent the absorption of sunlight. By extending the plateau region in the reflectance spectrum gradient, colloidal assemblies could realize the necessary reflectance. The contribution shows one example of how to improve solar management strategies for passive radiative daytime cooling. Besides strong solar reflectance, the systems for passive radiative cooling should have high thermal emittance and low solar absorptance for good performance. These aspects are the focus of the second contribution of this thesis.

In Chapter 6, we extended the methods for predicting the performance of materials for passive radiative cooling. Specifically, we studied the effect of layer thickness on the overall performance. While parameters like broadband or selective emitter and angle selectivity were previously regarded in detail in the literature, the contribution of material thickness received far less attention. Typically, an emitter material thickness was chosen to be sufficiently emissive within the atmospheric transparency window. However, this does not consider changes in solar absorption or emitter selectivity with varying thicknesses.

To address the thickness dependence, we used available complex refractive index data of typical polymeric materials to calculate the optical properties. An example of PDMS is shown

in Figure 3.3. The calculation yields the absorptance as a function of wavelength, a quantity also accessible by spectroscopic analysis. For the experimental verification, very simple radiative cooling films were prepared. They were built by combining a silver mirror for solar reflection and PDMS films of different thicknesses as emitter layers. Figure 3.3 compares the absorptance spectra of actual samples with known thicknesses (Figure 3.3a) and calculated spectra (Figure 3.3b).

The calculated spectra show that thin layers also show substantial absorptance for wavelengths with a high absorption coefficient k . In contrast, wavelengths with low magnitudes of k are only absorptive for thicker layers. Therefore, the layer thickness affects the sample's thermal emission and the loss of cooling power due to solar absorption or atmospheric radiation. The presented material transitions from selective emission within specific wavelengths for a thin film to unselective and broadband emission for thicker layers.

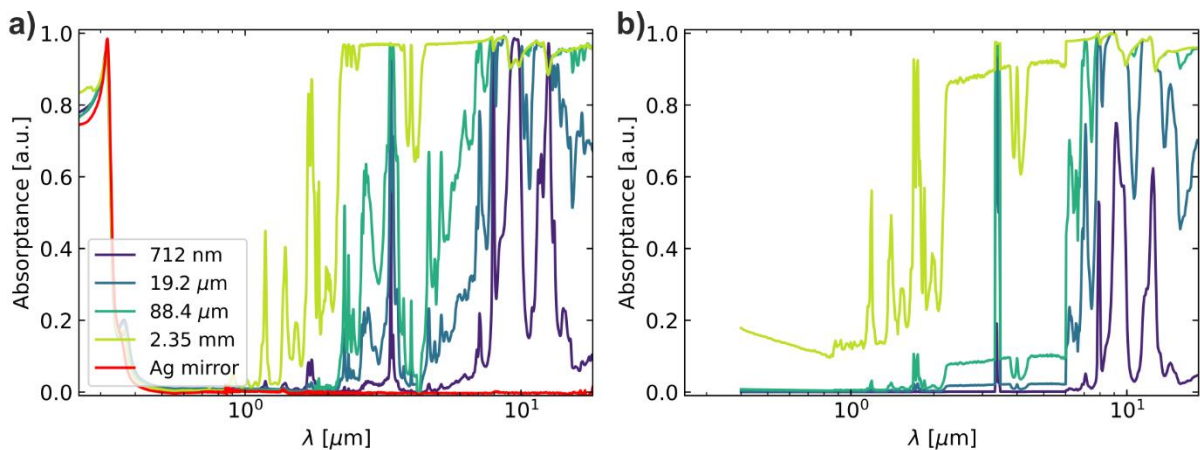


Figure 3.3: a) UV-Vis absorptance spectra calculated from integrating sphere experiments (1-R) for PDMS films with different thicknesses measured on a reflective silver mirror. The spectrum of the plain mirror is shown for reference. b) simulated absorptance spectra for the PDMS film thicknesses presented in a). The figure is adapted from the original publication²⁶ and used according to the permission granted under the Creative Commons Attribution license (CC BY 4.0).

The cooling performance of the material can be estimated after calculation of the respective emitted power of the material and consideration of loss due to atmospheric back radiation or solar irradiation. Discrimination between daytime and nighttime case (with and without solar irradiation) is practical. The calculations reveal a thickness dependency of the individual contributions. A positive net cooling power translates to a temperature reduction of the material until an equilibrium temperature is reached with $P_{\text{cool}} = 0$. The expected temperature reduction below ambient as a function of layer thickness (Figure 3.4a and c) reveals an optimum layer thickness for both day- and nighttime cases. The dotted line depicts the respective layer thickness with the highest cooling power. Consequently, the thickness with the highest possible cooling power at ambient temperature differs from that with the lowest possible

equilibrium temperature. This result is highly relevant for practical applications of passive cooling materials, as the material can only be optimized for one case. The calculated trend was also validated with a rooftop experiment. The temperature reduction compared to a plain substrate was measured for samples with thicknesses from hundreds of nanometers to several millimeters. The measurements (Figure 3.4b and d) confirm the predicted trend and reveal an optimum thickness for the daytime case.

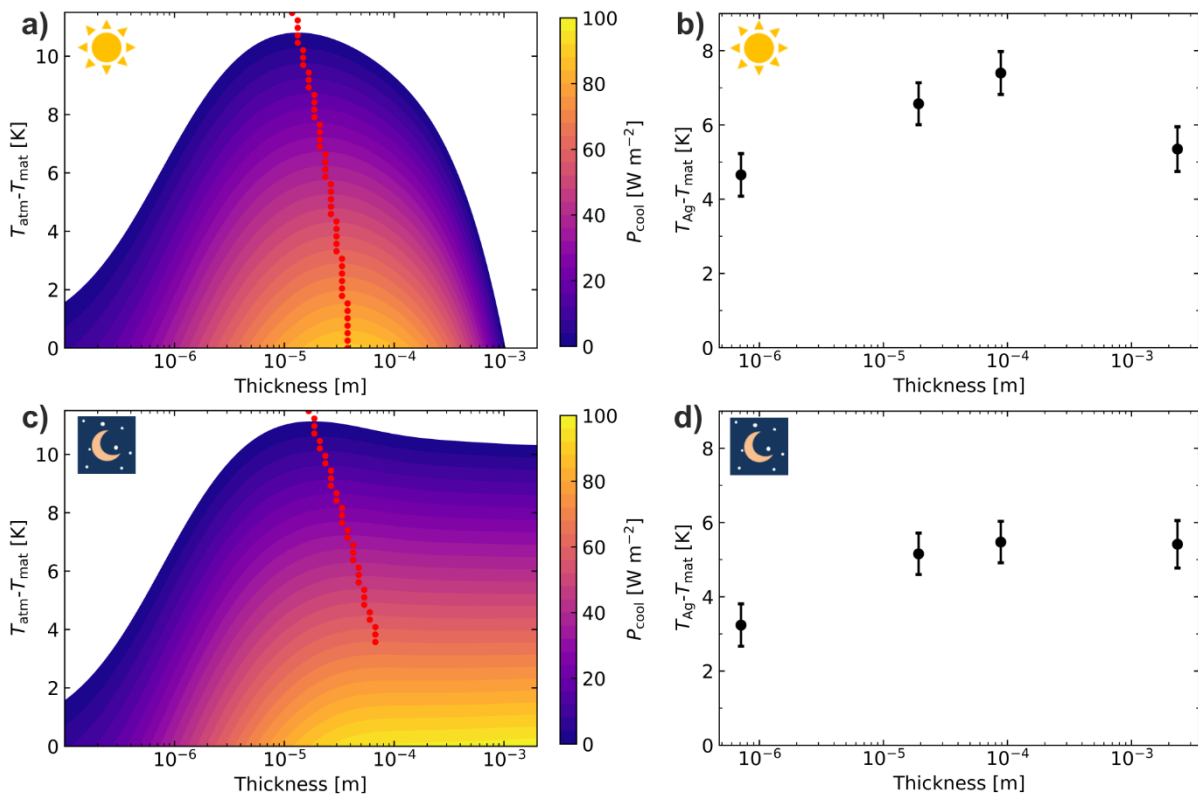


Figure 3.4: Cooling power (color coded) as a function of the material thickness (x-axis) and temperature difference to ambient (y-axis) for daytime- (a) and nighttime-case (c). The dotted line depicts the thickness with maximum cooling power. The measured temperature reduction of actual samples with distinct thicknesses is presented for daytime- (b) and nighttime-case (d). The error bars are the standard deviation of the average measurement interval. The figure is adapted from the original publication²⁶ and used according to the permission granted under the Creative Commons Attribution license (CC BY 4.0).

The shown optimization can be applied to other materials if complex refractive index data are available. This transfer based on optical properties can be challenging for complex architectures like composites or structured materials, as calculations or measurements for the relevant wavelength range are difficult. However, even if the calculation from complex refractive index data is not possible, after the measurement of the absorptance, the cooling power can be estimated and determined for different sample thicknesses. Note that for the calculation from measured absorptance data, the angle dependence of the emission is not considered, as the integrating sphere measurement does not discriminate the emission angle

but measures an ensemble signal. However, predictions for the optimum thickness (range) are made that can be verified in a field test.

For the application of passive cooling materials, more factors than performance optimization must be considered. One of those factors is the persistence time of the material in the environment. Especially for state-of-the-art cooling materials that use fluorinated polymers, very long persistence times can be expected.¹¹⁵ Alternatives are materials commonly found in nature, as they are known to be compatible with ecosystems. Strategies found in nature, like certain composites or structures, have also served as inspiration for advanced artificial materials.⁹³ Chapter 7 focuses on the biomaterials Chitosan and Chitin and their potential for passive radiative cooling.

Chitin is the acetylated form of the polysaccharide pol-N-glucosamine (Chitosan). The chemical structure of the two materials is very similar (Figure 3.5a), and conversion can be achieved with an N-acetylation or deacetylation reaction, respectively. Compared to many other polymer systems, chitosan has the advantage of being processable from a slightly acidic aqueous solution. After processing, chitosan can be transformed into chitin while retaining its solid-state structure. This combination of properties offers high flexibility for the application of the material.

To evaluate their potential for passive cooling, a set of Chitosan and Chitin films was produced, and their optical properties were compared (Figure 3.5b and d). As outlined in Chapter 6, the material thickness significantly influences the optical properties. Therefore, a set of different film thicknesses were realized. A silver mirror was used as a back reflector, an easy way to achieve high overall reflectance for solar wavelengths. The presented samples show very low solar absorption, between 3.1 % and 6.9 %, respectively. At the same time, a multitude of absorption peaks can be observed towards the IR region. Due to the diversity of functional groups within the chemical structure, a large variety of absorption frequencies can be expected that lead to the respective absorption resonances.

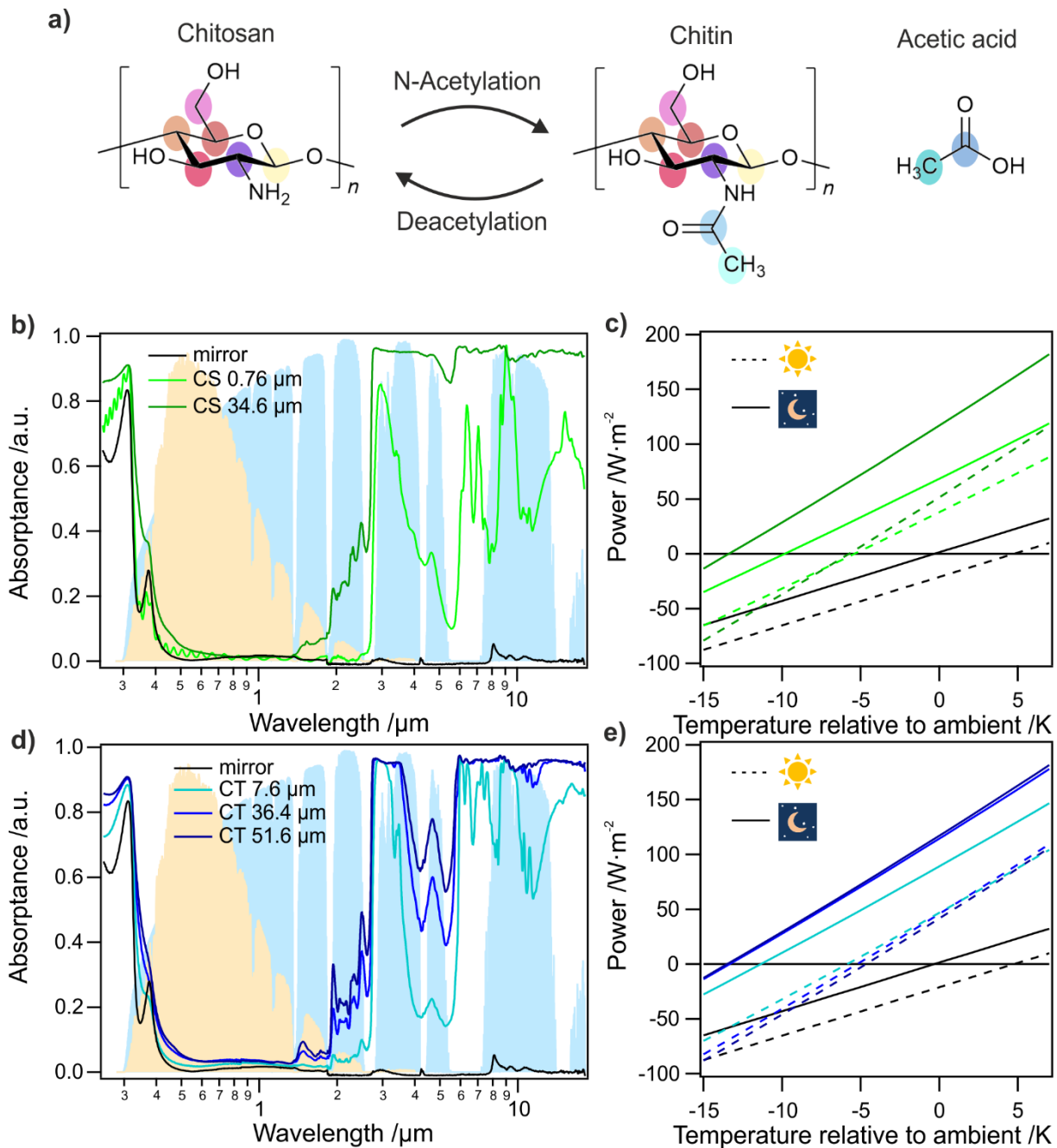


Figure 3.5: a) Chemical structure of poly-N-glucosamine (Chitosan) and its acetylated form poly-N-acetyl glucosamine (Chitin). UV-Vis and IR absorbance spectra of Chitosan b) and Chitin d) samples on reflective silver mirror substrates. The absorbance of the plain substrate is shown for reference. Calculated cooling power (based on the measured optical properties) as a function of temperature for Chitosan c) and Chitin e), respectively. The calculations discriminate between daytime (dashed) and nighttime (full). The intersection at $P_{cool} = 0$ is the predicted equilibrium temperature with respect to ambient. The figure is adapted from the original publication¹¹⁶ and used according to the permission granted under the Creative Commons Attribution license (CC BY 4.0).

For thin films, the individual absorption resonances can be resolved. Based on the observed absorbance, the material is expected to show passive cooling behavior between selective and broadband emitter cases, as it strongly absorbs within the atmospheric window but also outside of it. In contrast, thicker films are mostly opaque to IR radiation and, therefore, a broadband

emitter. The spectral data are used to calculate the cooling power as a function of material temperature. For both, Chitosan (Figure 3.5c) and Chitin (Figure 3.5e), the equilibrium temperature (the relative temperature at $P_{cool} = 0$) is negative. Therefore, based on our calculations, all presented samples are expected to show below ambient radiative cooling for both daytime- and nighttime-case.

The sample temperatures were recorded in a field test to investigate whether the predictions could also be observed in actual measurements. For these kinds of experiments, the temperature of the sample is monitored after exposing it to the sky for one to several day and night cycles. A picture and schematic cross-section of the used setup is shown in Figure 3.6a. The experimental results for chitosan films compared to the ambient temperature and a silver mirror reference confirm the passive cooling properties (Figure 3.6b). For both daytime and nighttime, the chitosan film temperature T_{mat} is always colder than the reference sample temperature T_{Ag} , while the sample with increased thickness shows higher temperature reduction (Figure 3.6c).

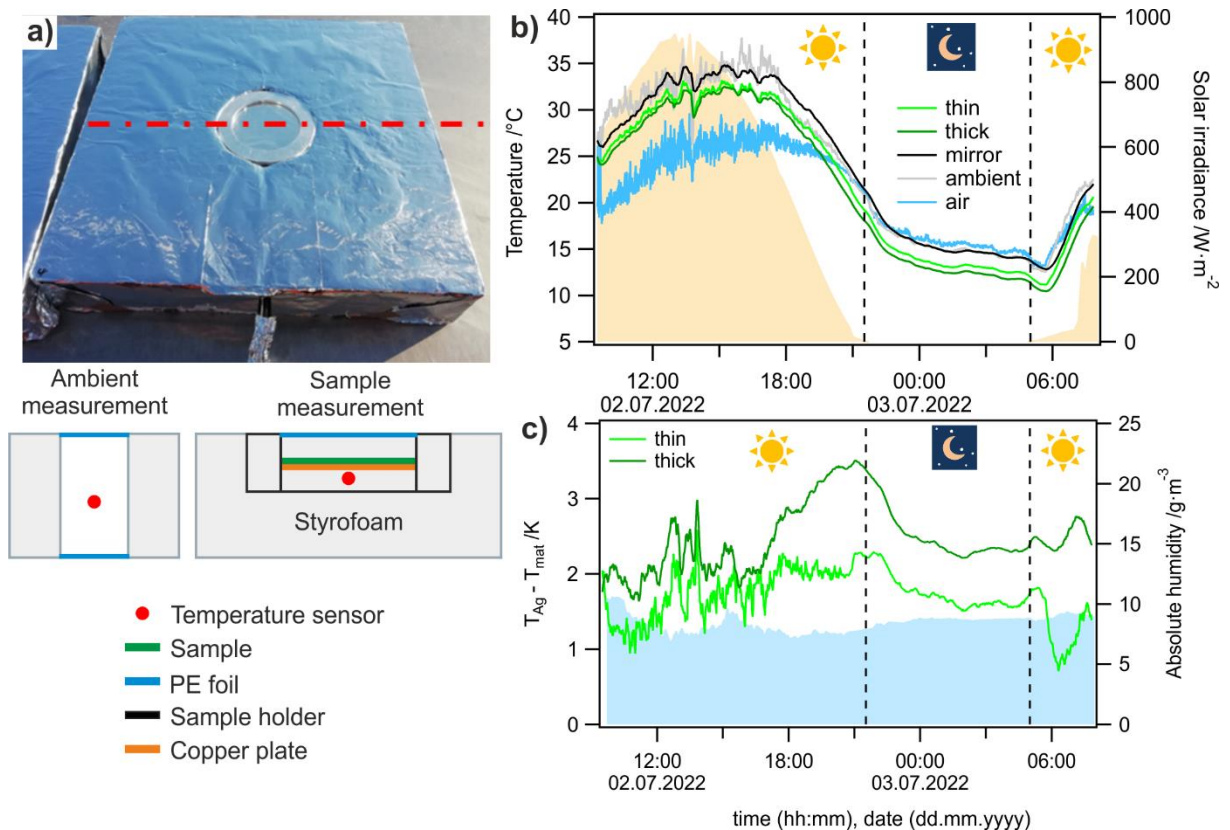


Figure 3.6: a) Photograph of the rooftop measurement setup and schematic drawing of the cross-section across the dashed line. b) Sample temperature measurements for different chitosan and reference samples for a day- and night cycle. The background displays the magnitude of solar irradiation. c) Temperature difference of Chitosan samples with respect to the mirror reference for the measurement period. The absolute humidity is on a constant level, as displayed in the background. The figure is adapted from the original publication¹¹⁶ and used according to the permission granted under the Creative Commons Attribution license (CC BY 4.0).

With our experiments, we could confirm that passive radiative daytime cooling below ambient temperature is possible with chitosan. Based on the absorptance measurements, chitin is expected to show similar cooling performance. However, experimental confirmation was not achieved because the contact between film and substrate could not be ensured in a comparable and reproducible way.

Within the field of passive radiative cooling, many new materials have been proposed and investigated over the last decade. With the addition of Chitosan and Chitin as candidate materials, the pool of available materials was extended in this work. At the same time, new characterization techniques were developed to evaluate the cooling materials. Chapters 8 and 9 revolve around contributions that advance the methodology of characterizing radiative heat transfer properties. In Chapter 8, a tailor-made setup is presented that aims to mimic different aspects of rooftop tests for passive cooling materials. This setup aimed to enable material testing with high reproducibility to become independent from outside weather conditions. The measured performance data can then be compared among various materials and structures, providing the first step to quantitatively evaluate the results among the various research groups worldwide.

The setup is schematically presented in Figure 3.7a and consists of a hemispherical aluminum dome that is intended to act as a heat sink and mimic outer space. For this purpose, it is cooled with liquid nitrogen, and the inside is covered with carbon black to absorb thermal radiation. The sample is presented in a sample holder with a temperature sensor and a copper plate for temperature distribution (Figure 3.7b), a similar design to typical field test setups. The sample holder and the dome area are separated by a convection shield that consists of several thin layers of PE foil to reduce convective temperature exchange. A flow of warm air is induced between the sample and the dome opening, which can also be used to set the sample temperature. To emulate the sun, a solar simulator is used that can illuminate the sample from the top of the dome. To the outside, expanded polystyrene (XPS) insulation is applied to reduce liquid nitrogen evaporation and, in combination with the air stream, prevent the sample area from cooling down.

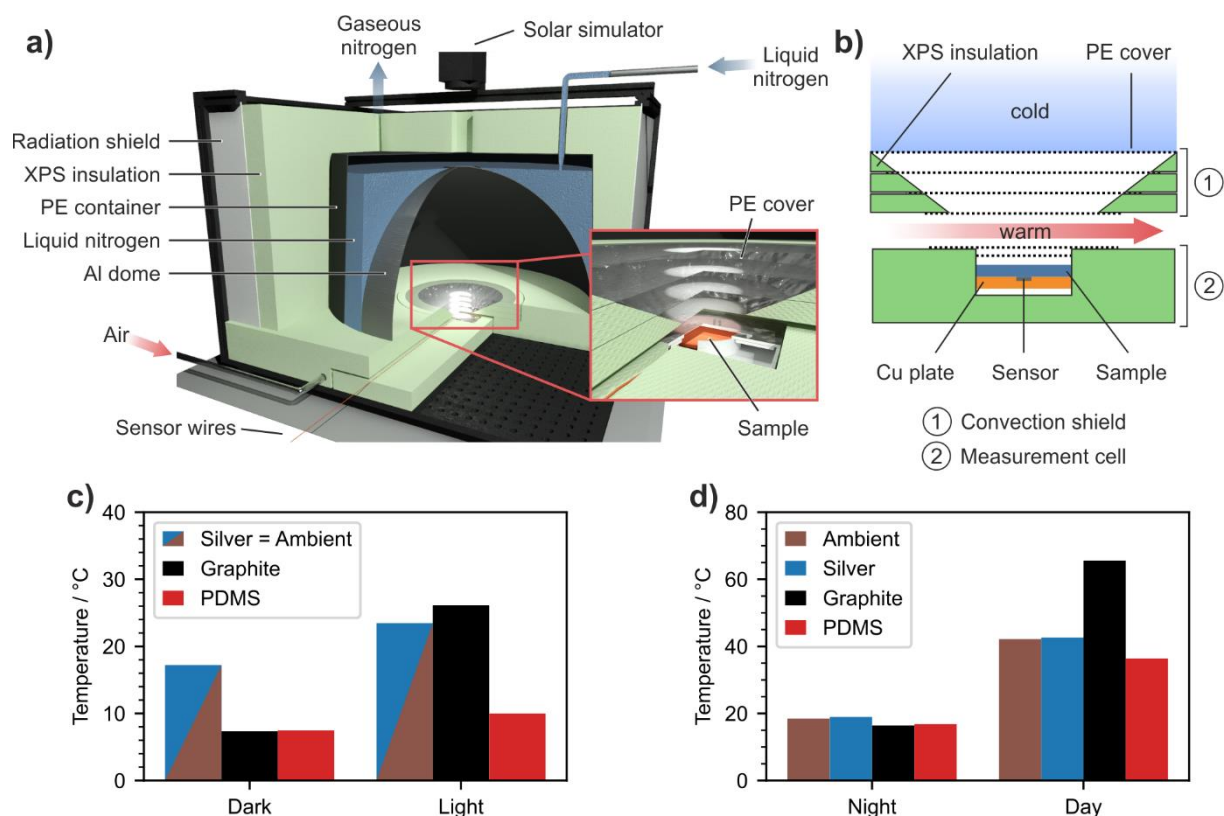


Figure 3.7: Schematic illustration of the artificial measurement setup (a) and a detailed view of the measurement cell and convection shield (b). Temperature measurements for different reference samples in outdoor conditions (c) and measured with the indoor setup (d). The figure is adapted from the original publication¹¹⁷ and used according to the permission granted under the Creative Commons Attribution license (CC BY 4.0).

The setup was verified with a series of samples with different emission properties. A silver mirror with high reflection from UV-Vis to mid-IR was used as a sample with low solar absorption and low thermal emission. A graphite coating was examined to represent a sample with high solar absorption and thermal emission properties. Finally, a PDMS layer on a silver mirror was chosen as a material with high reflectance for solar wavelengths and good emission properties in the mid-IR. In outdoor conditions (Figure 3.7c), the graphite coating and the PDMS layer cooled below ambient and the silver mirror during nighttime. In contrast, the graphite coating heated substantially above the references during the daytime, while the PDMS sample temperature stayed below ambient.

For indoor measurements, the definition and measurement of ambient temperature are challenging because significant temperature variations can be expected within the sample holder. Therefore, the temperature measured with the silver mirror was used as a reference to compare the performance between the samples. In the dark case, both samples cooled below the mirror temperature, indicating increased radiative heat transfer from the samples to the heat sink. For the case with solar simulator illumination, only the PDMS sample reaches lower temperatures than the mirror.

The most challenging aspect of an indoor setup for characterizing passive cooling materials is to emulate the transparency of the atmosphere. For the presented case, a selective emitter will always perform inferior to a broadband emitter because all the emitted radiation will reach the heat sink without wavelength discrimination. Including a material within the dome is no possible solution because of the contact with the heat sink the temperature will be lower than typical atmospheric temperatures. To overcome this obstacle and to enable also characterization of the spectral selectivity, a MIR filter is introduced between the sample holder and the convection shield of the dome (Figure 3.8a). This filter consists of a thin layer of PDMS and a PE foil for support. The thin layer of PDMS absorbs strongly in wavelength regions where the atmosphere is mostly transparent (Figure 3.8b). The idea of the filter is that if a selective emitter is investigated as a sample, the filter will block its emitted radiation, and the sample will not reach as low temperatures as it could without the filter. In contrast, a non-selective sample will not be influenced by the filter as strongly.

The samples' cooling power was determined to elucidate the selectivity of different layer thicknesses that lead to a transition from a selective to a broadband emitter. In this experiment, the sample holder was equipped with a feedback-controlled heater system that was set to keep the sample temperature constant. The power used to drive the heater directly correlates to the passive cooling power of the sample. The optical similarity of the sample to the (selective) filter is correlated by comparing the cooling power with and without the filter. For a selective emitter, the relative loss in cooling power should be highest compared to the spectrally non-selective measurement without the filter. This hypothesis is tested with a set of PDMS films with different thicknesses. As outlined in Chapter 6, the PDMS films transition from a more selective emitter to a more broadband emitter with increasing layer thickness. The results, highlighted in Figure 3.8c, show that the measured cooling power with the filter is always reduced for all film thicknesses. However, the relative decrease in cooling power is lowest for the thickest sample. The developed PE/PDMS filter, therefore, introduces sample discrimination based on selective emission in the sky window range, where the cooling performance of selectively emitting samples is strongly attenuated.

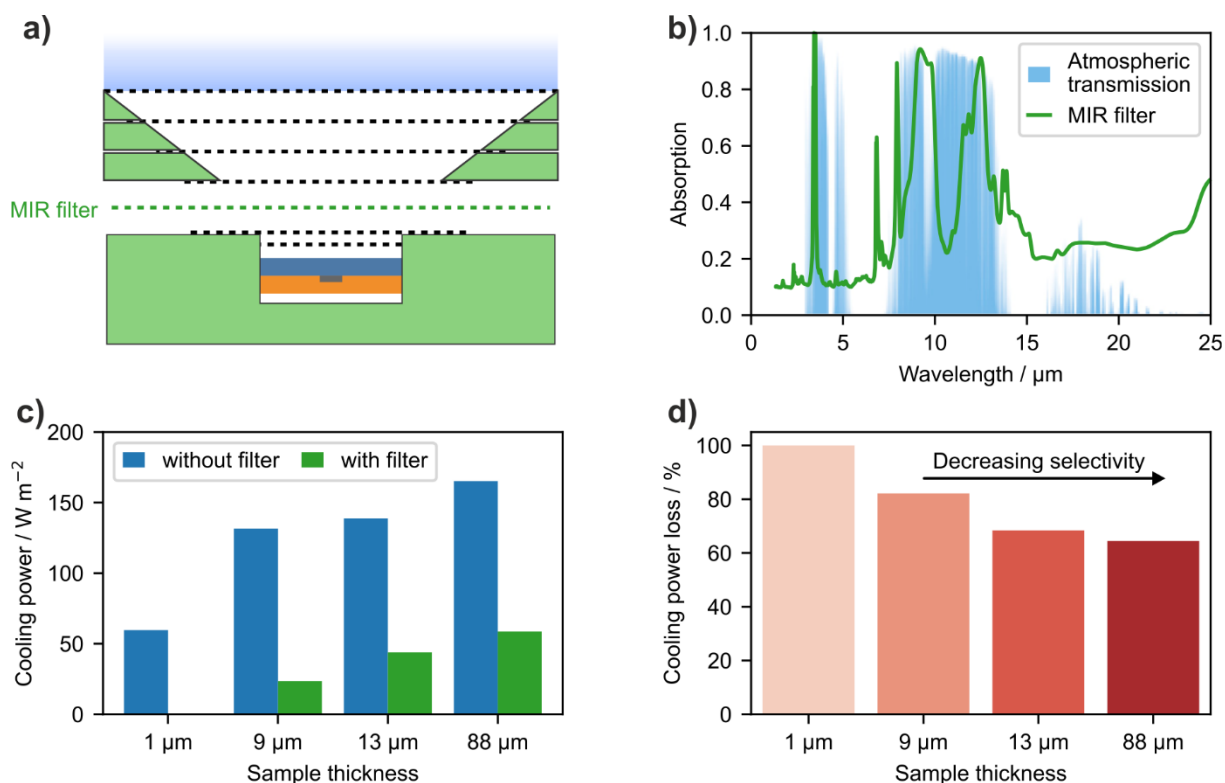


Figure 3.8: Schematic illustration of the sample holder and convection shield with included MIR filter. b) absorption spectrum of MIR filter with mainly selective absorption within the atmospheric window. c) cooling power of different samples with and without MIR filter. d) calculated cooling power loss for the presented samples. Thicker samples (broadband emitter) lose less cooling power with the inclusion of a filter (less selectivity). The figure is adapted from the original publication¹¹⁷ and used according to the permission granted under the Creative Commons Attribution license (CC BY 4.0).

With the presented setup, the performance of passive cooling materials can be reproducibly characterized independent of environmental conditions. The setup enables the direct comparison of materials independent of location and time. The most important features are the liquid nitrogen-cooled aluminum dome acting as the heat sink and a solar simulator simulating sun illumination. With a MIR filter, even the partial transparency of the atmosphere is considered, and the emission selectivity of different samples can be characterized.

With the hemispherical dome geometry, further questions of radiative heat transfer can be assessed. Chapter 9 introduces a novel dual-sided nonwoven textile, which offers a unique combination of personal thermal management strategies. The nonwoven was fabricated by Qiang Gao and consists of polyimide (PI) fibers on one side and silver nanowires (AgNW) on the other. This architecture aims to affect the heat dissipation from the human body to the surroundings when worn as apparel. The optical properties of the two sides are key to identifying which nonwoven side should be worn to the outside to minimize radiative heat loss. For this question, the optical properties in the mid-IR region are most relevant because the radiative heat transfer mainly occurs in this wavelength range at ambient temperatures.

Comparing the optical properties of the two sides of the nonwoven (Figure 3.9a), one notices that the reflectance and absorptance are different. While the PI side has a low average overall reflectance of ~18%, the silver side reflects ~80% of the incoming radiation in the mid-IR. In contrast, the PI side absorbs and therefore emits radiation very well compared to the reduced absorptance found for the silver side. Consequently, if the silver side is facing the surroundings, less thermal emission is expected, and the radiative heat loss of the body is reduced. In contrast, the high absorptance of the PI side indicates major heat loss to the surroundings when worn outside. When comparing the optical properties of the dual-sided nonwoven with a plain PI nonwoven, the main difference is found in the transmission capabilities (Figure 3.9c). The dual-sided nonwoven is mostly opaque, while substantial transmission of infrared radiation is apparent for the plain nonwoven. This transmittance will lead to a direct heat loss to the surrounding that is not affected by the nonwoven.

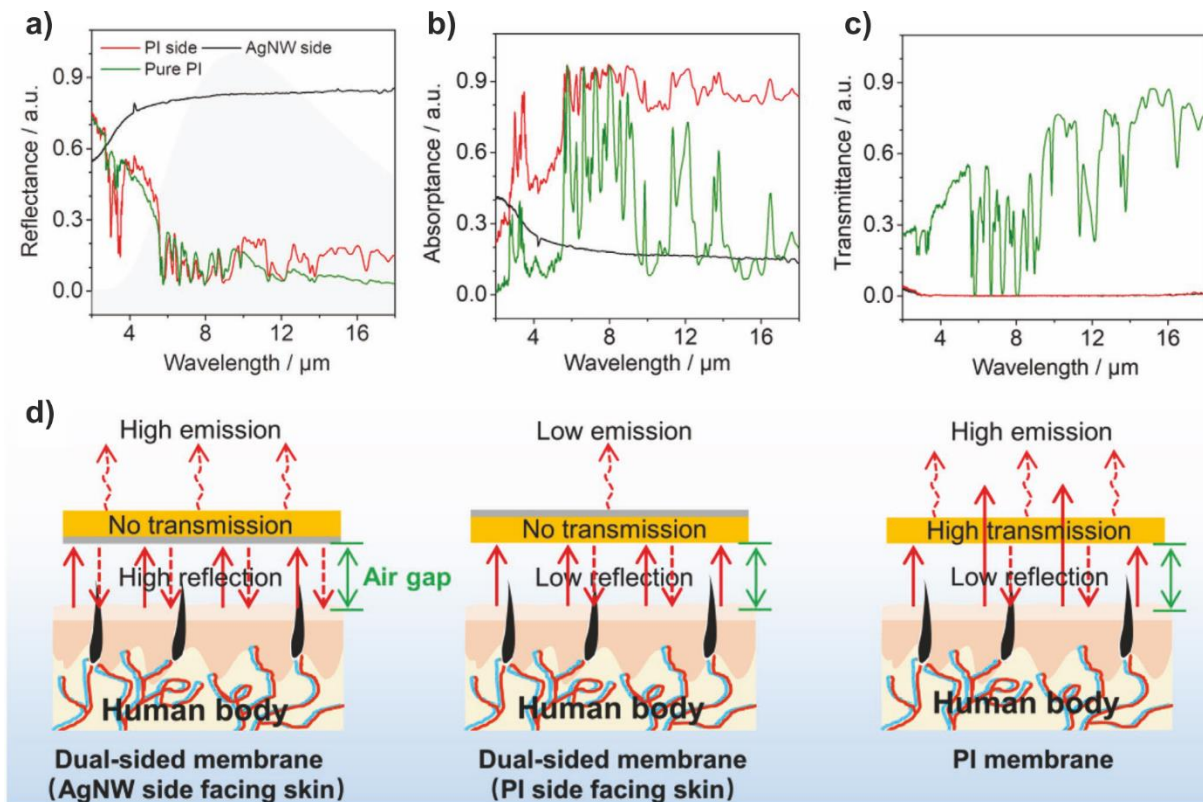


Figure 3.9: Reflectance, absorptance, and transmittance of different sides of the dual-sided nonwoven compared to a pure PI nonwoven. d) schematic illustration of the radiative energy transfer problem for the different scenarios when worn. The figure is adapted from the original publication¹¹⁸ and used according to the permission granted under the Creative Commons Attribution license (CC BY 4.0).

When applied as apparel, the energy transfer situation becomes more complex because the radiative energy transfer between the body and nonwoven must also be considered. The radiative energy transfer contributions are schematically summarized in Figure 3.9d. The plain nonwoven will have high emission towards the outside and low reflectance towards the body,

representing the highest expected radiative energy loss. For the case of the dual side nonwoven, the assessment is less clear. While the PI side has high emission to the outside, it will also absorb emitted radiation when facing the body. The AgNW side has low emission to the outside but will show substantial back reflectance when facing the body.

We constructed an energy transfer experiment to elucidate which side has the lowest energy transfer to the surrounding. The setup is schematically outlined in Figure 3.10a and consists of a heater for energy input below a copper plate to distribute the temperature evenly. The copper plate was coated with graphite to ensure high emission from the surface of the sample area. The excess surface area was coated with a low emissivity coating to reduce radiative energy transfer from areas without sample. A graphite-coated aluminum dome at ambient temperature acts as a heat sink and represents the surrounding temperature. The heater is set to hold a constant temperature of 37 °C to simulate the human body. In this situation, the power input to the heater directly correlates to the energy transferred from the high emissivity sample area to the heat sink.

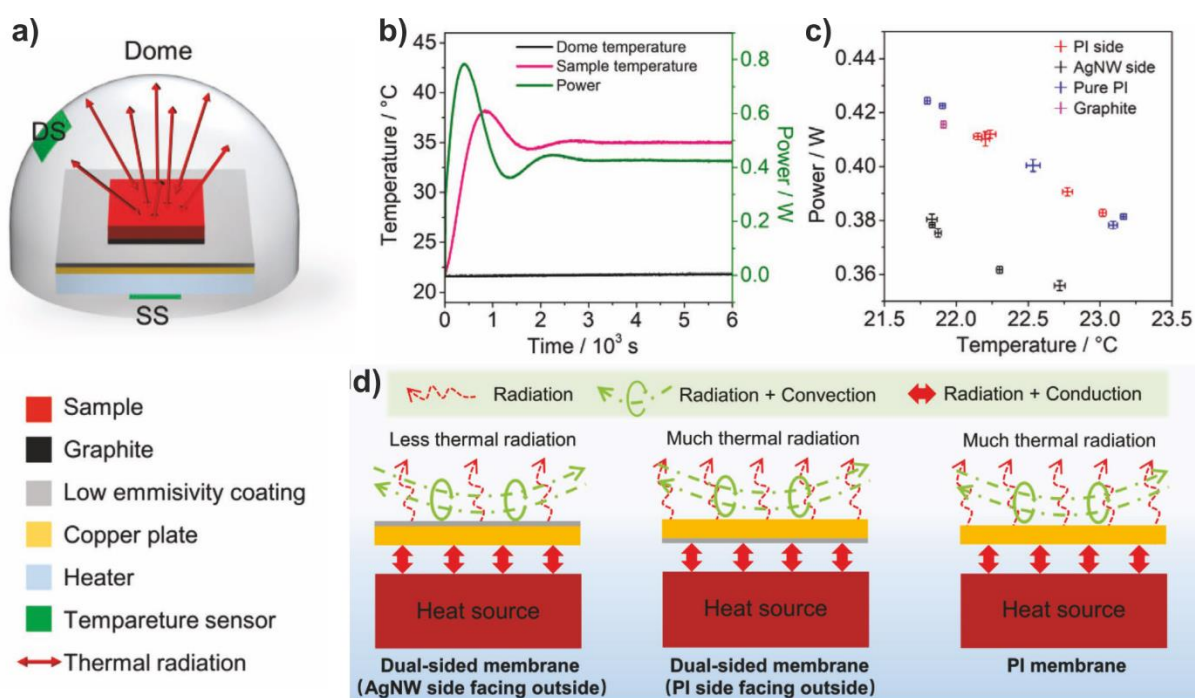


Figure 3.10: Schematic drawing of the radiative energy transfer experiment. The feedback-controlled heater system below the sample is held at body temperature, while the aluminum dome is at ambient temperature. b) sample temperature and heating power during the equilibration time. After 50 min (3000 s), an equilibrium state is reached. c) equilibrium power input as a function of dome temperature for the different PI configurations and the pure graphite coating as reference. Higher ambient temperature reduces the heating power loss to the dome. d) Illustration of the relevant heat dissipation pathways during the experiment, including conductive and convective pathways. The figure is adapted from the original publication¹¹⁸ and used according to the permission granted under the Creative Commons Attribution license (CC BY 4.0).

If a sample is presented, the heater feedback system needs a certain equilibration time (Figure 3.10b). After steady-state conditions are reached, the power for isothermal conditions can be determined. The power values for the different sample types and configurations are displayed as a function of ambient temperature in Figure 3.10c. Higher ambient temperatures will reduce the radiative energy transfer to the heat sink and, thus, must be considered when comparing the different samples. The experiment reveals that the radiative energy loss is only reduced if the AgNW side faces the outside. In comparison, the pure PI and the PI side facing the outside perform similarly to the high emissivity coating. This indicates that the radiative heat loss cannot be prevented with these materials facing the outside.

The full picture of the energy transfer from the human body to textile material and the surrounding also needs to include a non-radiative heat transfer mechanism (Figure 3.10d). Direct contact between the fabric and the skin will enable heat transfer through conduction. A gas phase will also enable convective transport, especially from the fabric surface to the surrounding. For all three cases, the non-radiative contributions will be very similar. Therefore, we conclude that the configuration with the AgNW facing the surrounding will be superior in preventing heat loss due to the reduced emission.

Our extensive study reveals that for applications involving radiative heat transfer, like clothing, the radiative pathway is only one mechanism for thermal comfort. A full description of the heat transfer problem is very complex, but with the presented measurement geometry, the question of which side of the nonwoven should face the outside could be answered.

While each of the contributions in this thesis discusses a different aspect of radiative heat management, they expand the state-of-the-art in the respective field. New materials were introduced, like the gradient colloidal glass. Calculations and simple experiments were used to consider the material thickness, a parameter formerly neglected for the optimization of passive cooling systems. The application of the existing bio-materials chitosan and chitin for passive radiative cooling expanded the toolbox of available materials within the field. The design of a tailor-made setup for indoor testing, including a selective filter to include atmospheric selectivity, is the next step toward a standardized, reproducible, and comparable characterization of passive cooling materials. Finally, the investigation of the different heat transport mechanisms in a Janus-like nonwoven answered the question of which side prevents radiative heat loss when worn.

3.2 Individual Contributions to Joint Publications

The results of this thesis are a combination of five scientific publications. These publications were prepared in collaboration with other researchers and colleagues. The individual contributions to the respective publications are specified in the following section. The corresponding authors are marked with asterisks.

Chapter 5: A Continuous Gradient Colloidal Glass

Marius Schöttle, Tobias Lauster, Lukas J. Roemling, Nicolas Vogel, and Markus Retsch*

This work was published in *Advanced Materials*, **2022**, 2208745.

I conducted the diffuse reflectance measurements, was involved in the discussion of the optical measurements, and edited the manuscript. Marius Schöttle led the conceptualization, investigation, formal analysis, and data curation. This included the development of a new type of synthesis procedure as well as the self-assembly processes. He conducted optical and electron microscopy, local spectroscopy, and structural characterization. He wrote all scripts for data analysis and the 2D simulations, visualized the data, and wrote the original manuscript. Lukas J. Roemling assisted with the local spectroscopy along the gradient. Nicolas Vogel and Markus Retsch supervised the project, reviewed, and edited the manuscript.

Chapter 6: Homogeneous Polymer Films for Passive Daytime Cooling: Optimized Thickness for Maximized Cooling Performance

Kai Herrmann‡, Tobias Lauster‡, Qimeng Song*, and Markus Retsch*

‡ These authors contributed equally.

This work was published in *Advanced Energy and Sustainability Research*, **2022**, 3, 2100166.

Kai Herrmann and I identified the lack of treatment of the sample thickness for passive daytime cooling. I prepared the samples and performed the optical characterization. Kai Herrmann and I wrote the manuscript. Kai Herrmann established a theoretical framework to depict the influence of sample thickness on cooling performance. Kai Herrmann performed the simulations based on this theoretical framework. Qimeng Song developed the outdoor setup for measuring the cooling performance, performed the cooling performance measurements, and was involved in scientific discussions. Markus Retsch supervised the project and corrected the manuscript.

Chapter 7: From Chitosan to Chitin: Bioinspired Thin Films for Passive Daytime Radiative Cooling Compact Chitosan

Tobias Lauster, Anika Mauel, Kai Herrmann, Viktoria Veitengruber, Qimeng Song, Jürgen Senker, and Markus Retsch*

This work was published in *Advanced Science*, **2023**, 2206616.

I conceptualized the storyline, developed the sample preparation, and performed water contact angle and resistance experiments. I measured the UV-Vis and IR spectra and wrote major parts of the manuscript. Anika Mauel performed the NMR experiments, evaluated the data, and contributed to the discussion and the manuscript. Kai Herrmann calculated the cooling performance from spectroscopic data, supported the general data evaluation, and was involved in the discussion. Viktoria Veitengruber assisted in sample preparation, water resistance tests, and NMR experiments. Qimeng Song developed the outdoor setup for the temperature measurements, performed the temperature measurements, and was involved in the discussion of the results. Jürgen Senker contributed to the discussion and corrected the manuscript. Markus Retsch supervised the project, contributed to the discussion, and corrected the manuscript. All authors contributed to the original draft writing.

Chapter 8: A Tailored Indoor Setup for Reproducible Passive Daytime Cooling Characterization

Qimeng Song, Thomas Tran, Kai Herrmann, Tobias Lauster, Maximilian Breitenbach, and Markus Retsch*

This work was published in *Cell Reports Physical Science*, **2022**, 3, 100986.

Qimeng Song and Thomas Tran led the conceptualization and investigation. Thomas Tran designed the measurement apparatus, established the communication between hardware components, analyzed the data, and visualized the data. Qimeng Song used the setup to characterize the steady-state temperatures and cooling powers. Kai Herrmann contributed formal analysis and validation. I contributed validation and resources, particularly in the form of reference samples and PDMS-coated specimens, as well as spectral analysis. I was also involved in the planning and improvement of the setup and the development of a spectral filter. Maximilian Breitenbach was involved in the investigation. Markus Retsch led supervision, project administration, and funding acquisition. All authors contributed to the original draft writing.

Chapter 9: Breathable and Flexible Dual-Sided Nonwovens with Adjustable Infrared Optical Performances for Smart Textile

Qiang Gao, Tobias Lauster, Bernd A. F. Kopera, Markus Retsch*, Seema Agarwal*, and Andreas Greiner*

This work was published in *Advanced Functional Materials*, **2022**, 32, 2108808.

Qiang Gao conducted synthesis and characterization of the nonwovens, including preparing the dual-sided nonwovens, characterizations of pore size, air permeability, mechanical property, most of the electrical properties, and thermal properties, and discussed results. Qiang Gao also wrote the first draft of the manuscript. I measured and discussed emittance, transmittance, reflectance, effusivity, and passive radiation. Bernd A. F. Kopera conducted some of the characterizations of AgNW's thermal stability and IR reflection properties. Prof. Markus Retsch proposed and discussed experiments on radiative transport and thermography and revised the manuscript. Prof. Seema Agarwal gave suggestions on conducting experiments and characterizations of the dual-sided nonwovens and revised the manuscript. Prof. Andreas Greiner proposed and discussed the experiment scheme with Qiang Gao and revised the manuscript.



4. References

1. R. S. H. Le Treut, U. Cubasch, Y. Ding, C. Mauritzen, A. Mokssit, T. Peterson, M. Prather, "Historical Overview of Climate Change." In *Climate Change 2007: The Physical Science Basis*, Cambridge University Press, Cambridge, **2007**.
2. IPCC, "Climate Change 2021: The Physical Science Basis," Cambridge University Press, Cambridge, **2021**.
3. IRENA, IEA, REN21, "Renewable Energy Policies in a Time of Transition: Heating and Cooling," IRENA, OECD/IEA, REN21, **2020**.
4. Z. Qin, M. Li, J. Flohn, Y. Hu, "Thermal management materials for energy-efficient and sustainable future buildings", *Chem. Commun.* **2021**, 57 (92), 12236-12253.
5. C. C. Gouwen Ding, "Silver-Based Low-Emissivity Coating Technology for Energy-Saving Window Applications." In *Modern Technologies for Creating the Thin-Film Systems and Coatings*, Nikitenkov, N. N., Ed. InTech, **2017**.
6. M. Santamouris, N. Papanikolaou, I. Livada, I. Koronakis, C. Georgakis, A. Argiriou, D. N. Assimakopoulos, "On the impact of urban climate on the energy consumption of buildings", *Solar Energy* **2001**, 70 (3), 201-216.
7. H. E. A. Mostafa, M. Mahvash In *Use of Eco-Energy in Ancient Architecture (Iranian Ice pits)*, International Conference on Biology, Environment and Chemistry, IACSIT Press: 2011; pp 379-382.
8. L. Carlosena, Á. Andueza, L. Torres, O. Irulegi, R. J. Hernández-Minguillón, J. Sevilla, M. Santamouris, "Experimental development and testing of low-cost scalable radiative cooling materials for building applications", *Sol. Energy Mater. Sol. Cells* **2021**, 230.
9. E. A. Goldstein, A. P. Raman, S. Fan, "Sub-ambient non-evaporative fluid cooling with the sky", *Nature Energy* **2017**, 2 (9).
10. L. Chen, K. Zhang, M. Ma, S. Tang, F. Li, X. Niu, "Sub-ambient radiative cooling and its application in buildings", *Build Simul* **2020**, 13 (6), 1165-1189.
11. S. Y. Heo, D. H. Kim, Y. M. Song, G. J. Lee, "Determining the Effectiveness of Radiative Cooler-Integrated Solar Cells", *Advanced Energy Materials* **2021**, 12 (10).
12. L. Zhu, A. Raman, K. X. Wang, M. A. Anoma, S. Fan, "Radiative cooling of solar cells", *Optica* **2014**, 1 (1).
13. E. Skoplaki, J. A. Palyvos, "On the temperature dependence of photovoltaic module electrical performance: A review of efficiency/power correlations", *Solar Energy* **2009**, 83 (5), 614-624.
14. I. Haechler, H. Park, G. Schnoering, T. Gulich, M. Rohner, A. Tripathy, A. Milionis, T. M. Schutzius, D. Poulidakos, "Exploiting radiative cooling for uninterrupted 24-hour water harvesting from the atmosphere", *Sci Adv* **2021**, 7 (26).
15. J. Xu, J. Zhang, B. Fu, C. Song, W. Shang, P. Tao, T. Deng, "All-Day Freshwater Harvesting through Combined Solar-Driven Interfacial Desalination and Passive Radiative Cooling", *ACS Appl. Mater. Interfaces* **2020**, 12 (42), 47612-47622.
16. Y. Peng, Y. Cui, "Advanced Textiles for Personal Thermal Management and Energy", *Joule* **2020**, 4 (4), 724-742.
17. J. D. Hardy, E. F. Dubois, "Regulation of Heat Loss from the Human Body", *PNAS* **1937**, 23 (12), 624-631.
18. S. Zeng, S. Pian, M. Su, Z. Wang, M. Wu, X. Liu, M. Chen, Y. Xiang, J. Wu, M. Zhang, Q. Cen, Y. Tang, X. Zhou, Z. Huang, R. Wang, A. Tunuhe, X. Sun, Z. Xia, M. Tian, M. Chen, X. Ma, L. Yang, J. Zhou, H. Zhou, Q. Yang, X. Li, Y. Ma, G. Tao, "Hierarchical-morphology metafabric for scalable passive daytime radiative cooling", *Science* **2021**, 373 (6555), 692-696.
19. X. Zhang, W. Yang, Z. Shao, Y. Li, Y. Su, Q. Zhang, C. Hou, H. Wang, "A Moisture-Wicking Passive Radiative Cooling Hierarchical Metafabric", *ACS Nano* **2022**, 16 (2), 2188-2197.
20. M. F. Modest, "Radiative Heat Transfer," **2013**.
21. H. A. Lorentz, "The Theory of Electrons and Its Applications to the Phenomena of Light and Radiant Heat," **1916**.

22. C. F. Bohren, D. R. Huffman, "Absorption and Scattering of Light by Small Particles," **1998**.
23. C. López, "Materials Aspects of Photonic Crystals", *Adv. Mater.* **2003**, *15* (20), 1679-1704.
24. D. Rüdisser, R. S. McLeod, W. Wagner, C. J. Hopfe, "Numerical derivation and validation of the angular, hemispherical and normal emissivity and reflectivity of common window glass", *Building and Environment* **2022**, *207*, 108536.
25. M. M. Hossain, M. Gu, "Radiative Cooling: Principles, Progress, and Potentials", *Adv. Sci.* **2016**, *3* (7), 1500360.
26. K. Herrmann, T. Lauster, Q. Song, M. Retsch, "Homogeneous Polymer Films for Passive Daytime Cooling: Optimized Thickness for Maximized Cooling Performance", *Adv. Energy Sustainability Res.* **2021**, *3* (2), 2100166.
27. A. A. Lacis, G. A. Schmidt, D. Rind, R. A. Ruedy, "Atmospheric CO₂: principal control knob governing Earth's temperature", *Science* **2010**, *330* (6002), 356-359.
28. M. Li, C. F. M. Coimbra, "On the effective spectral emissivity of clear skies and the radiative cooling potential of selectively designed materials", *Int. J. Heat Mass Transfer* **2019**, *135*, 1053-1062.
29. A. Berk, P. Conforti, R. Kennett, T. Perkins, F. Hawes, J. v. d. Bosch, "MODTRAN® 6: A major upgrade of the MODTRAN® radiative transfer code", *6th Workshop on Hyperspectral Image and Signal Processing: Evolution in Remote Sensing (WHISPERS)* **2014**, 1-4.
30. C. G. Granqvist, A. Hjortsberg, "Radiative cooling to low temperatures: General considerations and application to selectively emitting SiO films", *J. Appl. Phys.* **1981**, *52* (6), 4205-4220.
31. Y. Li, L. Li, L. Guo, B. An, "Systematical analysis of ideal absorptivity for passive radiative cooling", *Optical Materials Express* **2020**, *10* (8), 1767-1777.
32. B. Bartoli, S. Catalanotti, B. Coluzzi, V. Cuomo, V. Silvestrini, G. Troise, "Nocturnal and diurnal performances of selective radiators", *Applied Energy* **1977**, *3* (4), 267-286.
33. A. Guechi, M. Chegaar, M. Aillerie, "Air Mass Effect on the Performance of Organic Solar Cells", *Energy Procedia* **2013**, *36*, 714-721.
34. "ASTM G173-03, Standard Tables for Reference Solar Spectral Irradiances: Direct Normal and Hemispherical on 37° Tilted Surface", **2020**.
35. B. Zhao, M. K. Hu, X. Z. Ao, N. Chen, G. Pei, "Radiative cooling: A review of fundamentals, materials, applications, and prospects", *Applied Energy* **2019**, *236*, 489-513.
36. S. Catalanotti, V. Cuomo, G. Piro, D. Ruggi, V. Silvestrini, G. Troise, "The radiative cooling of selective surfaces", *Solar Energy* **1975**, *17* (2), 83-89.
37. C. G. Granqvist, A. Hjortsberg, "Surfaces for radiative cooling: Silicon monoxide films on aluminum", *Appl. Phys. Lett.* **1980**, *36* (2), 139-141.
38. P. Berdahl, M. Martin, F. Sakka, "Thermal performance of radiative cooling panels", *Int. J. Heat Mass Transfer* **1983**, *26* (6), 871-880.
39. P. Berdahl, "Radiative cooling with MgO and/or LiF layers", *Appl. Opt.* **1984**, *23* (3), 370.
40. A. P. Raman, M. A. Anoma, L. Zhu, E. Rephaeli, S. Fan, "Passive radiative cooling below ambient air temperature under direct sunlight", *Nature* **2014**, *515* (7528), 540-4.
41. M. Zeyghami, D. Y. Goswami, E. Stefanakos, "A review of clear sky radiative cooling developments and applications in renewable power systems and passive building cooling", *Sol. Energy Mater. Sol. Cells* **2018**, *178*, 115-128.
42. Q. Zhang, S. Wang, X. Wang, Y. Jiang, J. Li, W. Xu, B. Zhu, J. Zhu, "Recent Progress in Daytime Radiative Cooling: Advanced Material Designs and Applications", *Small Methods* **2022**, *6* (4), 2101379.
43. H. Günzler, "IR-Spektroskopie," Wiley-VCH, **2003**.
44. A. Aili, Z. Y. Wei, Y. Z. Chen, D. L. Zhao, R. G. Yang, X. B. Yin, "Selection of polymers with functional groups for daytime radiative cooling", *Materials Today Physics* **2019**, *10*.
45. Y. Tian, L. Qian, X. Liu, A. Ghanekar, G. Xiao, Y. Zheng, "Highly effective photon-to-cooling thermal device", *Sci. Rep.* **2019**, *9* (1), 19317.
46. J. Liu, D. Zhang, S. Jiao, Z. Zhou, Z. Zhang, F. Gao, "Daytime radiative cooling with clear epoxy resin", *Sol. Energy Mater. Sol. Cells* **2020**, *207*.

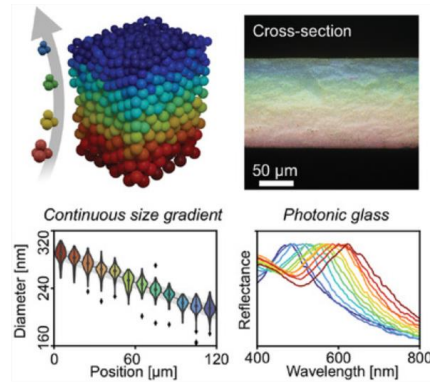
47. S. Meng, L. Long, Z. Wu, N. Denisuk, Y. Yang, L. Wang, F. Cao, Y. Zhu, "Scalable dual-layer film with broadband infrared emission for sub-ambient daytime radiative cooling", *Sol. Energy Mater. Sol. Cells* **2020**, 208.
48. J. Mandal, Y. Fu, A. C. Overvig, M. Jia, K. Sun, N. N. Shi, H. Zhou, X. Xiao, N. Yu, Y. Yang, "Hierarchically porous polymer coatings for highly efficient passive daytime radiative cooling", *Science* **2018**, 362 (6412), 315-319.
49. J. L. Kou, Z. Jurado, Z. Chen, S. Fan, A. J. Minnich, "Daytime Radiative Cooling Using Near-Black Infrared Emitters", *ACS Photonics* **2017**, 4 (3), 626-630.
50. L. Zhou, H. Song, J. Liang, M. Singer, M. Zhou, E. Stegenburgs, N. Zhang, C. Xu, T. Ng, Z. Yu, B. Ooi, Q. Gan, "A polydimethylsiloxane-coated metal structure for all-day radiative cooling", *Nat. Sustain.* **2019**, 2 (8), 718-724.
51. Y. Zhu, Y. Ye, D. Wang, Y. Cao, "Simple dual-layer emitter for daytime radiative cooling", *Osa Continuum* **2021**, 4 (2), 416-427.
52. Y. Lu, Z. Chen, L. Ai, X. Zhang, J. Zhang, J. Li, W. Wang, R. Tan, N. Dai, W. Song, "A Universal Route to Realize Radiative Cooling and Light Management in Photovoltaic Modules", *Sol. RRL* **2017**, 1 (10).
53. S. Lin, L. Ai, J. Zhang, T. Bu, H. Li, F. Huang, J. Zhang, Y. Lu, W. Song, "Silver ants-inspired flexible photonic architectures with improved transparency and heat radiation for photovoltaic devices", *Sol. Energy Mater. Sol. Cells* **2019**, 203, 110135.
54. J. Song, J. Seo, J. Han, J. Lee, B. J. Lee, "Ultrahigh emissivity of grating-patterned PDMS film from 8 to 13 μm wavelength regime", *Appl. Phys. Lett.* **2020**, 117 (9), 094101.
55. M. Chen, D. Pang, X. Chen, H. Yan, "Enhancing infrared emission behavior of polymer coatings for radiative cooling applications", *J Phys D Appl Phys* **2021**, 54 (29).
56. D. Chae, H. Lim, S. So, S. Son, S. Ju, W. Kim, J. Rho, H. Lee, "Spectrally Selective Nanoparticle Mixture Coating for Passive Daytime Radiative Cooling", *ACS Appl. Mater. Interfaces* **2021**, 13 (18), 21119-21126.
57. Y. Zhou, Y. Liu, Y. Li, R. Jiang, W. Li, W. Zhao, R. Mao, L. Deng, P. Zhou, "Flexible radiative cooling material based on amorphous alumina nanotubes", *Optical Materials Express* **2020**, 10 (7).
58. M. A. Kecebas, M. P. Menguc, A. Kosar, K. Sendur, "Passive radiative cooling design with broadband optical thin-film filters", *J Quant Spectrosc Radiat Transf* **2017**, 198, 179-186.
59. K. Yao, H. Ma, M. Huang, H. Zhao, J. Zhao, Y. Li, S. Dou, Y. Zhan, "Near-Perfect Selective Photonic Crystal Emitter with Nanoscale Layers for Daytime Radiative Cooling", *ACS Appl. Nano Matter.* **2019**, 2 (9), 5512-5519.
60. Y. Zhu, Y.-H. Ye, D. Wang, Y. Cao, "Quasi-periodic selective multilayer emitter for sub-ambient daytime radiative cooling", *AIP Advances* **2021**, 11 (2).
61. D. Wu, C. Liu, Z. Xu, Y. Liu, Z. Yu, L. Yu, L. Chen, R. Li, R. Ma, H. Ye, "The design of ultra-broadband selective near-perfect absorber based on photonic structures to achieve near-ideal daytime radiative cooling", *Materials & Design* **2018**, 139, 104-111.
62. H. Zhang, K. C. S. Ly, X. Liu, Z. Chen, M. Yan, Z. Wu, X. Wang, Y. Zheng, H. Zhou, T. Fan, "Biologically inspired flexible photonic films for efficient passive radiative cooling", *PNAS* **2020**, 117 (26), 14657-14666.
63. A. R. Gentle, G. B. Smith, "Radiative heat pumping from the Earth using surface phonon resonant nanoparticles", *Nano Lett.* **2010**, 10 (2), 373-9.
64. Y. Zhai, Y. Ma, S. N. David, D. Zhao, R. Lou, G. Tan, R. Yang, X. Yin, "Scalable-manufactured randomized glass-polymer hybrid metamaterial for daytime radiative cooling", *Science* **2017**, 355 (6329), 1062-1066.
65. D. Fan, H. Sun, Q. Li, "Thermal control properties of radiative cooling foil based on transparent fluorinated polyimide", *Sol. Energy Mater. Sol. Cells* **2019**, 195, 250-257.
66. T. Suichi, A. Ishikawa, T. Tanaka, Y. Hayashi, K. Tsuruta, "Whitish daytime radiative cooling using diffuse reflection of non-resonant silica nanoshells", *Sci. Rep.* **2020**, 10 (1), 6486.

67. Y. Liu, S. Son, D. Chae, P.-H. Jung, H. Lee, "Acrylic membrane doped with Al₂O₃ nanoparticle resonators for zero-energy consuming radiative cooling", *Sol. Energy Mater. Sol. Cells* **2020**, 213.
68. X. Li, J. Peoples, P. Yao, X. Ruan, "Ultrawhite BaSO₄ Paints and Films for Remarkable Daytime Subambient Radiative Cooling", *ACS Appl. Mater. Interfaces* **2021**, 13 (18), 21733-21739.
69. Z. Cheng, F. Wang, H. Wang, H. Liang, L. Ma, "Effect of embedded polydisperse glass microspheres on radiative cooling of a coating", *International Journal of Thermal Sciences* **2019**, 140, 358-367.
70. T. M. J. Nilsson, G. A. Niklasson, C. G. Granqvist, "A solar reflecting material for radiative cooling applications: ZnS pigmented polyethylene", *Sol. Energy Mater. Sol. Cells* **1992**, 28 (2), 175-193.
71. T. M. J. Nilsson, G. A. Niklasson, "Radiative cooling during the day: simulations and experiments on pigmented polyethylene cover foils", *Sol. Energy Mater. Sol. Cells* **1995**, 37 (1), 93-118.
72. A. Leroy, B. Bhatia, C. C. Kelsall, A. Castillejo-Cuberos, H. M. Di Capua, L. Zhao, L. Zhang, A. M. Guzman, E. N. Wang, "High-performance subambient radiative cooling enabled by optically selective and thermally insulating polyethylene aerogel", *Sci. Adv.* **2019**, 5 (10), eaat9480.
73. E. Torgerson, J. Hellhake, "Polymer solar filter for enabling direct daytime radiative cooling", *Sol. Energy Mater. Sol. Cells* **2020**, 206.
74. U. Banik, A. Agrawal, H. Meddeb, O. Sergeev, N. Reininghaus, M. Götz-Köhler, K. Gehrke, J. Stuhrenberg, M. Vehse, M. Sznajder, C. Agert, "Efficient Thin Polymer Coating as a Selective Thermal Emitter for Passive Daytime Radiative Cooling", *ACS Appl. Mater. Interfaces* **2021**, 13 (20), 24130-24137.
75. A. Grosjean, A. Soum-Glaude, L. Thomas, "Replacing silver by aluminum in solar mirrors by improving solar reflectance with dielectric top layers", *Sustainable Materials and Technologies* **2021**, 29.
76. D. Li, X. Liu, W. Li, Z. Lin, B. Zhu, Z. Li, J. Li, B. Li, S. Fan, J. Xie, J. Zhu, "Scalable and hierarchically designed polymer film as a selective thermal emitter for high-performance all-day radiative cooling", *Nat Nanotechnol* **2021**, 16, 153-158.
77. M. Chen, D. Pang, J. Mandal, X. Chen, H. Yan, Y. He, N. Yu, Y. Yang, "Designing Mesoporous Photonic Structures for High-Performance Passive Daytime Radiative Cooling", *Nano Lett.* **2021**, 21 (3), 1412-1418.
78. Y. Tian, H. Shao, X. Liu, F. Chen, Y. Li, C. Tang, Y. Zheng, "Superhydrophobic and Recyclable Cellulose-Fiber-Based Composites for High-Efficiency Passive Radiative Cooling", *ACS Appl. Mater. Interfaces* **2021**, 13 (19), 22521-22530.
79. J. Wang, J. Sun, T. Guo, H. Zhang, M. Xie, J. Yang, X. Jiang, Z. Chu, D. Liu, S. Bai, "High-Strength Flexible Membrane with Rational Pore Architecture as a Selective Radiator for High-Efficiency Daytime Radiative Cooling", *Advanced Materials Technologies* **2021**, 7 (1).
80. T. Wang, Y. Wu, L. Shi, X. Hu, M. Chen, L. Wu, "A structural polymer for highly efficient all-day passive radiative cooling", *Nat. Commun.* **2021**, 12 (1), 365.
81. B. Xiang, R. Zhang, Y. Luo, S. Zhang, L. Xu, H. Min, S. Tang, X. Meng, "3D porous polymer film with designed pore architecture and auto-deposited SiO₂ for highly efficient passive radiative cooling", *Nano Energy* **2021**, 81.
82. H. Zhong, Y. Li, P. Zhang, S. Gao, B. Liu, Y. Wang, T. Meng, Y. Zhou, H. Hou, C. Xue, Y. Zhao, Z. Wang, "Hierarchically Hollow Microfibers as a Scalable and Effective Thermal Insulating Cooler for Buildings", *ACS Nano* **2021**, 15 (6), 10076-10083.
83. L.-C. Hu, C.-H. Xue, B.-Y. Liu, X.-J. Guo, J.-H. Wang, F.-Q. Deng, "Scalable Superhydrophobic Flexible Nanofiber Film for Passive Daytime Radiative Cooling", *ACS Applied Polymer Materials* **2022**, 4 (5), 3343-3351.
84. J. Jaramillo-Fernandez, H. Yang, L. Schertel, G. L. Whitworth, P. D. Garcia, S. Vignolini, C. M. Sotomayor-Torres, "Highly-Scattering Cellulose-Based Films for Radiative Cooling", *Adv. Sci.* **2022**, 9 (8), 2104758.
85. H. Cong, B. Yu, J. Tang, Z. Li, X. Liu, "Current status and future developments in preparation and application of colloidal crystals", *Chem. Soc. Rev.* **2013**, 42 (19), 7774-800.

86. J. B. Kim, S. Y. Lee, J. M. Lee, S.-H. Kim, "Designing Structural-Color Patterns Composed of Colloidal Arrays", *ACS Appl. Mater. Interfaces* **2019**, *11* (16), 14485-14509.
87. J. F. Galisteo-Lopez, M. Ibisate, R. Sapienza, L. S. Froufe-Perez, A. Blanco, C. López, "Self-assembled photonic structures", *Adv. Mater.* **2011**, *23* (1), 30-69.
88. K. Ueno, A. Inaba, Y. Sano, M. Kondoh, M. Watanabe, "A soft glassy colloidal array in ionic liquid, which exhibits homogeneous, non-brilliant and angle-independent structural colours", *Chem. Commun.* **2009**, (24), 3603-3605
89. P. D. Garcia, R. Sapienza, C. Lopez, "Photonic glasses: a step beyond white paint", *Adv. Mater.* **2010**, *22* (1), 12-9.
90. S. Caixeiro, M. Peruzzo, O. D. Onelli, S. Vignolini, R. Sapienza, "Disordered Cellulose-Based Nanostructures for Enhanced Light Scattering", *ACS Appl. Mater. Interfaces* **2017**, *9* (9), 7885-7890.
91. J. Syurik, G. Jacucci, O. D. Onelli, H. Hölscher, S. Vignolini, "Bio-inspired Highly Scattering Networks via Polymer Phase Separation", *Adv. Funct. Mater.* **2018**, *28* (24).
92. N. N. Shi, C. C. Tsai, F. Camino, G. D. Bernard, N. Yu, R. Wehner, "Thermal physiology. Keeping cool: Enhanced optical reflection and radiative heat dissipation in Saharan silver ants", *Science* **2015**, *349* (6245), 298-301.
93. H. Zhou, J. Xu, X. Liu, H. Zhang, D. Wang, Z. Chen, D. Zhang, T. Fan, "Bio-Inspired Photonic Materials: Prototypes and Structural Effect Designs for Applications in Solar Energy Manipulation", *Adv. Funct. Mater.* **2017**, *28* (24).
94. G. Jacucci, L. Schertel, Y. Zhang, H. Yang, S. Vignolini, "Light Management with Natural Materials: From Whiteness to Transparency", *Adv. Mater.* **2020**, e2001215.
95. M. Buresi, L. Cortese, L. Pattelli, M. Kolle, P. Vukusic, D. S. Wiersma, U. Steiner, S. Vignolini, "Bright-White Beetle Scales Optimise Multiple Scattering of Light", *Sci. Rep.* **2014**, *4*, 6075.
96. D. Xie, Z. Yang, X. Liu, S. Cui, H. Zhou, T. Fan, "Broadband omnidirectional light reflection and radiative heat dissipation in white beetles *Goliathus goliatus*", *Soft Matter* **2019**, *15* (21), 4294-4300.
97. W. Zou, L. Pattelli, J. Guo, S. Yang, M. Yang, N. Zhao, J. Xu, D. S. Wiersma, "Biomimetic Polymer Film with Brilliant Brightness Using a One-Step Water Vapor-Induced Phase Separation Method", *Adv. Funct. Mater.* **2019**, *29* (23).
98. M. Yang, W. Zou, J. Guo, Z. Qian, H. Luo, S. Yang, N. Zhao, L. Pattelli, J. Xu, D. S. Wiersma, "Bioinspired "Skin" with Cooperative Thermo-Optical Effect for Daytime Radiative Cooling", *ACS Appl. Mater. Interfaces* **2020**, *12* (22), 25286-25293.
99. X. Liu, C. Xiao, P. Wang, M. Yan, H. Wang, P. Xie, G. Liu, H. Zhou, D. Zhang, T. Fan, "Biomimetic Photonic Multiform Composite for High-Performance Radiative Cooling", *Advanced Optical Materials* **2021**, *9* (22).
100. G. Crini, "Historical review on chitin and chitosan biopolymers", *Environmental Chemistry Letters* **2019**, *17* (4), 1623-1643.
101. T. Li, Y. Zhai, S. He, W. Gan, Z. Wei, M. Heidarinejad, D. Dalgo, R. Mi, X. Zhao, J. Song, J. Dai, C. Chen, A. Aili, A. Vellore, A. Martini, R. Yang, J. Srebric, X. Yin, L. Hu, "A radiative cooling structural material", *Science* **2019**, *364* (6442), 760-763.
102. Y. Chen, B. Dang, J. Fu, C. Wang, C. Li, Q. Sun, H. Li, "Cellulose-Based Hybrid Structural Material for Radiative Cooling", *Nano Lett.* **2021**, *21* (1), 397-404.
103. B. Zhu, W. Li, Q. Zhang, D. Li, X. Liu, Y. Wang, N. Xu, Z. Wu, J. Li, X. Li, P. B. Catrysse, W. Xu, S. Fan, J. Zhu, "Subambient daytime radiative cooling textile based on nanoprocessed silk", *Nat Nanotechnol* **2021**, *16* (12), 1342-1348.
104. Z. Yang, J. Zhang, "Bioinspired Radiative Cooling Structure with Randomly Stacked Fibers for Efficient All-Day Passive Cooling", *ACS Appl. Mater. Interfaces* **2021**, *13* (36), 43387-43395.
105. S. H. Choi, S. W. Kim, Z. Ku, M. A. Visbal-Onufrak, S. R. Kim, K. H. Choi, H. Ko, W. Choi, A. M. Urbas, T. W. Goo, Y. L. Kim, "Anderson light localization in biological nanostructures of native silk", *Nat. Commun.* **2018**, *9* (1), 452.

106. P. Li, A. Wang, J. Fan, Q. Kang, P. Jiang, H. Bao, X. Huang, "Thermo-Optically Designed Scalable Photonic Films with High Thermal Conductivity for Subambient and Above-Ambient Radiative Cooling", *Adv. Funct. Mater.* **2021**, 32 (5).
107. Z. Chen, L. Zhu, A. Raman, S. Fan, "Radiative cooling to deep sub-freezing temperatures through a 24-h day-night cycle", *Nat. Commun.* **2016**, 7, 13729.
108. W. Huang, Y. Chen, Y. Luo, J. Mandal, W. Li, M. Chen, C. C. Tsai, Z. Shan, N. Yu, Y. Yang, "Scalable Aqueous Processing-Based Passive Daytime Radiative Cooling Coatings", *Adv. Funct. Mater.* **2021**, 31 (19).
109. K. Zhou, W. Li, B. B. Patel, R. Tao, Y. Chang, S. Fan, Y. Diao, L. Cai, "Three-Dimensional Printable Nanoporous Polymer Matrix Composites for Daytime Radiative Cooling", *Nano Lett.* **2021**, 21 (3), 1493-1499.
110. S. Y. Heo, G. J. Lee, D. H. Kim, Y. J. Kim, S. Ishii, M. S. Kim, T. J. Seok, B. J. Lee, H. Lee, Y. M. Song, "A Janus emitter for passive heat release from enclosures", *Sci Adv* **2020**, 6 (36).
111. G. Park, K. Roh, H. Kim, S. Khan, M. Lee, B. W. Kim, W. Kim, "Universal Experimental Methods for Evaluating the Performance of Radiative Cooling Materials", *Advanced Materials Technologies* **2021**, 7 (6).
112. Labsphere Integrating Sphere Theory and Applications. <https://www.labsphere.com/wp-content/uploads/2021/09/Integrating-Sphere-Theory-and-Applications.pdf> (accessed 11.04.2023).
113. Polarizer and Depolarizer for the Agilent Cary Series UV-Vis-NIR. https://www.agilent.com/cs/library/datasheets/public/5991-0020EN_DataSheet_CaryUVVisNIRPolarizer.pdf (accessed 09.05.2023).
114. M. Schöttle, T. Lauster, L. J. Roemling, N. Vogel, M. Retsch, "A Continuous Gradient Colloidal Glass", *Adv. Mater.* **2023**, 35 (7), e2208745.
115. R. Lohmann, I. T. Cousins, J. C. DeWitt, J. Gluge, G. Goldenman, D. Herzke, A. B. Lindstrom, M. F. Miller, C. A. Ng, S. Patton, M. Scheringer, X. Trier, Z. Wang, "Are Fluoropolymers Really of Low Concern for Human and Environmental Health and Separate from Other PFAS?", *Environ. Sci. Technol.* **2020**, 54 (20), 12820-12828.
116. T. Lauster, A. Mauel, K. Herrmann, V. Veitengruber, Q. Song, J. Senker, M. Retsch, "From Chitosan to Chitin: Bio-Inspired Thin Films for Passive Daytime Radiative Cooling", *Adv. Sci.* **2023**, 10 (11), e2206616.
117. Q. Song, T. Tran, K. Herrmann, T. Lauster, M. Breitenbach, M. Retsch, "A tailored indoor setup for reproducible passive daytime cooling characterization", *Cell Rep Phys Sci* **2022**, 3 (8), 100986.
118. Q. Gao, T. Lauster, B. A. F. Kopera, M. Retsch, S. Agarwal, A. Greiner, "Breathable and Flexible Dual-Sided Nonwovens with Adjustable Infrared Optical Performances for Smart Textile", *Adv. Funct. Mater.* **2021**, 32 (5).

5. A Continuous Gradient Colloidal Glass



A controlled extraction emulsion process (CrEEP) allows the synthesis of monodisperse latex particles with a continuous size gradient. Subsequent self-assembly into a photonic glass results in a thin film with a continuous photonic gradient and structural colors ranging over the full visible spectrum. This concept is shown to improve the broadband reflectance of such a mesostructure compared to a non-gradient mixture.

A Continuous Gradient Colloidal Glass

Marius Schöttle, Tobias Lauster, Lukas J. Roemling, Nicolas Vogel, and Markus Retsch*

Colloidal crystals and glasses manipulate light propagation depending on their chemical composition, particle morphology, and mesoscopic structure. This light-matter interaction has been intensely investigated, but a knowledge gap remains for mesostructures comprising a continuous property gradient of the constituting particles. Here, a general synthetic approach to bottom-up fabrication of continuous size gradient colloidal ensembles is introduced. First, the technique synthesizes a dispersion with a specifically designed gradual particle size distribution. Second, self-assembly of this dispersion yields a photonic colloidal glass with a continuous size gradient from top to bottom. Local and bulk characterization methods are used to highlight the significant potential of this mesostructure, resulting in vivid structural colors along, and in superior light scattering across the gradient. The process describes a general pathway to mesoscopic gradients. It can be expectedly be transferred to a variety of other particle-based systems where continuous gradients will provide novel physical insights and functionalities.

1. Introduction

Structured materials show perceptible photonic properties when the characteristic length scale is similar to the wavelength of visible light. The interaction of photons with a periodically changing refractive index (n) in photonic crystals (PCs) creates a dispersion relation with wave-vector dependent gaps analogous to that of electrons in semiconductors.^[1] These stop bands are the cause of characteristic, iridescent structural colors.^[2] From sensors to optical metamaterials, increasingly complex structures allow tailoring of these properties.^[3,4] However, many are only accessible via simulations or in the microwave range,^[5,6] others are limited to high- n materials.^[7]

Complementary to the phenomenon of ballistic light transport in ordered structures is the dispersive light diffusion

in photonic glasses (PGs).^[8,510] These jammed packings of monodisperse, dielectric spheres show coherent scattering due to Mie resonances and short-range order.^[11,12] Because of the isotropic nature, the resulting colors are angle-independent.^[13,14] Particle size and morphology, such as core-shell and hollow sphere structures, have been shown to influence the optical properties and provide tunable scattering and broadband reflectance of PGs.^[15,19] Recently, anisotropic particles have also been shown to be useful for the adjustment of the scattering properties of the ensembles.^[20,21]

Hierarchical structural design can introduce further complexity to particulate system.^[22] For example, multilayer PC films with a cross-plane, stepwise change of the lattice constant show properties not found in single-component systems. These range from broadband reflectivity^[23] to angular selectivity.^[24] However, fabrication methods are often tedious and typically apply physical vapor deposition or repetitive colloidal assembly.^[25,26] Without precise optimization, the latter can suffer from degradation of preformed layers and delamination. Further issues include incoherent light scattering at the interfaces and small sample sizes.

Despite the intense research on photonic crystals and glasses, one major category of colloidal mesostructure has received surprisingly little attention: continuous gradient structures. Continuous gradients in colloidal assemblies is an emerging topic, with few examples and approaches being reported in literature. Gradual changes, e.g., in the interparticle distance or composition can be formed via centrifugation,^[27,28] post-assembly deformation^[29] or modified coating procedures.^[30,31] From a fundamental point of view, a better physical understanding of photonic materials with gradually changing properties needs to be developed and compared to experimental results.^[32,34] To our knowledge, no experimental realization of a photonic colloidal assembly with a continuous particle size gradient has been presented to date. To achieve such a structure, two major challenges need to be addressed: First, particle dispersions with precise control of size and a continuous size variation need to be reliably available. Second, self-assembly must retain, not mix, the particle size gradient and immobilize the particles gradually in the colloidal ensemble.

Here, we provide a solution to both challenges that conceivably can also be applied to other (functional) particles. This general approach to continuous gradient colloidal glasses will add a missing piece to the field of colloidal mesostructures and opens a new field for photonic engineering and beyond. At the heart

M. Schöttle, T. Lauster, M. Retsch
Department of Chemistry
University of Bayreuth
Universitätsstr. 30, 95447 Bayreuth, Germany
E-mail: markus.retsche@uni-bayreuth.de

L. J. Roemling, N. Vogel
Institute of Particle Technology
Friedrich-Alexander University Erlangen-Nürnberg
91058 Erlangen, Germany

 The ORCID identification number(s) for the author(s) of this article can be found under <https://doi.org/10.1002/adma.202208745>.

© 2022 The Authors. Advanced Materials published by Wiley-VCH GmbH. This is an open access article under the terms of the Creative Commons Attribution License, which permits use, distribution and reproduction in any medium, provided the original work is properly cited.

DOI: 10.1002/adma.202208745

of our work is a controlled emulsion extraction process (CrEEP) that enables us to store the time-dependent size increase of monodisperse latex particles in a thin extraction tube, where laminar flow prevails. Subsequent filtration assembly translates the gradient dispersion into a film with a fully continuous, cross-plane gradient of the particle size. First, we present the synthesis method and then show the characteristics of the 3D self-assembled colloidal gradient material.

2. Results and Discussion

Surfactant-free emulsion polymerization is an established method for the preparation of monodisperse latex particle suspensions.^[35,36] Further control can be obtained via a semibatch process by first preparing seed particles that then increase in size when more monomer is added.^[37,38] In our CrEEP-approach (Figures S1 and S2, Supporting Information), the monomer is added gradually, and the growing particle suspension is simultaneously extracted into a thin tube. The resulting time-dependent change of the particle diameter is thereby stored in the extraction tube and turned into a positional dependency. Slow extraction and the small diameter of the tube provide controlled laminar flow. To verify the controlled nature of this process, we show that the reaction rate of the emulsion polymerization is fast compared the rate of monomer addition by evaluating the kinetics of the particle growth during seed synthesis (Figure S3, Supporting information). Mixing is further inhibited by fractionation via the injection of air bubbles as separators inside the tube. Thereby the monodisperse nature inherent to the emulsion polymerization is maintained. Analogous experiments without injection of air result in a slightly less ordered assembly (Figure S4, Supporting information). The air bubbles have the additional benefit of quenching the remaining initiator molecules with ambient oxygen, inhibiting any further polymerization. The fact that the continuous particle growth and extraction take place in the same reactor as the seed synthesis ensures reproducible starting-conditions. Combined with the slow monomer addition, this results in a highly controlled reaction. Ultimately, a large number of equidistant fractions (in this case 110) are retained in the tube (Figure 1a). We examine every 10th fraction via dynamic light scattering (DLS) and correlate it to the respective reaction time during the extraction process (Figure 1b,c). We observe a near-linear increase of the hydrodynamic particle diameter and a low polydispersity throughout the synthesis. Both confirm the high degree of control that is necessary for the self-assembly process, which is dramatically influenced by both size and size distribution. In our example, we prepare a diameter range between 2205310 nm to specifically target photonic materials in the visible range. In combination with the number of fractions, this implies a sub-nm step size between neighboring fractions. Naturally, this is smaller than the size distribution of any given latex particle synthesis. Consequently, this constitutes a smooth and gradual size increase, a feature not accessible using a multi-pot approach.

To demonstrate the quality of fractions obtained via CrEEP, we induce self-assembly via heated drop-casting. The formation of PCs with structural colors dependent on the diameter

of the particles becomes apparent via white light microscopy (Figure 1d). Brilliant colors ranging from blue to red can be observed. Due to the fcc symmetry and the concomitant *k*-vector dependency of the optical stop-band, these are inherently angle-dependent. Increasing the angle between light source and observer causes a blue shift of all 12 drop-cast spots (Figure 1e) and verifies the crystallinity. Further optical characterization with normal incidence reflectance μ -UV-vis spectroscopy (Figure 1f) elucidates the size-dependent properties. As the particle diameter increases, the stop-band peak gradually shifts to higher wavelengths. The position of the peak with respect to the reaction time of the corresponding fraction follows a linear trend (Figure 1g). Considering the linear dependency of the lattice spacing and wavelength in the Bragg-Snell Equation,^[25] this corroborates the similar trend observed for the DLS results. Scanning electron microscopy (SEM) images of four selected PCs (Figure 1h) illustrate the monodisperse nature and hexagonal symmetry as well as the controlled increase of the particle size. An overview SEM image (Figure S5, Supporting Information) shows large domain sizes. Altogether this preliminary evaluation of the extracted fractions shows that the gradual increase of the particle size can be retained in a thin tube via CrEEP. Prevention of mixing thereby ensures that the monodisperse nature is maintained and allows self-assembly to form photonic structures.

After the CrEEP, a gradient colloidal dispersion is stored inside the extraction tube in a size-sorted manner. We now present a straightforward self-assembly process to transform this gradient dispersion into a colloidal glass with a smooth and continuous gradient. Our semicontinuous filtration technique involves dilution and subsequent filtration of each fraction. This allows us to fabricate a free-standing colloidal glass film with a gradually increasing particle size from top to bottom (Figure 2a; Figure S6a, Supporting Information). A sample 3.5 cm in diameter and with a thickness of $110 \pm 5 \mu\text{m}$ is thereby obtained (Figure S6b, Supporting Information).

We demonstrate the successful fabrication of the intended gradient colloidal glass by laser scanning confocal microscopy (LSCM)^[39] across the edge of a broken gradient film. An overlay of the height image obtained via laser-scanning and white light microscopy images from various focal positions provides a simple and intuitive impression (Figure 2b; Figure S7, Supporting Information). Complementary to the colorful appearance observed for self-assembled particles of separate fractions, we find structural colors continuously ranging from blue to red, reminiscent of a rainbow. The top and bottom faces appear blue and red, respectively, corresponding to the particle size of the first and last fraction. The addition of a broadband absorber is known to counteract the effect of diffuse scattering.^[40] We, therefore, improve the saturation of the side-view structural colors by a thin layer of carbon (10 nm) on the surface of the cross section (Figure S8, Supporting information). While the colloidal glass filtration is conducted in a semicontinuous way, we do not observe any layering or stepwise particle size increase. As outlined in the gradient dispersion synthesis, the mean particle size changes with $<1 \text{ nm}$ from fraction to fraction, which is too small to be resolved analytically. Another advantage of the filtration approach is that a large sample can be prepared with homogeneous gradient properties. The colloidal

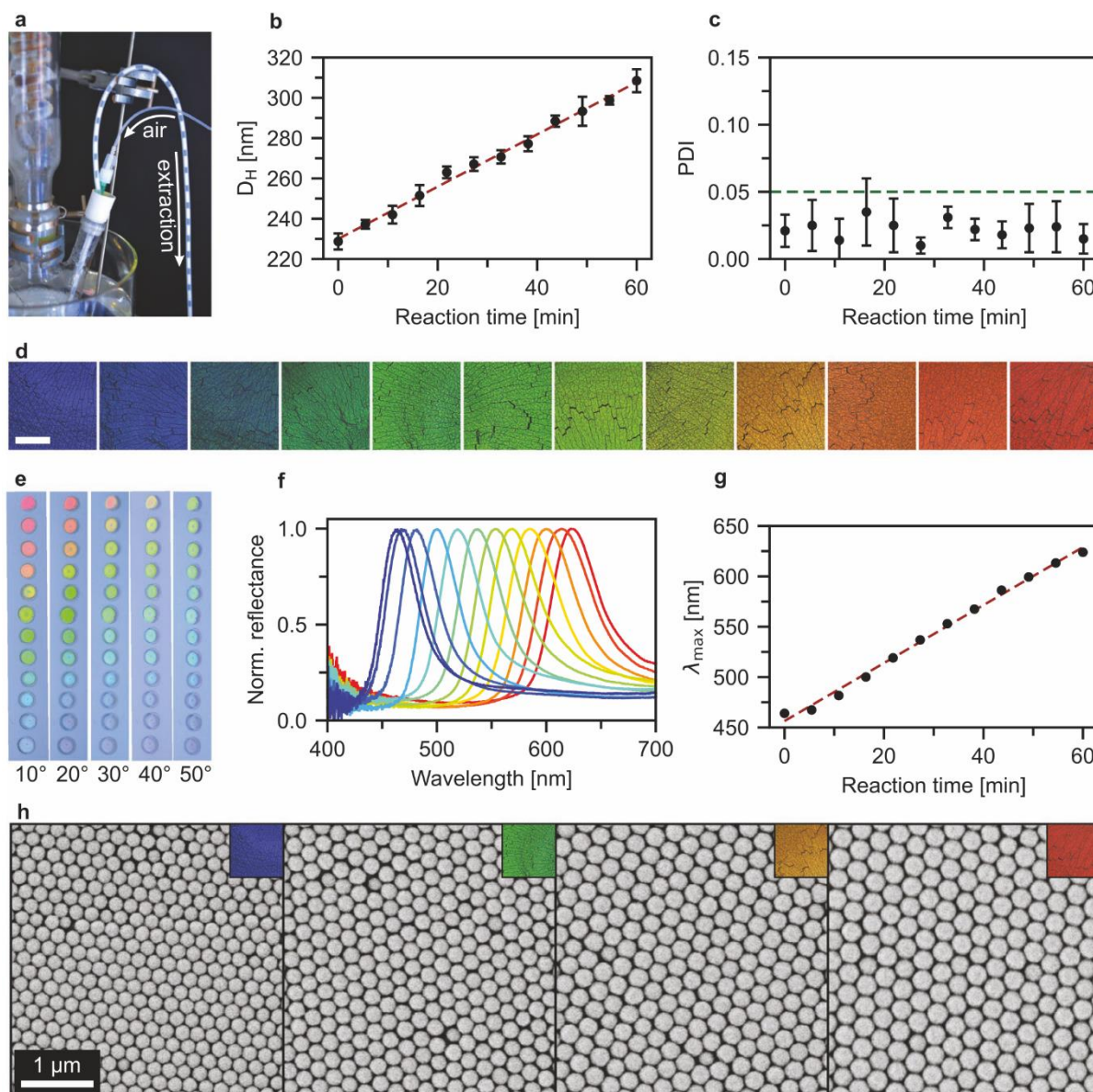


Figure 1. Characterization of equidistant fractions after the controlled emulsion extraction process (CrEEP). a) Snapshot of fractions during the extraction process showing even separation by air bubbles. b,c) Hydrodynamic diameter (D_H) and polydispersity index (PDI) obtained from DLS measurements of every 10th fraction. The reaction time noted here corresponds to the CrEEP starting with the gradual monomer addition. A linear fit shown in red elucidates the highly controlled nature of the gradual seeded growth. The polydispersity remains below 5% and is independent of the reaction time. d) Light microscopy images of these fractions after drop-casting showing size-dependent structural colors typical for colloidal crystals. Scale bar: 100 μm e) Photographs of the samples measured in (d) at different angles between camera and light source. f) μ -UV-vis reflectance spectra of the drop-cast fractions showing a gradual red-shift of the stop-band as the particle size increases. g) Peak position of the stop-band versus reaction time showing a linear relation. This stands in accordance with the DLS measurements and particle size. h) SEM images of selected drop-cast fractions. Insets show the corresponding light microscopy images. Both the increase in absolute size, as well as the consistently monodisperse nature, can be observed in the self-assembled colloidal crystals showing hexagonal symmetry.

gradient and hence the photonic properties are identical when examining cross sections via LSCM at several different macroscopic positions along the length of the filtered film (Figure S9, Supporting Information).

SEM images of selected positions along the cross section (Figure 2c) provide structural insights into the origin of colors in the gradient. The filtration assembly forces random aggregation of particles and thus a disordered structure. We

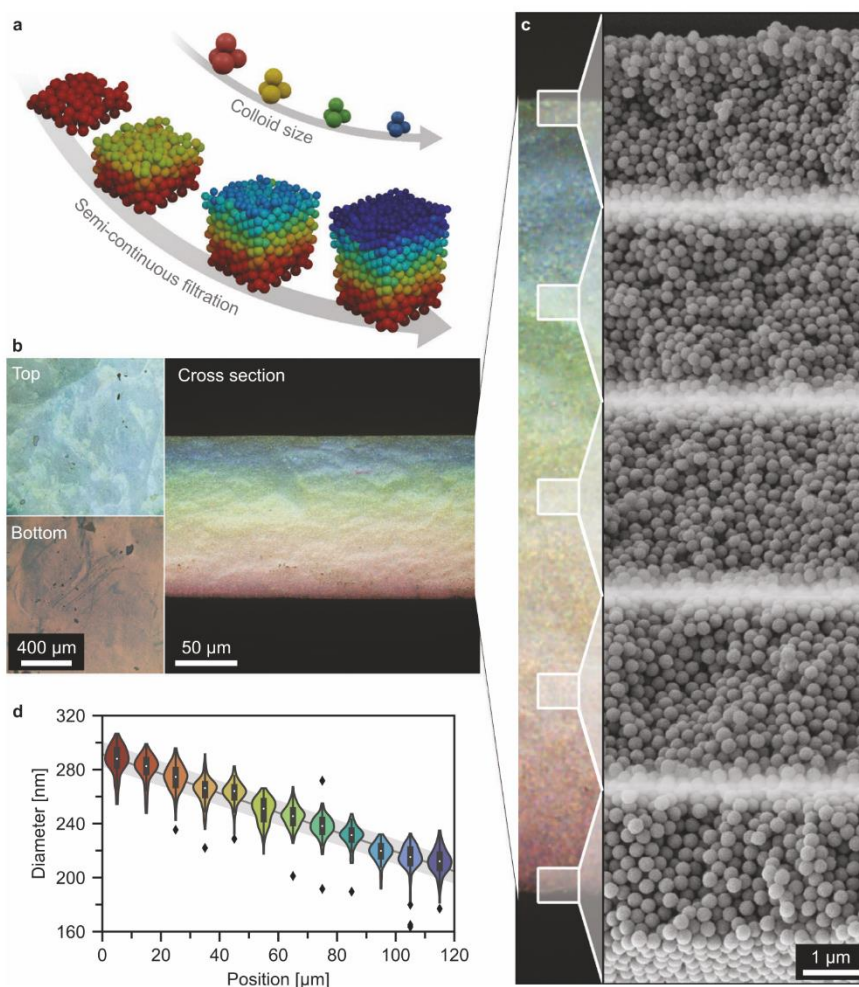


Figure 2. Gradient photonic glass prepared via semicontinuous filtration. a) Schematic illustration of the z -gradient structure resulting from the gradual assembly process. b) Light microscopy images of the top and bottom surface as well as the cross section showing the gradual transition of structural color throughout the entire visible spectrum. c) Representative SEM images of the colloidal assembly at the positions indicated in the cross-section. d) Size distribution of particles at equidistant positions along the gradient as obtained from the SEM images in Figure S10 (Supporting Information). At each position, more than 100 particles were measured. Outliers are shown as black diamonds.

attribute this to the fast kinetics of the filtration process and the absence of capillary forces.^[22] The result is a photonic glass that consists of monodisperse, dielectric Mie scatterers and shows a position-dependent resonance frequency. Measurement of particle diameters at equidistant z -positions along the cross section allowed statistical evaluation of the change in size (Figure 2d; Figure S10, Supporting Information). Two important observations can be made here: 1) The position-dependent particle size shows a linear trend. This, once more, emphasizes the high degree of control during synthesis and assembly. We achieve this linearity by careful optimization of the CrEEP (details are outlined in Figure S11, Supporting Information). 2) At any given z -position, all particles are nearly monodisperse, underlining the performance of the fractionation in our process. The efficiency of fractionation is better than the polydispersity of the emulsion polymerization itself; hence the

overlap of individual fractions is continuous. The result is one of the significant features presented in this work: the circumvention of discrete steps in a gradient particle assembly. The photonic glass shown here is consequently a fully continuous gradient structure.

For a full characterization analogous to that of discrete fractions, we show local μ -UV-vis reflectance spectra at equidistant positions along the gradient material (Figure 3a; Figure S12, Supporting Information). As the particle size increases, the reflectance peak shows a gradual red shift (Figure 3b). This positional dependency is linear, (Figure 3c) which correlates with the linear change in diameter examined via SEM evaluation. Compared to the spectra of colloidal crystals in Figure 1f, the width of these peaks is significantly larger. We attribute this to the short-range order and also partly to the fact that the measurement averages over a range

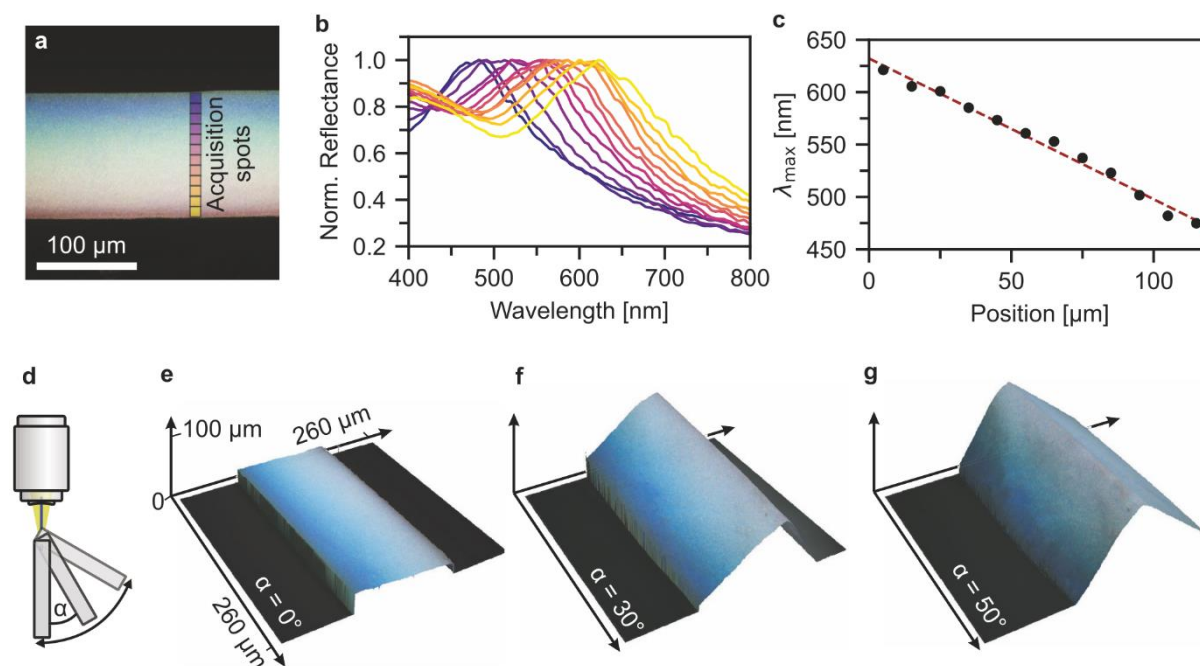


Figure 3. Local optical characterization of the gradient photonic glass. a) Microscopy image of a carbon-coated cross-section illustrating the spot size and position where individual spectra were obtained. b) Local spectra and c) wavelengths of the peak maxima showing a linear red-shift from the top to the bottom of the gradient. d) Microscopy setup used to examine different viewing angles of one gradient cross-section to prove the angle independence of the structural colors. e, f) Resulting overlay of height and white light microscopy images obtained via LSCM of a sample tilted between 0 and 50°. The color range of the gradient remains between blue and red, independent of the viewing angle.

of 10 μm, thereby covering a particle size increase of ≈8 nm in each area. The latter effect becomes more obvious when increasing the spot size (Figure S13d, Supporting Information). Averaging over half the cross section thereby naturally results in further peak broadening. Spectra obtained from samples without carbon-coating show stronger diffuse scattering, most visible toward smaller wavelengths (Figure S13a,c, Supporting Information).

The fact that isotropic colloidal assemblies exhibit no discrete peaks in Fourier space and, therefore, produce non-iridescent colors can be a significant advantage.^[16] We examine this property by tilting the cross section of a gradient photonic glass under a microscope and conducting LSCM measurements at different viewing angles from 0 to 50° (Figure 3d-g; Figure S14, Supporting Information). This approach is similar to previously shown characterization methods of colloidal supraparticles.^[41] Unlike the results obtained for the iridescent colloidal crystals in Figure 1e, the coloration remains unchanged and ranges between blue and red at all viewing angles. In summary, the local characterization reveals that the gradient colloidal glass exhibits angle-independent reflectivity throughout the visible spectrum.

We now compare the diffuse reflectance from the top surface of the colloidal gradient glass with different reference samples (Figure 4a-f) to establish how the continuous mesostructure affects the optical properties. Homogeneous, non-gradient samples are prepared via filtration of pure small (224 nm) and large (304 nm) particles, respectively. Additionally, these particles are

used for the fabrication of a statistical, binary mixture as well as a bilayer sample. The CrEEP technique is applied to prepare two different samples: 1) a statistical “gradient mixture” via mixing of all fractions and subsequent filtration and 2) the continuous gradient material discussed in Figure 2 and Figure 3. The two CrEEP-syntheses are shown to be identical via UV-vis spectroscopy and DLS measurements of the particles in the respective first and last fractions (Figure S15, Supporting Information). The film thickness is $112 \pm 3 \mu\text{m}$ throughout all samples (Figure S16, Supporting Information).

The single-component sample consisting of small particles shows an intense blue color, whereas the large particles result in a less saturated red appearance. The latter is more compromised by diffuse light scattering and, therefore, appears fainter. The UV-vis diffuse reflectance spectra of these samples show distinct peaks at 420 and 580 nm, respectively (Figure 4g), as expected from the increase in diameter.^[42]

Next, the two disordered structures, both binary and gradient mixture, are compared. Microscopy images of cross sections of the two show a white color. However, the reflectance spectra reveal a pronounced difference (Figure 4h), even though both samples comprise particles in the same size range. The binary mixture almost exclusively results in a profile characteristic for diffuse scattering. A slight shoulder at 550 nm hints toward a rather weak contribution of coherent scattering. Conversely, in the case of the gradient mixture, a distinct peak at 515 nm can be observed. This lies roughly in the middle of the peaks observed for the pure small and large particles, respectively.

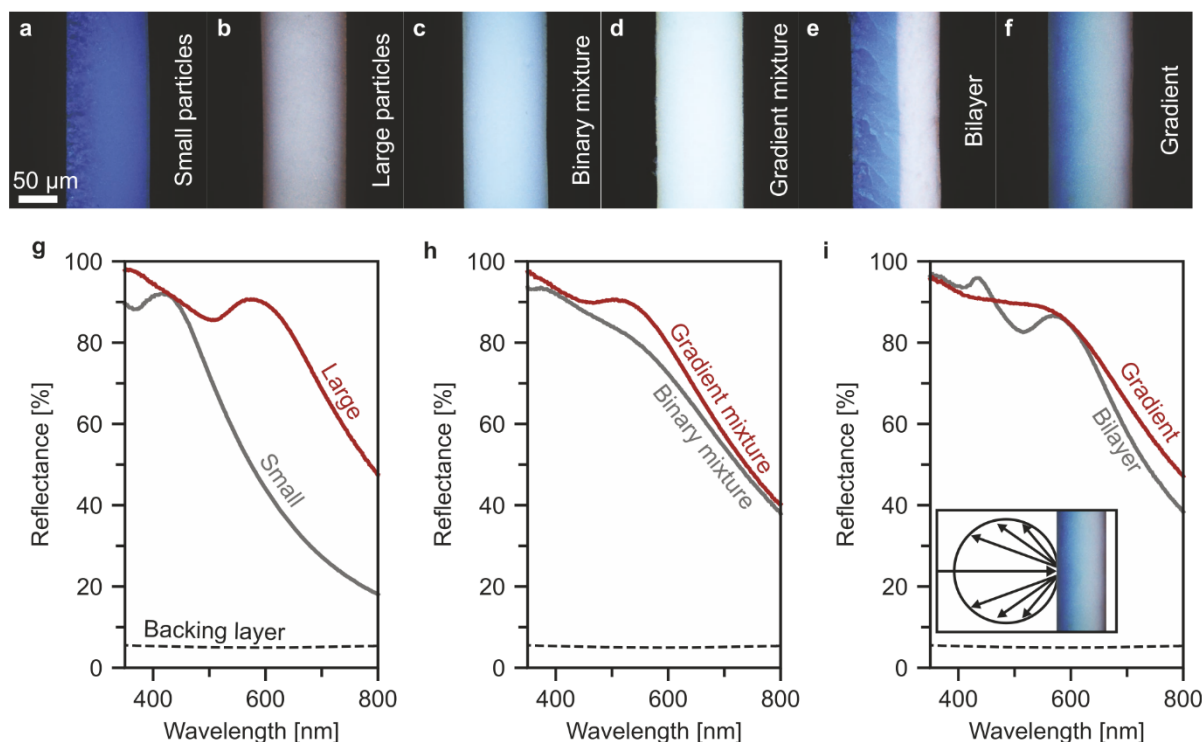


Figure 4. Diffuse reflectance UV-vis spectroscopy of colloidal assemblies prepared via filtration. a,b) Cross section light microscopy images of samples consisting of monodisperse particles. c) Disordered, binary mixture of these reference particles. d) Sample prepared by mixing all fractions obtained from the semibatch emulsion polymerization prior to filtration. e) Bilayer of small and large particles. f) Gradient sample prepared via the presented semicontinuous filtration approach after semibatch emulsion polymerization. g-i) UV-vis diffuse reflectance spectra of all samples measured with an integrating sphere. The inset in (i) elucidates the measurement geometry.

two pure SEM measurements show a statistical mixture of all particle sizes and no segregation (Figure S17, Supporting Information), corroborating that this coloration must be attributed to coherent scattering of the isotropic assembly. We rationalize the difference via the degree of disorder, elucidated by the pair distribution function, $g(r)$ of the two types of colloidal glasses. Simple 2D simulations (Figure S18, Supporting Information) of both cases and subsequent $g(r)$ evaluation^[43] show that the binary mixture shows a pair correlation function limited to a set of distinct pairs: small-small, small-large, and large-large. No additional peaks can be observed in subsequent coordination spheres. In the gradient mixture, peaks in the $g(r)$ can be observed up to the 5th coordination sphere. Since phase correlation and constructive interference of scattered waves depend on the short-range order^[8] this results in a more pronounced peak in the reflectance spectrum.

Lastly, we compare the bilayer and the gradient sample (Figure 4i). The former represents the most extreme case of a stepwise gradient, while the latter is the fully continuous counterpart. In both cases, the sample is oriented, so that the smallest particles are on top. The reasoning behind this is that waves of shorter wavelengths (blue light) are affected more by diffuse scattering of the large particles. Small particles that show Mie resonance at these frequencies should, therefore, interact with the light first.^[26] The spectrum of the

bilayer shows two discrete peaks at the same wavelengths as the single-component reference samples. This proves that the diffuse reflectance measurements are sensitive to photons coherently scattered in lower regions of the sample. This is possible due to an increased ratio of single- and multiple scattering events caused by the short-range order and near-field effects.^[13] These observations also hold for the interpretation of the optical properties of the gradient photonic glass. Here, we see a plateau over the full region between the two peaks of the bilayer. Unlike in the bilayer, no local minima and maxima are observed. Instead, a uniform reflectance results over the visible range. We attribute this unique property to the gradual mesoscale structure of this material. In comparison, step-gradient samples prepared via deposition of discrete layers always show distinct peaks (Figure S19, Supporting Information). The gradient spectrum is in accordance with the local optical characterization, as the plateau of the diffuse reflectance spans the same wavelength range as the maxima of peaks measured along the cross section in Figure 3b. Additionally, the plateau and general shape closely resemble the reflectance spectrum obtained from a non carbon-coated cross section measured with a large spot size (Figure S13c, Supporting Information). This implies the applicability of such a gradient material as a broadband reflector in a wavelength range of choice. We confirmed this possibility by a separate CrEEP synthesis with an

extended size range from 220 nm up to 450 nm (Figure S20, Supporting Information). The gradient colloidal glass, consequently, covers a much broader spectral range compared to the system outlined here (Figure S21, Supporting Information). The critical role of the mesoscopic structure becomes apparent when directly comparing the gradient superstructure to the gradient mixture (Figure S22, Supporting Information). Self-assembly of a gradient particle dispersion mixture without an additional mesoscopic gradient does not show a plateau in the visible range. Furthermore, the diffuse reflectance of the gradient photonic glass is superior to the disordered case across the entire spectral range.

Enhanced scattering of visible light is of great importance in fields such as thin reflective coatings and passive cooling applications.^[44,45] Beside the use of high-*n* materials such as titania, recent studies have examined alternative approaches such as the variation of the particle morphology of low-*n* materials to improve the scattering performance.^[21,46] An alternative/complementary approach is our optimized mesostructure. The gradient colloidal glass provides a tuneable approach to enhanced broadband reflectance, opening an alternative approach to create the whitest white. The fabrication proceeds without any stacking faults or cracks that can arise during the much more complicated fabrication of multilayer inverse opals or (2+1) photonic crystals.^[15,25] Recent theoretical work has examined the passive cooling properties of gradient particulate assemblies.^[33] These simulations are corroborated by our observation that the gradient colloidal glass shows superior diffuse reflectance compared to the mixed case. Overall, gradient mesostructures are a highly attractive materials class from which novel applications in the field of wave-matter interaction, granular mechanics, and filtration can be expected. This interest will be further expedited by the fact that this type of gradient can conceivably be assembled using any type of particle that can be fabricated via seeded growth.

3. Conclusion

We have introduced a general method that makes use of a previously untapped feature of colloid synthesis. The time-dependent growth of colloidal particles is stored in a thin extraction tube prior to self-assembly. The self-assembly process retains the gradual dispersion composition and provides access to fully continuous mesoscopic gradients. Local optical and structural characterization corroborated the gradient mesostructure, and diffuse reflectance measurements showcased the unique broadband reflectivity. Our method will be of immediate relevance for a broad interdisciplinary community investigating and optimizing photonic glasses toward highly efficient scattering systems^[44,46] with potential applications in areas such as passive cooling.^[45,47] Considering the generality of our synthetic approach, we expect that a wide range of novel, functional materials with a gradient composition will become available that reach far beyond model polymeric particles. Perfecting the self-assembly process may lead to elusive chirped colloidal crystals,^[32,48] while infiltration can provide further insight as to the superior mechanical properties of composite and porous graded materials.^[49,50]

4. Experimental Section

Materials: Water used in this work was of Millipore quality. Methyl methacrylate (MMA 99%), sodium styrene sulfonate (NaSS, 99.99%) and potassium persulfate (KPS, 99.99%) were obtained from Sigma Aldrich.

Seed Particle Synthesis: A 100 mL three-necked flask equipped with a reflux condenser and septa was loaded with 48 mL water and degassed for 75 min under a constant nitrogen stream at 80 °C and 650 rpm stirring speed. With 5 min of equilibration time between each addition, the following reactants are added: 1) 2 mg NaSS in 1 mL water, 2) 1.7 mL MMA, 3) 40 mg KPS in 1 mL water. The reaction was then allowed to proceed for 30 min before the semibatch process was initiated.

Semibatch Growth and Extraction: The setup preparation proceeds before the seed synthesis is started, so no oxygen enters the system between seed synthesis and gradual growth. Silicone tube (2 m) with an inner diameter of 2 mm was attached to a syringe, and both were filled with water. The free end of the tube was inserted through a septum and dipped into the reaction mixture. The cannula used for the injection of air was bent and inserted into this end of the tube. Two processes were started simultaneously after the 30 min of seed synthesis: 1) Monomer feed was initiated, and 3.0 mL MMA was added at 3.0 mL h⁻¹. 2) Extraction was initiated, and 5.0 mL were drawn into the tube at 5.0 mL h⁻¹. Air fractions of 16 μL were pumped into the tube end every 30 s. This resulted in 556 drops of monomer being added during the time it took to extract one fraction. After 60 min, 110 fractions were stored in the tube with a gradually increasing size of polymer latex particles. For the extended size range, the reaction proceeds analogously while adding 6.0 mL MMA at 6.0 mL h⁻¹. The introduction of air-bubbles to fractionate the extracted particle dispersion improved the particle size monodispersity during the filtration process (compare Figure S4, Supporting Information). It eliminated a boundary layer at the tube solid-liquid interface with zero flow velocity and quenches the polymerization. In combination with the laminar flow inside the tube any turbulent mixing was effectively suppressed by this technique and the extracted size distribution was retained.

Semicontinuous Filtration Assembly: The setup used for the filtration mediated self-assembly can schematically be seen in Figure S6 (Supporting information). The tube, filled with all fractions and still connected to the syringe, was used directly after the synthesis. Dispersion droplets were slowly pumped into an intermediate vessel at 0.4 mL h⁻¹. Water was simultaneously added dropwise at 60 mL h⁻¹. During dilution, the dispersion was mixed, and upon reaching a total volume of 5 mL, the vessel was periodically emptied via a Pythagorean cup mechanism. The diluted dispersion was thereby transferred into a vacuum filtration setup, and particles were deposited on a hydrophilized poly(tetrafluoroethylene) (PTFE) filter (Omnipore) with a pore size of 200 nm. The timing was adjusted, so that the filter process was completed before the next emptying of the intermediate vessel. During this time, the assembly did not dry but remained an aqueous paste. After completion, the swollen particle film was transferred from the filter via pressing and adhesion to a poly(dimethylsiloxane) (PDMS) substrate from which it could be removed after drying.

Reference samples were prepared via filtration of diluted dispersions of the seed particles and/or the particle dispersion remaining in the reaction vessel after the termination of the semibatch process.

Drop-Casting: Rapid self-assembly of every 10th fraction was done by direct drop-casting of 2 μL dispersion onto a clean glass substrate preheated to 80 °C.

Dynamic Light Scattering: Diluted dispersions were measured with a Zetasizer (Malvern) with 175° backscattering geometry to obtain the hydrodynamic diameter and the size distribution of the latex particles.

Viscosimetry: The relative viscosity of two dispersions with small (224 nm) and large (304 nm) particles in water was determined with an Ubbelohde viscosimeter at 30 °C. An Ubbelohde capillary type 0c in combination with a visco-clock was used to determine the flow times, respectively. The relative viscosity of the dispersion was calculated by $\eta_{\text{Disp}} = t(\eta_{\text{H}_2\text{O}}/t_{\text{H}_2\text{O}})$.

Carbon-Coating: A Leica EM ACE 600 coater with planetary stage and quartz crystal thickness measurement was used to deposit carbon nanolayers on the cross sections of samples with a sub-nanometer thickness accuracy.

Laser Scanning Confocal Microscopy: Both 2D color images, as well as 3D-reconstructed images, were obtained using a laser scanning confocal microscope (Olympus, OLS5000) with a white light source as well as a 405 nm laser, respectively. Cross sections were examined using a 50 \times lens with N.A. 0.95, and for the reconstruction, a pitch size of 0.12 μ m was applied.

Scanning Electron Microscopy: Images were obtained with a Zeiss Leo 1530 (Carl Zeiss AG, Germany) at operating voltages of 153 kV and both in-lens as well as secondary-electron detection after sputtering of 2 nm of platinum.

Micro UV-vis Spectroscopy: UV-vis spectra of drop-cast suspensions were measured on an Olympus IX71 inverted microscope with a 4 \times lens (numerical aperture (NA) 0.10) in reflection geometry with a halogen light source. An OceanOptics USB4000 spectrometer was coupled via fiber optics.

The local measurements of the gradient cross section were conducted using a Zeiss Axio Imager Z2 light microscope with either a 20 \times lens (NA 0.5, EC Epiplan-NEOFLUAR, Zeiss) or a 50 \times lens (NA 0.55, LD EC Epiplan-NEOFLUAR, Zeiss). Spectra were measured using an MCS CCD UV-NIR Spectrometer (Zeiss, Germany) coupled to the light microscope. The spot size was further adjusted using mechanical apertures in the optical path toward the detector. A silver mirror was used as reference.

Diffuse Reflectance Spectroscopy: Diffuse reflectance spectra were collected with a Cary 5000 UV-vis spectrometer (Agilent Technologies) in combination with an integrating sphere accessory (Labspheres). The samples were mounted at the reflectance port of the sphere after adhesion to a glass substrate with carbon adhesive tape. As a reference, a Spectralon diffuse white standard (Labspheres) was used.

2D Simulation of Particle Assemblies: 2D-rigid body physics of circles with different diameters falling into a rectangular basin were simulated using the Pymunk library in Python 3. Circles were initiated as dynamic bodies one after the other at a random x-position at the top of the plane. They experienced only downward directed gravitational force as well as rigid body interactions with other circles as well as the walls and floor of the basin. A total number of 4000 particles were simulated in each case in a basin measuring 1500 \times 1000 units. The diameters were set to one of two specific integers (8 and 12) with a probability of 50% each for the binary case (Figure S18a,b, Supporting Information) and to random floating-point numbers between 8 and 12 for the mixed gradient case (Figure S18c,d, Supporting Information). The crystalline assembly was simulated by letting circles with a diameter of exactly 10 fall into the basin (Figure S18e,f, Supporting Information).

Supporting Information

Supporting Information is available from the Wiley Online Library or from the author.

Acknowledgements

N.V. acknowledges funding by the Deutsche Forschungsgemeinschaft (DFG, German Research Foundation) - Project-ID 416229255 - SFB 1411. M.S. and T.L. thank the Elite Network of Bavaria (ENB). The help from the Keylab Electron Microscopy is appreciated. This project has received funding from the European Research Council (ERC) under the European Union's Horizon 2020 research and innovation program (grant agreement no. #714968).

Open access funding enabled and organized by Projekt DEAL.

Conflict of Interest

The authors declare no conflict of interest.

Data Availability Statement

The data that support the findings of this study are available from the corresponding author upon reasonable request.

Keywords

colloidal self-assembly, gradient size distribution, light scattering, mesoscale gradients

Received: September 22, 2022

Revised: November 7, 2022

Published online:

- [1] J. D. Joannopoulos, P. R. Villeneuve, S. Fan *Nature* **1997**, 386, 143.
- [2] S. John, *Phys. Rev. Lett.* **1987**, 58, 2486.
- [3] E. Ducrot, M. He, G. R. Yi, D. J. Pine, *Nat. Mater.* **2017**, 16, 652.
- [4] J. H. Holtz, S. A. Asher, *Nature* **1997**, 389, 829.
- [5] L. Maiwald, T. Sommer, M. S. Sidorenko, R. R. Yafyasov, M. E. Mustafa, M. Schulz, M. V. Rybin, M. Eich, A. Y. Petrov, *Adv. Opt. Mater.* **2021**, 10, 2100785.
- [6] Z. Hayran, H. Kurt, K. Staliunas, *Sci. Rep.* **2017**, 7, 3046.
- [7] Y. Takeoka, S. Yoshioka, A. Takano, S. Arai, K. Nueangnoraj, H. Nishihara, M. Teshima, Y. Ohtsuka, T. Seki, *Angew. Chem., Int. Ed.* **2013**, 52, 7261.
- [8] E. S. A. Goerlitzer, R. N. Klupp Taylor, N. Vogel, *Adv. Mater.* **2018**, 30, 1706654.
- [9] P. D. Garcia, R. Sapienza, A. Blanco, C. Lopez, *Adv. Mater.* **2007**, 19, 2597.
- [10] P. D. Garcia, R. Sapienza, C. Lopez, *Adv. Mater.* **2010**, 22, 12.
- [11] K. Ueno, A. Inaba, Y. Sano, M. Kondoh, M. Watanabe, *Chem. Commun.* **2009**, 24, 3603.
- [12] J. F. Galisteo-Lopez, M. Ibisate, R. Sapienza, L. S. Froufe-Perez, A. Blanco, C. Lopez, *Adv. Mater.* **2011**, 23, 30.
- [13] S. F. Liew, J. Forster, H. Noh, C. F. Schreck, V. Saranathan, X. Lu, L. Yang, R. O. Prum, C. S. O'Hern, E. R. Dufresne, H. Cao, *Opt. Express* **2011**, 19, 8208.
- [14] M. Harun-Ur-Rashid, A. Bin Imran, T. Seki, M. Ishii, H. Nakamura, Y. Takeoka, *ChemPhysChem* **2010**, 11, 579.
- [15] P. N. Dyachenko, J. J. do Rosário, E. W. Leib, A. Y. Petrov, R. Kubrin, G. A. Schneider, H. Weller, T. Vossmeier, M. Eich, *ACS Photonics* **2014**, 1, 1127.
- [16] G. Shang, Y. Häntsch, K. P. Furlan, R. Janßen, G. A. Schneider, A. Petrov, M. Eich, *APL Photonics* **2019**, 4, 046101.
- [17] M. Retsch, M. Schmelzeisen, H. J. Butt, E. L. Thomas, *Nano Lett.* **2011**, 11, 1389.
- [18] S. Yu, C.-W. Qiu, Y. Chong, S. Torquato, N. Park, *Nat. Rev. Mater.* **2020**, 6, 226.
- [19] V. Hwang, A. B. Stephenson, S. Barkley, S. Brandt, M. Xiao, J. Aizenberg, V. N. Manoharan, *Proc. Natl. Acad. Sci. USA* **2021**, 118, 201551118.
- [20] H. Yang, G. Jacucci, L. Schertel, S. Vignolini, *ACS Nano* **2022**, 16, 7373.
- [21] G. Jacucci, B. W. Longbottom, C. C. Parkins, S. A. F. Bon, S. Vignolini, *J. Mater. Chem. C* **2021**, 9, 2695.
- [22] N. Vogel, M. Retsch, C.-A. Fustin, A. del Campo, U. Jonas, *Chem. Rev.* **2015**, 115, 6265.
- [23] L. Zhang, J. Wang, S. Tao, C. Geng, Q. Yan, *Adv. Opt. Mater.* **2018**, 6, 1701344.
- [24] Y. Shen, D. Ye, I. Celanovic, S. G. Johnson, J. D. Joannopoulos, M. Soljačić, *Science* **2014**, 343, 1499.

- [25] L. Zhang, Z. Xiong, L. Shan, L. Zheng, T. Wei, Q. Yan, *Small* **2015**, *11*, 4910.
- [26] R. Kubrin, R. M. Pasquarelli, M. Waleczek, H. S. Lee, R. Zierold, J. J. do Rosario, P. N. Dyachenko, J. M. Montero Moreno, A. Y. Petrov, R. Janssen, M. Eich, K. Nielsch, G. A. Schneider, *ACS Appl. Mater. Interfaces* **2016**, *8*, 10466.
- [27] M. Chen, H. Colfen, S. Polarz, *ACS Nano* **2015**, *9*, 6944.
- [28] J. Bahner, N. Klinkenberg, M. Frisch, L. Brauchle, S. Polarz, *Adv. Funct. Mater.* **2019**, *29*, 44.
- [29] H. Ding, C. Liu, B. Ye, F. Fu, H. Wang, Y. Zhao, Z. Gu, *ACS Appl. Mater. Interfaces* **2016**, *8*, 6796.
- [30] S. H. Kim, W. C. Jeong, H. Hwang, S. M. Yang, *Angew. Chem., Int. Ed.* **2011**, *50*, 11649.
- [31] M. Schöttle, T. Tran, T. Feller, M. Retsch, *Adv. Mater.* **2021**, *33*, 2101948.
- [32] J. S. Skibina, R. Iliew, J. Bethge, M. Bock, D. Fischer, V. I. Beloglasov, R. Wedell, G. Steinmeyer, *Nat. Photonics* **2008**, *2*, 679.
- [33] Y. Fu, Y. An, Y. Xu, J. Dai, D. Lei, *EcoMat* **2022**, *4*, e12169.
- [34] N. Vaidya, O. Solgaard, *Microsyst. Nanoeng.* **2022**, *8*, 69.
- [35] F. A. Nutz, M. Retsch, *Sci. Adv.* **2017**, *3*, eaao5238.
- [36] J. W. Goodwin, J. Hearn, C. C. Ho, R. H. Ottewill, *Colloid Polym. Sci.* **1974**, *252*, 464.
- [37] J. Q. Li, R. Salovey, *J. Polym. Sci., Part A: Polym. Chem.* **2000**, *38*, 3181.
- [38] F. J. Schork, W. H. Ray, *J. Appl. Polym. Sci.* **1987**, *34*, 1259.
- [39] L. R. P. Areias, I. Mariz, E. Macoas, J. P. S. Farinha, *ACS Nano* **2021**, *15*, 11779.
- [40] Y. Takeoka, M. Iwata, T. Seki, K. Nueangnoraj, H. Nishihara, S. Yoshioka, *Langmuir* **2018**, *34*, 4282.
- [41] J. G. Park, S. H. Kim, S. Magkiriadou, T. M. Choi, Y. S. Kim, V. N. Manoharan, *Angew. Chem., Int. Ed.* **2014**, *53*, 2899.
- [42] C. F. Bohren, D. R. Huffman, *Absorption and Scattering of Light by Small Particles*, John Wiley & Sons, New York, USA **1998**.
- [43] B. A. F. Kopera, M. Retsch, *Anal. Chem.* **2018**, *90*, 13909.
- [44] B. D. Wilts, X. Sheng, M. Holler, A. Diaz, M. Guizar-Sicairos, J. Raabe, R. Hoppe, S. H. Liu, R. Langford, O. D. Onelli, D. Chen, S. Torquato, U. Steiner, C. G. Schroer, S. Vignolini, A. Sepe, *Adv. Mater.* **2018**, *30*, 1702057.
- [45] Q. Zhang, S. Wang, X. Wang, Y. Jiang, J. Li, W. Xu, B. Zhu, J. Zhu, *Small Methods* **2022**, *6*, e2101379.
- [46] M. S. Toivonen, O. D. Onelli, G. Jacucci, V. Lovikka, O. J. Rojas, O. Ikkala, S. Vignolini, *Adv. Mater.* **2018**, *30*, 1704050.
- [47] T. Wang, Y. Wu, L. Shi, X. Hu, M. Chen, L. Wu, *Nat. Commun.* **2021**, *12*, 365.
- [48] B. Gates, Y. Xia, *Adv. Mater.* **2000**, *12*, 1329.
- [49] C. Zhu, J. Qiu, S. Pongkitwitoon, S. Thomopoulos, Y. Xia, *Adv. Mater.* **2018**, *30*, 1706706.
- [50] U. G. Wegst, H. Bai, E. Saiz, A. P. Tomsia, R. O. Ritchie, *Nat. Mater.* **2015**, *14*, 23.

ADVANCED MATERIALS

Supporting Information

for *Adv. Mater.*, DOI: 10.1002/adma.202208745

A Continuous Gradient Colloidal Glass

*Marius Schöttle, Tobias Lauster, Lukas J. Roemling,
Nicolas Vogel, and Markus Retsch**

A continuous gradient colloidal glass (Supporting information)

Marius Schöttle Tobias Lauster Lukas J. Roemling Nicolas Vogel Markus Retsch*

Marius Schöttle, Tobias Lauster, Markus Retsch

Department of Chemistry, University of Bayreuth, Universitätsstr. 30, 95447 Bayreuth, Germany

Email Address: markus.retsch@uni-bayreuth.de

Lukas J. Roemling, Nicolas Vogel

Institute of Particle Technology, Friedrich-Alexander University Erlangen-Nürnberg, 91058 Erlangen, Germany

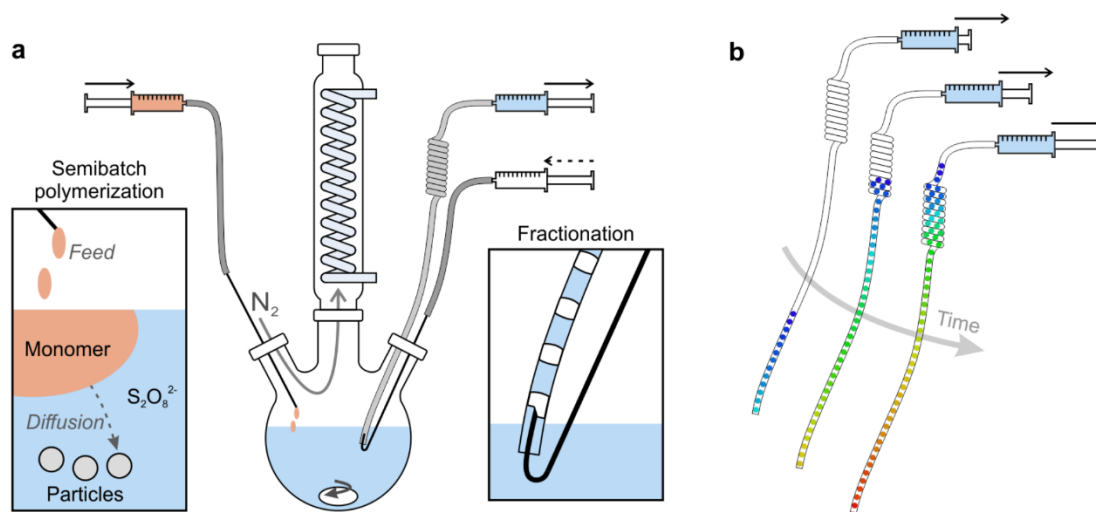


Figure S1: a) Reactor used for the controlled emulsion extraction process (CrEEP). Gradual addition of monomer (orange) to the seed particle suspension (blue) causes continuous diffusion of monomer to the growing particles. Simultaneous extraction, accompanied by fractionation via air bubble separation (white), retains the time-dependent increase of the particle diameter. Arrows indicate extraction and (periodic) infusion, respectively. b) Schematic showing the direction in which the growing particles are extracted. Blue fractions represent the smallest particles, red fractions the largest. During the assembly process, fractions are pushed out of the tube in the opposite direction.

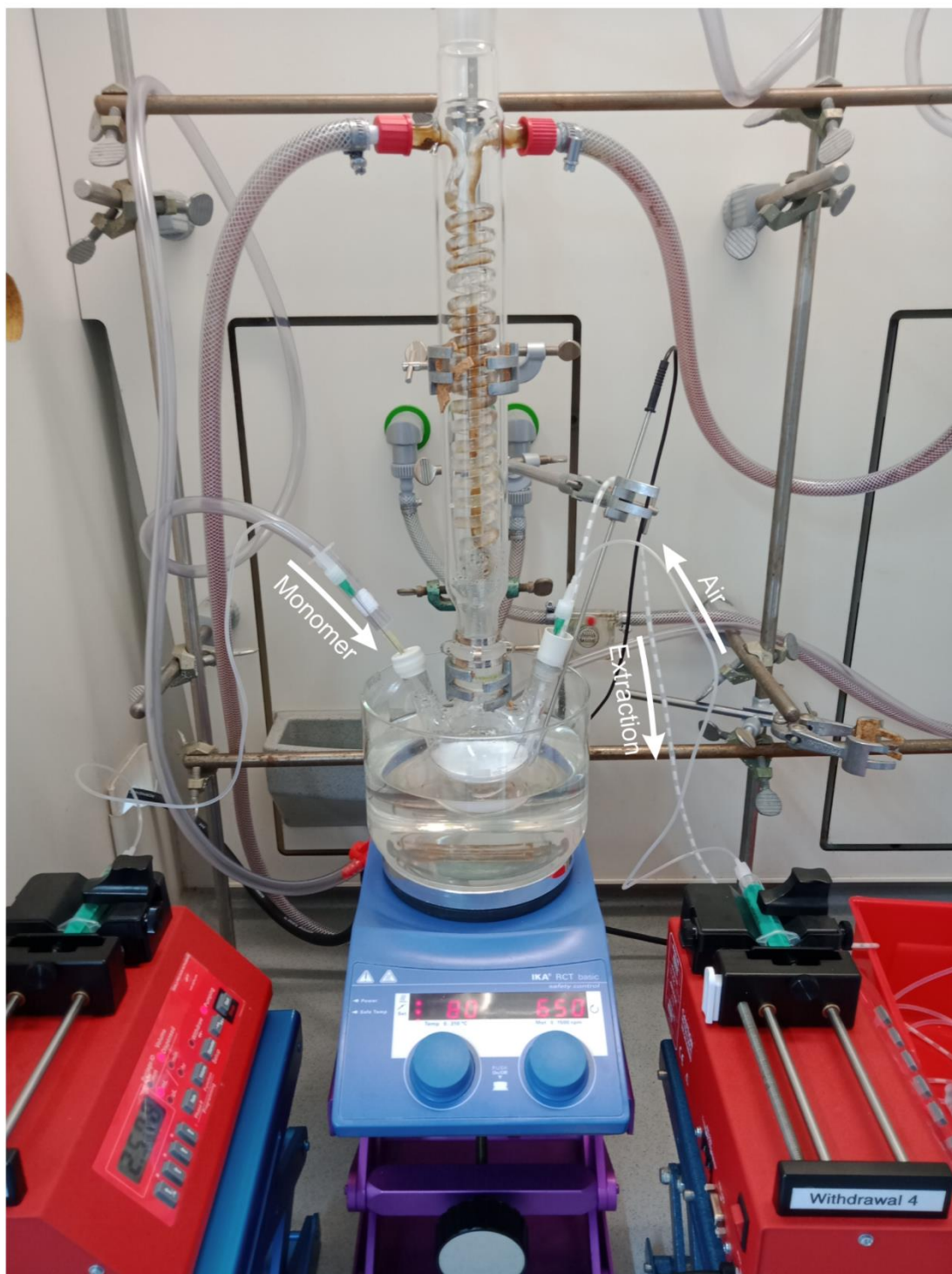


Figure S2: Photograph of the CrEEP setup during the synthesis. Infusion and withdrawal points are identical to Fig. S1. Inert gas flow and monomer feed proceed through the left joint, whereas extraction and the periodic airflow needed for fractionation can be seen on the right. The total volume in the reactor is significantly larger than the extracted volume. Thereby, a near-constant addition rate with respect to the concentration of particles is ensured.

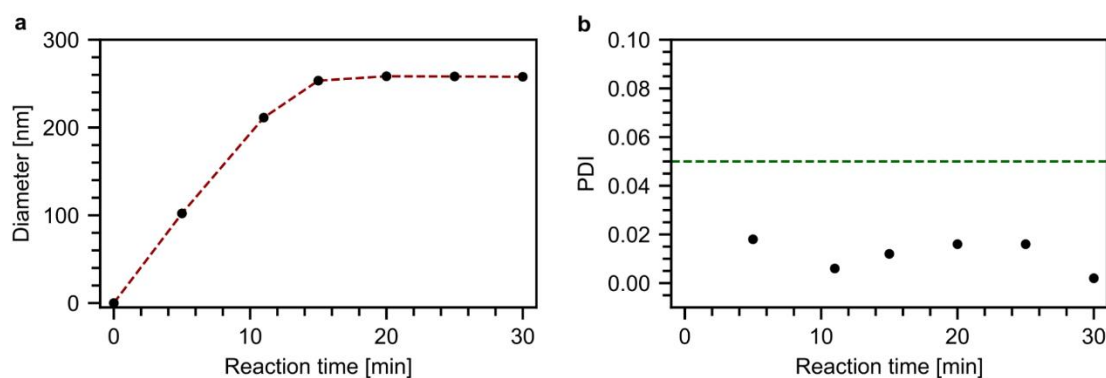


Figure S3: Evaluation of the kinetics of the particle growth during the surfactant-free emulsion polymerization to produce the seed particles. Here: 1.7 mL MMA are added at once and left to react. Samples are withdrawn every 5 minutes and examined via DLS to determine the growing particle diameter (a) and the polydispersity (b). Two important mechanistic insights can be obtained thereby: 1) Already at low conversions, the growing particles are shown to have a polydispersity index below 0.02 and can be considered monodisperse. 2) The reaction rate is fast compared to the gradual monomer addition. A volume of 1.7 mL monomer reacts in a matter of approx. 15 minutes, giving a reaction rate of 0.1 mL/min. During the 30 s it takes to extract one fraction, 25 μL of monomer are added to the system (approx. 5-6 drops) which gives an addition rate of 0.05 mL/min. Since the monomer-addition rate is much smaller than the reaction rate we can assume monomer-starved conditions. The benefit of this starved-feed procedure is that the extracted dispersion possesses a high conversion and low polydispersity. Consequently, it can be used for self-assembly without any purification steps. The presence of any unreacted monomer would soften the latex beads leading to a film formation, which we don't observe. Overall, the CrEEP process can be considered robust and applicable for emulsion polymerizations as long as the extraction rate is lower than the reaction rate.

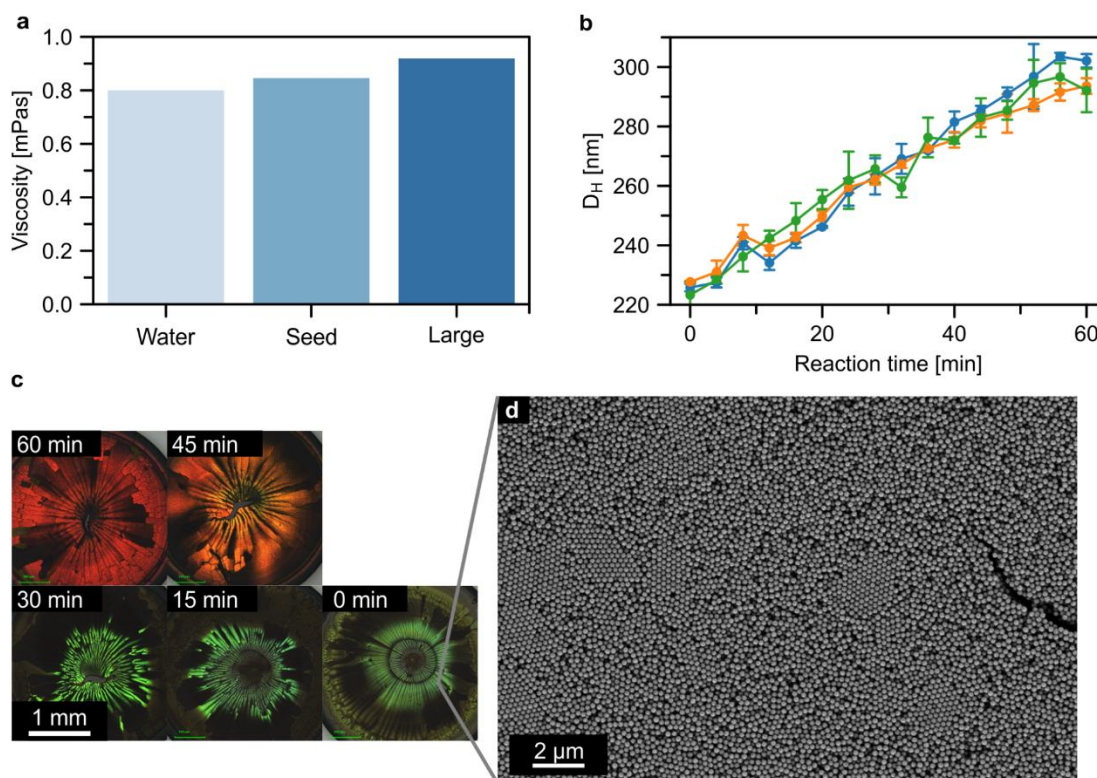


Figure S4: a) Results of viscosity measurements using an Ubbelohde viscometer. Measurements of the seed particle suspension, as well as the reaction mixture after CrEEP, show a slight increase in viscosity with a rising volume percentage of atex particles. These measurements allowed approximate calculation of the Reynolds number in the tube during extraction using a density of 10^{-3} kg/m^3 , a flow rate of $6 \cdot 10^{-3} \text{ m/s}$ and an inner diameter of $2 \cdot 10^{-3} \text{ m}$. The Reynolds numbers lie in the range of 1-5, which indicates laminar flow. It could, therefore, in principle, be possible to omit the fractionation and simply rely on the absence of turbulence. b) Results of DLS measurements of three identical CrEEP syntheses without air-fractionation. This shows both the pronounced reproducibility as well as the possibility of making use of the low Reynolds number system instead of fractionation to minimize mixing. In principle, the time-dependent increase in size can thereby still be translated into a positional dependency due to the laminar flow during extraction. c) Light microscopy images of drop-cast particle assemblies. For larger particles (30 - 60 minutes), the assembly into colloidal crystals seems adequate, but smaller particles do not show the characteristic blue color that can be seen with fractionation. As exhibited in the SEM image in d), small crystalline domains exist but the greater part of the structure is disordered. We attribute this to a near-zero flow rate at the tube walls, which causes mixing of large and small particles. As the assembly is known to be highly dependent on polydispersity, we, therefore, apply the fractionation approach in all further experiments to minimize the mixing of particles with different diameters.

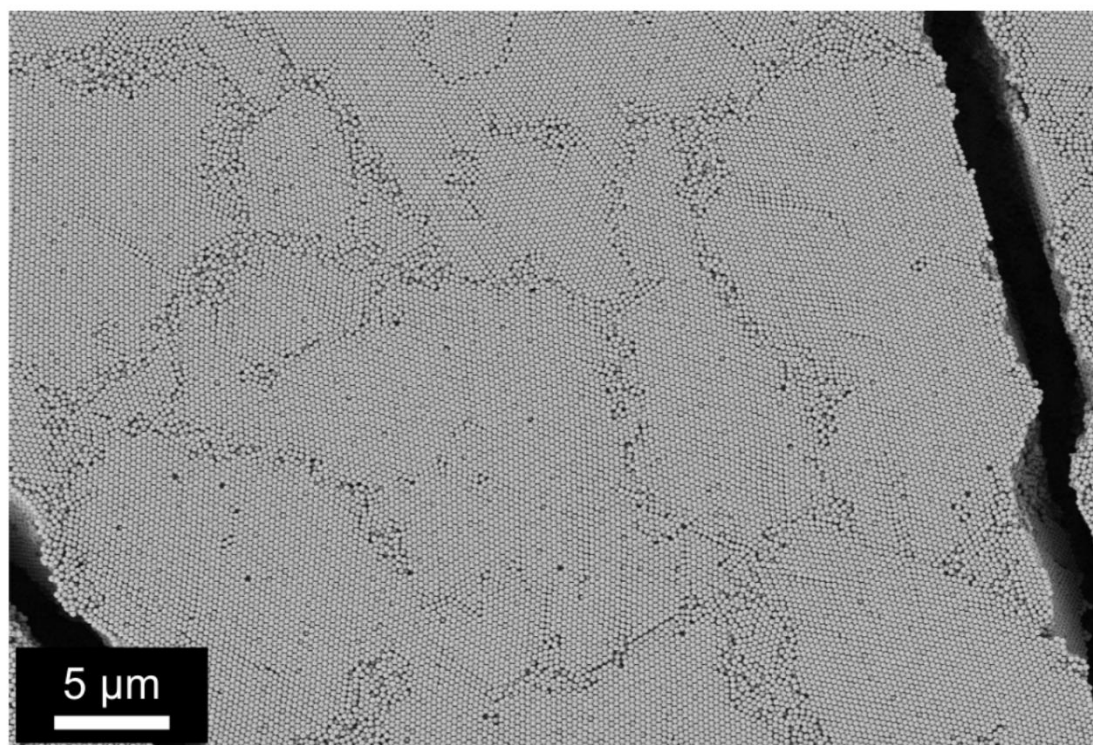


Figure S5: Overview SEM-image of the yellow sample shown in Figure 1h. The crystalline nature of the assembly proves the low polydispersity of each fraction.

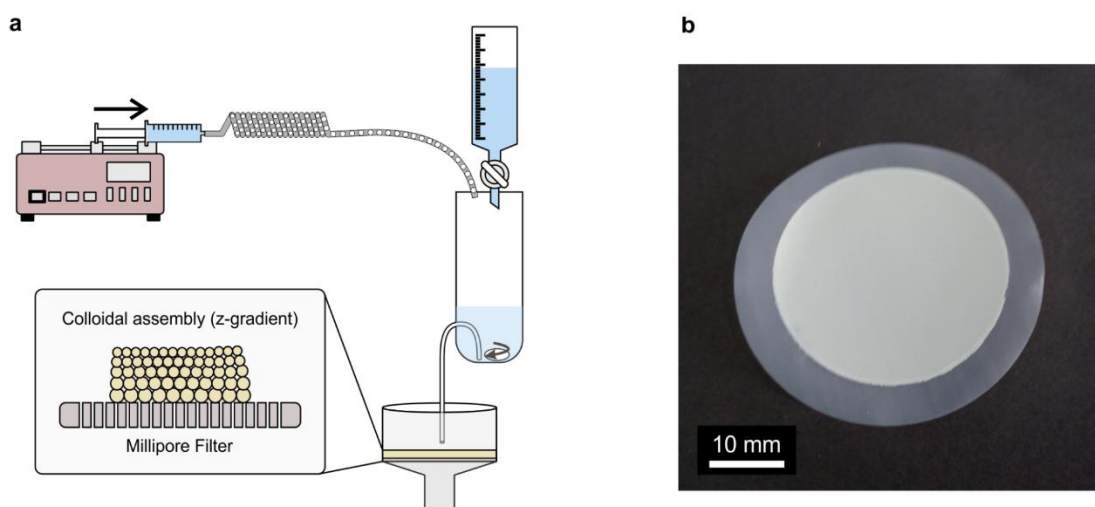


Figure S6: a) Schematic of the setup used for the semi-continuous filtration assembly of the 3D gradient structure. The fractionated suspension is added slowly and discretely into an intermediate container equipped with a stirrer bar. Here, the suspension is diluted with MilliQ water. The container is periodically emptied via a Pythagorean cup mechanism, and the diluted suspension is transferred into a filtration setup allowing a particle assembly to be formed. Due to the gradually decreasing diameters of the particles in the tube, this results in a size gradient in the z-direction. b) A photograph of the assembly after the last fraction was added.

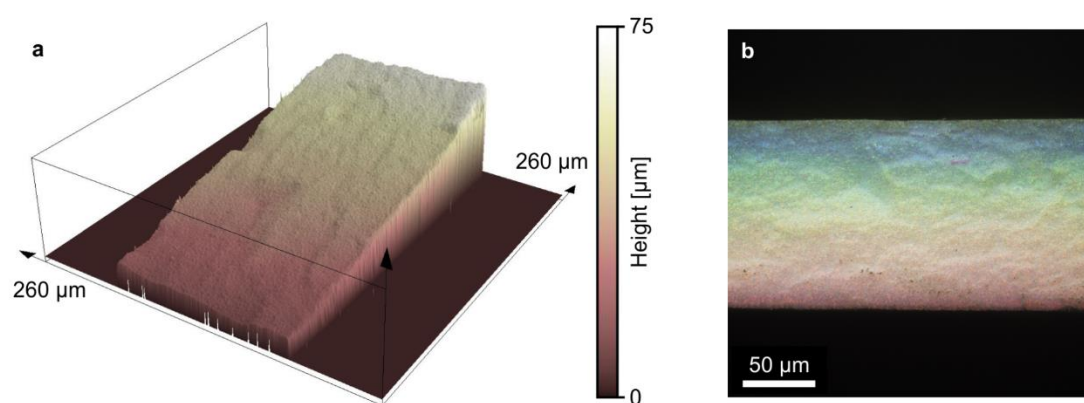


Figure S7: Microscopy images of a cross-section of a gradient colloidal glass that has been coated with 10 nm of carbon to reduce the effect of diffuse light scattering a) Height image obtained via laser scanning confocal microscopy b) The resulting image obtained from light microscopy at various focal positions after correlation with the height image.

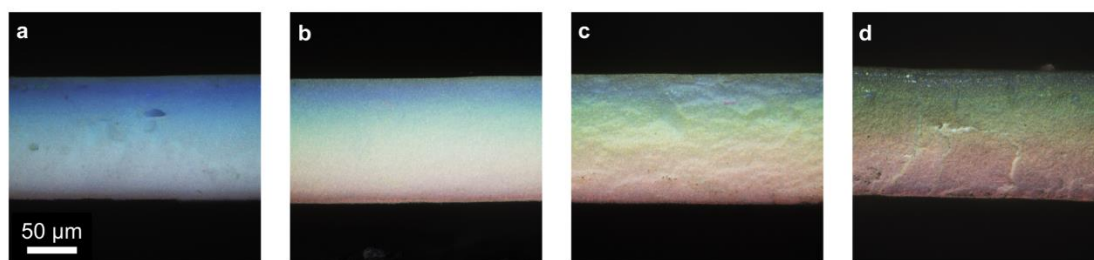


Figure S8: Cross-sections of gradient colloidal glasses coated with 0, 5, 10, and 20 nm carbon (a-d, respectively).

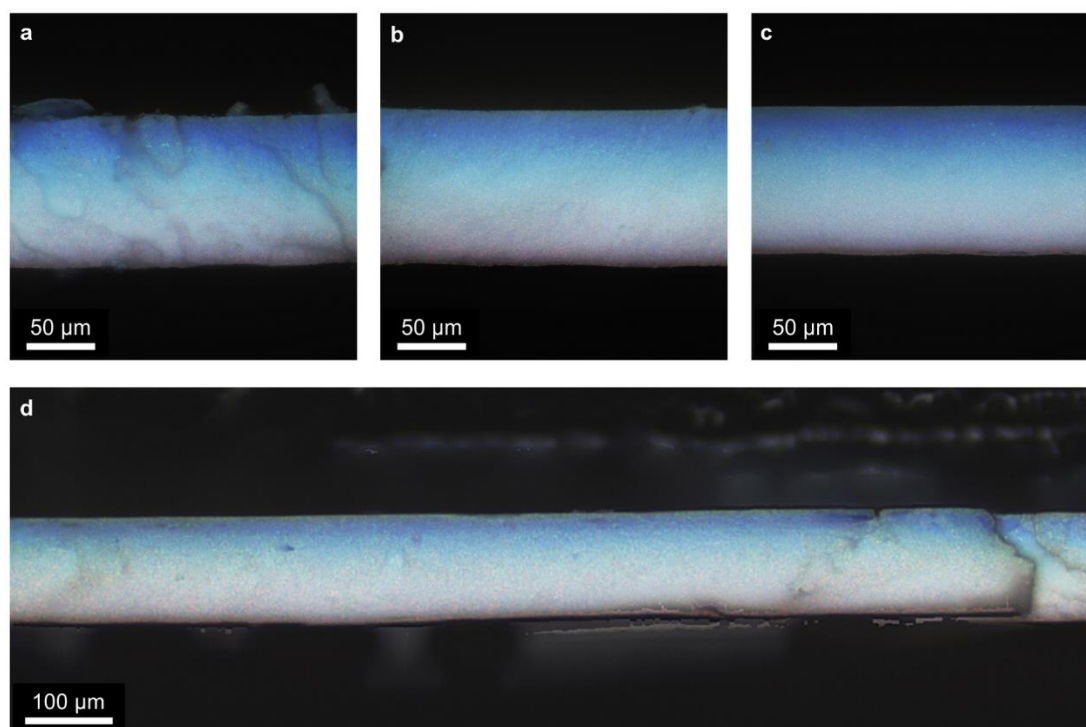


Figure S9: Microscopy images of cross-sections taken from different parts of the sample. These have not been carbon-coated prior to the measurement. This highlights the in-plane homogeneity of the gradual size distribution in the entire sample.

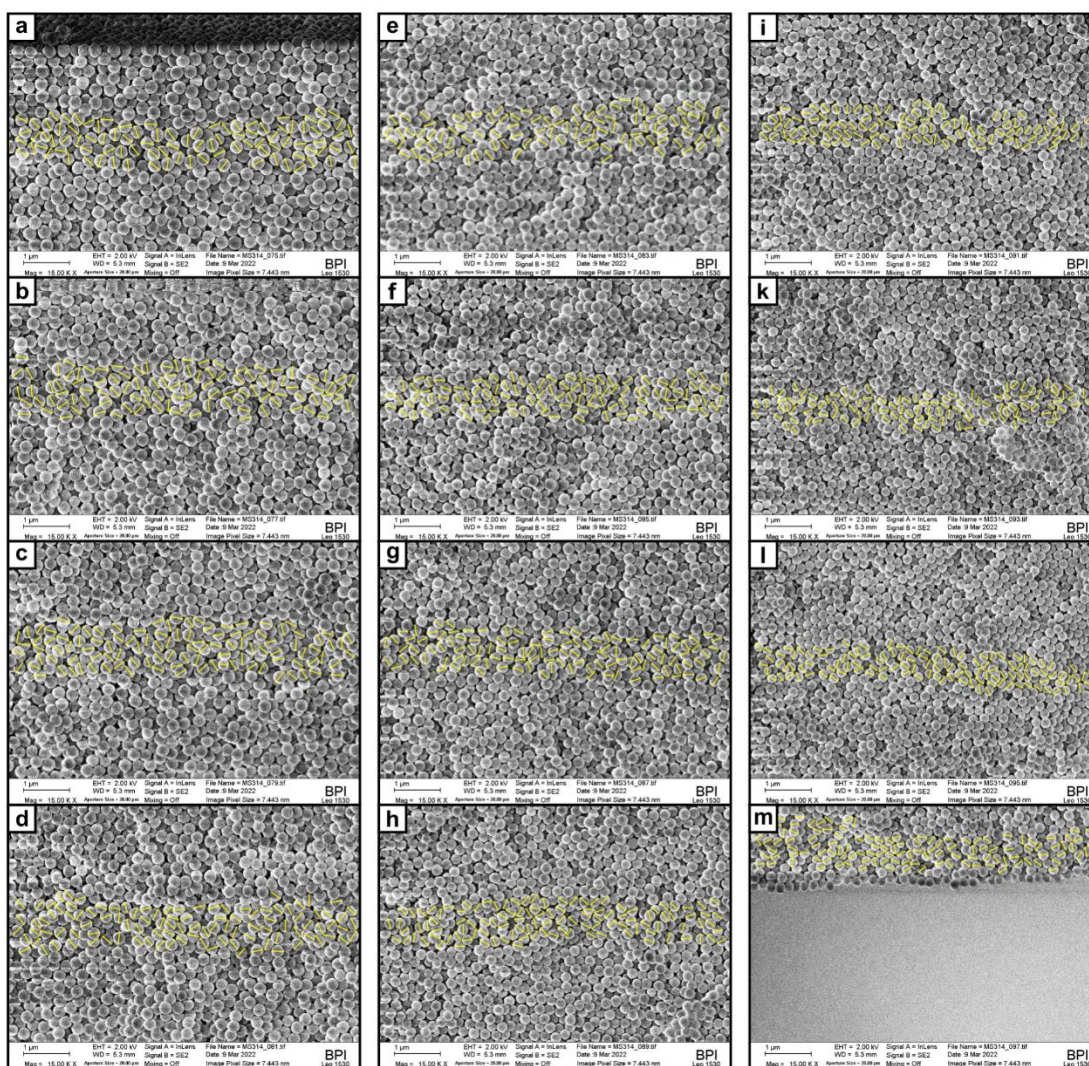


Figure S10: SEM images obtained at equidistant positions along the z-direction of a gradient colloidal glass. The yellow lines show the manual determination of the particle diameter of all evaluated particles. The examined regions are approximately $1 \mu\text{m}$ wide and $10 \mu\text{m}$ apart from each other.

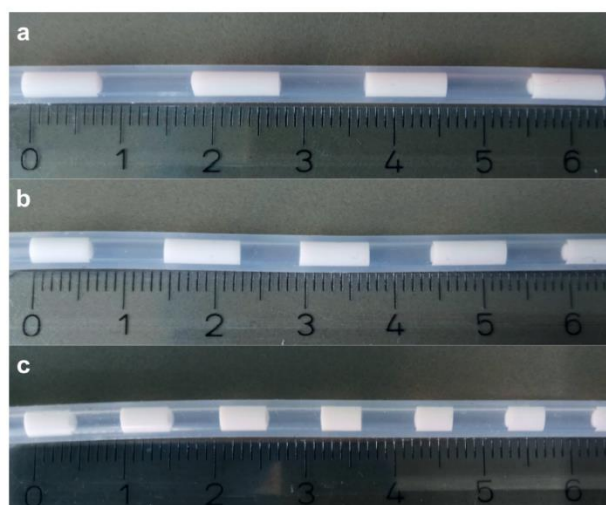


Figure S11: Comparison of the size of fractions in the beginning (a), after 30 minutes (b), and towards the end (c) of the CrEEP synthesis. The gradual decrease of the size of the fractions is an effect of the low gas barrier of the silicone tube. The extraction process is sufficiently slow for the diffusion of air from the outside of the tube into the preformed gas separators to play a role. As the reaction proceeds and the amount of these gas fractions increases, this effect becomes more pronounced, and the effective extraction speed gradually decreases. This counteracts the increase in volume percentage of latex particles during monomer feed and plays an important role in ensuring a linear gradient in later 3D self-assembly. Whereas the particle size increases from top to bottom, the optical impression of the dispersion remains white for all fractions, which is caused by multiple light scattering. The structural colors only evolve during the self-assembly process and are shown in Figure 1d and e in the main manuscript.

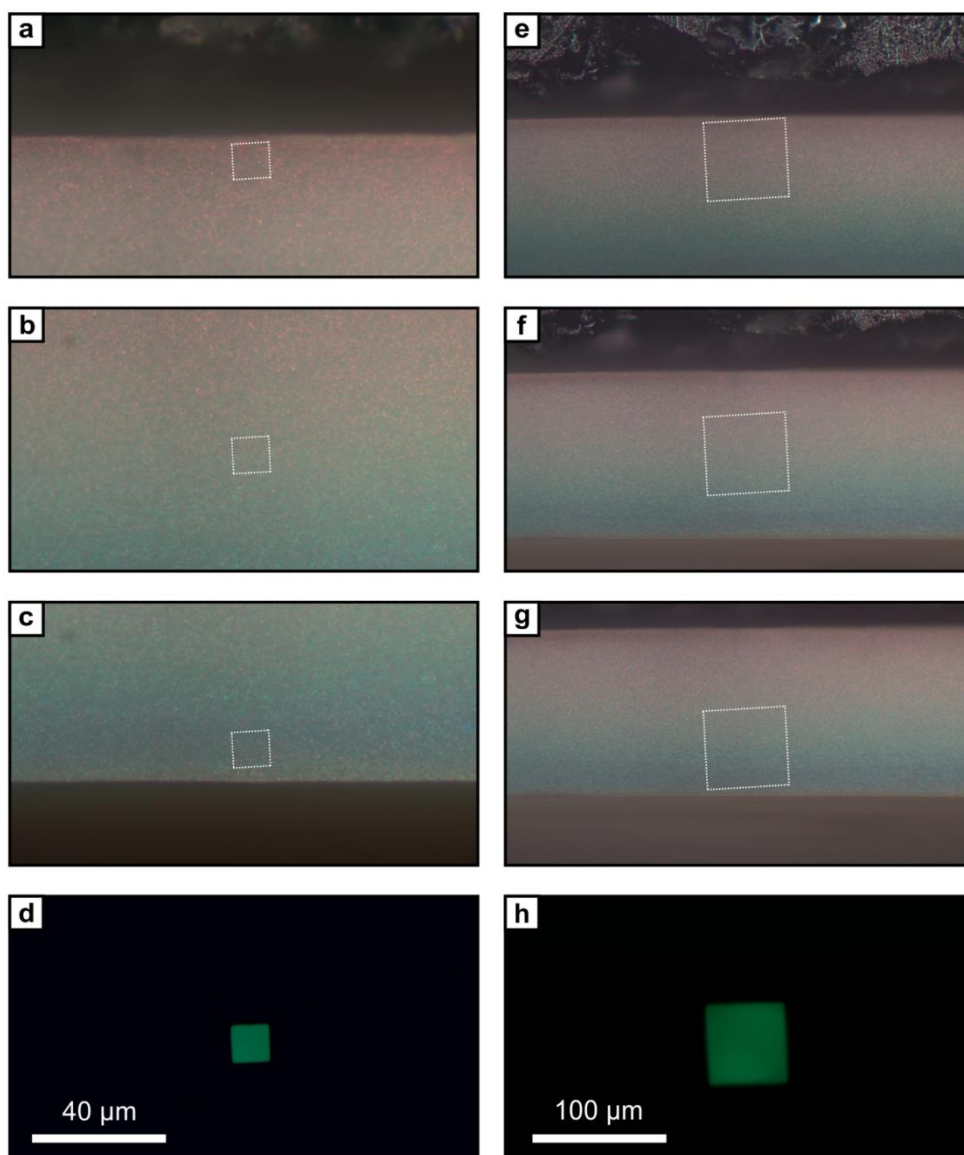


Figure S12: a)-c) Selection of microscopy images taken during microspectroscopy with a 50x-magnification objective. The white box is an overlay of the actual spot size as shown in d). The latter is determined by shining a green LED through the optical path leading to the spectrometer. e)-f) Microscopy images with overlay and g) spot-size corresponding to microspectroscopy using a 20x-magnification objective.

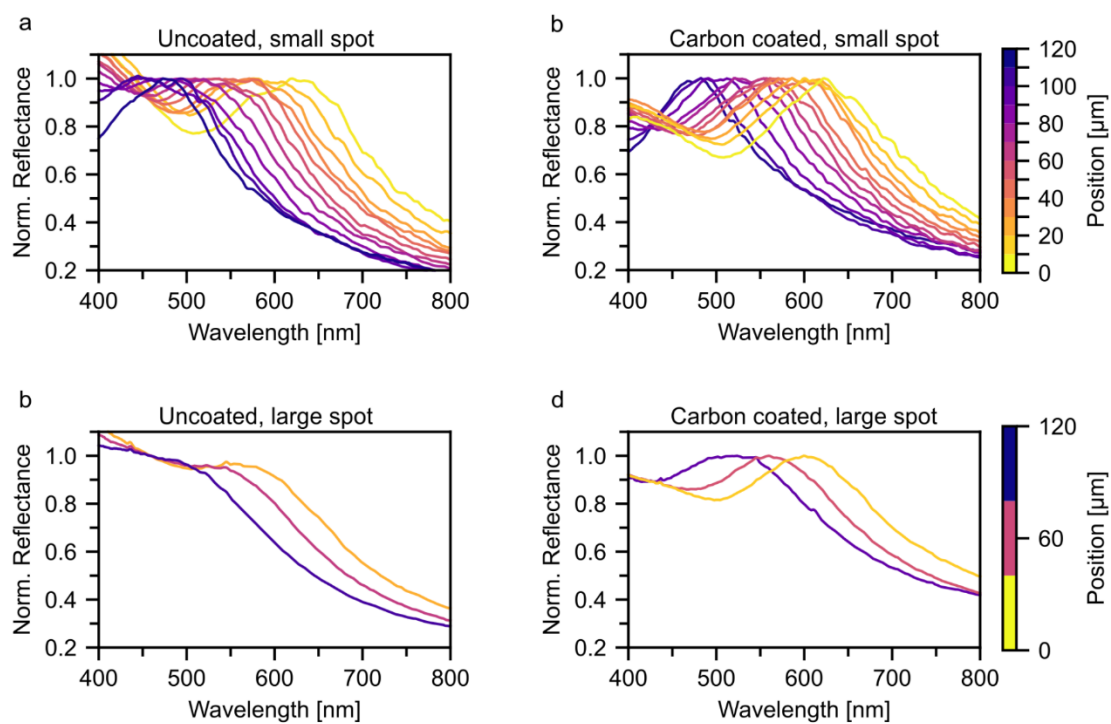


Figure S13: a), b) Spectra taken using the small spot-size at equidistant positions along cross-sections of gradient colloidal glasses without and with 5 nm carbon coating, respectively. c), d) Spectra taken using the large spot-size at equidistant positions along cross-sections of gradient colloidal glasses without and with 5 nm carbon coating, respectively.

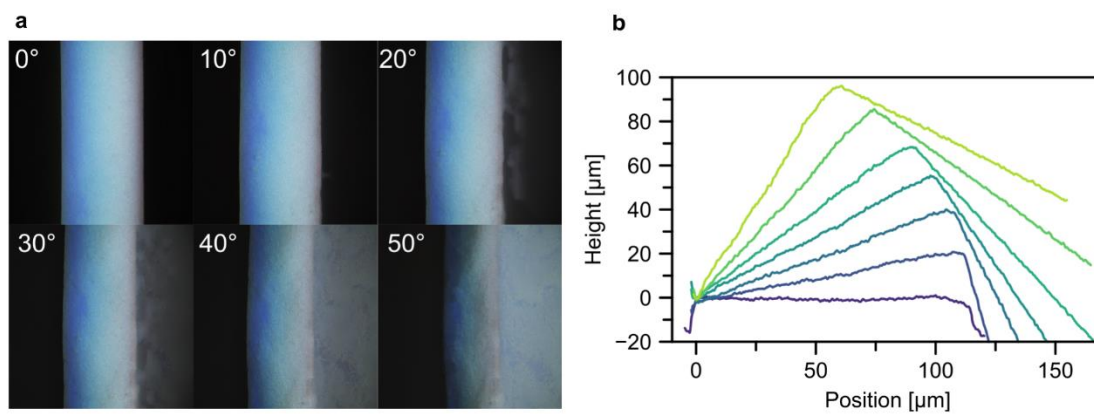


Figure S14: a) Light microscopy images of a cross-section tilted at angles between 0-50°. The range of colors observed in the gradient does not change with the viewing angle. b) Height profiles corresponding to the images in a) showing how the tilt-angle was determined from the LSCM evaluation.

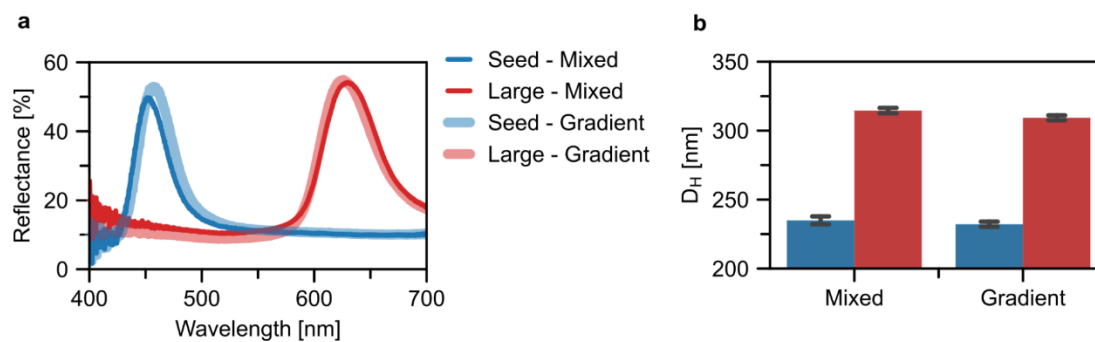


Figure S15: Comparison of the first fraction (seed particles, blue) and last fraction (large particles, red) of the two CrEEP syntheses used for the fabrication of the gradient colloidal glass and the mixed structure, respectively. a) UV-Vis microspectra of drop-cast suspensions. b) DLS results showing the hydrodynamic diameter of the dispersed particles.

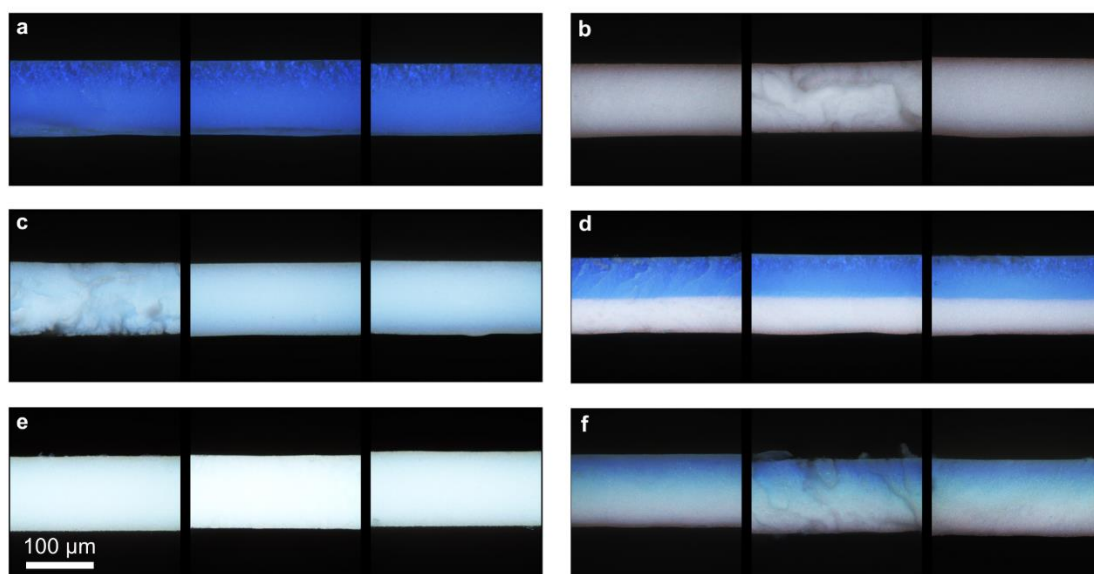


Figure S16: LSCM images of cross-sections of all samples prepared via filtration. Three different cross-sections of each sample are examined and verify that the thickness of all samples is comparable. a) small particles, b) large particles, c) binary mixture, d) bilayer, e) gradient mixture, and f) gradient colloidal glass.

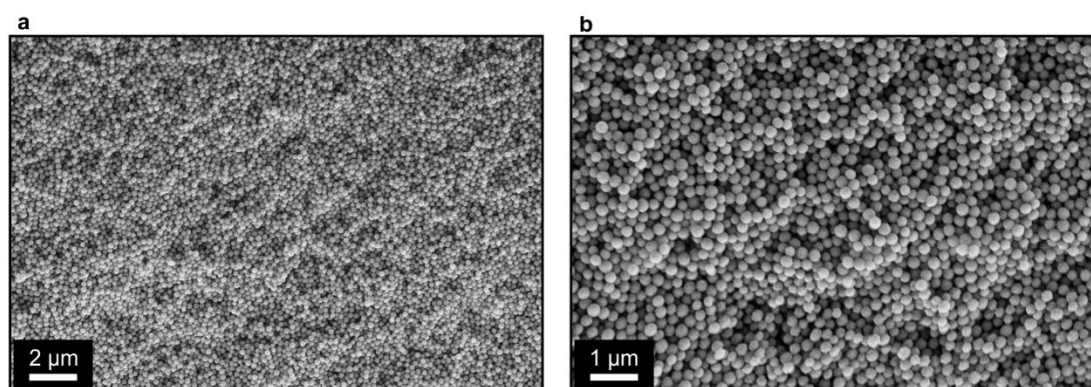


Figure S17: SEM images of the sample prepared via filtration after mixing of all fractions obtained CrEEP synthesis.

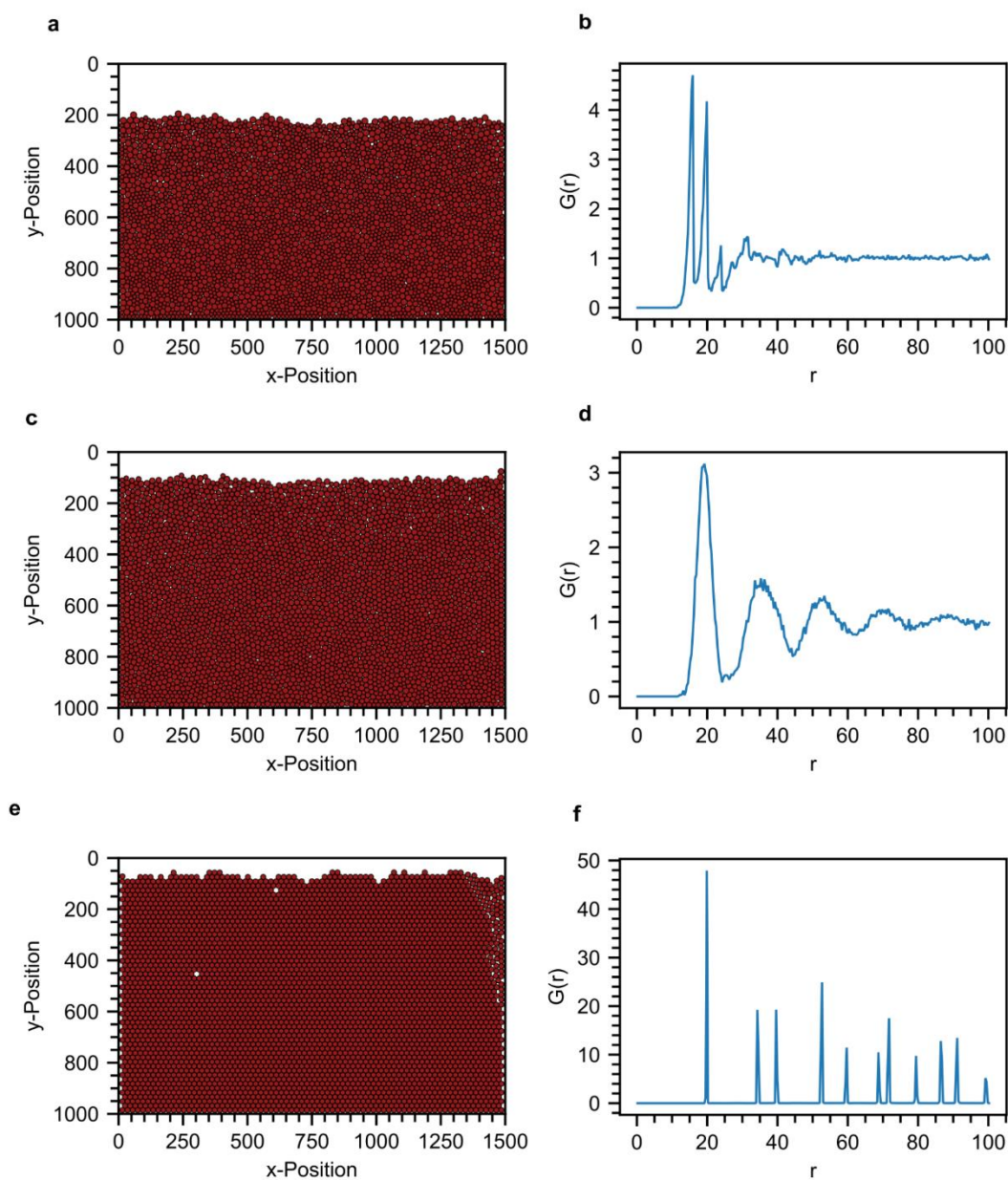


Figure S18: a) 2D rigid body simulation of two types of circles with different diameters falling into a rectangular basin. Diameters are set to exactly 8 or 12 units, respectively, and the total number of each type of circle is the same. b) Radial distribution function ($G(r)$) of the circles after simulation. c) and d) Analogous simulation and $G(r)$ -evaluation of particles with diameters set to arbitrary floating point numbers between 8 and 12 units. e), f) Simulation and $G(r)$ -evaluation of monodisperse circles with a diameter of exactly 10 units resulting in an ordered hexagonal array.

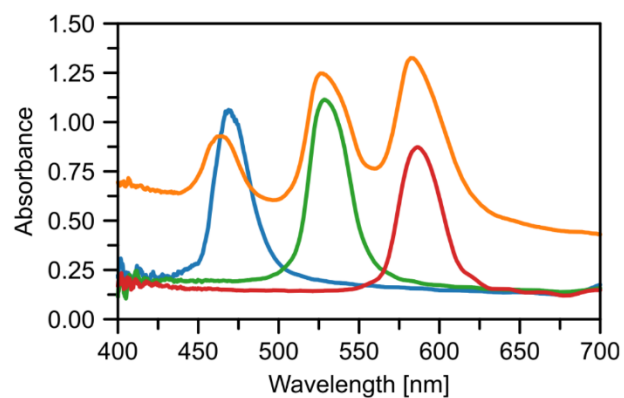


Figure S19: Transmission UV-Vis microspectroscopy of dip-coated colloidal crystals. The blue, green, and red plots correspond to colloidal crystals comprising particles of three different sizes. The orange curve shows the spectrum of a trilayer sample where these three particle types were dip-coated one after the other.

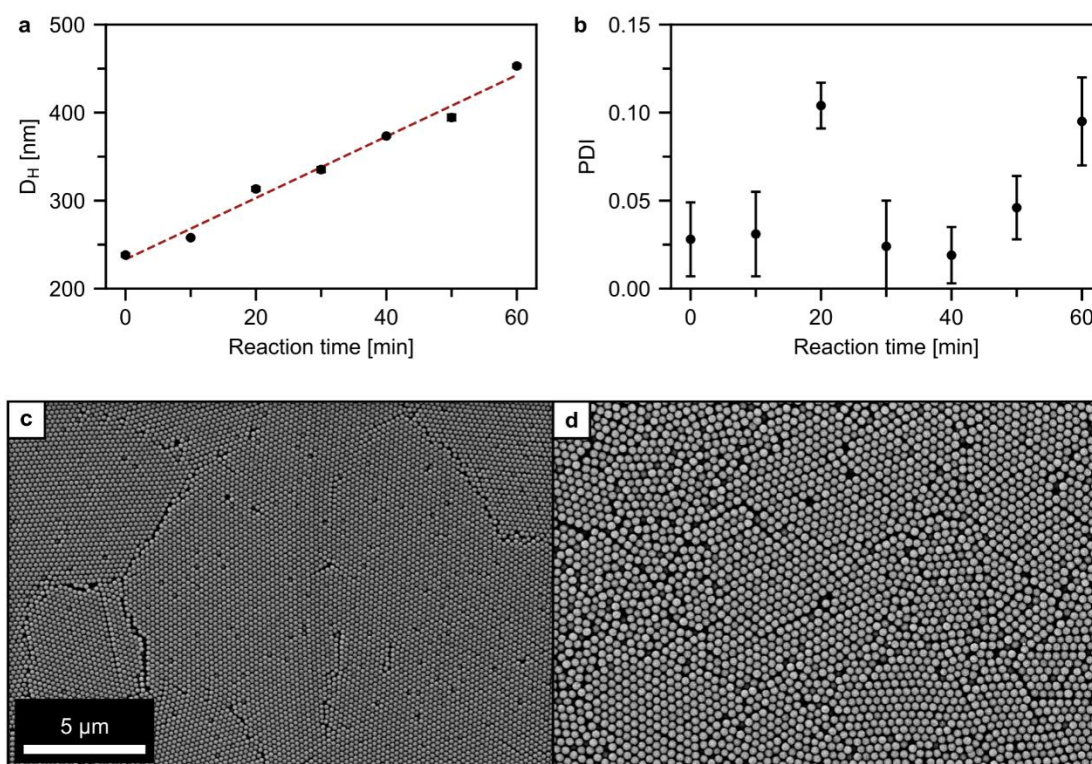


Figure S20: Characterization of a semibatch synthesis with an extended size range. a), b) DLS evaluation of equidistant, monodisperse fractions, showing the linear increase in size and a larger range up to 450 nm. For comparison: the maximum diameter in the synthesis shown in Fig. 1 is 320 nm c), d) SEM images of drop-cast colloidal crystals originating from the first and last fraction, respectively.

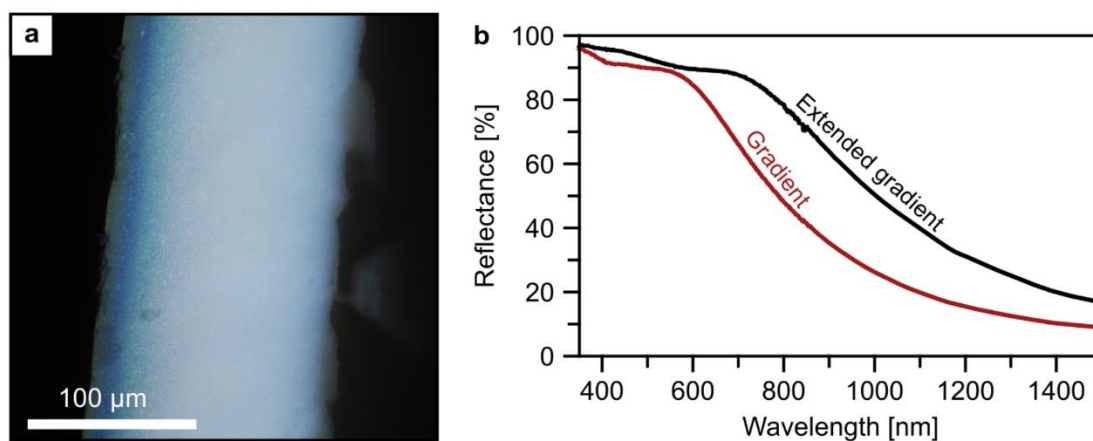


Figure S21: Characterization of the gradient colloidal glass obtained from the synthesis with an extended size range. a) Cross-section image obtained via LSCM of the gradient colloidal glass. The color gradient from blue to red can be observed in the top half of the gradient, whereas the bottom part appears white due to coherent scattering at wavelengths outside the visible region. b) Diffuse reflectance UV-Vis measurements of the extended gradient structure as well as the gradient shown in Fig. 4i. As was targeted, the plateau of the extended gradient covers a greater spectral bandwidth. This result is reminiscent of the red-shift of the step in local UV-Vis spectra obtained with a large spot size shown in Fig. S13c.

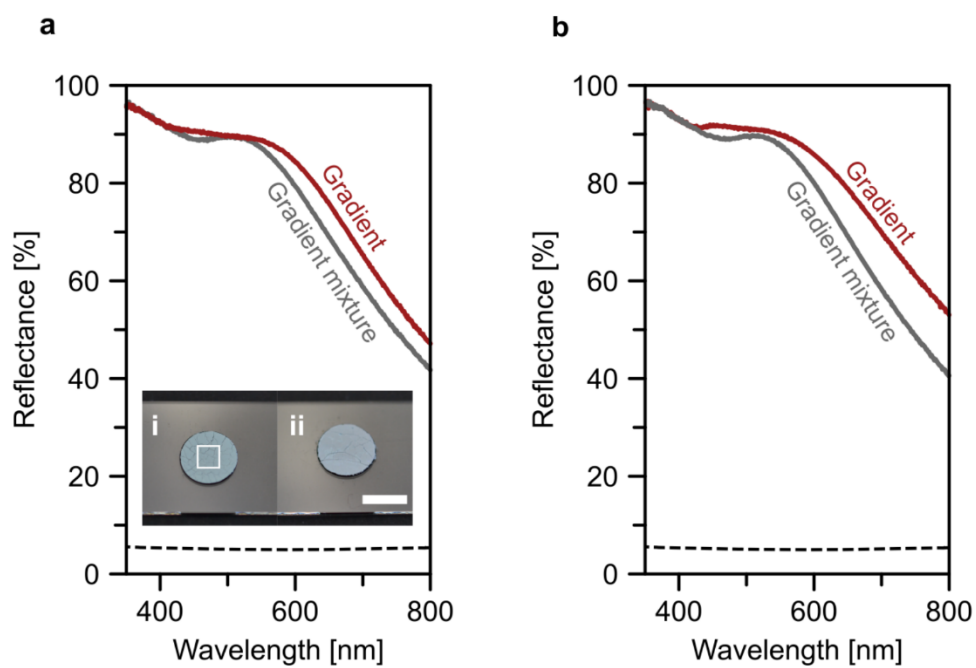
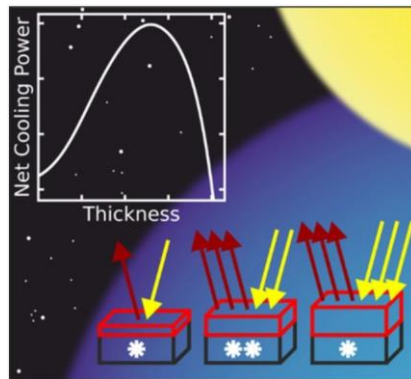


Figure S22: Diffuse reflectance measurements of gradient colloidal glasses as well as the mixed assembly. a) and b) show spectra of colloidal assemblies prepared from a total of 4 different CrEEP syntheses to show the consistent results between samples. The insets in a) show how the samples are prepared for spectroscopy by immobilization on black double-sided tape, i) Mixture and ii) Gradient assembly. The scale bar is 10 mm. The white square shows the spot size of the spectrometer. The black dotted line in the spectra is the reflectance spectrum of the black backing layer.



6. Homogeneous Polymer Films for Passive Daytime Cooling: Optimized Thickness for Maximized Cooling



Materials that spontaneously cool below ambient temperature are of great interest to fight global warming. Increased film thicknesses typically improve thermal radiation, but simultaneously increase uptake of solar radiance. A general approach is presented to balance these two contributions and to determine the optimum thickness for passive daytime cooling films.

Homogeneous Polymer Films for Passive Daytime Cooling: Optimized Thickness for Maximized Cooling Performance

Kai Herrmann, Tobias Lauster, Qimeng Song,* and Markus Retsch*

Passive radiative cooling materials that spontaneously cool below ambient temperature can save tremendous amounts of energy used for cooling applications. A multitude of materials, structures, and fabrication strategies have been reported in recent years. Important material parameters like a tailored or broadband emissivity, angle selectivity, or the influence of nonradiative heat losses were discussed in detail. The material thickness has been far less researched and is typically chosen sufficiently thick to ensure high emission in the atmospheric transparency window between wavelengths of 8–13 μm . However, not only the material emittance but also atmospheric and solar energy uptake depend on the material thickness. This broadband interplay has been less addressed so far. Herein, it is shown how an optimum thickness of a passive cooling material can be predicted when the optical properties of the material are known. Using complex refractive index data, the thickness-dependent cooling performance of polydimethylsiloxane (PDMS) in back-reflector geometry as exemplary material is calculated. For both day- and nighttime operation, an optimum emitter thickness is reported. The findings are verified experimentally by measuring the equilibrium temperatures of PDMS films with different thicknesses in a rooftop experiment. The presented analytical approach is directly transferable to other materials.

emerged that show a cooling effect below ambient temperature, even with direct sunlight illumination.^[1] The key to achieving a net cooling power is minimizing energy absorption and maximizing energy emission. A multitude of approaches were proposed that lead to the desired optical properties, including photonic structures,^[2] polymeric materials,^[3] and composite materials.^[4]

A material is primarily a good candidate for passive radiative cooling if it exhibits a high emissivity in the wavelength range of thermal radiation at ambient temperature. This wavelength range is located in the mid to far infrared (IR) region ($\approx 3\text{--}50\ \mu\text{m}$). Second, a low absorptivity in the solar region is required because any energy uptake from the sun directly reduces the cooling power. This energy absorption is prevented by including a reflective metal layer below the emitter material,^[4b,5] using a solar filter approach,^[6] or by efficient scattering of solar wavelengths by the material itself.^[3a,7] Third and most complex is to avoid radiative energy uptake by the surrounding atmosphere. As this radiance


appears in a similar wavelength regime as the emitted thermal radiation, special care must be taken. The most common approach here is to focus emission on the first (8–13 μm) and second (16–28 μm) atmospheric transmission window where low atmospheric radiation is present. With a confined emission in this spectral region, the lowest temperatures below ambient can be reached. However, the cooling power at ambient temperature is reduced in comparison to a blackbody emitter.^[1a,8]

The material thickness is an essential parameter for the applicability of passive cooling materials and was discussed by several groups in the literature.^[5b,9] For example, in the work of Zhou et al., a PDMS layer on an aluminum substrate is considered.^[5b] The authors chose a 150 μm -thick layer and found that above 100 μm thickness, the emissivity in the 8–13 μm wavelength range was close to unity. In the work of Zhu et al., the thickness of a PDMS layer on a reflective silver layer was discussed, and a thickness of 200 μm was suggested.^[9b] The authors found that up to this thickness, the emissivity in the wavelength range from 2.5 to 25 μm was increasing, but for a higher thickness of 300 μm , there were only minor changes. Besides PDMS as emitting layer, the group of Zhu et al. investigated the thickness of a composite material consisting of In_2O_3 particles in a polymethyl methacrylate matrix.^[10] They found the thickness of their composite needs to be larger than 25 μm to have high emissivity within the

1. Introduction

The field of passive daytime radiative cooling materials has significantly developed in the last decade. Many new materials

K. Herrmann, T. Lauster, Q. Song, M. Retsch
Department of Chemistry, Physical Chemistry I
University of Bayreuth
Universitätsstraße 30, 95447 Bayreuth, Germany
E-mail: qimeng.song@uni-bayreuth.de; markus.retsch@uni-bayreuth.de
M. Retsch
Bavarian Polymer Institute
Bayreuth Center for Colloids and Interfaces
and Bavarian Center for Battery Technology (BayBatt)
University of Bayreuth
Universitätsstraße 30, 95447 Bayreuth, Germany

 The ORCID identification number(s) for the author(s) of this article can be found under <https://doi.org/10.1002/aesr.202100166>.

© 2021 The Authors. Advanced Energy and Sustainability Research published by Wiley-VCH GmbH. This is an open access article under the terms of the Creative Commons Attribution License, which permits use, distribution and reproduction in any medium, provided the original work is properly cited.

DOI: 10.1002/aesr.202100166

first and second atmospheric window. In the work of Tian et al., poly-4-methyl-1-pentene (PMP) films of different thicknesses are used to determine the complex refractive index of the material.^[9a] In this work, the investigated film with a thickness of 1283 μm was found to have the highest absorptance within the first and second atmospheric window. In all this previous work, the emitter thickness was optimized to maximize the emission within the first and/or second atmospheric window. However, the material thickness also affects the solar absorption and atmospheric energy uptake behavior of a material simultaneously. This interplay of thickness dependencies for the different energetic contributions has been barely addressed so far. The relevance of optical thickness in the solar range becomes even more relevant, considering emerging aesthetic passive cooling designs, where colored films are fabricated. As long as coloration is not based on Bragg diffraction,^[11] a suitable tradeoff between color impression and thermal load based on the absorption and thermalization process^[12] needs to be found.

This work focuses on PDMS as an often used and well-characterized passive cooling material to conceptually address the optimum thickness of an emitter material. Our study provides a theoretical approach based only on the fundamental optical constants for estimating the optimum emitter thickness. Experimental data subsequently verify the outlined theoretical framework. Therefore, PDMS thin films of several thicknesses on Ag mirrors were prepared to determine the equilibrium temperatures below ambient during day- and nighttime. In conclusion, we point out how to optimize the sample thickness of a given emitter material for passive day- and nighttime cooling applications in the back-reflector geometry.

2. Theoretical Approach

To determine the optimum thickness, we first derive how the individual energetic contributions of a passive cooling material depend on the emitter material thickness. Taking into account all the energy exchange processes, the net cooling power P_{cool} can be defined as^[1a]

$$P_{\text{cool}} = P_{\text{mat}} - P_{\text{sun}} - P_{\text{atm}} - P_{\text{nonrad}} \quad (1)$$

where P_{mat} represents the energy radiated by the material, P_{sun} the absorbed energy due to solar radiation, P_{atm} the absorbed energy due to atmospheric radiation, and P_{nonrad} intrinsic losses due to convection and conduction. The considered energy exchange processes are schematically shown in **Figure 1**.

To calculate the different energetic contributions, the broadband optical constants of the emitter material, a solar radiation spectrum, an atmospheric transmission spectrum, and the nonradiative heat transfer coefficient are required. Typically, the AM1.5 spectrum is used to model solar radiation. An atmospheric transmission spectrum at the measuring location is modeled using Modtran to allow for the highest accuracy possible.^[13] The data used for the calculations performed in this article and a schematic for calculating the thickness-dependent angular and spectral emissivity are shown in **Figure 2**.

The energy radiated by the emitter material can be calculated using the spectral radiance I_b , described by Planck's law, which depends on the emitter material temperature T_{mat} and the

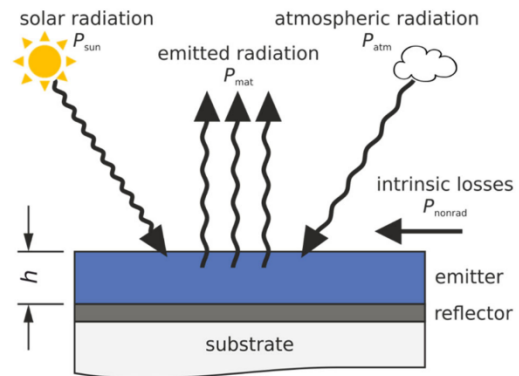


Figure 1. Schematics of the radiative cooler containing the considered energy exchange processes.

emissivity of the emitter material $\epsilon_{\text{mat}}(\lambda, h, \theta)$, depending on wavelength λ , thickness h and polar angle θ , and the azimuthal angle φ .^[1b]

$$P_{\text{mat}} = \int_0^{2\pi} d\varphi \int_0^{\pi/2} \sin\theta \cos\theta d\theta \int_0^{\infty} I_b(\lambda, T_{\text{mat}}) \cdot \epsilon_{\text{mat}}(\lambda, h, \theta) d\lambda \quad (2)$$

Azimuthal dependency is not considered in our spectral-dependent and directional-dependent viewpoint and therefore reduces to a factor of 2π .

$$P_{\text{mat}} = 2\pi \int_0^{\pi/2} \sin\theta \cos\theta d\theta \int_0^{\infty} I_b(\lambda, T_{\text{mat}}) \cdot \epsilon_{\text{mat}}(\lambda, h, \theta) d\lambda d\theta \quad (3)$$

Here, the thickness dependency becomes evident because the emittance of the film depends on the material thickness h . The angular and spectral emittance of the film $\epsilon_{\text{mat}}(\lambda, h, \theta)$ is defined as $1 - R(\lambda, h, \theta)$, where $R(\lambda, h, \theta) = \frac{|E_0|^2}{|E_1|^2}$ is the reflectance, as proposed by Zhu et al.^[10] A schematic representation for calculating the angular and spectral emittance is shown in **Figure 2b**.

To calculate the emittance, the following parameters are introduced with the Fresnel equation for s- and p-polarized waves, respectively

$$r_{\text{air,mat}}^s = \frac{n_{\text{air}} \cos\theta_i - n_{\text{mat}} \cos\theta_t}{n_{\text{air}} \cos\theta_i + n_{\text{mat}} \cos\theta_t} \quad (4)$$

$$r_{\text{air,mat}}^p = \frac{n_{\text{mat}} \cos\theta_i - n_{\text{air}} \cos\theta_t}{n_{\text{mat}} \cos\theta_i + n_{\text{air}} \cos\theta_t} \quad (5)$$

$$\cos\theta_t = \sqrt{1 - \left(\frac{n_{\text{air}}}{n_{\text{mat}}}\right)^2 \sin^2\theta_i} \quad (6)$$

Perfect reflection at the material–silver interface results in

$$\frac{|E_3|^2}{|E_2|^2} = \exp(-2\alpha \cdot h_{\text{eff}}) \quad (7)$$

With the absorption coefficient α and the angle-dependent effective thickness h_{eff} as

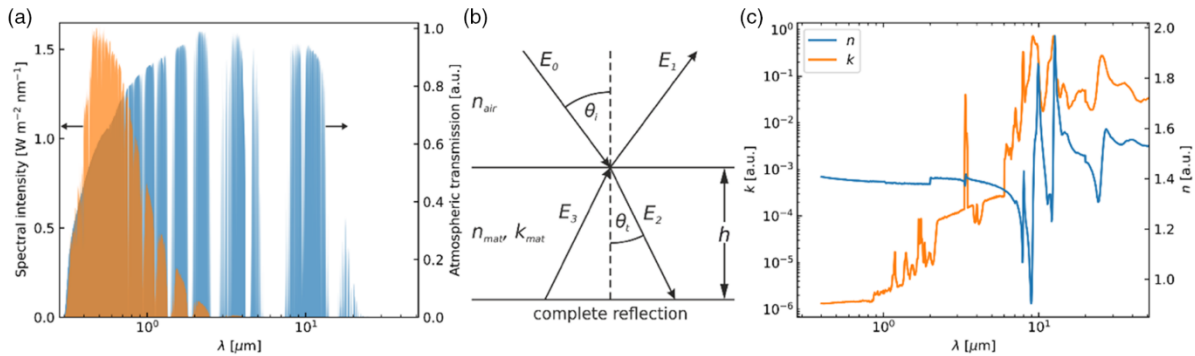


Figure 2. a) Atmospheric transmittance spectrum generated using Modtran for the measurement location (Bayreuth), as well as the employed AM1.5 solar spectrum.^[13a] b) Schematics for calculating the angular and spectral emittance based on the complex refractive index of the material and its thickness. c) Utilized complex refractive index data for PDMS.^[16]

$$\alpha = \frac{4\pi \cdot k}{\lambda}, \quad h_{\text{eff}} = h / \cos \theta_t \quad (8)$$

For an incoherent wave, one can calculate the reflectance for s- and p-polarization following the derivation of Zhu et al.^[10] as

$$R^{\text{s,p}} = |r_{\text{air,mat}}^{\text{s,p}}|^2 + \frac{|1 - (r_{\text{air,mat}}^{\text{s,p}})^2|^2 \exp(-2\alpha \cdot h_{\text{eff}})}{1 - |r_{\text{air,mat}}^{\text{s,p}}|^2 \exp(-2\alpha \cdot h_{\text{eff}})} \quad (9)$$

The spectral-, thickness-, and angular-dependent emittance is then finally calculated as

$$\varepsilon_{\text{mat}}(\lambda, h, \theta) = 1 - \frac{R^{\text{s}} + R^{\text{p}}}{2} \quad (10)$$

The thickness dependency of the material's emittance is apparent in the energy radiated by the material and the energies absorbed due to solar and atmospheric radiation. As for the incoming radiation from the sun, a fixed position is used with $\theta_{\text{sun}} = 48.2^\circ$ for AM1.5 conditions, the angular integration vanishes, and only a spectral integration is performed.

$$P_{\text{sun}} = \int_0^\infty I_{\text{AM1.5}}(\lambda) \cdot \varepsilon_{\text{mat}}(\lambda, h, \theta_{\text{sun}}) d\lambda \quad (11)$$

Here, $I_{\text{AM1.5}}$ denotes the AM1.5 spectral distribution of solar radiation depicted in Figure 2a. In contrast, for incoming radiation from the atmosphere, the angular integration has to be performed.

$$P_{\text{atm}} = 2\pi \int_0^{\pi/2} \sin \theta \cos \theta \int_0^\infty I_b(\lambda, T_{\text{atm}}) \cdot \varepsilon_{\text{atm}}(\lambda, \theta) \cdot \varepsilon_{\text{mat}}(\lambda, h, \theta) d\lambda d\theta \quad (12)$$

where $\varepsilon_{\text{atm}}(\lambda, \theta) = 1 - \tau_{\text{atm}}(\lambda, 0)^{1/\cos \theta}$ with $\tau_{\text{atm}}(\lambda, 0)$ being the spectral transmittance of the atmosphere at zero zenith angle depicted in Figure 2a.^[14] Intrinsic losses due to convection and conduction are treated with a comprehensive heat transfer coefficient h_{nonrad} .

$$P_{\text{nonrad}} = h_{\text{nonrad}} \cdot (T_{\text{atm}} - T_{\text{mat}}) \quad (13)$$

This heat transfer coefficient is taken as an average of literature values with $h_{\text{nonrad}} = 4.4 \text{ W m}^{-2} \text{ K}^{-1}$.^[1b,2a,10,14,15] Instead of performing the spectral integration from zero to infinity, the upper boundary is set to $55 \mu\text{m}$ due to limited data availability. This limit is justified because approximately 97% of the emitted thermal energy at 298 K is confined to wavelengths below $55 \mu\text{m}$. Furthermore, convergence of the resulting cooling power as a function of the upper integration boundary is shown in Figure S1, Supporting Information. Moreover, the influence of the comprehensive heat transfer coefficient h_{nonrad} is also shown in Figure S2, Supporting Information.

3. Results and Discussion

3.1. Calculations

To illustrate the concept of an optimum emitter thickness, we first examine the individual energetic contributions for PDMS at T_{amb} . At ambient temperature, the nonradiative contributions P_{nonrad} can be discarded, as no intrinsic losses due to conduction or convection are present, and emitter and atmospheric thermal radiation are modeled at the same temperature. The remaining contributions of Equation (1) and the resulting cooling power at ambient temperature are depicted in **Figure 3**.

Figure 3a displays the daytime case, revealing an optimum emitter thickness where the resulting cooling power is maximized. At low thicknesses P_{mat} and P_{atm} exhibit an increase. This is the case because the absorption coefficient of PDMS has the highest order of magnitude in the IR regime where P_{mat} and P_{atm} have their origin. At thicknesses above $1 \times 10^{-4} \text{ m}$, those contributions reach a quasiplateau, where the difference between them remains approximately constant. At the same time, for emitter thicknesses above $1 \times 10^{-5} \text{ m}$, the absorption in the solar wavelength regime is no longer negligible. The absorbed energy due to solar radiation increases, with further increasing the emitter thickness. The counterbalance between the increasing emitted power below $1 \times 10^{-4} \text{ m}$ and the

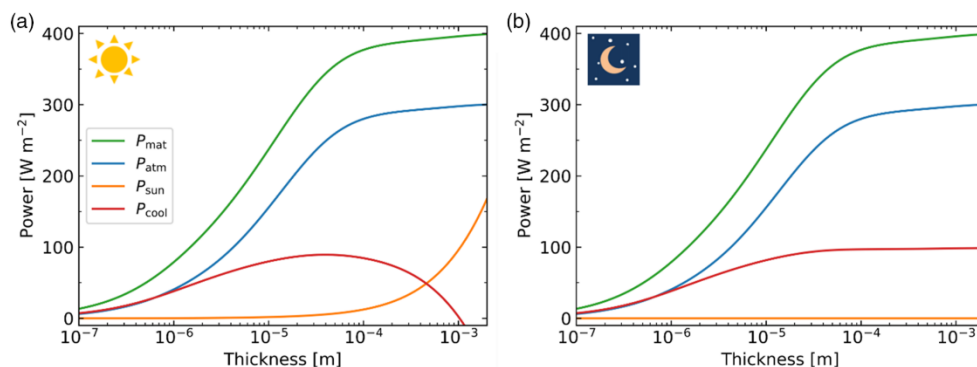


Figure 3. Individual energetic components contributing at ambient temperature as a function of thickness, as well as the resulting cooling power, during a) daytime and b) nighttime.

increasing absorbed power due to solar radiation above 1×10^{-5} m, therefore, leads to a maximum cooling power as a function of emitter thickness. For the nighttime case in Figure 3b, the contribution of solar radiation is zero, leading to a plateau being reached at high emitter thicknesses. Even as the emitted power and the power absorbed due to atmospheric radiation both continue to increase with increasing emitter thickness, the resulting cooling power asymptotically approaches a constant value. Therefore, no optimum thickness is apparent, but a minimum thickness required to reach the highest cooling power can be estimated.

After the individual contributions have been treated as a function of thickness at ambient temperature, the resulting cooling power for PDMS as a function of emitter thickness and emitter temperature is shown in Figure 4. Here, the cooling power is color-coded and displayed as a function of thickness and temperature difference relative to the atmospheric temperature. Negative cooling powers, equivalent to a sample that heats up, are not shown for simplicity. The boundary of the color-coded area thus represents the achievable equilibrium temperatures below ambient for the respective thickness. Red dots highlight the thickness with the highest cooling power at the respective temperature below ambient.

In general, the cooling power decreases as the material cools below ambient temperature ($T_{\text{atm}} - T_{\text{mat}} > 0$), as the blackbody

radiation is reduced, and nonradiative heat transfer is apparent. An optimum thickness effect can be recognized in both the maximum cooling power at ambient, as discussed above, and the minimum equilibrium temperature below ambient, and therefore the highest temperature difference, for the daytime case. A slight shift of the highest cooling power to lower thicknesses with increasing the temperature difference between material and ambient is apparent. This shift can be understood as the emitted power approximately scales with temperature to the fourth power. A lower emitted power due to a lower emitter temperature is then counterbalanced by the incoming solar and atmospheric radiation at lower thicknesses. Our result confirms that a cooler with a certain thickness can either reach the lowest possible equilibrium temperature or the highest cooling power at ambient temperature. Conceptually, both cannot be optimized simultaneously, even as the absolute thickness values only differ by half an order of magnitude. This distinction was also the subject of discussion by other researchers when comparing different artificial emitter materials, where a blackbody emitter has higher cooling power at ambient but selective emitters can reach lower equilibrium temperatures.^[1a,8]

The resulting cooling power as a function of thickness and temperature during nighttime for PDMS is shown in Figure 4b. Close to ambient, as discussed in Figure 3b, the cooling power asymptotically approaches a maximum value, where

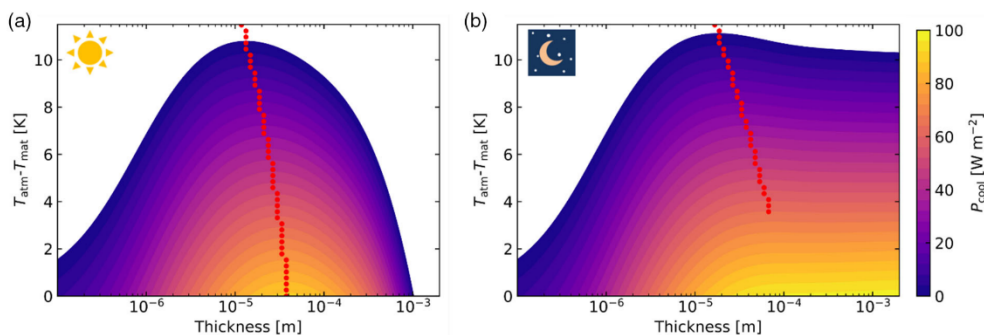


Figure 4. Resulting cooling power as a function of thickness and emitter temperature, as well as highlighted thickness (red dots) with the highest cooling power at the respective temperature, during a) daytime and b) nighttime.

an increase in thickness only incrementally increases the maximum cooling power due to the exponential nature of the material emissivity. Compared to the daytime case, higher cooling powers and lower equilibrium temperatures can be reached due to the absence of solar radiation. Only above a certain temperature difference threshold, an optimum thickness in a similar order of magnitude as for the daytime case becomes apparent. This effect is discussed in Figure S3, Supporting Information, as the effect is significantly less pronounced than during daytime. In general, for materials with different optical properties, an optimum thickness for the nighttime cooling power may be more strongly pronounced and should, therefore, be separately verified.

The main difference between day- and nighttime is a clearly defined optimum emitter thickness during daytime. In contrast, a plateau is reached at high emitter thicknesses during nighttime, and only above a certain temperature difference threshold, an optimum thickness becomes apparent.

To point out that this is a general effect and not only applicable to PDMS, we performed similar calculations for other commercial polymeric materials, i.e., polystyrene (PS), polymethyl methacrylate (PMMA), and polyethylene terephthalate (PET), where broadband complex refractive index data are available in the literature.^[16a] There, the same basic principles of optimum emitter thickness apply and are shown in Figure S4, Supporting Information.

3.2. Sample Characterization

To confirm our theoretical observations, we prepared a set of PDMS films with different thicknesses and characterized their absorption properties with UV-vis and FTIR spectroscopy. Further, we conducted rooftop experiments to determine the reached equilibrium temperatures (see Experimental Section).

The actual absorbance of PDMS films with different thicknesses on reflecting Ag films is displayed in Figure 5. For thinner PDMS layers, the emission is more confined within the first atmospheric window. We attribute this to the high absorption coefficient of the material in this spectral region. For higher thicknesses, the absorbance in the near-IR region is substantially increasing, leading to an overall increase in emitted radiation. However, at the same time, the absorption of solar radiation is promoted. The silver mirror efficiently reflects all wavelengths larger than 400 nm and, therefore, prevents absorption of solar radiation by the underlying substrate. However, for shorter wavelengths, the absorbance increases. This loss in cooling power cannot be avoided in our sample geometry and leads to reduced cooling power in the daytime case.

To compare if the used optical data can adequately describe our samples, we calculated the absorbance for the respective thicknesses based on the complex refractive index. The resulting absorbance spectra (Figure S5, Supporting Information) capture the main features in the mid-IR region. However, in the solar region, larger deviations for the thickest sample are evident. Therefore, the exact determination of the complex refractive index is crucial for a prediction of the cooling performance. Substantial variations in the absorption coefficient can be expected for every material due to the large wavelength range relevant for passive cooling materials. The availability of precise

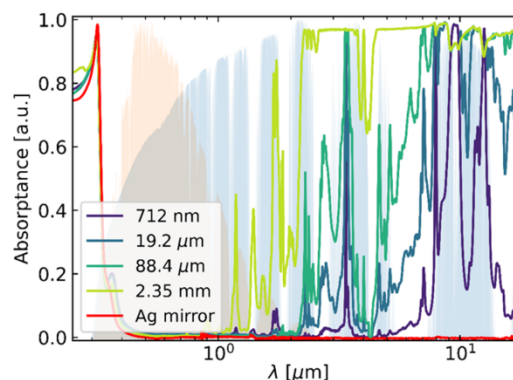


Figure 5. Absorbance of the respective PDMS samples with different thicknesses on Ag mirrors from UV-vis to mid-IR range.

theoretical data spanning several orders of magnitude is a limitation of our theoretical approach.

3.3. Rooftop Measurements

We experimentally determined the passive cooling performance of PDMS films with different thicknesses by a rooftop experiment to verify the theoretical expectation. PDMS films were prepared on Ag-coated silicon wafers by spin coating or attachment (see Experimental Section). As shown in Figure 6, samples were placed individually in self-built setups for rooftop measurements.

Styrofoam insulation was applied to the outside to reduce conduction, and a low-density polyethylene (LDPE) cover was used to minimize convection, respectively. Additionally, the entire setup was covered with Al foil to reflect most of the solar irradiation. To ensure comparability between the different setups, the variety between each setup was first checked by tracking the temperature of five identical Al mirrors in daytime (Figure S6, Supporting Information). A minor deviation of $\approx 0.5^\circ\text{C}$ was observed during a 1.5 h rooftop measurement, under the average direct sunlight irradiation of 857 W m^{-2} .

In the daytime experiment, as an LDPE foil is applied to prevent convection, a slight greenhouse effect is apparent in the measurement cell,^[17] which results in a temperature elevation of all measured samples when exposed to the sunlight. As shown in Figure 6b, the temperature of the bare Ag mirror itself increased by $\approx 7^\circ\text{C}$ at an average direct sunlight irradiation of 754 W m^{-2} , compared to air temperature. We attribute this greenhouse effect to a parasitic solar absorption of the sample holder and of the Ag mirror itself. Consistently, we do not observe this increase of the temperature baseline during nighttime, where the Ag mirror exhibits a similar temperature to air. To have a precise comparison and to emphasize the impact of the layer thickness on the passive cooling performance of the emitter, the measured temperature of the PDMS films with different thicknesses is, therefore, compared to the bare Ag mirror. During the experiment, the Ag mirror is exposed to comparable measurement conditions as the samples (Figure 6c,e). We, therefore, use the Ag mirror temperature as reference

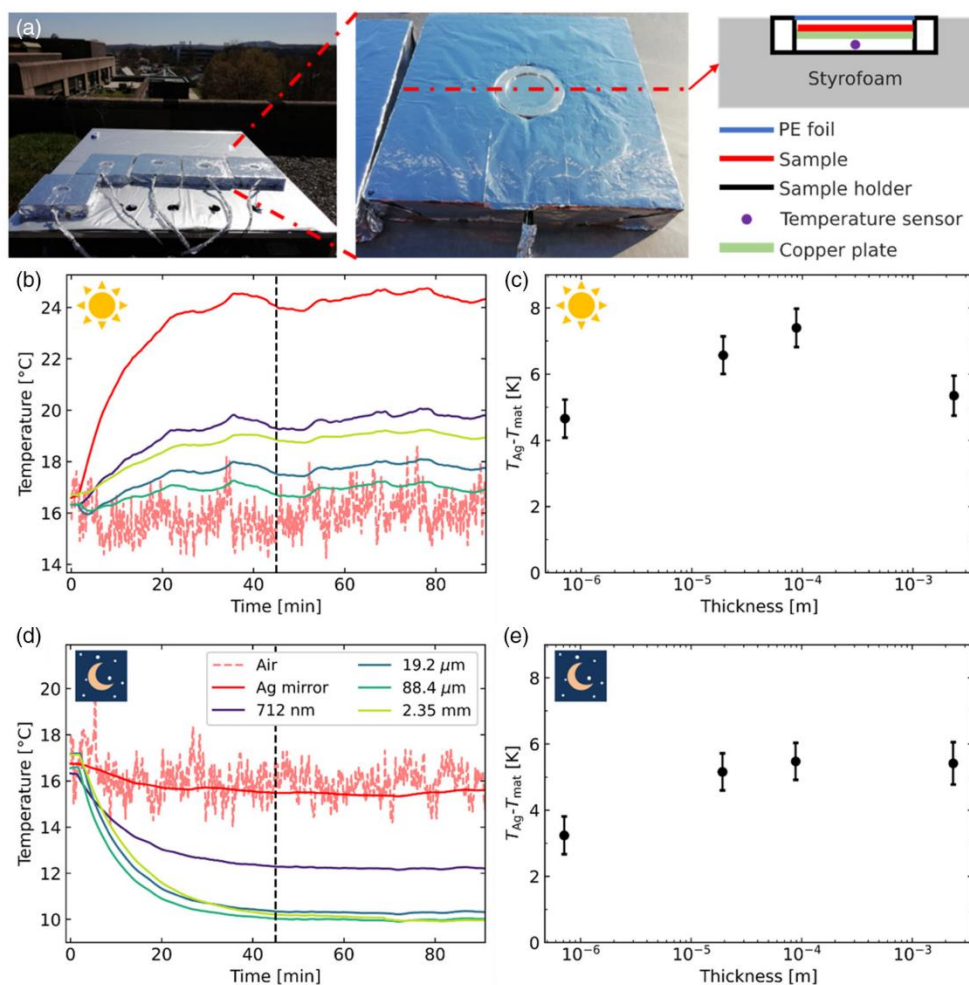


Figure 6. Rooftop measurement for PDMS films at day- and nighttime. a) Photographs and schematic of the setup for rooftop measurements. Temperature tracking of PDMS films on Ag mirror with different thicknesses, i.e., 712 nm, 19.2 μm, 88.4 μm, and 2.35 mm, and the bare Ag mirror, b) daytime and d) nighttime. The average solar irradiation during the entire daytime measurement was 754 W m^{-2} . The temperature difference between the bare Ag mirror and the PDMS films as a function of layer thickness at c) daytime and e) nighttime, respectively. The measurement was carried out under a clear sky on 23.04.2021, Bayreuth, Germany.

instead of the air temperature, which is susceptible to measurement conditions, e.g., location or wind speed.

In the nighttime experiment (Figure 6d), the passive cooling effect of the PDMS films is directly observable. All films cool down from their initial temperature (air temperature) after exposure to the clear sky until a steady state was approached. By contrast, the Ag mirror reference exhibited only an insignificant temperature reduction, which is likely attributed to the thin passivating layer of SiO_2 .

To compare the cooling performance of the samples, we extracted the steady-state temperature difference between PDMS films and the Ag mirror reference from the experiments. The average temperature difference data in the steady state regime (after 45 min) are displayed in Figure 6c,e. During daytime, the temperature difference increased from 4.7 K for

the 712 nm thick film to 7.4 K for the 88.4 μm film. We attribute this increase in passive cooling performance to the increased overall emittance of the film. In contrast, the passive cooling performance is reduced for the much thicker 2.35 mm PDMS film. In this case, the temperature difference dropped to 5.3 K. We attribute this drop to the increased absorption of solar radiation, as discussed in Section 4.1 (Figure 3a). For the nighttime case, the observed temperature difference between films and reference increases with increasing film thickness, reaching a plateau at high thicknesses. For the larger thicknesses, the temperature difference is not significantly increased further.

Despite the differences in the assumptions made in the calculations and actual experimental conditions, the observations of thickness-dependent passive cooling performance of PDMS films are in good agreement with the results obtained from

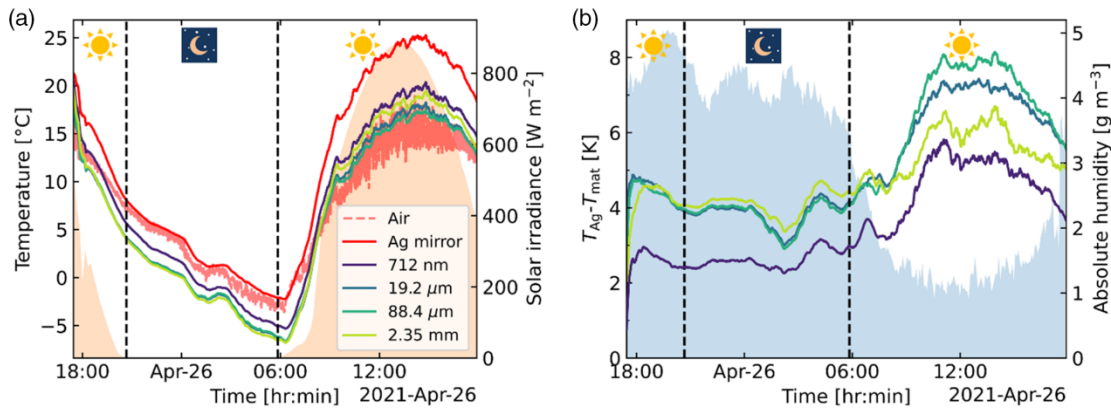


Figure 7. 24 h rooftop measurement of PDMS films with different thicknesses. a) Temperature tracking of different samples. Corresponding solar irradiance is plotted as the background. b) Temperature difference between Ag mirror and the PDMS films ($T_{Ag} - T_{mat}$) during the entire measurement, along with the absolute humidity (AH). The measurement was carried out under a clear sky, on 25–26.04.2021, Bayreuth, Germany.

our theoretical calculations. Sources of error having the most significant influence are deviations of the actual solar and atmospheric spectra to the ones used for calculation, as well as deviations of the sample's optical properties from those calculated by the optical constants. Also, the exact determination of the comprehensive heat transfer coefficient would increase the accuracy of the calculations but is a nontrivial task. As many parameters influence the net cooling power in complex and entangled dependencies, the agreement of theory and experiment is nevertheless very convincing. All the mentioned sources of error affect the absolute values of the equilibrium temperature, but not the day- and nighttime dependence trend.

To ensure that the observed behavior of the samples with different thicknesses is also valid for a more extended measurement time, we performed continuous measurements (from 18:00, 25th to 18:00, 26th April 2021, University of Bayreuth, Bayreuth, Germany). The measured temperatures of the different samples and an Ag reference are presented in **Figure 7a**. All PDMS films with different thicknesses exhibit a lower temperature than the Ag mirror in the entire 24 h measurement. The overall temperatures are lower during nighttime and increase with the onset of solar irradiance. To further reveal the thickness dependence on the cooling performance of PDMS films, the temperature difference ($T_{Ag} - T_{mat}$) is plotted in **Figure 7b**. A maximum temperature difference of 3.2, 4.4, 4.3, and 4.7 K was obtained for the 712 nm, 19.2 μm, 88.4 μm, and 2.35 mm PDMS films during nighttime, respectively. In contrast, a maximum temperature difference of 5.8, 7.4, 8.1, and 6.7 K was observed from the 712 nm, 19.2 μm, 88.4 μm, and 2.35 mm PDMS films in daytime. The observed temperature difference is consistent with our previous observations in short-time rooftop measurements and the simulation result. Again, for the nighttime case, except for the thinnest sample, the different thicknesses reach similar temperature differences in accordance with the short-time measurement. During daytime, the different thicknesses spread out, revealing the optimum thickness effect.

The absolute temperature difference is smaller for the nighttime period of the experiment compared to the daytime. This

observation is counterintuitive because, during daytime, additional cooling power is lost by the absorption of solar radiation. However, the absolute sample temperature is lower at nighttime, so a reduced cooling power is apparent. Besides the absolute temperature also the humidity in the atmosphere is affecting the cooling potential. We monitored the relative humidity (RH) next to the experimental setup and calculated the AH present to account for changes in temperature (**Figure 7b**). The atmosphere's higher water content during nighttime decreases the atmospheric transparency, and hence the atmospheric radiance increases, leading to a smaller equilibrium temperature difference.

4. Conclusion

In this work, we presented a complex refractive index-based method to determine the optimum thickness for passive-cooling emitter materials in a back-reflector configuration. We observed optimum thicknesses in both day- and nighttime applications, depending on the optical properties of the material. The optimum thickness significantly influences the daytime application, while it is rather a factor in minimizing fabrication costs at maximum cooling capacity during nighttime. Our calculations further confirmed that a cooler with the highest ambient temperature cooling power does not necessarily reach the lowest equilibrium temperature. Our approach focuses on materials that use a back-reflector geometry to prevent solar heat uptake. The theoretical prediction can also be used for coolers that operate with a solar filter layer or rely on a scattering approach. For these calculations, the model needs to be adjusted to deal with the solar radiation term properly. Especially, proper complex refractive index characterization and theoretical description of a highly scattering material can be challenging. Overall, we emphasize that in addition to the passive cooling material and its nano/microstructure, the layer thicknesses of the passive cooling device needs to be optimized as well.

5. Experimental Section

Calculations: An atmospheric temperature of 298.15 K was used for both day- and nighttime to calculate the cooling power. All integrations were done using the trapezoidal integration method in Matlab. As functions inside the integrals need to have the same energy spacing to perform numerical integration, the spectral radiative powers of the sun and atmosphere are adapted to the complex refractive index spacing of the material because they are available in higher resolution. This adaptation was done using the 1D data interpolation method in Matlab.

Fabrication of PDMS Films on Ag Mirrors: PDMS films with different thicknesses were prepared on protected silver mirrors. For the mirrors, a 100 nm-thick Ag layer was thermally evaporated on the wafer. Following, a 10 nm-thick layer of silicon oxide was deposited with a sputter coating step. This additional protection layer is used to prevent oxidation of the silver layer after PDMS deposition. A prepolymer mixture of PDMS (Sylgard 184, Dow Chemical) with a mixing ratio of prepolymer to cross-linker of 10:1 (by mass) was degassed in a desiccator with reduced pressure. The mixture was spin-coated on the mirrors with 1000 and 3000 rpm to obtain layers with ≈ 100 and $20 \mu\text{m}$ thickness, respectively. For the approximately $1 \mu\text{m}$ -thick PDMS layer, the prepolymer/cross-linker mixture was diluted to a 25 wt% solution with *n*-hexane. The mixture was then spin-coated onto the silver mirror with 4000 rpm. The layers were cured at room temperature over 48 h. For the sample with 2.35 mm thickness, the prepolymer mixture was filled in a mold and cured at 75°C for 1.5 h. A circular piece with a diameter of approximately 5 cm was cut and gently placed on a silver mirror.

The sample thickness of the thinner samples (712 nm , $19.2 \mu\text{m}$, and $88.4 \mu\text{m}$) was determined with a 3D laser scanning microscope (LEXT OLS 5000, Olympus). A small incision was made to determine the actual height of the polymer layer. An area of $258 \mu\text{m}^2$ around the incisions was imaged, and the height difference was determined by averaging the two major height fractions present in the image. The 2.35 mm high sample height was determined with a touch probe (Litematic VL-50, Mitutoyo). Different spots on the sample were measured, and the resulting height values were averaged.

Optical Characterization with UV-vis and FTIR Spectroscopy: UV-vis reflectance R was measured with a UV-vis spectrometer (Cary 5000, Agilent Technologies) equipped with an integrating sphere accessory (Labspheres). The measurements were conducted at the reflection port of the sphere with a fixed incident angle of 8° . As a reference, a Spectralon diffuse reflectance standard (Labspheres) was used. The FTIR spectroscopy measurements were conducted with an IR spectrometer (Vertex 70, Bruker) combined with a gold-coated integrating sphere accessory (A562, Bruker). The measurements were performed at the lower reflection port of the accessory (non-normal incidence). As a reference, a gold mirror was used. The absorbance (emittance) A was calculated considering the energy conservation with $A = 1 - R$ assuming that transmission can be neglected due to the silver layer.

Rooftop Performance Experiment: All rooftop measurements were carried out on the roof of a four-floor building (University of Bayreuth, Bayreuth, Germany) under a clear sky. The emitter was placed in a homemade sample holder (3D printed with material of acrylonitrile butadiene styrene), which was thermally insulated by Styrofoam and covered with Mylar aluminum Foil (Figure 6a). LDPE foil with a thickness of $\approx 10 \mu\text{m}$ was applied to the sample holder to prevent convection. The emitter temperatures were measured by PT100 temperature sensors and recorded by a digital multimeter (DAQ6510, Tektronix, Germany) every 5 s. Air temperature is measured with a thermal couple (T-type) which is placed in the ambient environment next to the setup. The solar irradiance data are obtained from the weather station University Bayreuth (Ecological-Botanical Garden, 400 m away from the rooftop measurement). During the rooftop measurement, all sample setups were first stored under the table to achieve a similar starting temperature. A few minutes after the start of data recording, the sample setups were placed on the table to face the sky. Short- and long-term measurements were conducted for 1.5 and 24 h, respectively. During the measurements, the RH was tracked with a temperature logger (LOG220, DOSTMANN electronic

GmbH) next to the setup. The AH in g m^{-3} was calculated using RH in percent and the ambient temperature T_{amb} in $^\circ\text{C}$ by

$$\text{AH} = \frac{6.112 \cdot \exp\left(\frac{17.67 \cdot T_{\text{amb}}}{T_{\text{amb}} + 243.5}\right) \cdot \text{RH} \cdot 2.1674}{273.15 + T_{\text{amb}}}$$

Supporting Information

Supporting Information is available from the Wiley Online Library or from the author.

Acknowledgements

K.H. and T.L. contributed equally to this work. The authors gratefully acknowledge the contributions of M.Sc. Thomas Tran, Stefan Rettinger for technical support and Klaus Müller for the metal evaporation. The solar radiance data were kindly provided by Prof. Christoph Thomas. This project has received funding from the European Research Council (ERC) under the European Union's Horizon 2020 research and innovation program (grant agreement no. 714968).

Conflict of Interest

The authors declare no conflict of interest.

Data Availability Statement

Research data are not shared.

Keywords

complex refractive index, radiative cooling, radiative heat transfer, thermal emission, thermal management

Received: October 6, 2021

Revised: October 30, 2021

Published online: November 16, 2021

- [1] a) M. M. Hossain, M. Gu, *Adv. Sci.* **2016**, *3*, 1500360; b) B. Zhao, M. K. Hu, X. Z. Ao, N. Chen, G. Pei, *Appl. Energy* **2019**, *236*, 489.
- [2] a) A. P. Raman, M. A. Anoma, L. Zhu, E. Rephaeli, S. Fan, *Nature* **2014**, *515*, 540; b) N. W. Pech-May, T. Lauster, M. Retsch, *ACS Appl. Mater. Interfaces* **2021**, *13*, 1921.
- [3] a) J. Mandal, Y. Fu, A. C. Overvig, M. Jia, K. Sun, N. N. Shi, H. Zhou, X. Xiao, N. Yu, Y. Yang, *Science* **2018**, *362*, 315; b) T. Wang, Y. Wu, L. Shi, X. Hu, M. Chen, L. Wu, *Nat. Commun.* **2021**, *12*, 365.
- [4] a) A. R. Gentle, G. B. Smith, *Nano Lett.* **2010**, *10*, 373; b) Y. Zhai, Y. Ma, S. N. David, D. Zhao, R. Lou, G. Tan, R. Yang, X. Yin, *Science* **2017**, *355*, 1062.
- [5] a) J. L. Kou, Z. Jurado, Z. Chen, S. H. Fan, A. J. Minnich, *ACS Photonics* **2017**, *4*, 626; b) Y. Zhou, H. M. Song, J. W. Liang, M. Singer, M. Zhou, E. Stegenburgs, N. Zhang, C. Xu, T. Ng, Z. F. Yu, B. Ooi, Q. Q. Gan, *Nat. Sustain.* **2019**, *2*, 718; c) U. Banik, A. Agrawal, H. Meddeb, O. Sergeev, N. Reininghaus, M. Gotz-Kohler, K. Gehrke, J. Stuhrenberg, M. Vehse, M. Sznajder, C. Agert, *ACS Appl. Mater. Interfaces* **2021**, *13*, 24130.
- [6] a) E. Torgerson, J. Hellhake, *Sol. Energy Mater. Sol. Cells* **2020**, *206*, 110319; b) N. W. Pech-May, M. Retsch, *Nanoscale Adv.* **2020**, *2*, 249.
- [7] a) W. L. Huang, Y. J. Chen, Y. Luo, J. Mandal, W. X. Li, M. J. Chen, C. C. Tsai, Z. Q. Shan, N. F. Yu, Y. Yang, *Adv. Funct. Mater.* **2021**, *31*,

- 2010334; b) H. Kim, S. McSherry, B. Brown, A. Lenert, *ACS Appl. Mater. Interfaces* **2020**, *12*, 43553.
- [8] Y. L. Li, L. Z. Li, L. Guo, B. W. An, *Opt. Mater. Express* **2020**, *10*, 1767.
- [9] a) Y. Tian, L. Qian, X. Liu, A. Ghanekar, G. Xiao, Y. Zheng, *Sci. Rep.* **2019**, *9*, 19317; b) Y. Q. Zhu, Y. H. Ye, D. Wang, Y. R. Cao, *OSA Continuum* **2021**, *4*, 416.
- [10] R. Zhu, D. Hu, Z. Chen, X. Xu, Y. Zou, L. Wang, Y. Gu, *Nano Lett.* **2020**, *20*, 6974.
- [11] a) H. H. Kim, E. Im, S. Lee, *Langmuir* **2020**, *36*, 6589; b) C. Sheng, Y. An, J. Du, X. Li, *ACS Photonics* **2019**, *6*, 2545; c) L. Zhu, A. P. Raman, S. Fan, *Appl. Phys. Lett.* **2013**, *103*, 223902; d) Y. Chen, J. Mandal, W. Li, A. Smith-Washington, C. C. Tsai, W. Huang, S. Shrestha, N. Yu, R. P. S. Han, A. Cao, Y. Yang, *Sci. Adv.* **2020**, *6*, eaaz5413; e) G. J. Lee, Y. J. Kim, H. M. Kim, Y. J. Yoo, Y. M. Song, *Adv. Opt. Mater.* **2018**, *6*, 1800707.
- [12] R. A. Yalçın, E. Blandre, K. Joulain, J. Drévuillon, *ACS Photonics* **2020**, *7*, 1312.
- [13] a) B. J. Park, J. P. Pantina, E. M. Furst, M. Oettel, S. Reynaert, J. Vermant, *Langmuir* **2008**, *24*, 1686; b) A. Berk, P. Conforti, R. Kennett, T. Perkins, F. Hawes, J. v. d. Bosch, in *6th Workshop on Hyperspectral Image and Signal Processing: Evolution in Remote Sensing (WHISPERS)*, IEEE, Lausanne, Switzerland **2014**, p. 1.
- [14] B. Bhatia, A. Leroy, Y. Shen, L. Zhao, M. Gianello, D. Li, T. Gu, J. Hu, M. Soljacic, E. N. Wang, *Nat. Commun.* **2018**, *9*, 5001.
- [15] C. G. Granqvist, A. Hjortsberg, *J. Appl. Phys.* **1981**, *52*, 4205.
- [16] a) X. Zhang, J. Qiu, X. Li, J. Zhao, L. Liu, *Appl. Opt.* **2020**, *59*, 2337; b) X. Zhang, J. Qiu, J. Zhao, X. Li, L. Liu, *J. Quant. Spectrosc. Radiat. Transfer* **2020**, *252*, 107063; c) M. Querry, in *US Army Rep. CRDECCR-88009*, **1987**.
- [17] a) S. Y. Jeong, C. Y. Tso, J. Ha, Y. M. Wong, C. Y. H. Chao, B. Huang, H. Qiu, *Renewable Energy* **2020**, *146*, 44; b) D. Chae, M. Kim, P. H. Jung, S. Son, J. Seo, Y. Liu, B. J. Lee, H. Lee, *ACS Appl. Mater. Interfaces* **2020**, *12*, 8073.

Supporting Information

Homogeneous Polymer Films for Passive Daytime Cooling: Optimized Thickness for Maximized Cooling Performance

Kai Herrmann, Tobias Lauster, Qimeng Song, Markus Retsch**

K. Herrmann, T. Lauster, Q. Song, M. Retsch

Department of Chemistry, Physical Chemistry I

University of Bayreuth

Universitätsstraße 30, 95447 Bayreuth, Germany

E-mail: markus.retsch@uni-bayreuth.de , qimeng.song@uni-bayreuth.de

M. Retsch

Bavarian Polymer Institute, Bayreuth Center for Colloids and Interfaces, and Bavarian Center for Battery Technology (BayBatt)

University of Bayreuth

Universitätsstraße 30, 95447 Bayreuth

SI 1. Convergence of the resulting calculated cooling power

To verify the convergence of the resulting cooling power as a function of the upper integration boundary, we map out the corner points of the thickness-temperature space shown in Figure 4. Namely, those are thicknesses of $1 \cdot 10^{-7}$ m and $1 \cdot 10^{-3}$ m and temperature differences of 0 K and 12.5 K relative to ambient.

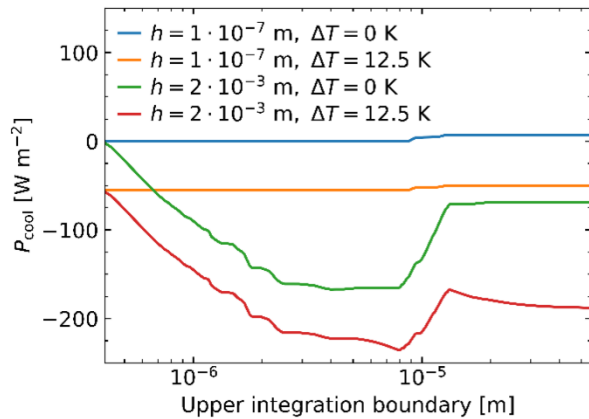


Figure S1: Convergence of the integrated total cooling power as a function of upper integration boundary for the points enclosing the analyzed temperature and thickness space.

Convergence of the resulting cooling power as a function of the upper integration can be seen. For high thickness and temperature differences, maybe higher integration boundaries might be needed, but for the calculations performed in this work, the upper integration boundary of 55 μm is sufficient.

SI 2. Influence of the non-radiative heat transfer coefficient

To analyze the influence of the comprehensive heat transfer coefficient due to convection and conduction, several coefficients are used spanning two orders of magnitude. Regardless of the absolute value, an optimum thickness is always apparent. As intrinsic losses increase, smaller temperature differences to ambient are apparent, as to be expected.

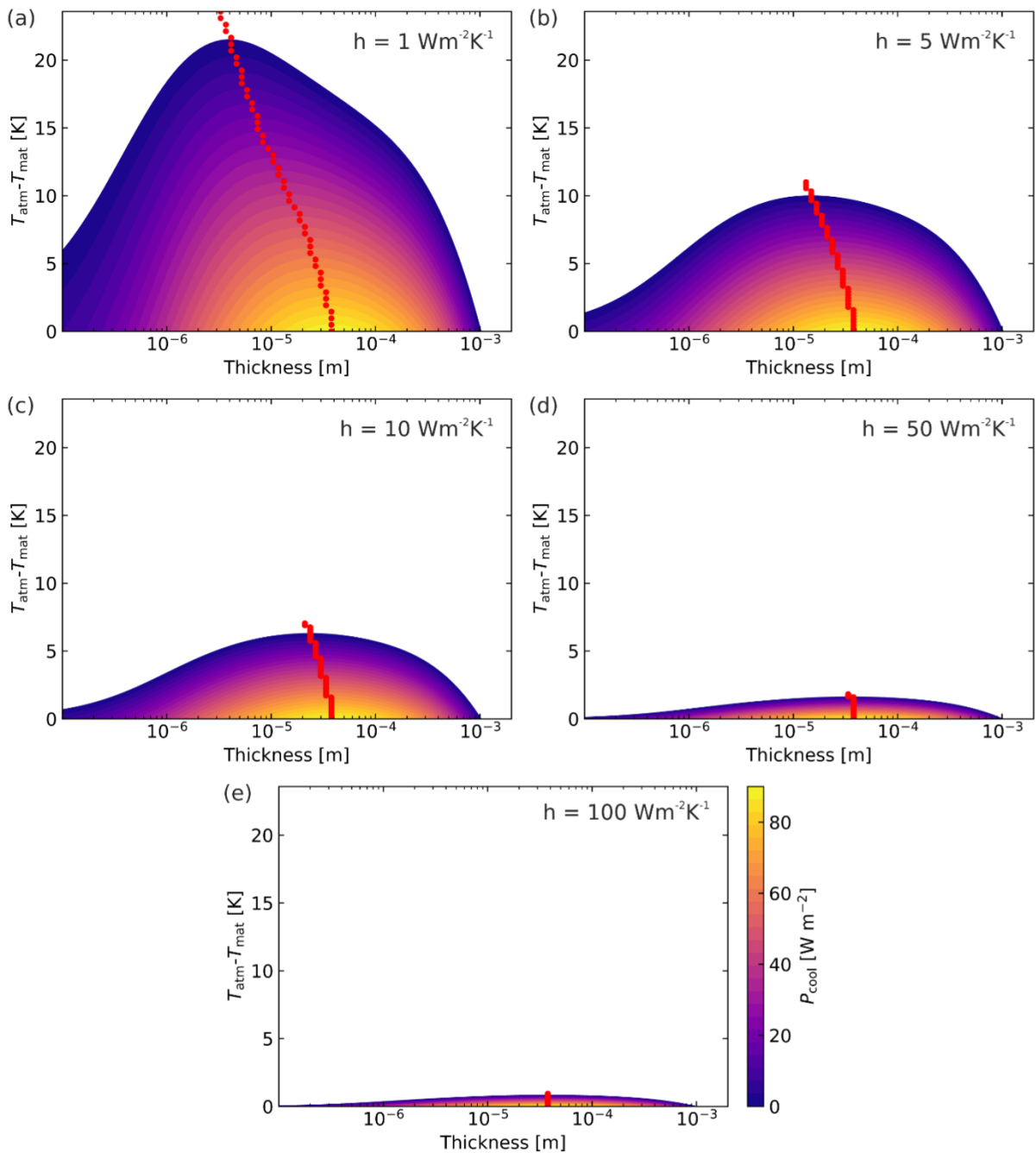


Figure S2: Influence of the non-radiative heat transfer coefficient on the net cooling power for PDMS.

SI 3. Optimum emitter thickness during night-time

Only above a certain temperature difference threshold, an optimum thickness in a similar order of magnitude as for the daytime case becomes apparent. This maximum has a different origin compared to the daytime case. As the emitter temperature decreases, the power radiated decreases due to Planck's law of radiation. Above a certain threshold, for PDMS approximately 3 K below ambient, the derivatives regarding the thickness of the power absorbed and emitted have an intersection point. This intersection point represents a zero crossing in the derivative of the net cooling power, and in this case, a maximum cooling power. To better illustrate this effect, we focus on a temperature difference of 0 K and 10 K relative to ambient temperature.

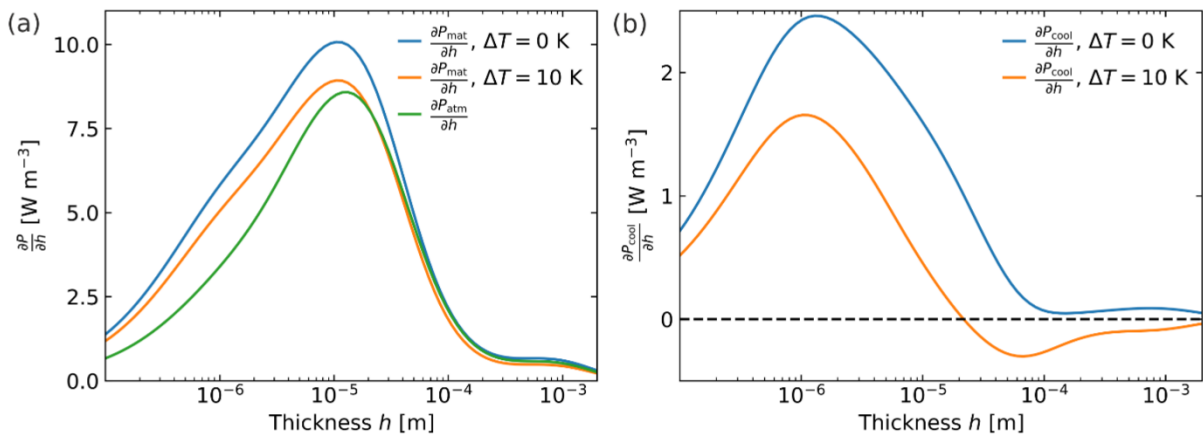


Figure S3: Numerical derivatives of the individual energetic contributions of material and atmosphere as a function of thickness during night-time (a), as well as the total cooling power (b) with respect to thickness. For $\Delta T = 10$ K, there is an optimum thickness apparent, while there is none for $\Delta T = 0$ K.

At ambient temperature, the derivative of the power emitted is continuously higher than the derivative of the power absorbed by the atmosphere. As the emitter temperature decreases, above a certain thickness, here approximately 20 μm , the derivative of the power absorbed by the atmosphere exceeds the derivative of the power emitted. This point represents a zero crossing of the total cooling power, depicted in Figure S3b, and in this case, a maximum cooling power that is not apparent at ambient temperature.

SI 4. Verification of the calculations by means of further materials

We also performed calculations based on the complex refractive index of other polymeric materials to verify the optimum thickness effect for passive cooling in back-reflector geometry.^[1] For polystyrene, polymethyl methacrylate, and polyethylene terephthalate, the cooling powers as a function of thickness and temperature are shown in Figure S4.

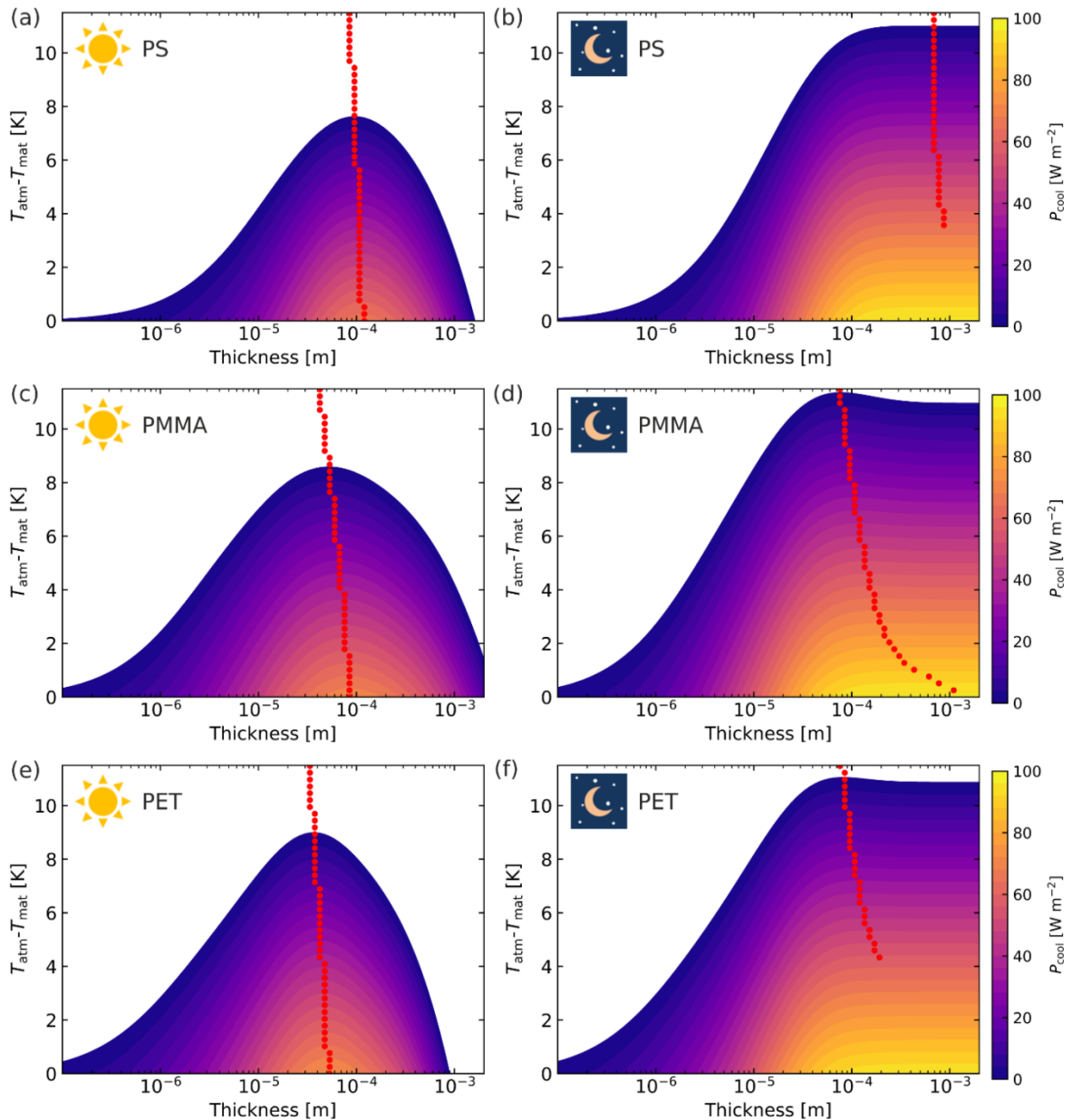


Figure S4: Resulting cooling power as a function of thickness and emitter temperature, as well as highlighted thickness (red dots) with the highest cooling power at the respective temperature, during daytime and night-time for polystyrene (a), (b) polymethyl methacrylate (c), (d) and polyethylene terephthalate (e), (f).

All materials investigated exhibit an optimum thickness during daytime, while the position, as well as the absolute cooling powers, vary. The same can be seen during night-time, whereas the temperature threshold below which an optimum thickness becomes apparent is also dependent on the emitter material. In summary, this can be interpreted as a general confirmation of the effect.

SI 5. Complex refractive index data as a source of error

The primary source of error, in addition to the atmospheric and solar spectrum, are the complex refractive index data of the investigated emitter material. A comparison of the measured absorptance spectrum and the expected absorptance based on the measured thickness and the complex refractive index is shown in Figure S5.

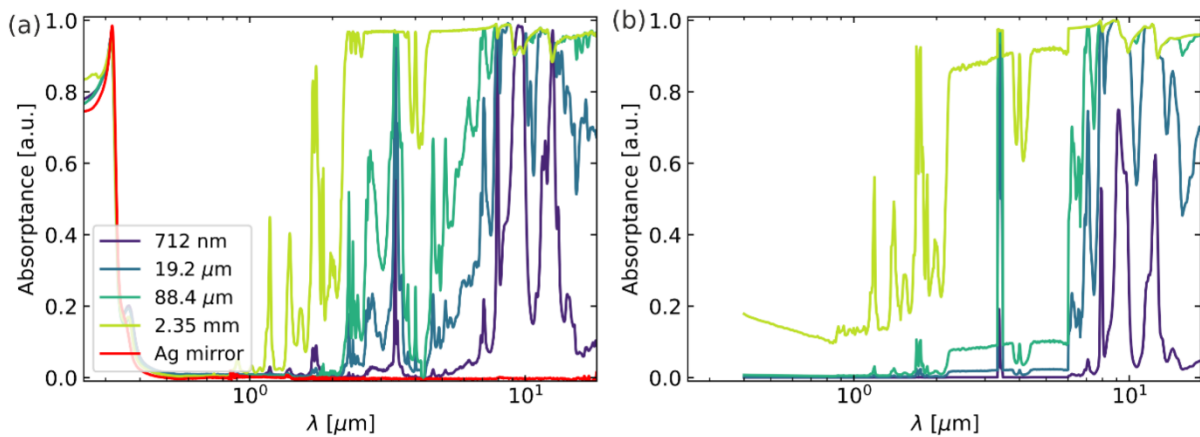


Figure S5: Measured absorptance (a) in comparison to the estimated absorptance based on the complex refractive index data and thickness (b) for an angle of incidence of 8° .

A qualitative agreement between measured and estimated absorptance spectrum is apparent, while the absolute values exhibit clear deviations. The main drawback is the overestimation of the absorption in the solar regime, leading to an optimum cooling power at lower thicknesses. For further work based on this approach, accurate complex refractive index data are, therefore, crucial.

SI 6. Verification of the measurement setup

To determine errors induced by the measurement setup, a measurement with five identical Al mirrors was performed.

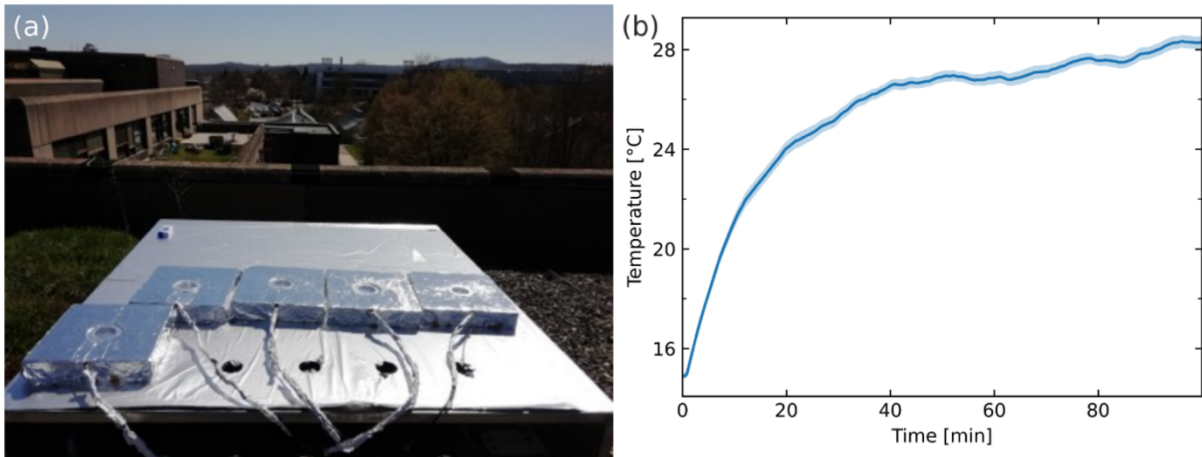


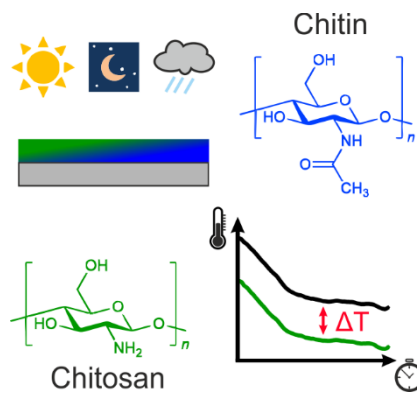
Figure S6: (a) photography of the setups used to measure the samples' daytime cooling performance. (b) Comparison of sample temperatures for the samples during the measurement time. Mean and standard deviation of five identical Al mirrors under the average solar irradiation of approximately 856 W/m^2 . (Start at 12:20, 23rd April 2021, University of Bayreuth, Bayreuth, Germany)

As the identical Al mirrors exhibit a maximum standard deviation of $\pm 0.3 \text{ K}$, not to overstate our results an error of the measurement setup of $\pm 0.5 \text{ K}$ is assumed.

References

- [1] a) X. Zhang, J. Qiu, X. Li, J. Zhao, L. Liu, *J. Quant. Spectrosc. Radiat. Transfer* **2020**, 252, 107063. b) X. Zhang, J. Qiu, X. Li, J. Zhao, L. Liu, *Appl. Opt.* **2020**, 59 (8), 2337-2344.

7. From Chitosan to Chitin: Bio-Inspired Thin Films for Passive Daytime Radiative Cooling



The potential of chitosan and chitin for the application as passive radiative cooling materials is investigated. A solid-state reaction is used to convert chitosan to its insoluble form chitin. Based on extensive optical characterization, both biopolymers are capable of below ambient temperature passive cooling.

From Chitosan to Chitin: Bio-Inspired Thin Films for Passive Daytime Radiative Cooling

Tobias Lauster, Anika Mauel, Kai Herrmann, Viktoria Veitengruber, Qimeng Song, Jürgen Senker, and Markus Retsch*

Passive radiative daytime cooling is an emerging technology contributing to carbon-neutral heat management. Optically engineered materials with distinct absorption and emission properties in the solar and mid-infrared range are at the heart of this technology. Owing to their low emissive power of about 100 W m^{-2} during daytime, substantial areas need to be covered with passive cooling materials or coatings to achieve a sizeable effect on global warming. Consequently, biocompatible materials are urgently needed to develop suitable coatings with no adverse environmental impact. It is shown how chitosan films with different thicknesses can be produced from slightly acidic aqueous solutions. The conversion to their insoluble form chitin in the solid state is demonstrated and the conversion is monitored with infrared (IR) and NMR spectroscopy. In combination with a reflective backing material, the films show below-ambient temperature cooling capabilities with a suitable emissivity in the mid-IR region and low solar absorption of 3.1–6.9%, depending on the film thickness. This work highlights the potential of chitosan and chitin as widely available biocompatible polymers for passive radiative cooling applications.

1. Introduction

With the prospects of global warming, the demand for cooling applications is expected to increase in the future. In classical active cooling technologies like air conditioning, the heat is spatially displaced but remains in close vicinity. Furthermore, the AC unit releases excess waste heat into the environment. This leads to heat accumulation, especially in urban areas. Therefore, developing new materials to save energy for cooling applications is of great interest. One promising concept to mitigate the heat island effect can be found in materials that cool in a passive manner. By tuning the optical properties of a material such that it efficiently emits energy in the form of thermal radiation, cooling can be achieved without energy input during operation.

This potential for cooling applications was already identified and theoretically described several decades ago.^[1]

Passive radiative cooling materials dissipate heat into outer space. For this heat sink to be accessible, the radiation needs to pass the atmosphere, which is only partially transparent. The most crucial wavelength region is located in the mid-infrared (mid-IR) region between 8 and $13 \mu\text{m}$, where the atmosphere is mostly transparent, and blackbody radiation at typical ambient temperatures (298 K) shows an emission maximum. If a material emits energy in only partially transparent or opaque wavelength regions, it depends on the temperatures of the material and the atmosphere whether cooling occurs.

During the daytime, sunlight absorption must be prevented to provide a net cooling effect. Beginning with the first works that demonstrated cooling under direct sunlight illumination,^[2] the field of passive radiative daytime cooling significantly developed over the last decade.^[3]

Polymeric materials such as polydimethylsiloxane^[4] or fluorinated polymers^[5] are heavily investigated because they show beneficial absorption (and therefore emission) characteristics in the mid-IR region due to resonance of molecular vibrations. At the same time, those materials absorb very little sunlight. In combination with a metallic reflection layer to prevent sunlight absorption of the underlying substrate, simple and low-cost passive radiative coolers were realized. Other works combine inorganic particles with a polymeric matrix to achieve the desired optical properties^[6] or utilize metal-dielectric multilayer

T. Lauster, K. Herrmann, V. Veitengruber, Q. Song

Department of Chemistry
Physical Chemistry I
University of Bayreuth
Universitätsstraße 30, 95447 Bayreuth, Germany

A. Mauel, J. Senker
Department of Chemistry
Inorganic Chemistry III and Northern Bavarian NMR Center
University of Bayreuth
95447, Universitätsstraße 30 Bayreuth, Germany

M. Retsch
Department of Chemistry
Physical Chemistry I
Bavarian Polymer Institute
Bayreuth Center for Colloids and Interfaces and Bavarian Center for
Battery Technology (BayBatt)
University of Bayreuth
Universitätsstraße 30, 95447 Bayreuth, Germany
E-mail: markus.retsch@uni-bayreuth.de

 The ORCID identification number(s) for the author(s) of this article can be found under <https://doi.org/10.1002/advs.202206616>

© 2023 The Authors. Advanced Science published by Wiley-VCH GmbH. This is an open access article under the terms of the Creative Commons Attribution License, which permits use, distribution and reproduction in any medium, provided the original work is properly cited.

DOI: 10.1002/advs.202206616

photonic structures to tune the absorption and reflection.^[7] The use of metallic reflection layers can even be omitted if the material sufficiently backscatters the sunlight. This was shown in recent works, where porosity was introduced to the systems to enable scattering.^[5a] Besides synthetic materials, bio-based materials have been researched. Especially, cellulose-based materials like wood or cellulose fibers drew increasing attention because they are abundant, low cost, and have a minimum environmental impact.^[8] Cellulose derivatives like cellulose acetate showed remarkable scattering properties when structured, as demonstrated in recent works.^[9] Also, natural silk showed cooling capabilities with strong reflectance attributed to Anderson localization within the fibers.^[10] Another natural source of inspiration has been the Silver Sahara Ant for passive daytime cooling concepts and materials.^[11] An intricate multiscale structure of nano-corrugated prismatic fibers based on chitin (CT) was shown to cool the Silver Sahara Ant by reflection in the solar range and enhanced emission in the mid-IR range. Furthermore, chitosan (CS) or its acetylated form CT is a material that can form structures with extraordinary optical properties. For example, the scales of the *Cyphochilus* beetle exhibit whiteness due to light scattering at the random CT network structure.^[12] A property that is also very desirable for passive radiative cooling materials. CS is, after cellulose, the second most abundant polymer in nature but has received very little attention for passive radiative cooling. Due to the polycationic nature of the polymer, it has been shown that CS sponges are excellent for the adsorption of anionic pollutants.^[13] Further applications are found in medical fields as support for tissue engineering,^[14] as a sensor for bacteria detection,^[15] or as template source for the fabrication of synthetic nacre.^[16] Besides the abundance, CS has the advantage of being soluble in dilute acetic acid, enabling the processing from solution. However, CS's potential for passive radiative cooling remains widely unexplored. An exception is the work of Chang et al., who used electrophoretically deposited CS to alternate the emission properties of stainless steel.^[17] Also, the group around Liu et al. used CS as a matrix material for lignin nanoparticles to produce a photothermal film but focused on the UV–vis absorption properties within their study.^[18]

Our work demonstrates the capabilities of CS as passive cooling material. To make it useable for passive cooling applications under outdoor conditions, CS must be transformed into CT. CT is the sturdy and water-insoluble form prevalent in nature, whereas CS is necessary to allow for processing it from solution. We, therefore, focus in this contribution on the processing and transformation of CS into CT with a particular focus on its broadband optical properties and passive cooling performance.

2. Results and Discussion

The CS films investigated in this work were cast from solutions of CS powder in dilute acetic acid. After casting, an aqueous gel film forms on the substrate, and compact CS films remain after evaporation of the solvent. With this approach, a variety of film thicknesses can be realized. The cast solution can be spread by doctor blading to obtain thin films. Several layers of CS can be stacked for thicker films by adding another layer of solution after drying the previous layer. The overall thickness can be controlled by the amount of solution and the concentration. However, the

concentration regime that can be used is limited to low concentrations (<4 wt%) because the viscosity of the solution is strongly increasing for higher concentrations. With the mentioned techniques, film thicknesses ranging from 6 to >100 μm can be prepared. With the spin coating technique, even thinner films can also be realized.

2.1. Acetylation Reaction to CT

The advantage of water processability of CS becomes a drawback when considering outside applications as passive cooling material. Water or humidity exposure will lead to the destruction of the material and its functionality. We performed a re-acetylation reaction to counter this disadvantage and to render the material insoluble. We followed the procedure of Hirano et al.,^[19] in which the reaction of a CS fiber with acetic anhydride (AcAH) in methanol is performed. The proposed reaction can be done at room temperature, and the material's structure is retained. A detailed description of our reaction conditions can be found in the Experimental Section.

2.1.1. Degree of Acetylation

To characterize if the reaction was successful, we determined the degree of acetylation (DA) via IR and NMR spectroscopic measurements. The DA describes the relative amount of *N*-acetyl glucosamine units within the polymer. CS mainly consists of glucosamine units. Consequently, DA values are low. In contrast, the polymer is named CT for DA values above 50%. The chemical structures of the predominant repeating units in each of the two polymers are displayed in **Figure 1a**.

NMR and FTIR spectroscopy are complementary, non-destructive methods to determine the DA. NMR spectroscopy is an element-sensitive bulk method that enables quantitative characterization. In contrast, FTIR spectroscopy is fast and requires minimal sample preparation, but has limited sample penetration depth when the attenuated total reflection (ATR) technique is used. Several procedures have been proposed to determine the DA from IR spectra. However, the evaluation can lead to deviations depending on the chosen probe and reference signals. An overview can be found in the work of Duarte et al.,^[20] in which they compare the results of different evaluation procedures of IR spectra to the DA values obtained with NMR spectroscopy. Nevertheless, ATR-FTIR spectroscopy is well suited to gain qualitative insights into CT conversion.

Particularly the –NH vibrational mode and the amidic carbonyl stretching vibration serves as an indicator of acetylation. According to the literature, the corresponding absorptions are found at wavenumbers of 1561 and 1663 cm^{-1} , respectively.^[20] Before functionalization, the –NH absorption was more pronounced than the amidic carbonyl absorption in both the pristine CS powder and film sample (Figure 1b). In contrast, similar intensities are observed after the functionalization reaction with AcAH. The absorption increase from the amidic carbonyl groups indicates that CS was acetylated. Note that the actual peak positions (1549 and 1641 cm^{-1}) slightly deviate from literature values. This deviation can result from different orientations or microstructure of

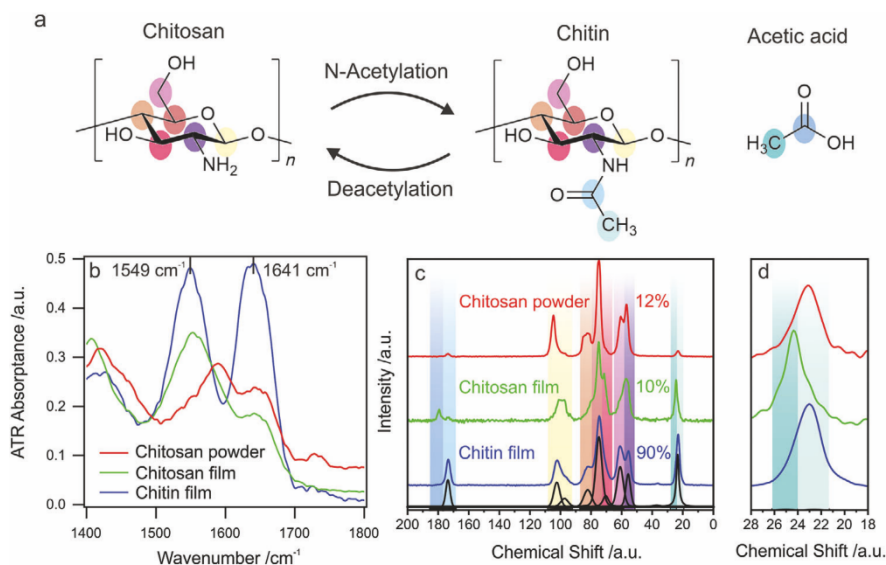


Figure 1. a) Chemical structure of chitosan (Poly-D-Glucosamine), chitin (*N*-Acetyl Poly-D-Glucosamine), and acetic acid. b) Normalized ATR-FTIR spectra were collected from CS powder, a CS film, and after the conversion to CT. The vibrational resonances corresponding to -NH at 1549 cm^{-1} and the amidic carbonyl resonance at 1641 cm^{-1} are marked. A slight difference in the intensity ratio between the NH deformation and amidic carbonyl stretching vibration for the chitosan powder and film indicates a different alignment and stronger involvement in hydrogen bonding for the chitosan films. This is in agreement with the observed shift in the resonance frequency of the NH-deformation vibration. The relative increase of the amide absorptions indicates a conversion from CS to CT. c) $^1\text{H}^{13}\text{C}$ CP MAS NMR spectra of CS powder, CS films, and a film after the conversion reaction with a color-coded signal assignment. The spectra are normalized to the backbone resonances (C1-C6: 120–40 ppm) and shifted vertically for a better overview. Upon treatment with AcAH, the DA increases. Exemplarily, the refinement of the CT film spectrum is shown (black). Intensities derived from the refinements are given in Table S1, Supporting Information. d) Enlarged section of the ^{13}C CP MAS NMR spectra to show the different CH_3 resonances of CT and acetic acid. The spectra are normalized to the CH_3 resonances (28–18 ppm) and shifted horizontally for a better overview.

our actual polymer. The collected spectra for the full wavenumber range are shown in Figure S1, Supporting Information. Theoretically, the hydroxyl groups within the polymer could also react with AcAH. However, the carbonyl vibration of the resulting esters would be expected at wavenumbers $>1700\text{ cm}^{-1}$, where no new signals arise.

To confirm our qualitative observations from FTIR spectroscopy and extend these to a quantitative level, we performed solid-state NMR spectroscopy. While IR spectra of the film samples prepared on glass substrates could be measured directly, the films needed to be detached from the substrate, cryomilled, and packed into magic-angle spinning (MAS) rotors prior to NMR spectroscopic measurements. The resulting ^{13}C CP MAS NMR spectra of pristine CS powder and a CS film before and after the acetylation reaction are displayed in Figure 1c,d. The signals corresponding to the glucosamine backbone (C1-C6) of the polymer are located between 110 and 50 ppm. Chemical shifts and signal shapes vary with local molecular conformations and, consequently with the degree of crystallinity and the present polymorphs. Generally, the crystallinity increases with the DA.^[21] Additional to the backbone signals, peaks at 174 ppm and 23 ppm are present in all spectra. These signals correspond to the carbonyl carbon and methyl carbon in the *N*-acetyl group, respectively. A significant increase in their intensity upon acetylation is observed, confirming the qualitative IR spectroscopic results. Small amounts of residual acetic acid (180 ppm for the carboxyl function and 25 ppm for the methyl group) were

observed in the CS film sample prior to functionalization. The films are prepared by dissolving the pristine CS powder in dilute acetic acid, followed by drying on glass substrates and removal of residual acetic acid via treatment with NaOH in methanol (see Experimental Section). The ^{13}C CP MAS NMR spectra show that the removal of acetic acid was incomplete. However, those additional signals vanish after the acetylation reaction, indicating that no acetic acid remains within the final film.

To quantify the DA of our product, CP NMR spectra were measured with a set of optimized parameters as previously determined in detailed relaxation and CP kinetics studies by Duarte et al.^[22] (see Experimental Section). They ensure similar intensities for the resonances of primary, secondary, and tertiary carbon units, thus avoiding the drawback of a CP pulse sequence not necessarily leading to quantitative results.^[23] Still, the resonance intensities of carbon units without covalently attached protons will be underestimated as the magnetization transfer from ^1H to ^{13}C in a CP sequence is achieved via heteronuclear dipolar interactions and consequently depends on the proximity of protons.^[24] Thus, the DA needs to be determined as the ratio of the methyl signal of acetic acid to the six backbone carbon atoms. After deconvolution of the spectra with pseudo-Voigt profiles (Figure 1d and Table S1, Supporting Information), we calculated DA values. It is important to consider the residual acetic acid to prevent overestimation of the DA. For the pristine CS powder and the unreacted film, we determined low DA values of 12% and 10%. After

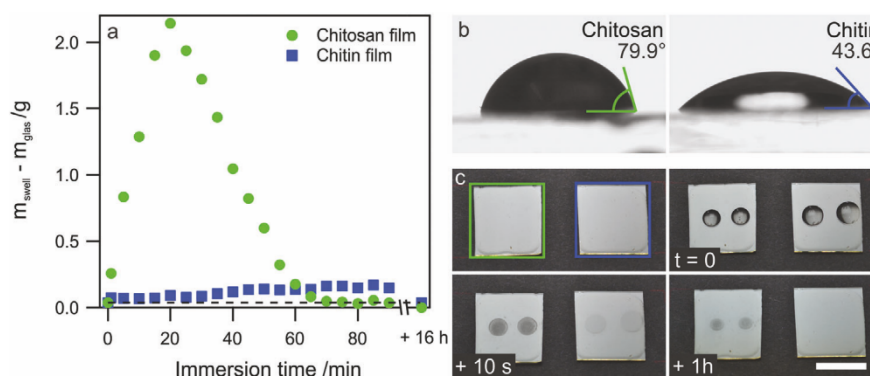


Figure 2. a) Mass change of CS and CT films after consecutive water immersion for 90 min and after complete drying. b) The water contact angle of CS and CT film was determined in a sessile drop experiment. The presented values are mean \pm SD. c) Photographs of CS and CT films before and at different times after water droplet exposure. The scale bar is 2 cm.

the reaction, a DA value of 90% confirms successful acetylation and conversion of the film to CT.

2.1.2. Water Resistance and Contact Angle

The main goal of the acetylation reaction was to increase the water resistance of the films. We prepared a set of CS and CT samples on glass substrates to compare the dissolution behavior. The weight of the sample m_{swell} (sample + substrate) was monitored after a certain immersion time in the water for each sample, and the mass difference to the substrate (m_{glass}) was calculated. The results of this test are shown in **Figure 2a**. The mass difference is strongly increasing for the CS film within the first 20 min of immersion. During the experiment, a strong swelling of the film can be observed, and we attribute the increase in mass to this swelling. Also, a mass increase can be observed for the CT film, but this increase is much less pronounced. For longer immersion times, the mass of the CS film starts to decrease, indicating dissolution or detachment of the film. After 90 min of the experiment, only a minor fraction is left. The last data points in **Figure 2a** were recorded after drying the samples overnight. The experiment reveals that the CT film is completely recovered, and the initial mass is restored (dashed line), while the CS film was completely removed during the experiment.

The significant differences between CS and CT are further highlighted by water contact angle measurements in a sessile drop experiment (**Figure 2b**). The contact angle of water strongly decreases upon transformation to CT and presents a more hydrophilic surface despite its increased water resilience. We noticed after the experiment that the sample surface of the pristine CS film could not be recovered due to the partial dissolution of the film. **Figure 2c** shows a time series of photographs showing the samples before and after water droplet exposure. In contrast, the acetylated film can fully recover to its original state.

2.2. Optical Characterization

To test the cooling potential of our films, we chose a reflective silver mirror as an underlying substrate to ensure high solar

reflectivity. The material's absorption (and consequently emission) properties strongly depend on the thickness of the film. For comparison, we prepared samples with different thicknesses and measured the broadband optical properties between 0.25 and 18.2 μm (**Figure 3a**). This wavelength range covers the entire solar and the mid-IR range. The absorptance was calculated from integrated reflectance measurements considering energy conservation with $1 - \text{reflectance}$. Transmittance can be neglected due to the underlying silver mirror substrate. As a reference, we plotted the absorptance of the plain mirror substrate (black line).

For comparison, an AM 1.5 solar emission spectra and the atmospheric transmittance regions are displayed in the background. Increasing film thickness from 0.76 to 34.6 μm has only minor effects within the solar spectral region. The strong absorption toward UV wavelengths is a combination of absorption of the underlying Ag substrate and CS itself since the absorptance increases with material thickness, but it is also present for the plain Ag substrate. Toward the NIR regime, more pronounced solar absorption occurs for the thicker sample. We calculated the overall solar absorption based on the collected spectra and the displayed AM 1.5 solar spectrum (details in experimental). We found solar absorption of 3.1% and 6.6% for the thin and thick samples, respectively. Based on the low solar absorption, both samples are capable of exhibiting below ambient radiative daytime cooling.

In the IR region, distinct peaks are visible for the thin sample, which are only partially located within regions of atmospheric transparency. With increasing thickness, the absorptance is more comparable to a broadband emitter. We expect a cooling power characteristic between the selective and broadband cases for thin samples.^[3a] Besides the absorptance in the UV region, the silver mirror substrate also shows minor absorptance in the mid-IR region. Those can be attributed to the presence of a glassy protection layer on the mirror surface.

To further elucidate the cooling characteristics of the two samples, we calculated the theoretical temperature reduction based on the measured absorptance (**Figure 3b**). Details about the calculations can be found in the Experimental Section. In short, we considered an AM 1.5 solar spectrum with irradiation of 1000 W m^{-2} , the atmospheric transmission spectrum modeled with Modtran, an ambient temperature of 25 $^{\circ}\text{C}$, and a non-radiative heat

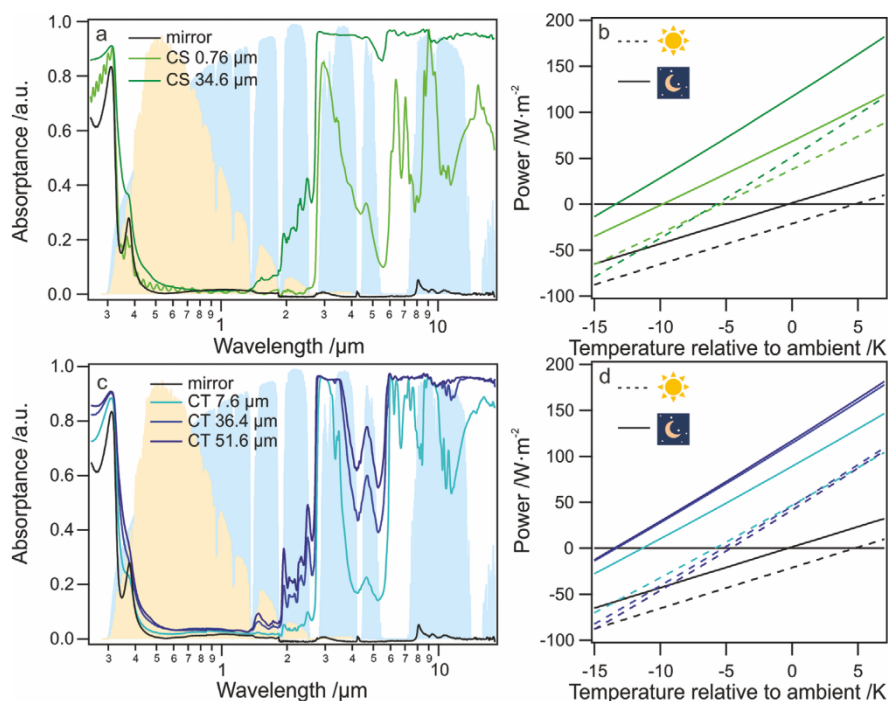


Figure 3. Absorbance of a) chitosan films (CS) and c) chitin films (CT) with different thicknesses on silver mirror substrates. As a reference, the absorbance of the plain silver mirror is shown. For comparison, the atmospheric transmittance (blue) and an AM 1.5 solar spectrum (yellow) are shown in the background. Calculated cooling power as a function of temperature below ambient for b) CS films and d) CT films with different thicknesses for daytime (dashed lines) and nighttime (solid lines). The intersection at zero cooling power represents the equilibrium temperature below ambient that can be reached.

transfer coefficient of $h = 4.4 \text{ Wm}^{-2} \text{ K}^{-1}$. For the daytime case (dashed lines), we found that both samples should reach almost comparable temperatures. In contrast, for the nighttime case (solid lines), the thicker sample should reach lower equilibrium temperatures (temperature at $P = 0 \text{ Wm}^{-2}$). Our calculations further reveal that the silver substrate is expected to heat above ambient temperature during the daytime. However, in combination with the CS films, both samples reach below ambient temperatures in the calculations.

We also prepared a set of CT films and measured the absorbance. Unfortunately, the direct preparation and reaction on the mirror substrates were unsuccessful since the films deformed and detached during the reaction. We, therefore, prepared the films on separate glass plate substrates, performed the reaction, and attached the CT films afterward to the mirror substrates. Note that we did not succeed in the preparation of very thin ($<5 \mu\text{m}$) CT films of sufficient macroscopic size because they ruptured during the transfer process. The absorbance spectra of the CT films (Figure 3c) are comparable to the previously discussed CS spectra. Especially the two films with $\approx 35 \mu\text{m}$ thickness show a similar low solar absorbance with 6.6% for CS and 6.9% for CT, respectively. A direct comparison of spectra collected from the films without the silver substrate is shown in Figure S2, Supporting Information.

We also calculated the expected cooling performance for CT films (Figure 3d) and found that during nighttime operation,

thicker CT films reach similar below ambient temperatures as found for CS. All CT samples are expected to reach similar below ambient temperatures during the daytime.

2.3. Passive Cooling Properties

To confirm the calculated cooling performance, we conducted a rooftop experiment with the CS samples on mirror substrates and measured the temperature over a full day and night cycle (from 09:30, 9th to 08:00, 10th of July 2022, University of Bayreuth, Bayreuth, Germany). The setup is shown in Figure 4a and Figure S3, Supporting Information. We used polystyrene foam insulation to reduce conductive losses to the surrounding air and an LDPE cover foil to reduce convective losses, respectively. The entire setup was covered with Al foil to reflect solar radiation. The sample (Ag mirror with coated CS layer, Figure 4b) was placed on a thin copper plate inside the Styrofoam chamber, ensuring a good temperature distribution, which was monitored with a thermocouple directly at the underside of the copper plate.

The resulting temperature measurements (Figure 4c) confirm a below-ambient temperature for both samples for the nighttime and daytime cases. The ambient temperature is measured in a reference box without convective losses and without any other optical components other than the styrofoam container and the LDPE cover. Comparable to the silver mirror reference, we

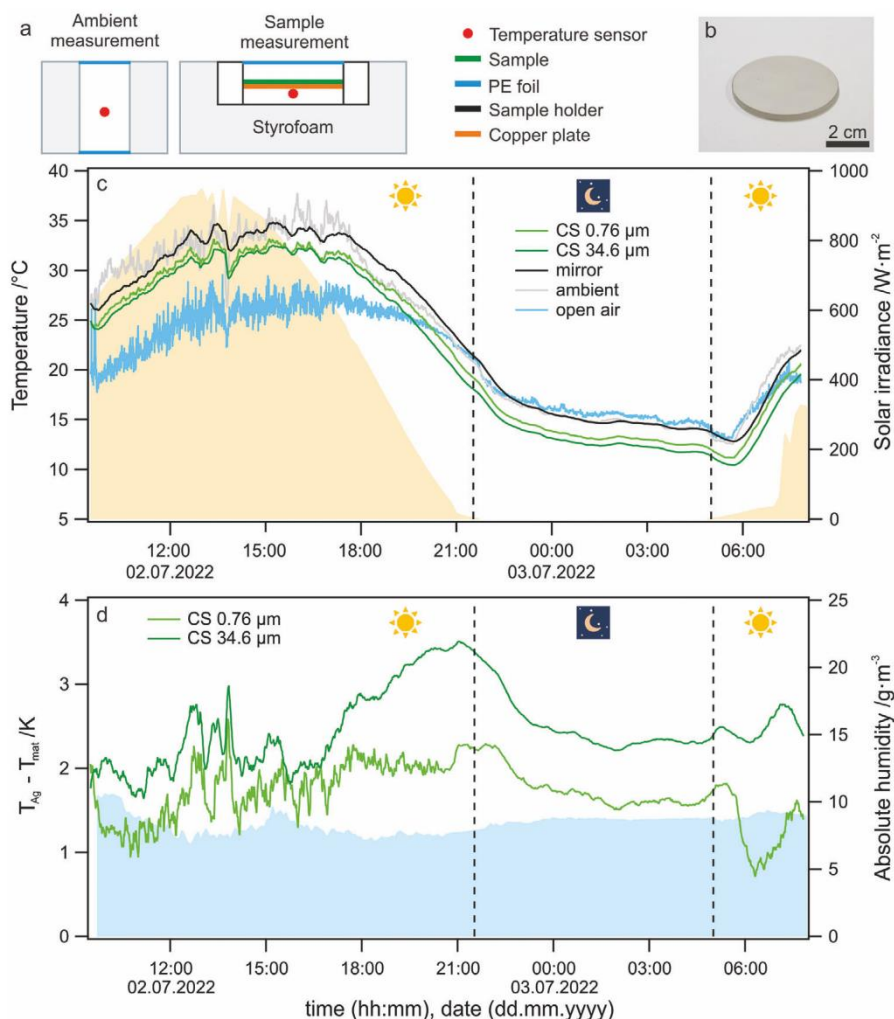


Figure 4. a) Scheme of the measurement environment of the ambient reference and the passive cooling sample temperature. The sample (dark green line) is a layered construction with CS being directly deposited on a quartz glass substrate coated with a silver layer shown in b). The sample is placed on a copper plate (orange line) to ensure an even temperature distribution. The temperature measurement of the sample is conducted at the underside of the copper plate. c) Temperature measurement for CS samples of different thicknesses on mirror substrates over a day and night cycle. A plain mirror substrate, the ambient temperature, and the open air temperature are shown as references. The solar irradiance during the measurement is displayed in the background. d) Temperature difference of the CS samples compared to the plain silver mirror over the entire measurement period. In the background, the absolute humidity (blue) during the measurement is shown, confirming constant atmospheric conditions.

observe a temperature increase during the daytime of about 8 °C relative to the open-air temperature. We attribute this to parasitic solar absorption by the sample holder and a resulting greenhouse effect within the measurement and reference chamber.^[25] The Ag mirror absorption in the UV range (Figure 3a,c) apparently has a minor effect on the temperature in the sample chamber since the ambient and Ag mirror reference temperature coincide. Considering the CS coated samples, we observe that the thicker (more broadband emitter) sample reaches lower overall temperatures, indicating that the additional cooling power gained with increasing thickness is outweighing the solar absorption (as discussed in Section 2.3). This trend is in line with the expect-

tation based on the calculation in Figure 3b). We attribute the quantitative difference between the calculation and experiment to the actual setup's unknown non-radiative heat loss coefficient and the additional heat input caused by the aforementioned greenhouse effect within the measurement box. Additionally, we calculated the experimental temperature difference between the samples and the silver mirror reference (Figure 4d) to highlight the contribution of the CS layers. Both samples are colder than the mirror, and the thicker sample reaches up to ≈3.5 °C lower temperatures. We calculated the absolute humidity from relative humidity measurements, which remained almost constant for the entire measurement duration. The higher variability of the

temperature reduction relative to the silver mirror reference during daytime is, consequently, caused by subtle changes to the solar radiance influx on the cooling films.

Based on the optical similarity between CS and CT film (see Figure 3a,c) one can expect a comparable cooling performance in the case of CT films. However, the direct measurement of the temperature reduction is affected by the increased brittleness and detachment of the CT film, which renders accurate temperature measurements difficult in this case.

3. Conclusion

In conclusion, we outlined the potential of CS and CT as biocompatible polymers for passive cooling applications. Therefore, we presented how CS films of different thicknesses can be produced from a slightly acidic aqueous solution. We demonstrated that the films can be converted to CT within the solid state. We confirmed the selective *N*-Acetylation of CS with solid-state ^{13}C CP MAS NMR spectroscopy and FTIR-spectroscopy and determined the degree of acetylation. Our presented approach can evaluate the DA even when residual free acetic acid remains in the sample. We further show that the conversion to CT strongly enhances the film's water resistance, a property especially important for outdoor applications as passive cooling material. To evaluate the passive cooling potential, we used silver mirror substrates as reflectors and measured the absorption properties of the films with UV-vis and FTIR-spectroscopy. CS and CT have very similar optical properties and excel with low solar absorptance in combination with good IR-emission. Based on the optical properties, we calculated the potential cooling power and found that both materials can show below ambient radiative daytime cooling without adding fillers. We demonstrate the cooling potential of CS in a field test and measure reduced temperatures compared to the plain silver mirror for day and nighttime. We believe that these natural polymers expand the toolbox of available materials to realize passive cooling systems. Especially factors like abundance, water processability, biocompatibility, and biodegradability are clear advantages, and we encourage other researchers to utilize those.

4. Experimental Section

Materials: CS (medium molecular weight, Aldrich), acetic anhydride (>99% for synthesis, Carl Roth chemicals), glacial acetic acid (Merck), and sodium hydroxide (Sigma Aldrich) were used without further purification. Methanol (VWR chemicals) was dried over a molecular sieve with a pore diameter of 3 Å before use. Protected round silver mirrors (2" Ø, Thorlabs)

Preparation of Films: Films with different thicknesses were produced by drying a certain amount of solution on a glass or silver mirror substrate in air. For the formation of thick films, 3–6 g of a 3 wt% solution of CS in diluted acetic acid (1 v%) were poured on the substrate and left to dry. For thin films, the solution was spread by doctor blading with a slit size of 400 µm. To access intermediate thicknesses, the doctor blading process was repeated upon drying of a previous layer. A 0.79 µm CS film was produced by spin coating of a 3 wt% solution on the silver mirror substrate at 3000 rpm for 90 s and left to dry in air.

Acetylation to CT: An acetylation reaction was performed with a procedure described by Hirano et al.^[19] to increase the degree of *N*-acetylation. Before the reaction, the CS films were washed with 0.5 M NaOH dissolved in methanol to remove acetic acid, followed by pure methanol to remove

the excess base. The film was immersed in methanol, and acetic acid anhydride was added (5 mol/mol Glucosamine) and stirred overnight. The films were washed with 0.5 M NaOH solution in methanol and pure methanol and then dried with compressed air. The resulting films were stored in a desiccator over saturated NaCl solution in water for at least 1 h, with the aim to reduce mechanical stress within the film. The so-produced film was transferred to a silver mirror substrate (protected round silver mirror, Thorlabs) for the cooling experiments.

Optical Characterization: UV-vis spectroscopy was performed with a Cary 5000 spectrometer (Agilent Technologies, Germany) for the wavelength range from 250–2500 nm. The total reflectance was measured with an integrating sphere accessory (Labspheres) at the respective port of the sphere. As a reference, a Spectralon white standard (Labspheres) was used. The absorptance of the samples was calculated considering energy conservation with $1 - \text{reflectance}$. Transmittance can be neglected because the silver mirror prevents any light transmission. The relative solar absorptance was calculated by multiplication of the measured absorptance $A(\lambda)$ with the solar radiance of the AM 1.5 spectrum $I_{\text{AM1.5}}(\lambda)$ and divided by the total radiance $\frac{A(\lambda) \cdot I_{\text{AM1.5}}(\lambda)}{I_{\text{AM1.5}}(\lambda)}$.

FTIR spectroscopy was performed with a Vertex 70 spectrometer (Bruker) combined with a gold-coated integrating sphere accessory (A562, Bruker). The reflectance was measured in the wavelength range from 1.33–18.3 µm at the respective port of the sphere. As a reference, a gold mirror was used. The absorptance was calculated with $1 - \text{reflectance}$, neglecting transmission due to the silver mirror below the samples.

Degree of Acetylation: The acetylation reaction was confirmed by ATR-FTIR spectroscopy using a Platinum ATR diamond accessory (A225/Q, Bruker) in combination with a Vertex 70 IR spectrometer (Bruker).

Solid State NMR Spectroscopy: The degree of acetylation of the CS samples was monitored via ^{13}C CP MAS NMR spectroscopy. The film samples were ground with the CryoMill SPEX CertiPrep 6750 (C3 Prozess- und Analysetechnik) and packed into 3.2 mm zirconium rotors. The spectra were recorded using a Bruker Avance-III HD spectrometer operating at a B_0 field of 9.4 T ($\nu_0(^1\text{H}) = 400.01$ MHz and $\nu_0(^{13}\text{C}) = 100.62$ MHz), a 3.2 mm triple resonance probe (Bruker) and a spinning speed of 13.75 kHz. The used pulse sequence consisted of presaturation pulses, a proton 90° pulse ($\nu_{\text{nut}}(^1\text{H}) = 100$ kHz), and a ramped ^1H - ^{13}C CP sequence ($\nu_{\text{nut}}(^{13}\text{C}) = 41$ kHz and 47 kHz $\leq \nu_{\text{nut}}(^1\text{H}) \leq 67$ kHz) with a contact time of 1.0 ms. This contact time was chosen for semi-quantitative measurements according to Duarte et al.^[22] During acquisition, proton broadband decoupling with a spinal-64 sequence ($\nu_{\text{nut}}(^1\text{H}) = 70$ kHz) was applied. The spectra were referenced to tetramethylsilane (TMS) using the secondary standard adamantane. The signal assignment was performed according to the literature^[22,26] and was aided by ^{13}C NMR prediction packages included in ChemSketch (ACD/Labs). To deconvolute the spectra with pseudo-Voigt profiles, the simulation package SOLA, included in TopSpin 3.2 (Bruker), was used. After deconvolution (Table S1, Supporting Information), the DA was given by the ratio of methyl carbons (CH_3) to CS repeating units. One CS repeating unit consisted of 6 carbons, thus the DA was calculated as follows.

$$\text{DA} = \frac{n(\text{CH}_3) \times 6}{n(\text{backbone})} \quad (1)$$

Water Contact Angle: The water contact angle was measured with a Contact Angle System OCA (DataPhysics Instruments GmbH) in sitting drop geometry. A 10 µL droplet was placed on the solid/air interface, and a picture was collected from side view with a camera. The contact angle was determined graphically at the three interface (solid/liquid/gas) contact points.

Calculation of Passive Cooling Performance: The calculated cooling power was based on the measured optical properties. Following the approach presented previously,^[27] an AM1.5 solar spectrum and an atmospheric transmittance spectrum generated for the measurement location (Bayreuth) using Modtran were employed. The non-radiative heat transfer coefficient was assumed to be $4.4 \text{ W m}^{-2} \text{ K}^{-1}$, while the atmospheric temperature was taken as 298.15 K. The angle-dependent emissivity is,

furthermore, considered to be Lambertian diffuse. All integrations were done using the trapezoidal integration method in Matlab. As functions inside the integrals need to have the same energy spacing to perform numerical integration, the sun's and atmosphere's spectral radiative powers were adapted to the spacing of the measured emissivity because they were available in higher resolution. This adaptation was made using the 1D data interpolation method in Matlab.

Outdoor Passive Cooling: The rooftop experiments were conducted in a self-built measurement setup on the roof of a four-floor building at the university of Bayreuth (Germany) under a clear sky. The samples and mirror reference were placed in a 3D printed sample holder (acrylonitrile butadiene styrene) on top of a copper plate for temperature distribution. A Pt100 thermocouple below the copper plate was used for temperature recording with a digital multimeter (DAQ6510, Tektronix, Germany) every 5 s. The sample holder was placed in a Styrofoam box for thermal insulation to the surroundings, and an LDPE foil was used to cover the sample and reduce convection. The entire Styrofoam box was covered with mylar aluminum foil to ensure high solar reflectance. The ambient temperature was recorded by a Pt100 thermocouple enclosed in a similar Styrofoam box with LDPE foil covered on top and bottom to allow sunlight transmission but include the parasitic heating within the box in the ambient reference measurement. The weather data were obtained from the weather station at the University of Bayreuth (Ecological-Botanical Garden, 400 m away from the experiment).

The relative humidity RH was tracked next to the setup with a temperature logger (LOG220, DOSTMANN electronic GmbH). The absolute humidity AH was calculated with RH in % and the ambient temperature T_{amb}

$$\text{in } ^\circ\text{C with AH} = \frac{6.112 \cdot e^{\frac{17.67 \cdot T_{amb}}{T_{amb} + 243.5}} \cdot \text{RH} \cdot 2.1674}{273.15 + T_{amb}}$$

Statistical Analysis: The FTIR spectra shown in Figure 1b were normalized to the most intense peak at $\approx 1000 \text{ cm}^{-1}$ for each spectrum, respectively. The full normalized spectra are shown in Figure S1, Supporting Information. The water contact angle presented in Figure 2b was determined by three separate measurements on the same substrate, and the presented value was mean \pm SD. The spectra shown in Figure 3a,c were calculated by $1 - \text{reflectance}$, without further statistical analysis. Figures 2a and 4c are raw data.

Supporting Information

Supporting Information is available from the Wiley Online Library or from the author.

Acknowledgements

The solar radiance data were kindly provided by Prof. Christoph Thomas. This project received funding from the European Research Council (ERC) under the European Union's Horizon 2020 research and innovation program (grant agreement no. 714968). A.M. and J.S. acknowledge funding by the Deutsche Forschungsgemeinschaft (DFG, German Research Foundation)—project number 391977956—SFB 1357, subproject C01. This project was also funded by the Deutsche Forschungsgemeinschaft (DFG, German Research Foundation)—491183248 and the Open Access Publishing Fund of the University of Bayreuth.

Open access funding enabled and organized by Projekt DEAL.

Conflict of Interest

The authors declare no conflict of interest.

Data Availability Statement

The data that support the findings of this study are available from the corresponding author upon reasonable request.

Keywords

absorption spectroscopy, broadband optical characterization, passive cooling, solid-state nuclear magnetic resonance spectroscopy, thermal emission

Received: November 11, 2022

Revised: January 5, 2023

Published online:

- [1] a) S. Catalanotti, V. Cuomo, G. Piro, D. Ruggi, V. Silvestrini, G. Troise, *Sol. Energy* **1975**, *17*, 83; b) B. Bartoli, S. Catalanotti, B. Coluzzi, V. Cuomo, V. Silvestrini, G. Troise, *Appl. Energy* **1977**, *3*, 267; c) C. G. Granqvist, A. Hjortsberg, *Appl. Phys. Lett.* **1980**, *36*, 139; d) C. G. Granqvist, A. Hjortsberg, *J. Appl. Phys.* **1981**, *52*, 4205.
- [2] A. P. Raman, M. A. Anoma, L. Zhu, E. Rephaeli, S. Fan, *Nature* **2014**, *515*, 540.
- [3] a) M. M. Hossain, M. Gu, *Adv. Sci.* **2016**, *3*, 1500360; b) Q. Zhang, S. Wang, X. Wang, Y. Jiang, J. Li, W. Xu, B. Zhu, J. Zhu, *Small Methods* **2022**, *6*, 2101379.
- [4] a) J. L. Kou, Z. Jurado, Z. Chen, S. Fan, A. J. Minnich, *ACS Photonics* **2017**, *4*, 626; b) L. Zhou, H. Song, J. Liang, M. Singer, M. Zhou, E. Stegenburgs, N. Zhang, C. Xu, T. Ng, Z. Yu, B. Ooi, Q. Gan, *Nat. Sustainability* **2019**, *2*, 718; c) S. Y. Jeong, C. Y. Tso, Y. M. Wong, C. Y. H. Chao, B. Huang, *Sol. Energy Mater. Sol. Cells* **2020**, *206*, 110296; d) S. Lin, L. Ai, J. Zhang, T. Bu, H. Li, F. Huang, J. Zhang, Y. Lu, W. Song, *Sol. Energy Mater. Sol. Cells* **2019**, *203*, 110135; e) J. Song, J. Seo, J. Han, J. Lee, B. J. Lee, *Appl. Phys. Lett.* **2020**, *117*, 094101.
- [5] a) J. Mandal, Y. Fu, A. C. Overvig, M. Jia, K. Sun, N. N. Shi, H. Zhou, X. Xiao, N. Yu, Y. Yang, *Science* **2018**, *362*, 315; b) P. Yang, C. Chen, Z. M. Zhang, *Sol. Energy* **2018**, *169*, 316; c) W. Huang, Y. Chen, Y. Luo, J. Mandal, W. Li, M. Chen, C. C. Tsai, Z. Shan, N. Yu, Y. Yang, *Adv. Funct. Mater.* **2021**, *31*, 2010334.
- [6] a) Y. Zhai, Y. Ma, S. N. David, D. Zhao, R. Lou, G. Tan, R. Yang, X. Yin, *Science* **2017**, *355*, 1062; b) Z. Cheng, F. Wang, H. Wang, H. Liang, L. Ma, *Int. J. Therm. Sci.* **2019**, *140*, 358; c) D. Chae, H. Lim, S. So, S. Son, S. Ju, W. Kim, J. Rho, H. Lee, *ACS Appl. Mater. Interfaces* **2021**, *13*, 21119; d) X. Li, J. Peoples, P. Yao, X. Ruan, *ACS Appl. Mater. Interfaces* **2021**, *13*, 21733.
- [7] a) E. Rephaeli, A. Raman, S. Fan, *Nano Lett.* **2013**, *13*, 1457; b) M. A. Kecebas, M. P. Menguc, A. Kosar, K. Sendur, *J. Quant. Spectrosc. Radiat. Transfer* **2017**, *198*, 179; c) N. W. Pech-May, T. Lauster, M. Retsch, *ACS Appl. Mater. Interfaces* **2021**, *13*, 1921.
- [8] a) T. Li, Y. Zhai, S. He, W. Gan, Z. Wei, M. Heidarinejad, D. Dalgo, R. Mi, X. Zhao, J. Song, J. Dai, C. Chen, A. Aili, A. Vellore, A. Martini, R. Yang, J. Srebric, X. Yin, L. Hu, *Science* **2019**, *364*, 760; b) Y. Tian, H. Shao, X. Liu, F. Chen, Y. Li, C. Tang, Y. Zheng, *ACS Appl. Mater. Interfaces* **2021**, *13*, 22521; c) Y. Chen, B. Dang, J. Fu, C. Wang, C. Li, Q. Sun, H. Li, *Nano Lett.* **2021**, *21*, 397.
- [9] a) J. Jaramillo-Fernandez, H. Yang, L. Schertel, G. L. Whitworth, P. D. Garcia, S. Vignolini, C. M. Sotomayor-Torres, *Adv. Sci.* **2022**, *9*, 2104758; b) J. Li, Y. Liang, W. Li, N. Xu, B. Zhu, Z. Wu, X. Wang, S. Fan, M. Wang, J. Zhu, *Sci. Adv.* **2022**, *8*, eabj9756.
- [10] S. H. Choi, S. W. Kim, Z. Ku, M. A. Visbal-Onufrak, S. R. Kim, K. H. Choi, H. Ko, W. Choi, A. M. Urbas, T. W. Goo, Y. L. Kim, *Nat. Commun.* **2018**, *9*, 452.
- [11] N. N. Shi, C. C. Tsai, F. Camino, G. D. Bernard, N. Yu, R. Wehner, *Science* **2015**, *349*, 298.
- [12] M. Burrelli, L. Cortese, L. Pattelli, M. Kolle, P. Vukusic, D. S. Wiersma, U. Steiner, S. Vignolini, *Sci. Rep.* **2014**, *4*, 6075.
- [13] M. Wang, Y. Ma, Y. Sun, S. Y. Hong, S. K. Lee, B. Yoon, L. Chen, L. Ci, J. D. Nam, X. Chen, J. Suhr, *Sci. Rep.* **2017**, *7*, 18054.

- [14] F. Croisier, C. Jérôme, *Eur. Polym. J.* **2013**, *49*, 780.
- [15] a) Z. Jia, I. Sukker, M. Müller, H. Schönherr, *ACS Appl. Mater. Interfaces* **2018**, *10*, 5175; b) Z. Jia, M. Müller, T. L. Gall, M. Riool, M. Müller, S. A. J. Zaat, T. Montier, H. Schönherr, *Bioact. Mater.* **2021**, *6*, 4286.
- [16] L. B. Mao, H. L. Gao, H. B. Yao, L. Liu, H. Cölfen, G. Liu, S. M. Chen, S. K. Li, Y. X. Yan, Y. Y. Liu, S. H. Yu, *Science* **2016**, *354*, 107.
- [17] J. Y. Chang, H. S. Han, C. Y. Wang, L. S. Long, L. P. Wang, M. Sheremet, I. Miroshnichenko, Y. B. Chen, *Sol. Energy Mater. Sol. Cells* **2020**, *216*, 110707.
- [18] J. Liu, A. Moreno, J. Chang, M. Morsali, J. Yuan, M. H. Sipponen, *ACS Appl. Mater. Interfaces* **2022**, *14*, 12693.
- [19] S. Hirano, M. Zhang, B. G. Chung, S. K. Kim, *Carbohydr. Polym.* **2000**, *41*, 175.
- [20] M. L. Duarte, M. C. Ferreira, M. R. Marvão, J. Rocha, *Int. J. Biol. Macromol.* **2002**, *31*, 1.
- [21] W. M. Facchinatto, D. M. dos Santos, A. Fiamingo, R. Bernardes-Filho, S. P. Campana-Filho, E. R. de Azevedo, L. A. Colnago, *Carbohydr. Polym.* **2020**, *250*, 116891.
- [22] M. L. Duarte, M. C. Ferreira, M. R. Marvão, J. Rocha, *Int. J. Biol. Macromol.* **2001**, *28*, 359.
- [23] A. Mael, B. Pötzschner, N. Meides, R. Siegel, P. Strohschl, J. Senker, *RSC Adv.* **2022**, *12*, 10875.
- [24] W. Kolodziejski, J. Klinowski, *Chem. Rev.* **2002**, *102*, 613.
- [25] a) D. Chae, M. Kim, P. H. Jung, S. Son, J. Seo, Y. Liu, B. J. Lee, H. Lee, *ACS Appl. Mater. Interfaces* **2020**, *12*, 8073; b) S. Y. Jeong, C. Y. Tso, J. Ha, Y. M. Wong, C. Y. H. Chao, B. Huang, H. Qiu, *Renewable Energy* **2019**, *146*, 44.
- [26] S. F. Tanner, H. Chanzy, M. Vincendon, J. C. Roux, F. Gaill, *Macromolecules* **1990**, *23*, 3576.
- [27] K. Herrmann, T. Lauster, Q. Song, M. Retsch, *Adv. Energy Sustainability Res.* **2021**, *3*, 2100166.

Supporting Information

From Chitosan to Chitin: Bio-inspired Thin Films for Passive Daytime Radiative Cooling

Tobias Lauster, Anika Mauel, Kai Herrmann, Viktoria Veitengruber, Qimeng Song, Jürgen Senker, Markus Retsch*

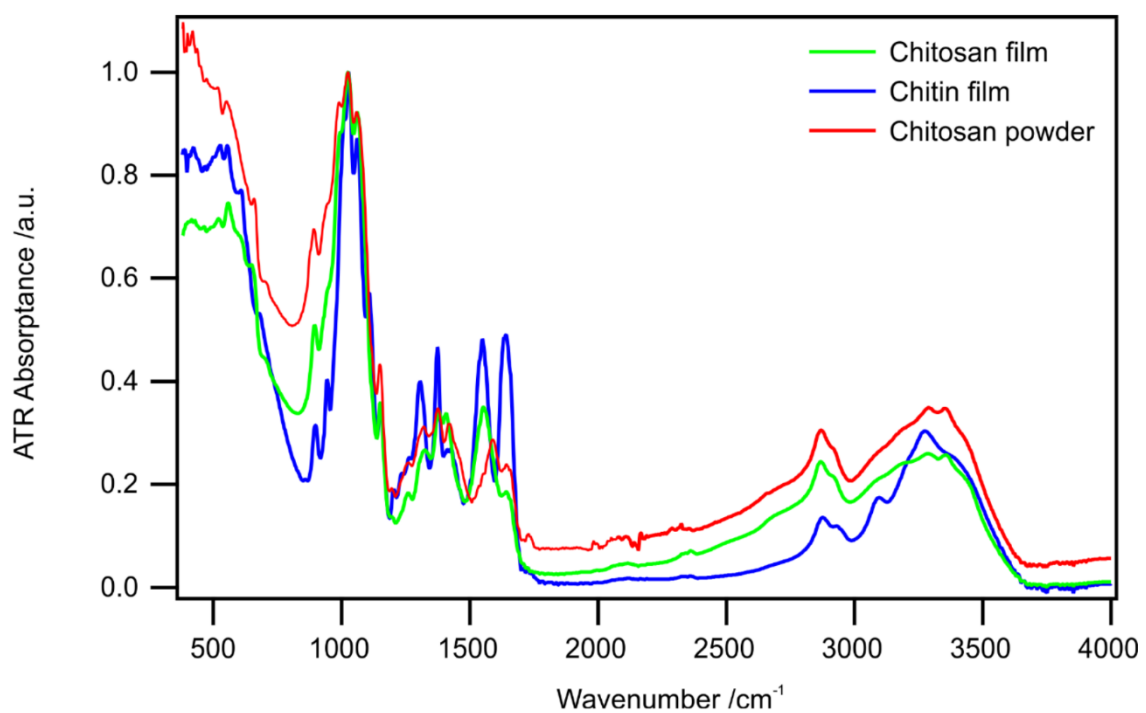


Figure S1. ATR-Absorbance of chitosan powder, a chitosan, and a chitin film. The spectra were normalized to the peak maximum at around 1000 cm⁻¹ for better comparability.

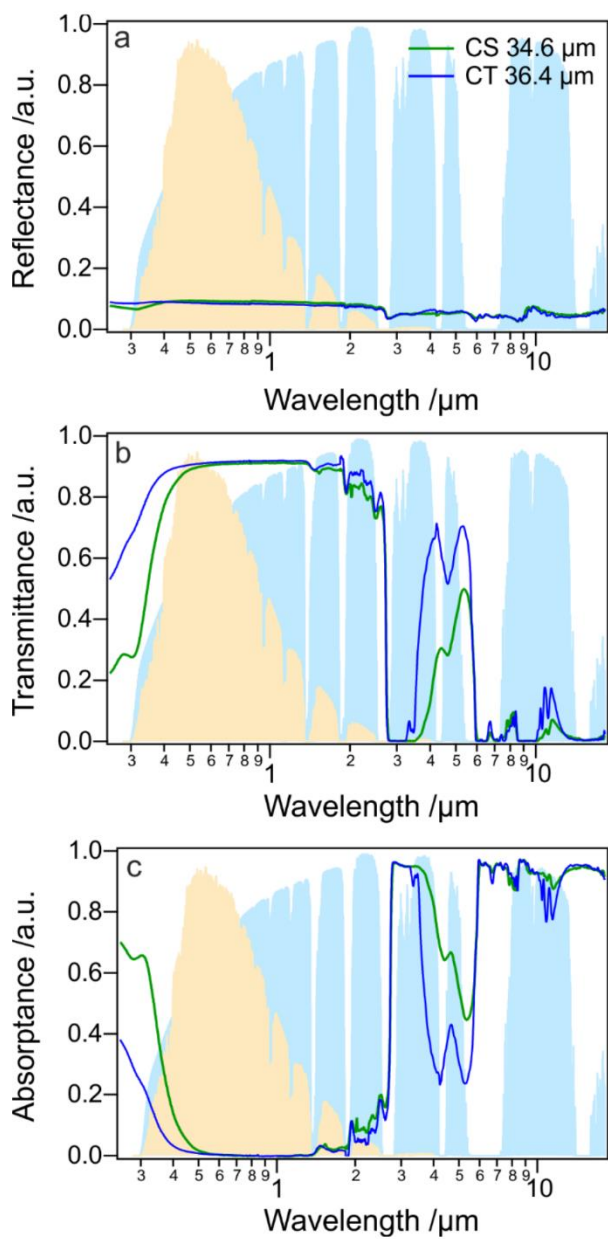


Figure S2 Reflectance (a), transmittance (b), and absorbance (c) spectra of a CS and CT film with comparable thickness. The spectra were collected from freestanding films without a silver substrate.

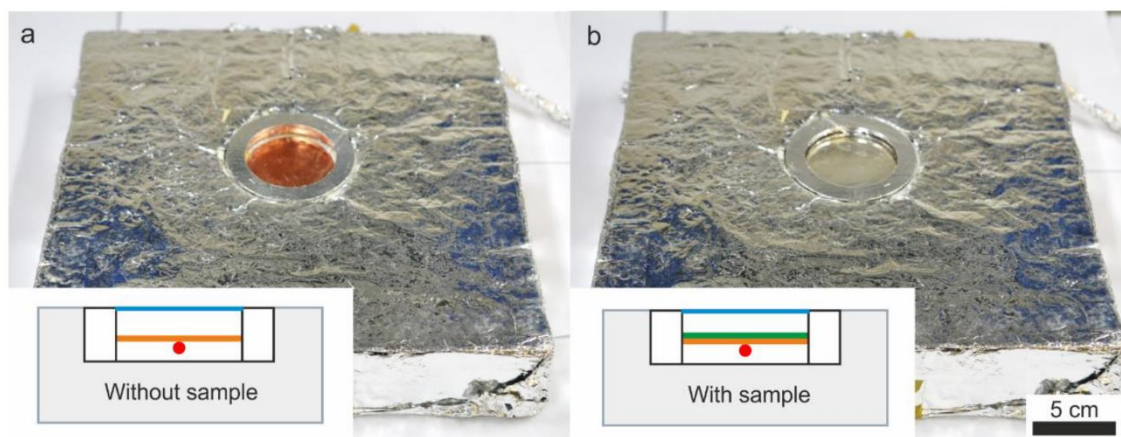


Figure S3 Photograph of the rooftop measurement setup (a) without sample and (b) with sample. The inset shows a schematic of the presented setup (as described in Figure 4 main text), respectively. The Styrofoam box is covered with Al foil to reflect sunlight and enclosed by PE foil to prevent convective losses. A copper plate visible in (a) is used to ensure good temperature distribution. The scale bar is 5 cm.

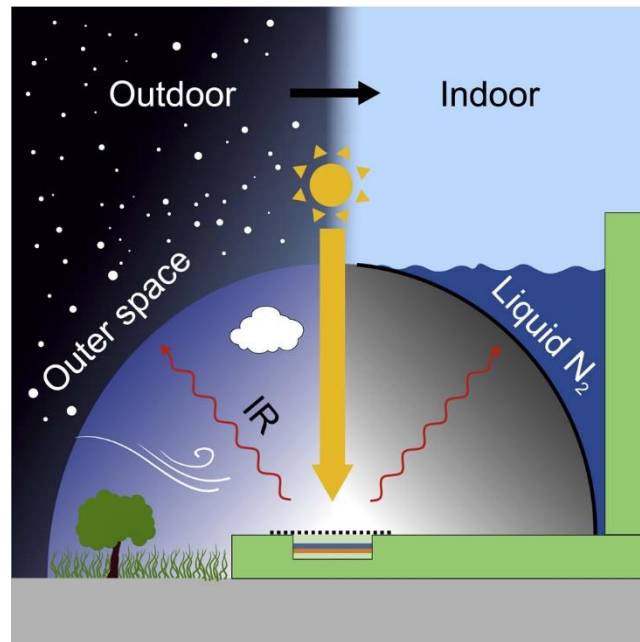
Table S1. Relative intensities I of the deconvoluted signals in the ^{13}C CP NMR spectra of chitosan powder, chitosan film, and chitin film samples. The sum of relative intensities of backbone carbons was normalized to six. Refinements were carried out with pseudo-Voigt lineshapes (Eq. 1) where δ_{iso} is the isotropic chemical shift, LB the line broadening, x the Gauss/Lorentz ratio, and I the relative intensity.

$$f(\delta) = I \cdot \left[(1 - x) \frac{2 \text{LB}}{4\pi \cdot (\delta - \delta_{\text{iso}})^2 + \pi \cdot \text{LB}^2} + x \cdot \frac{\sqrt{4 \ln(2)}}{\sqrt{\pi} \text{LB}} \cdot e^{-\frac{4 \ln(2)}{\text{LB}^2} (\delta - \delta_{\text{iso}})^2} \right] \quad (\text{Eq. 1})$$

Assignment	Acetyl group chitin		Chitosan and chitin backbone				Acetic acid	
	C=O	CH ₃	C1	C2	C3 + C4 + C5	C6	C=O	CH ₃
Shift	174 ppm	23 ppm	105 ppm	57 ppm	71; 83 and 75 ppm	61 ppm	180 ppm	25 ppm
Chitosan powder	0.046	0.119	1.056	0.939	3.014	0.991	/	/
Chitosan film	0.063	0.105	0.985	0.97	3.192	0.853	0.083	0.273
Chitin film	0.508	0.912	0.982	0.718	3.078	1.221	/	/



8.A tailored indoor setup for reproducible passive daytime cooling characterization



Standardized test methods are urgently required to characterize the performance of passive daytime cooling materials in a reliable and reproducible way worldwide. Song et al. introduce a robust test setup that unites cool space, solar radiance and ambient environmental conditions in a compact indoor test setup with superior characterization performance.



Article

A tailored indoor setup for reproducible passive daytime cooling characterization

Qimeng Song,^{1,3} Thomas Tran,^{1,3} Kai Herrmann,¹ Tobias Lauster,¹ Maximilian Breitenbach,¹ and Markus Retsch^{1,2,4,*}

SUMMARY

Passive daytime cooling materials can lower global energy consumption owing to their autonomous cooling capability. Although a significant number of passive cooling materials have been developed recently, their performance characterization is still challenging. Field tests experience high variability due to uncontrollable changes in environmental conditions. Here, we design an indoor setup to characterize the performance of passive cooling materials reproducibly and independently of weather and season. Outdoor measurement conditions are approximated using a liquid-nitrogen-cooled aluminum dome, a solar simulator, and a wavelength-selective inverse sky-window filter. In contrast to outdoor measurements, the results of various reference materials show remarkable precision and repeatability. Additionally, the impact of solar light intensity and temperature on the passive cooling performance can be experimentally investigated. Our setup is a first step in the development of a standardized test method to bring accuracy, reproducibility, and comparability to the emerging field of passive cooling materials.

INTRODUCTION

Passive daytime cooling has emerged as a strong candidate to alleviate the global energy demand for cooling.^{1,2} It conveys heat from a material to outer space through the atmospheric window (8–13 μm) without external energy consumption. For an ideal daytime passive cooling performance, low absorption in the solar range (0.3–2.5 μm) and high emission over the mid-infrared (MIR) region is stringently required. In the last few years, advanced fabrication techniques have led to various novel materials, including photonically structured materials,^{3–5} hybrid composites,^{6–9} highly porous materials,^{10–13} and hierarchically structured materials.^{14–17} These classes of materials promote the development of devices for daytime passive cooling applications.

Two essential techniques are usually used to evaluate a material's passive cooling performance: optical spectroscopy and field testing.^{2,18} The former determines the spectral absorption of a material in both the solar and MIR regions. Utilizing a theoretical model based on energy balance considerations, the net passive cooling power of a material can be calculated. Li et al. introduced a simple figure of merit to fairly assess the performance of distinct cooling materials based on their optical properties.¹⁹ However, the comprehensive optical properties, including angle and temperature dependence, of a material, are rather hard to access, especially for complex materials, e.g., multilayer composites, self-adaptive metamaterials,^{20,21} and materials with irregular surface topography, making it difficult to achieve a precise comparison.

¹Department of Chemistry, Physical Chemistry I, University of Bayreuth, 95447 Bayreuth, Germany

²Bavarian Polymer Institute, Bayreuth Center for Colloids and Interfaces, and Bavarian Center for Battery Technology (BayBatt), University of Bayreuth, 95447 Bayreuth, Germany

³These authors contributed equally

⁴Lead contact

*Correspondence: retsch@uni-bayreuth.de
<https://doi.org/10.1016/j.xcrp.2022.100986>



During field testing, the steady-state temperature of a sample and its cooling power at ambient temperature are obtained. However, outdoor measurements are impressionable and uncontrollable, and the outcome strongly depends on measurement conditions,^{22,23} e.g., geographical location, solar intensity, ambient temperature, humidity, wind speed, and air pressure. The uncontrollable and unsteady atmospheric conditions limit the comprehensive characterization of passive cooling materials firstly, and replication of the measurement results secondly. Due to this challenge, different materials cannot be compared reasonably. Therefore, a comparable and standardized test method is urgently required to push the development of passive daytime cooling materials forward. In contrast to outdoor environments, an indoor setup is independent of weather conditions and provides a stable and controllable environment for passive cooling characterization. A simple indoor setup for passive cooling characterization was reported by Zhou et al.²⁴ By using liquid-nitrogen-cooled black aluminum foil as a heat sink, the nighttime passive cooling behavior of a PDMS film was imitated. However, their indoor setup did not include a light source. The characterization was thus limited to nighttime conditions. A similar setup was also constructed by Park et al. in a glovebox.²⁵ With applying a solar simulator, the characterization can be performed in the presence of solar light. Very recently, a hybrid refrigerative thermoelectric cooling system was built by Wong et al. to simulate the radiative cooling effect artificially under controlled conditions.²⁶ Their sophisticated setup achieved a reasonable accuracy (deviation of 17%–33%). Still, a repeatable and comprehensive characterization method for passive daytime cooling materials remains an enormous challenge.

In this work, we present a tailored indoor setup for comprehensively characterizing the performance of daytime passive cooling materials. The setup allows measurements with and without illumination of the sample, analogous to daytime and nighttime field testing, respectively. It consists of a liquid-nitrogen-cooled, hemispherical aluminum (Al) dome as a heat sink and an air mass (AM) 1.5 solar simulator as a light source. To the best of our knowledge, our method is the first indoor setup for the experimental characterization of passive cooling materials in both nighttime and daytime, with outstanding repeatability showcased for three distinct materials, namely, a silver (Ag) mirror, a polydimethylsiloxane (PDMS) film, and a graphite coating. Furthermore, our setup can experimentally determine the impact of environmental changes, such as the ambient temperature or solar irradiation intensity, on the material's cooling performance. Such a parametric investigation is unfeasible with field tests due to uncontrollable environmental conditions. Lastly, our indoor setup is robust and simple to build, opening a promising pathway to quantitatively compare passive cooling materials designed in different research groups.

RESULTS AND DISCUSSION

Indoor setup design

The most important aspects of passive cooling field testing that a feasible indoor setup must capture are (1) radiative heat transfer from the sample to outer space; (2) illumination of the sample by the sun; and (3) measurement at moderate temperatures. The realization of these key measurement aspects can each be attributed to distinct parts of the proposed setup.

Radiative heat transfer

The samples emit hemispherically to outer space, which acts as a heat sink, with a temperature of ~ 3 K. To imitate this behavior, we utilize a hemispherical Al dome with a diameter of 60 cm. The high thermal diffusivity of Al ensures a homogeneous

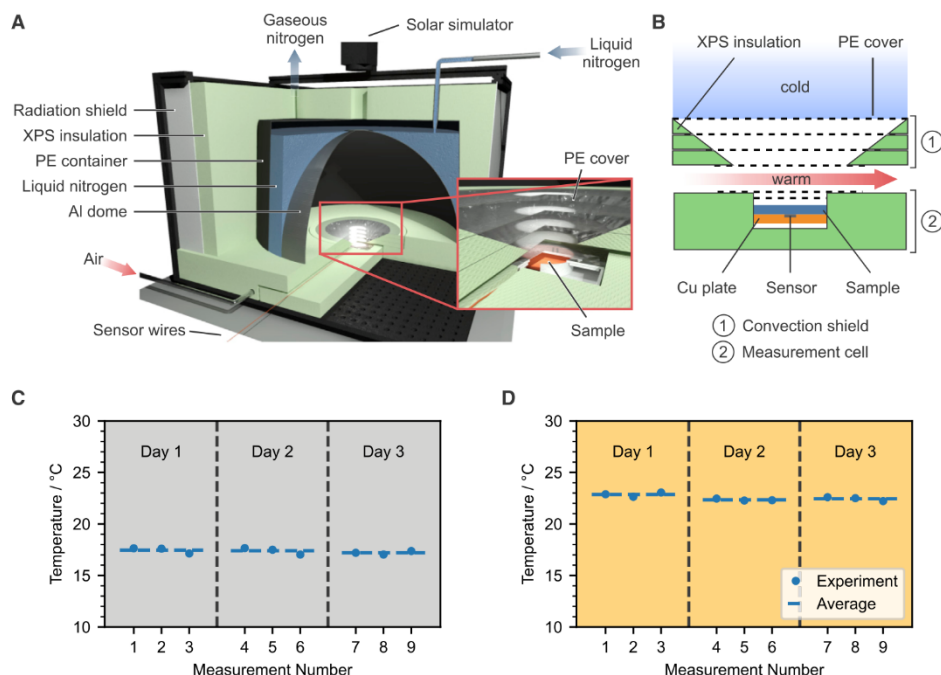


Figure 1. Indoor setup design and repeatability

(A and B) Schematic of the indoor setup for characterizing passive daytime cooling. A liquid-nitrogen-cooled aluminum dome imitates outer space, while a solar simulator illuminates the sample. A convection shield in combination with XPS minimizes non-radiative heat transfer between the dome and sample. Detailed schematic of the sample holder (B). A warm gas flow between the convection shield and the sample holder allows controlling the temperature inside the measurement cell.

(C and D) The steady-state temperature of an Ag mirror measured (C) w/o and (D) w/ solar light. Results show outstanding precision that cannot be achieved with outdoor measurements.

temperature distribution across the entire surface. The inner surface of the dome was coated with graphite to enhance its broadband absorption, thus resembling space as a heat sink for radiative heat transport. A polyethylene (PE) container is imposed on the hemisphere, creating a reservoir around the Al dome. Liquid nitrogen is filled inside this reservoir and cools the dome down to ~ 80 K. The entire setup is thermally insulated using extruded polystyrene foam (XPS, Styrodur, BASF) with a thickness of 8 cm to prevent cold loss. A schematic of the indoor setup is shown in Figure 1. Detailed dimensions and a photograph are in Figure S1. During the measurement, a small steady influx of liquid nitrogen compensates for all remaining heat losses to the environment. The sample is placed in a homemade measurement cell constructed by XPS under the center of the dome. Low-density polyethylene (LDPE) foils were applied above the sample to prevent convection.

Solar illumination

The average solar irradiation is generally presented by the AM 1.5 spectrum with a power of $\sim 1000 \text{ W m}^{-2}$, which is well established in the characterization of photovoltaic devices.¹⁸ In the laboratory environment, a solar simulator was placed directly on the top of the dome to provide AM 1.5 solar light with an illumination area of $5 \times 5 \text{ cm}^2$. The hole in the dome accounts for 0.8% of the total area seen by the sample and is thus negligible. The similarity between the light of the solar



simulator and the sun is shown in Figure S2. The light hits the sample at an angle of 8° to prevent back reflection into the solar simulator.

Sample temperature

The most challenging part of the indoor setup is to keep the sample at moderate temperatures while cooling the dome down to liquid nitrogen temperatures. The significant temperature difference across the short distance between the cooled dome and the sample holder naturally leads not only to the desired radiative heat transfer but also to undesired convection and conduction. Conduction is minimized by employing XPS insulation in combination with air gaps between the sample and the dome. Several LDPE foils (thickness $\sim 15 \mu\text{m}$), possessing a high solar and IR transparency, act as a convection barrier between the sample and the cold air inside the dome. These PE layers reduce the solar radiation intensity in the sample by 25%, due to absorption, reflection, and scattering. Furthermore, the reduction of the transmittance is angle-dependent (Figure S3). Previous reports showed that angles $<60^\circ$ have a dominant contribution to the emission of passive cooling materials.^{4,27,28} Therefore, the convection shield made from XPS and LDPE has a cone-shaped inner part, with a zenith angle of 60° to reduce the thermal loss (conduction and convection) area while marginally blocking the pathway of thermal radiation from the sample. Conductive heat transport from each gas compartment to the next would eventually cool the air below the convection shield. A heated flow of dry air offsets this effect. The constant airflow and the stable laboratory environment (Figure S4) ensure highly stable and reproducible experiments. Moreover, controlling the temperature by tuning the airflow temperature allows for experimentally setting the ambient temperature and elaborating the temperature-dependent performance of passive cooling materials.

Performance assessment

We investigated the repeatability of the indoor setup without (w/o) and with (w/) solar light. Multiple measurements of the steady-state temperature of an Ag mirror on different days are shown in Figures 1C and 1D. An SD of $\pm 0.24 \text{ K}$ and $\pm 0.26 \text{ K}$ was obtained from nine measurements over three consecutive days w/o and w/ light, respectively. This minor deviation shows that our indoor setup possesses outstanding repeatability in both nighttime and daytime-like measurements. When shining solar light with one sun power on the Ag mirror, the temperature increased by about 6 K. Since a LDPE foil is applied to the measurement cell to prevent convection, we thus attribute the temperature increase to the greenhouse effect caused by the parasitic solar light absorption of the Ag mirror and sample holder. This phenomenon has also been observed in outdoor measurements.^{29,30}

For outdoor measurements, an intuitive definition of the ambient temperature is the air temperature, which can be measured simultaneously with the sample temperature. For indoor measurements, however, the environment temperature results from the interplay between the cold dome and the warm gas flow. The large temperature gradient between the sample holder and the dome surface prevents a meaningful ambient temperature measurement in the vicinity of the actual sample. Therefore, an alternative way to define the ambient temperature is needed. Ag possesses a low emissivity in both the solar and IR region and, therefore, closely resembles the ambient temperature inside of the measurement cell without any major radiative heat losses or gains. We confirm this assumption by comparing the Ag mirror temperature with the ambient temperature in a field test (Figures 2A and 2B), where both temperatures almost overlap. The ambient temperature for the indoor setup is thus defined as the temperature obtained with an Ag mirror.

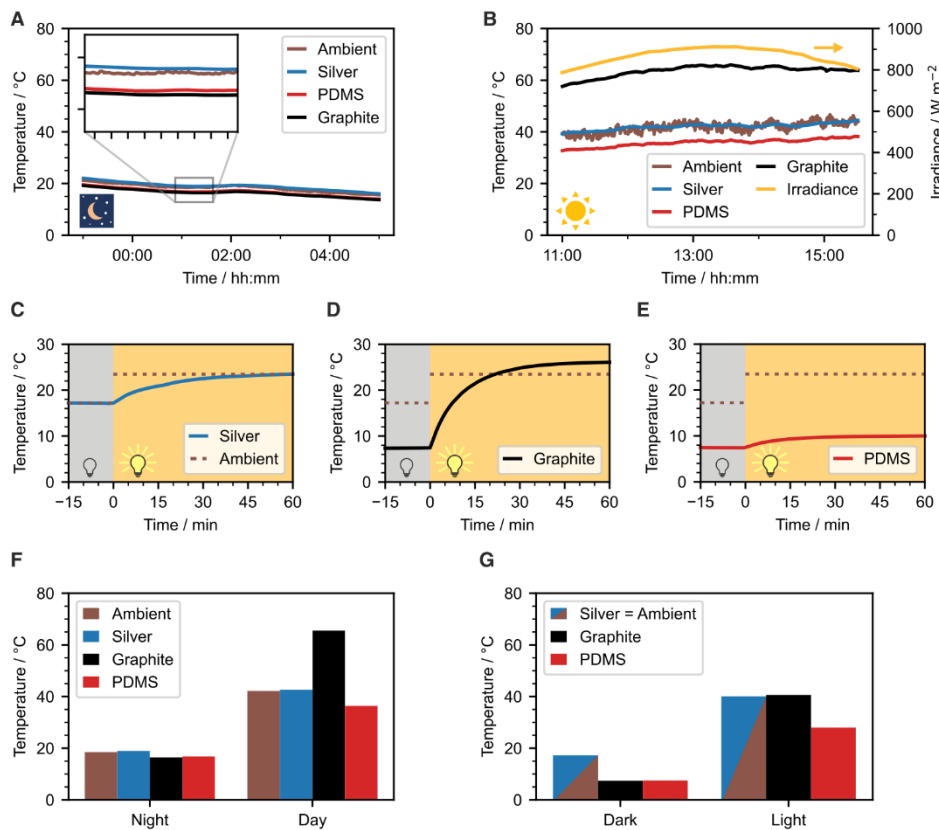


Figure 2. Performance assessment

(A and B) Outdoor rooftop measurement for the reference materials at (A) nighttime and (B) daytime. The measurement was carried out under a clear sky, on June 17–18, 2021 in Bayreuth, Germany.

(C–E) Indoor measurements of the (C) Ag mirror, (D) PDMS film, and (E) graphite coating. The turn-on point of the solar simulator was defined as 0 min. The dashed lines indicate the respective ambient temperatures for measurements w/o and w/ light. (F and G) The steady-state temperature of the reference materials in the (F) outdoor and (G) indoor measurements, respectively.

To verify the reliability of the indoor setup, we analyzed three reference materials: an Ag mirror, a PDMS film on an Ag mirror, and a graphite-coated silicon wafer. The chosen materials possess very different optical properties. Ag has a very low emissivity in both the visible and MIR regions, as outlined above. Furthermore, it has been widely applied to the backside of daytime passive cooling devices to minimize solar absorption.^{6,31} PDMS is a good passive cooling material due to its inherent selective emissivity in the MIR region. By combining the PDMS film and an Ag mirror, a practical daytime passive cooler is easily constructed.^{24,32} As the last sample, we use a graphite coating exhibiting broadband absorption in the solar and MIR regions. The spectral emissivity of all reference materials is shown in Figure S5.

Measurements of the reference materials were carried out w/o and w/ light irradiation (Figures 2C–2E). For measurements w/o light, a steady-state temperature of 17.2°C, 7.5°C, and 7.4°C was observed for the Ag mirror, the PDMS film, and the graphite coating, respectively. The PDMS film and graphite coating show a



steady-state temperature ~ 10 K lower than the Ag mirror. This is caused by the emissivity dependence of the radiative heat transfer. In contrast to the PDMS film and graphite coating, the Ag mirror shows negligible emissivity in the MIR region.

Subsequently, the solar simulator was used to simulate daytime measurements. After the reference materials reached a steady-state temperature in the dark, the solar simulator with one sun power was switched on. The temperature of all reference samples increased, and a new steady-state temperature was reached within 1 h. Compared with the Ag mirror (+6.3 K) and the PDMS film (+2.6 K), the temperature increase of the graphite coating was substantial (+18.8 K). The temperature increase of the Ag mirror can be explained by the absorption of the sample holder and the greenhouse effect. The different light response of the reference materials occurs because graphite has a significantly higher absorption in the solar regime. In addition, more than a 10 K difference in the steady-state temperature was observed between the Ag mirror and the PDMS film. The much lower final temperature of PDMS film demonstrates the good passive daytime cooling performance of the PDMS film agreeing with field testing in the literature.^{24,29}

To compare the results of the indoor experiment with the conventionally used field testing, outdoor measurements of the reference materials (Figures 2A and 2B) were conducted in both nighttime (23:00–05:00) and daytime (11:00–15:30). The setup for the outdoor measurements is shown in Figure S6. The PDMS film and graphite coating show similar steady-state temperatures at nighttime, ~ 2.5 K lower than the Ag mirror (Figure 2F). During the daytime, the Ag back mirror of the PDMS sample reflected most solar irradiation, while the PDMS transferred heat to outer space via IR radiation. Therefore, the PDMS film keeps its sub-ambient temperature even with an average solar intensity of around 850 W m^{-2} . In contrast, the graphite coating absorbed considerable solar energy and warmed up to $\sim 60^\circ\text{C}$.

Indoor measurements were performed with the respective ambient outdoor temperatures, 17°C and 40°C (Figure 2G). We observe that the absolute values of steady-state temperature for the reference materials obtained from indoor and outdoor measurements do not agree with each other. A daytime sub-ambient cooling by 6.2 K was observed from an outdoor measurement of a PDMS film, while 12.1 K was obtained from the indoor setup. We attribute this difference to two main contributions. First, the black-coated Al dome represents a broadband black body. More radiative heat can be transferred to it compared with the higher selectivity of the atmospheric window in outdoor measurements. Hence, the sub-ambient cooling power is increased. Second, the irradiance in the outdoor measurement is 900 W m^{-2} , while the irradiance in the indoor measurement is only 750 W m^{-2} . Consequently, the absorbance in the visible spectrum leads to a higher heat input for the outdoor case. Considering these effects, the values agree reasonably well. The reproducible values of the indoor setup allow for better comparison between different measurements as displayed in the literature. PDMS samples measured at different locations and times show an even larger range of temperature reductions. For instance, Zhou et al. observed a sub-ambient cooling of 11 K at Buffalo, NY, USA (February 2018).²⁴ Zhu et al. reported 3.3 K at Nanjing, China (November 2019),³³ and our previous study showed 7.4 K at Bayreuth, Germany (April 2020).²⁹ The disparity in the investigation of similar PDMS films from different groups is attributed to the distinct measurement conditions, e.g., ambient air temperature, humidity, and solar irradiation. Even subsequent measurements with the same setup from one group at a fixed location are prone to fluctuations, due to the equilibration time and the natural changes in temperature, humidity, and solar radiation. Consequently,

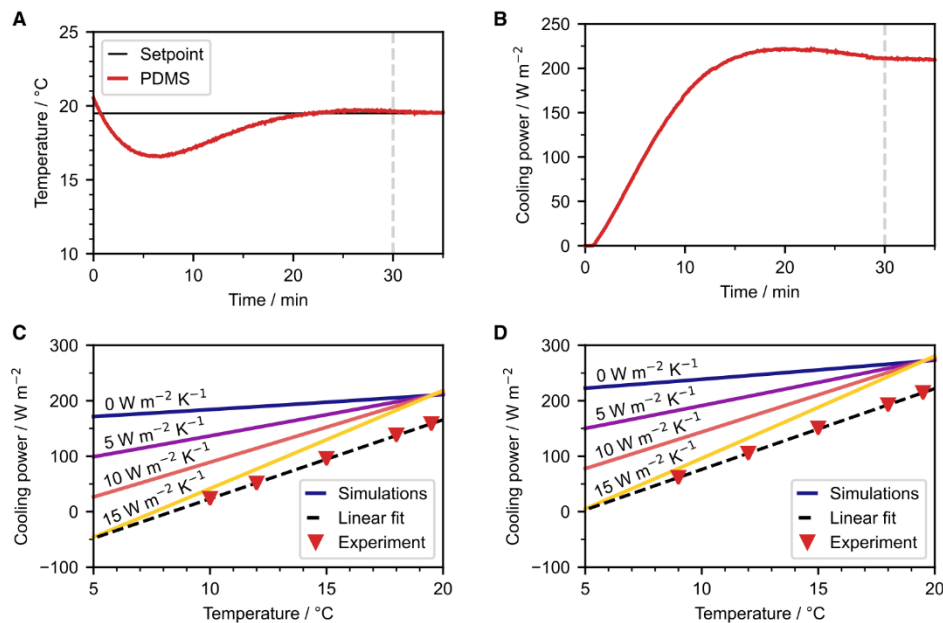


Figure 3. Comparison with numerical calculations

(A and B) Temperature tracking (A) and net cooling power measurement (B) of a PDMS film ($\sim 88.4 \mu\text{m}$) via the indoor setup. (C and D) A steady net cooling power could be obtained within 30 min. Numerically calculated net cooling power as a function of emitter temperature with different non-radiative heat transfer coefficients (h_c) for (C) a thin PDMS film ($\sim 19.2 \mu\text{m}$) and (D) a thick PDMS film ($\sim 88.4 \mu\text{m}$), based on the configuration of the indoor setup. The respective experimental values are measured and plotted to estimate h_c for our setup. Values of 11.6 and $11.2 \text{ W m}^{-2} \text{ K}^{-1}$ were obtained for the thin and thick PDMS samples, respectively. For the experiments, the setpoint was 19.5°C and solar light was excluded.

multiple tests are typically run simultaneously to allow for comparability among different samples. In contrast, the proposed indoor setup enables measurements with a predetermined condition and, thus, allows a quantitative comparison of measurements from different days.

Cooling power characterization

Besides the sub-ambient temperature that a passive cooling material can reach, its net cooling power is another important parameter for quantifying the cooling performance. The standard technique to measure the net cooling power is using a feedback-controlled electrical heater underneath the sample to maintain the ambient temperature. As a result, the recorded input heating power is equivalent to the net cooling power.⁴ However, the cooling power obtained from outdoor measurements, in most cases, fluctuates over time due to the unstable conditions, mainly solar intensity, wind speed, and cloud coverage. Hence, such outdoor measurements are typically carried out for many hours and merely reach a temporary steady-state condition, making quantification of the cooling power difficult.^{7,11,34} By contrast, a steady net cooling power can be measured with the presented indoor setup in a matter of minutes. The ambient temperature is set to the Ag mirror temperature determined under the same measurement condition. We assume that at this temperature, no non-radiative losses, i.e., convection and conduction, occur. As shown in Figures 3A and 3B, the net cooling power of a PDMS film ($\sim 88.4 \mu\text{m}$) was obtained within 30 min. The PDMS film exhibits a net cooling power of about 200 W m^{-2} at an ambient temperature of 19.5°C , w/o solar light. Compared with the net cooling



power of the PDMS-based passive cooling devices reported in the literature, i.e., up to $\sim 130 \text{ W m}^{-2}$,³¹ the value obtained from the indoor setup is relatively high. This is attributed to the absence of atmospheric thermal radiation outside of the sky-window range in the indoor setup.³⁵ Nevertheless, characterizing the passive cooling power with the indoor setup allows for a precise and defined measurement with a reasonably fast equilibration time.

For materials exposed to the clear sky, the net cooling power can be calculated with the radiative model, $P_{\text{cool}} = P_{\text{mat}} - P_{\text{sun}} - P_{\text{atm}} - P_{\text{nonrad}}$. Here, P_{mat} is the thermal irradiation power of the emitter, P_{sun} is the solar power absorbed by the material, P_{atm} is the absorbed power from the atmosphere, and P_{nonrad} is the absorbed power due to conduction and convection. P_{nonrad} can be expressed as $P_{\text{nonrad}} = h_c \cdot (T_{\text{atm}} - T_{\text{mat}})$, where h_c is the non-radiative heat transfer coefficient. For the indoor setup, the inner space is filled with nitrogen and the path between the sample and the dome is short. Thus, P_{atm} can be omitted and the equation can be simplified to $P_{\text{cool}} = P_{\text{mat}} - P_{\text{sun}} - P_{\text{nonrad}}$ and $P_{\text{cool}} = P_{\text{mat}} - P_{\text{nonrad}}$ for daytime and nighttime, respectively. It needs to be noted that h_c varies from measurement to measurement, because of the distinct measurement conditions, and the estimation of h_c has been widely conducted,^{4,36} whereas, it should not depend on the material optical properties.

To better understand our indoor setup and verify that h_c is indeed independent of the optical properties for all indoor setup measurements, we calculated the theoretical net cooling powers of PDMS films with various optical properties and compared them with the actual indoor measurements. The h_c -dependent net cooling power of PDMS films with two different thicknesses, 88.4 and 19.2 μm , was calculated via the radiative cooling model based on the indoor setup configuration. The model was thoroughly discussed in our previous work, which demonstrated the thickness dependence on optical properties and passive cooling performance.²⁹ The complex refractive index of PDMS films used in the calculation was obtained from the literature.^{37,38} To determine h_c of our indoor setup measurements, the net cooling powers of the PDMS samples were measured at five different temperatures. We observed a linear relationship between the sample temperature and the cooling power that agreed with the expected trend obtained from the numerical calculations (Figures 3C and 3D). Based on the linear fitting of the measurement points, we estimate h_c of the indoor measurements to be 11.6 and 11.2 $\text{W m}^{-2} \text{K}^{-1}$ for the measurements of thin and thick PDMS films, respectively (Figure S7). The consistent h_c value obtained from the indoor measurements with different samples proves the stability and reliability of the indoor setup. In addition, we observed a slight offset between the measured and calculated net cooling power. We attribute this to the approximations in the theoretical model, the adopted complex refractive index value from the literature,²⁹ and the uncertainty of the measurement.

Variation of environmental parameters

Solar irradiance and ambient temperature vary with time and location. They strongly influence the cooling capacity of passive daytime cooling devices. As shown in Figures 4A and 4B, solar irradiance changes from 0 to $\sim 950 \text{ W m}^{-2}$ during a summer day and ambient air temperature changes between about -10°C to about 35°C over a year in Bayreuth, Germany. How do temperature and solar radiance influence the cooling performance? In our indoor setup, the solar irradiance can be changed between 0 and 100% of one sun via the solar simulator. We, therefore, examined the sub-ambient cooling as well as the net cooling power of a graphite coating at various solar intensities, from 0% to 100%. As illustrated in Figure 4C, the temperature difference ($T_{\text{graphite}} - T_{\text{amb}}$) increased from about -10 K to $+10 \text{ K}$ with increasing solar

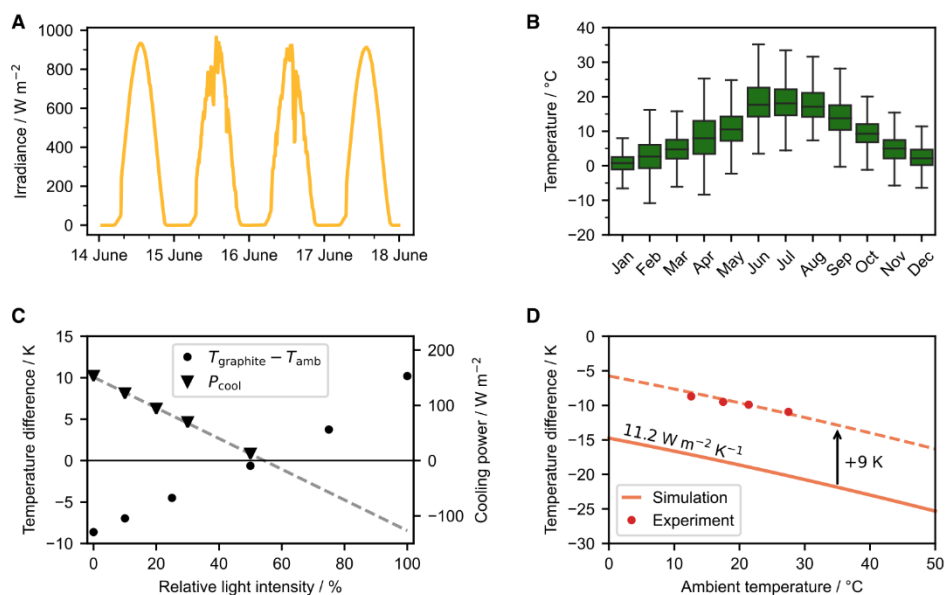


Figure 4. Variation of environmental parameters

(A) Solar irradiance over four days in Bayreuth, Germany.

(B) Ambient air temperature of different months in Bayreuth, Germany, over the last three years. The error bars represent the standard deviation of the data.

(C) Impact of solar intensity on the passive cooling performance of a graphite coating. The temperature difference ($T_{\text{graphite}} - T_{\text{amb}}$) and net cooling power (P_{cool}) show a linear trend when increasing the solar light intensity from 0% to 100% of one sun ($\sim 1000 \text{ W m}^{-2}$).

(D) The impact of ambient temperature (T_{amb}) on the cooling performance of a PDMS film. Both the simulation and experiment show that T_{amb} enhances the cooling performance leading to a decrease in the temperature difference ($T_{\text{PDMS}} - T_{\text{amb}}$).

intensity from 0% to 100%. Concomitantly, the net cooling power declined gradually. Moreover, the temperature difference and the net cooling power showed a linear trend with respect to the solar intensity.

The temperature controllable gas flow allows tuning of the ambient temperature in the measurement cell between 10°C and 35°C (Figure S8). The temperature dependence of blackbody radiation is well known. An increasing emitter temperature enhances the thermal irradiation, and, therefore, the cooling performance. We measured the steady-state temperature of a PDMS film ($88.4 \mu\text{m}$) at various ambient temperatures. We found that with increasing the ambient temperature, the cooling performance was also enhanced, as indicated by the increased sub-ambient cooling (Figure 4D). The sub-ambient cooling rose from 8.7 K to 11.0 K , with increasing the ambient temperature from 12.6°C to 27.5°C . We confirmed this temperature dependence by a numerical calculation with $h_c = 11.2 \text{ W m}^{-2} \text{ K}^{-1}$. Despite the offset between the experimental and theoretical values ($\sim 9 \text{ K}$), the trends agree well.

In general, passive cooling materials can be divided into two groups. The first group is selective emitters, which emit only at the atmospheric window ($8\text{--}13 \mu\text{m}$). These emitters transfer heat directly to outer space without interference from the atmosphere. The second one is broadband emitters. Broadband emitters emit not only at the atmospheric window but also outside, resulting in heat exchange with the atmosphere itself.³⁹ It is controversial which kind of emitter is better suited for passive cooling applications.^{31,40} In its current form, our setup is best suited to compare

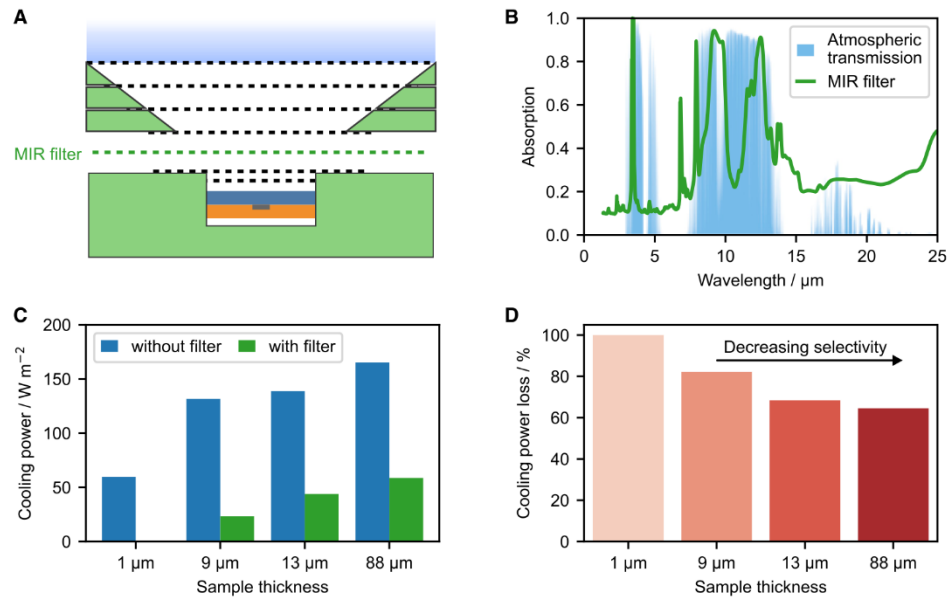


Figure 5. Distinguishing broadband and selective emitters

(A) An MIR filter consisting of PDMS on PE is inserted between the sample and the convection shield.

(B) The absorption spectrum of the PDMS-PE filter is comparable with the transmission of the atmosphere.

(C) Cooling power measurements of differently thick PDMS samples with and without the filter. With increasing thickness, the cooling power rises. The introduction of the MIR filter results in a significant reduction of cooling power.

(D) The relative cooling power loss decreases with increasing PDMS film thickness. The loss correlates with the emission selectivity of the samples.

emitters of the same type, i.e., compare broadband with broadband and selective with selective emitters. However, the discrimination between broadband and selective emitters is limited due to the lack of an atmospheric window. Directly simulating the atmosphere within the indoor setup is rather challenging.

Instead of equipping the indoor setup with a direct MIR filter with a transmission similar to the atmosphere to further imitate the field testing, an inverse MIR filter that emits only in the atmosphere window regime can be introduced. By placing the inverse MIR filter, which possesses ambient temperature, between the sample and the cold dome during the measurement, only the spectral radiation outside the atmosphere window regime can reach the cold dome (Figure 5A). The filter will block the rest. Selective emitters can thus be distinguished from broadband emitters by comparing the proportion of cooling power loss in a two-step measurement without and with the inverse MIR filter installed. The radiation in the atmosphere window regime contributes distinctly to the radiative cooling ability of broadband emitters and selective emitters.

We demonstrate such an inverse MIR filter by coating an LDPE foil with a thin layer of PDMS. A thin PDMS film with the desired thickness on an LDPE foil ensures a high absorption in the regime of 8–13 μm and simultaneously high transmission in the remaining spectral range (Figure 5B). The cooling power of PDMS films with different thicknesses, i.e., 712 nm and 8.6, 13.1, and 88.4 μm , is determined w/o and w/ the PDMS-PE filter to prove the concept (Figures 5C and S9). The optical properties of the PDMS films show that with increasing film thickness, they gradually transition

from a selective to a broadband emitter (Figure S10). Consequently, the cooling power without the MIR filter increased gradually. This is in good agreement with our previous work based on outdoor measurements.²⁹ The cooling power reduces dramatically when applying the PDMS-PE filter. The decrease varies for the differently thick PDMS films. To highlight the cooling power difference caused by the PDMS-PE filter, the relative power loss was calculated as $\text{power loss} = (P_{w/o} - P_{w})/P_{w/o}$ and is shown in Figure 5D. The increasing thickness of the PDMS films reduces the cooling power loss, which indicates that the PDMS-PE filter affects selective emitters more importantly than broadband emitters. Besides, we also calculated the cooling power loss of the PDMS films w/and w/o atmosphere with outdoor conditions (Figure S11). Despite the deviation of the absolute value between the experiment and the simulation, the trend agrees well. The deviation is mainly attributed to the imperfect match between the PDMS-PE filter and the atmosphere. The inverse MIR filter design can assess the influence of the sky-window transmission on the cooling power but is not suitable to compare the temperature reduction with outdoor measurements. A direct temperature comparison required a filter matching the sky-window properties.

Although it is hard to imitate the atmosphere in the indoor setup, with the inverse MIR filter, the indoor setup can distinguish between selective and broadband emitters. The possibility to add a tailor-made filter to our setup further expands the scope for its applicability to characterize passive daytime cooling materials close to field testing conditions. Further additions may include filters that account for a specific relative humidity or cloud coverage. Another class of filters may address the angular dependence of the thermal emission of a given material by controlling the view factor of the dome in dependence on the polar angle. Such a measurement capability is highly demanded to characterize emissive materials with diffusive reflectance properties. For instance, the heat management properties of smart textiles can be investigated with such a sample-dome layout, when operated at body heat and room temperature, respectively.⁴¹

In summary, we constructed a versatile indoor setup to thoroughly characterize the performance of passive cooling materials for both daytime and nighttime. Our setup combines a liquid-nitrogen-cooled Al dome with a solar simulator. Unlike conventional outdoor measurements, our setup allows controlling the measurement conditions, leading to outstanding reproducibility and time-saving measurements. Characterizing materials in a laboratory environment makes measuring and comparing materials independent of weather, time, and location. Additionally, the impact of solar intensity and ambient temperature on the cooling performance can be practically studied. Such comprehensive investigations are impossible for outdoor measurements due to the uncontrollable atmospheric conditions. We are convinced that our test setup is a first step toward a standardized passive cooling test routine. A standardized method to practically compare the cooling performance of various innovative materials from research groups all over the world is, however, a gatekeeper to turning passive cooling into a widespread and applied technology.

EXPERIMENTAL PROCEDURES

Resource availability

Lead contact

Further information and requests for resources should be directed to and will be fulfilled by the lead contact, Markus Retsch (retsch@uni-bayreuth.de).

Materials availability

This study did not generate new unique reagents.



Data and code availability

All data from this study are available from the corresponding author upon reasonable request.

Preparation of reference materials

Ag mirrors

Ag with a thickness of 100 nm was thermally evaporated on a silicon wafer ($r = 2.5$ cm), followed by a deposition of 10 nm silicon oxide (SiO_2) with a sputter coating step.

PDMS films

PDMS films with different thicknesses (88.4, 13.1, and 8.6 μm and 712 nm) were prepared on top of the Ag mirrors. For this, a prepolymer of PDMS (Sylgard 184, Dow Chemical) was mixed with a curing agent in a ratio of 10:1 (by weight) and degassed in a desiccator under vacuum. Subsequently, films with a thickness of 88.4 and 13.1 μm were prepared via spin-coating (1,000 and 3,000 rpm) on the Ag mirror. For films with a thickness of 8.6 and 13.1 μm , the prepolymer/cross-linker mixture was diluted to 75 wt % and 25 wt % solutions, respectively, with n-hexane. The films were then prepared via spin coating (3,000 and 4,000 rpm) on the Ag mirror. The PDMS layers were cured at room temperature for 48 h.

Graphite coating

The graphite coating is prepared by spray coating graphite (Cramolin, ITW Spraytec, Germany) onto a precleaned silicon wafer ($r = 2.5$ cm), followed by evaporation of the solvent at ambient temperature.

The layer thickness of the reference samples, namely PDMS films and graphite, was determined by using a three-dimensional (3D) laser scanning microscope (LEXT OLS5000, Olympus). A thickness of 88.4 μm , 13.1 μm , 8.6 μm , 712 nm, and 3.2 μm was obtained for the four PDMS films and the graphite coating, respectively.

PDMS-PE window

A prepolymer of PDMS (Sylgard 184, Dow Chemical) was mixed with a curing agent in a ratio of 10:1 (by weight) and degassed in a desiccator under a vacuum. The resulting mixture was diluted to a 50 wt % solution with n-hexane. A PDMS thin film was spin-coated (3,500 rpm) on an LDPE foil (thickness of around 15 μm), which was evenly attached to a silicon wafer ($r = 7.5$ cm). A PDMS-PE window was obtained by detaching the PDMS-PE foil from the silicon wafer.

Optical characterization with UV-Vis and FTIR spectroscopy

Broadband optical properties of the reference materials were characterized by ultraviolet-visible (UV-Vis) and Fourier transform infrared (FTIR) spectroscopy. UV-Vis reflectance of the reference materials was measured with a UV-Vis spectrometer (Cary 5000, Agilent Technologies) equipped with an integrating sphere accessory (Labspheres). A Spectralon diffuse reflectance standard (Labspheres) was used as a reference. The FTIR spectroscopy measurements were carried out on an IR spectrometer (Vertex 70, Bruker) coupled with a gold-coated integrating sphere accessory (A562, Bruker). A gold mirror was used as a reference. The absorbance (emittance) was calculated as absorbance (emittance) = $1 - \text{reflectance}$. We assume that the transmission can be neglected because of the Ag layer at the back.

Transmittance characterization of the convection shield

We used a pyroelectric sensor (FieldMaxII, Coherent) to measure the power of the solar simulator irradiation. Triplicate measurements were performed with and

without the convection shield between the simulator and the sensor. The transmittance was calculated as $1 - P_{w/\text{shield}}/P_{w/o\text{ shield}}$.

Indoor measurements

Daytime measurements are imitated by applying solar light provided by a solar simulator (AX-LAN400, Sciencetech, Canada) with an illumination area of $5 \times 5 \text{ cm}^2$. For nighttime measurements, the solar simulator was turned off. For all indoor measurements, dried air was warmed up by a water bath with a controlled temperature and flushed the area between the convection shield and measurement cell. Liquid nitrogen was filled into the setup to cool down the Al dome. Before filling the liquid nitrogen into the setup, the inner space of the dome is flushed with N_2 to remove air. Thus, no pronounced water condensation was observed on the convection shield. The temperature of the dome is maintained during the entire measurement by continuously filling liquid nitrogen into the setup. The sample temperature is measured with a thermocouple (type T) and collected by a digital multimeter (DAQ6510, Tektronix, Germany) every 5 s. To determine the steady-state temperature, data from the last 5 min of the measurement were averaged.

For the indoor measurements with the PDMS-PE window, the prepared PDMS-PE foil was placed above the sample holder at a distance of around 5 mm.

Repeatability test

An Ag mirror was used to check the repeatability of the setup. The temperature of the airflow was controlled by setting the water bath to 40°C . The steady-state temperature of the Ag mirror was measured three times per day on three different days, w/ and w/o one sun power of solar light ($\sim 1000 \text{ W m}^{-2}$).

Solar intensity dependence test

The graphite coating was measured to highlight the influence of solar intensity on the cooling performance. The temperature of the airflow was set to 40°C . The intensity of the solar light was varied from 0% to 100% of one sun power ($\sim 1000 \text{ W m}^{-2}$). The steady-state temperature and the cooling power of the graphite coating were then obtained under each condition. The net cooling power was measured by actively heating the graphite coating to keep it at the same temperature as an Ag mirror under the same conditions (water bath temperature and solar irradiance).

Ambient temperature dependence test

A PDMS film ($88.4 \mu\text{m}$) was applied to prove the temperature dependence of the thermal irradiation. The temperature of the airflow was set to 35°C , 40°C , 50°C , and 60°C . Subsequently, the steady-state temperature of the Ag mirror and the PDMS film was measured w/o the solar light.

Rooftop measurements

Rooftop measurements for daytime and nighttime were carried out on the roof of a four-floor building (June 17–18, 2021, University of Bayreuth, Bayreuth, Germany) under a clear sky. The reference samples were each placed in identical homemade sample holders. The holders were thermally insulated by Styrofoam and covered with Mylar Al foil. Convective heat transfer was prevented by applying an LDPE foil, with a thickness of approximately $15 \mu\text{m}$. The emitter temperatures were measured by Pt100 temperature sensors and recorded with a digital multimeter (DAQ6510, Tektronix, Germany) every 5 s. Temperatures between 1:00–1:30 and



13:00–13:30 were averaged to obtain steady-state temperatures. One sample holder covered with Al foil but without LDPE foil was used to obtain the ambient temperature. The solar irradiance data were collected from the weather station at the University of Bayreuth (Ecological-Botanical Garden, 400 m away from the rooftop measurement).

Numerical calculations

The numerical calculations for theoretically estimating the steady-state temperature and cooling power of the PDMS films are based on a model that is described in our previous study.²⁹ The broadband optical properties of the PDMS film are obtained from the literature.^{37,38,42} The sample was tilted 8° to avoid direct reflection of the solar light. For simplicity, this has been neglected in numerical calculations. A polar angle θ of 60° and an azimuthal angle of 360° was applied to the calculation based on the configuration of the indoor setup. We assume that no thermal radiation was emitted by the liquid-nitrogen-cooled dome.

To calculate the cooling powers of PDMS films with different thicknesses, i.e., 88.4, 13.1, 8.6 μm and 712 nm, with the outdoor condition, a polar angle θ of 90° and an azimuthal angle of 360° were applied. The ambient temperature of the emitter is set to 18.5°C, which is the preset temperature of PDMS films for indoor cooling power measurement. For emitters with a temperature as same as ambient temperature, the nighttime cooling power is calculated as $P_{\text{mat}} - P_{\text{atm}}$. P_{mat} is the total power emitted by the sample. P_{atm} is the absorbed power from the atmosphere. The cooling power loss is calculated as $(P_{\text{mat}} - P_{\text{atm}})/P_{\text{mat}}$.

SUPPLEMENTAL INFORMATION

Supplemental information can be found online at <https://doi.org/10.1016/j.xcrp.2022.100986>.

ACKNOWLEDGMENTS

The authors gratefully thank Stefan Rettinger and the mechanical and electrical workshop (University of Bayreuth) for technical support and Klaus Müller for the metal evaporation. We are indebted to Prof. Christoph Thomas for kindly providing the solar radiance and air temperature data. T.T. and T.L. acknowledge support from the Elite Network Bavaria (ENB). The authors acknowledge financial support from the European Research Council (ERC) under the European Union's Horizon 2020 research and innovation program (grant agreement no. 714968).

AUTHOR CONTRIBUTIONS

Q.S. and T.T. led the conceptualization and investigation. K.H. contributed formal analysis and validation. T.L. contributed validation and resources. M.B. was involved in the investigation. M.R. led supervision, project administration, and funding acquisition. All authors contributed to the original draft writing.

DECLARATION OF INTERESTS

The authors declare no competing interests.

Received: February 18, 2022

Revised: June 13, 2022

Accepted: June 21, 2022

Published: July 18, 2022

REFERENCES

- Santamouris, M., and Feng, J. (2018). Recent progress in daytime radiative cooling: is it the air conditioner of the future? *Buildings* 8, 168. <https://doi.org/10.3390/buildings8120168>.
- Li, Z., Chen, Q., Song, Y., Zhu, B., and Zhu, J. (2020). Fundamentals, materials, and applications for daytime radiative cooling. *Adv. Mater. Technol.* 5, 1901007. <https://doi.org/10.1002/admt.201901007>.
- Rephaeli, E., Raman, A., and Fan, S. (2013). Ultrabroadband photonic structures to achieve high-performance daytime radiative cooling. *Nano Lett.* 13, 1457–1461. <https://doi.org/10.1021/nl4004283>.
- Raman, A.P., Anoma, M.A., Zhu, L., Rephaeli, E., and Fan, S. (2014). Passive radiative cooling below ambient air temperature under direct sunlight. *Nature* 510, 544–544. <https://doi.org/10.1038/nature13883>.
- Chae, D., Kim, M., Jung, P.H., Son, S., Seo, J., Liu, Y., Lee, B.J., and Lee, H. (2020). Spectrally selective inorganic-based multilayer emitter for daytime radiative cooling. *ACS Appl. Mater. Interfaces* 12, 8073–8081. <https://doi.org/10.1021/acsami.9b16742>.
- Zhai, Y., Ma, Y., David, S.N., Zhao, D., Lou, R., Tan, G., Yang, R., and Yin, X. (2017). Scalable-manufactured randomized glass-polymer hybrid metamaterial for daytime radiative cooling. *Science* 355, 1062–1066. <https://doi.org/10.1126/science.aai7899>.
- Wang, X., Liu, X.H., Li, Z.Y., Zhang, H.W., Yang, Z.W., Zhou, H., and Fan, T.X. (2020). Scalable flexible hybrid membranes with photonic structures for daytime radiative cooling. *Adv. Funct. Mater.* 30, 1907562. <https://doi.org/10.1002/adfm.201907562>.
- Zhu, B., Li, W., Zhang, Q., Li, D., Liu, X., Wang, Y., Xu, N., Wu, Z., Li, J., Li, X., et al. (2021). Subambient daytime radiative cooling textile based on nanoprocessed silk. *Nat. Nanotechnol.* 16, 1342–1348. <https://doi.org/10.1038/s41565-021-00987-0>.
- Zeng, S., Pian, S., Su, M., Wang, Z., Wu, M., Liu, X., Chen, M., Xiang, Y., Wu, J., Zhang, M., et al. (2021). Hierarchical-morphology metafabric for scalable passive daytime radiative cooling. *Science* 373, 692–696. <https://doi.org/10.1126/science.abi5484>.
- Leroy, A., Bhatia, B., Kelsall, C.C., Castillejo-Cuberos, A., Di Capua H, M., Zhao, L., Zhang, L., Guzman, A.M., Wang, E.N., Leroy, A., and Castillejo-Cuberos, A. (2019). High-performance subambient radiative cooling enabled by optically selective and thermally insulating polyethylene aerogel. *Sci. Adv.* 5, eaat9480. <https://doi.org/10.1126/sciadv.aat9480>.
- Mandal, J., Fu, Y., Overvig, A.C., Jia, M., Sun, K., Shi, N.N., Zhou, H., Xiao, X., Yu, N., and Yang, Y. (2018). Hierarchically porous polymer coatings for highly efficient passive daytime radiative cooling. *Science* 362, 315–319. <https://doi.org/10.1126/science.aat9513>.
- Wang, J., Sun, J., Guo, T., Zhang, H., Xie, M., Yang, J., Jiang, X., Chu, Z., Liu, D., and Bai, S. (2022). High-strength flexible membrane with rational pore architecture as a selective radiator for high-efficiency daytime radiative cooling. *Adv. Mater. Technol.* 7, 2100528. <https://doi.org/10.1002/admt.202100528>.
- Zhong, H., Zhang, P., Li, Y., Yang, X., Zhao, Y., and Wang, Z. (2020). Highly solar-reflective structures for daytime radiative cooling under high humidity. *ACS Appl. Mater. Interfaces* 12, 51409–51417. <https://doi.org/10.1021/acsami.0c14075>.
- Shi, N.N., Tsai, C.C., Camino, F., Bernard, G.D., Yu, N., and Wehner, R. (2015). Keeping cool: enhanced optical reflection and radiative heat dissipation in Saharan silver ants. *Science* 349, 298–301. <https://doi.org/10.1126/science.aab3564>.
- Zhang, H., Ly, K.C.S., Liu, X., Chen, Z., Yan, M., Wu, Z., Wang, X., Zheng, Y., Zhou, H., and Fan, T. (2020). Biologically inspired flexible photonic films for efficient passive radiative cooling. *Proc. Natl. Acad. Sci. USA* 117, 14657–14666. <https://doi.org/10.1073/pnas.2001802117>.
- Wang, T., Wu, Y., Shi, L., Hu, X., Chen, M., and Wu, L. (2021). A structural polymer for highly efficient all-day passive radiative cooling. *Nat. Commun.* 12, 365. <https://doi.org/10.1038/s41467-020-20646-7>.
- Wang, S., Wang, Y., Zou, Y., Chen, G., Ouyang, J., Jia, D., and Zhou, Y. (2021). Biologically inspired scalable-manufactured dual-layer coating with a hierarchical micropattern for highly efficient passive radiative cooling and robust superhydrophobicity. *ACS Appl. Mater. Interfaces* 13, 21888–21897. <https://doi.org/10.1021/acsami.1c05651>.
- Zhao, B., Hu, M., Ao, X., Chen, N., and Pei, G. (2019). Radiative cooling: a review of fundamentals, materials, applications, and prospects. *Appl. Energy* 236, 489–513. <https://doi.org/10.1016/j.apenergy.2018.12.018>.
- Li, X., Peoples, J., Huang, Z., Zhao, Z., Qiu, J., and Ruan, X. (2020). Full daytime sub-ambient radiative cooling in commercial-like paints with high figure of merit. *Cell Rep. Phys. Sci.* 1, 100221. <https://doi.org/10.1016/j.xcrp.2020.100221>.
- Wang, S., Jiang, T., Meng, Y., Yang, R., Tan, G., and Long, Y. (2021). Scalable thermochromic smart windows with passive radiative cooling regulation. *Science* 374, 1501–1504. <https://doi.org/10.1126/science.abg0291>.
- Tang, K., Dong, K., Li, J., Gordon, M.P., Reichertz, F.G., Kim, H., Rho, Y., Wang, Q., Lin, C.Y., Grigoropoulos, C.P., et al. (2021). Temperature-adaptive radiative coating for all-season household thermal regulation. *Science* 374, 1504–1509. <https://doi.org/10.1126/science.abf7136>.
- Hossain, M.M., and Gu, M. (2016). Radiative cooling: principles, progress, and potentials. *Adv. Sci.* 3, 1500360. <https://doi.org/10.1002/advs.201500360>.
- Dong, M., Chen, N., Zhao, X., Fan, S., and Chen, Z. (2019). Nighttime radiative cooling in hot and humid climates. *Opt Express* 27, 31587. <https://doi.org/10.1364/OE.27.031587>.
- Zhou, L., Song, H., Liang, J., Singer, M., Zhou, M., Stegenburgs, E., Zhang, N., Xu, C., Ng, T., Yu, Z., et al. (2019). A polydimethylsiloxane-coated metal structure for all-day radiative cooling. *Nat. Sustain.* 2, 718–724. <https://doi.org/10.1038/s41893-019-0348-5>.
- Park, G., Roh, K., Kim, H., Khan, S., Lee, M., Kim, B.W., and Kim, W. (2022). Universal experimental methods for evaluating the performance of radiative cooling materials. *Adv. Mater. Technol.* 2101205. <https://doi.org/10.1002/admt.202101205>.
- Wong, R.Y.M., Tso, C.Y., and Chao, C.Y.H. (2021). Corrected radiative cooling power measured by equivalent dissipative thermal reservoir method. *Int. J. Heat Mass Tran.* 174, 121341. <https://doi.org/10.1016/j.ijheatmasstransfer.2021.121341>.
- Huang, Z., and Ruan, X. (2017). Nanoparticle embedded double-layer coating for daytime radiative cooling. *Int. J. Heat Mass Tran.* 104, 890–896. <https://doi.org/10.1016/j.ijheatmasstransfer.2016.08.009>.
- Banik, U., Agrawal, A., Meddeb, H., Sergeev, O., Reininghaus, N., Götz-Köhler, M., Gehrke, K., Stührenberg, J., Vehse, M., Sznajder, M., and Agert, C. (2021). Efficient thin polymer coating as a selective thermal emitter for passive daytime radiative cooling. *ACS Appl. Mater. Interfaces* 13, 24130–24137. <https://doi.org/10.1021/acsami.1c04056>.
- Herrmann, K., Lauster, T., Song, Q., and Retsch, M. (2021). Homogeneous polymer films for passive daytime cooling: optimized thickness for maximized cooling performance. *Adv. Energy Sustainability Res.* 3, 2100166. <https://doi.org/10.1002/aesr.202100166>.
- Jeong, S.Y., Tso, C.Y., Ha, J., Wong, Y.M., Chao, C.Y.H., Huang, B., and Qiu, H. (2020). Field investigation of a photonic multi-layered TiO₂ passive radiative cooler in sub-tropical climate. *Renew. Energy* 146, 44–55. <https://doi.org/10.1016/j.renene.2019.06.119>.
- Kou, J.-I., Jurado, Z., Chen, Z., Fan, S., and Minnich, A.J. (2017). Daytime radiative cooling using near-black infrared emitters. *ACS Photonics* 4, 626–630. <https://doi.org/10.1021/acsp Photonics.6b00991>.
- Haechler, I., Park, H., Schnoering, G., Gulich, T., Rohner, M., Tripathy, A., Milionis, A., Schütz, T.M., and Poulidakos, D. (2021). Exploiting radiative cooling for uninterrupted 24-hour water harvesting from the atmosphere. *Sci. Adv.* 7, eabf3978. <https://doi.org/10.1126/sciadv.aabf3978>.
- Zhu, Y.Q., Ye, Y.H., Wang, D., and Cao, Y.R. (2021). Simple dual-layer emitter for daytime radiative cooling. *Osa Continuum* 4, 416. <https://doi.org/10.1364/Osa.398685>.
- Li, T., Zhai, Y., He, S., Gan, W., Wei, Z., Heidarinejad, M., Dalgo, D., Mi, R., Zhao, X., Song, J., et al. (2019). A radiative cooling structural material. *Science* 364, 760–763. <https://doi.org/10.1126/science.aau9101>.
- Chen, M., Pang, D., Chen, X., and Yan, H. (2021). Enhancing infrared emission behavior of polymer coatings for radiative cooling applications. *J. Phys. D Appl. Phys.* 54, 295501. <https://doi.org/10.1088/1361-6463/abfb19>.



36. Nilsson, T.M.J., and Niklasson, G.A. (1995). Radiative cooling during the day: simulations and experiments on pigmented polyethylene cover foils. *Sol. Energy Mater. Sol. Cells* 37, 93–118. [https://doi.org/10.1016/0927-0248\(94\)00200-2](https://doi.org/10.1016/0927-0248(94)00200-2).
37. Zhang, X., Qiu, J., Li, X., Zhao, J., and Liu, L. (2020). Complex refractive indices measurements of polymers in visible and near-infrared bands. *Appl. Opt.* 59, 2337. <https://doi.org/10.1364/AO.383831>.
38. Zhang, X., Qiu, J., Zhao, J., Li, X., and Liu, L. (2020). Complex refractive indices measurements of polymers in infrared bands. *J. Quant. Spectrosc. Radiat. Transfer* 252, 107063. <https://doi.org/10.1016/j.jqsrt.2020.107063>.
39. Zhao, D., Aili, A., Zhai, Y., Xu, S., Tan, G., Yin, X., and Yang, R. (2019). Radiative sky cooling: fundamental principles, materials, and applications. *Appl. Phys. Rev.* 6, 021306. <https://doi.org/10.1063/1.5087281>.
40. Li, Y.L., Li, L.Z., Guo, L., and An, B.W. (2020). Systematical analysis of ideal absorptivity for passive radiative cooling. *Opt. Mater. Express* 10, 1767. <https://doi.org/10.1364/Ome.397617>.
41. Gao, Q., Lauster, T., Kopera, B.A.F., Retsch, M., Agarwal, S., and Greiner, A. (2022). Breathable and flexible dual-sided nonwovens with adjustable infrared optical performances for smart textile. *Adv. Funct. Mater.* 32, 2108808. <https://doi.org/10.1002/adfm.202108808>.
42. Query, M.R. (1987). *Optical Constants of Minerals and Other Materials from the Millimeter to the Ultraviolet* (US Army Report CRDECCR). 88009.

Supplemental information

A tailored indoor setup for reproducible passive daytime cooling characterization

Qimeng Song, Thomas Tran, Kai Herrmann, Tobias Lauster, Maximilian Breitenbach, and Markus Retsch

Supplemental Information

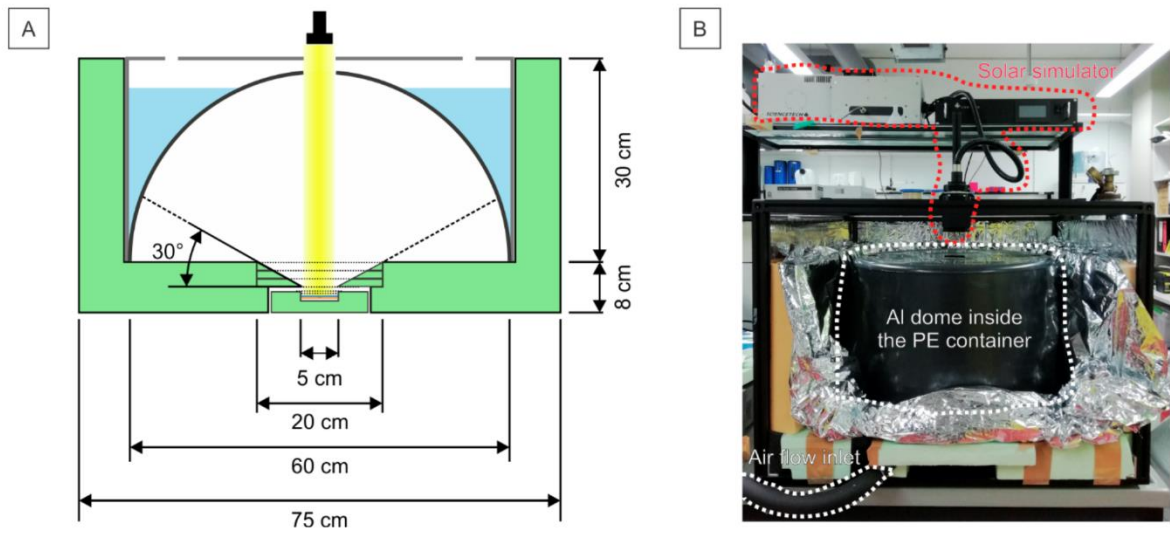


Figure S1. Indoor setup design. (A) Detailed dimensions and (B) photograph of the indoor setup. Related to Figure 1 and Indoor Setup Design.

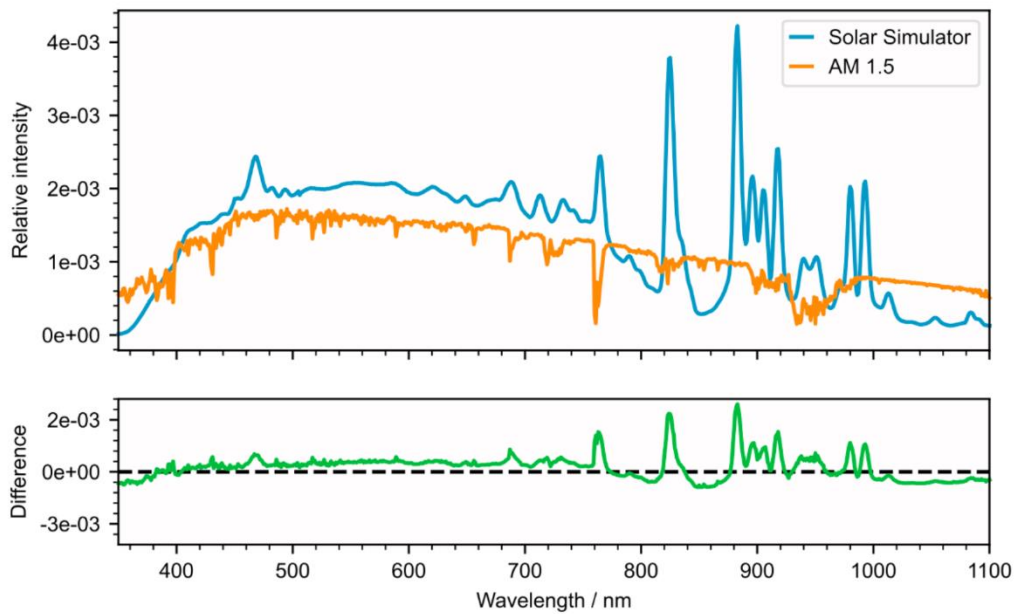


Figure S2. Comparison between the solar light from the sun (AM 1.5) and the solar simulator. The intensity shown is relative to the total intensity of the light source, i.e., the integral from 0 to infinity is 1 for each individual curve. Related to Indoor Setup Design.

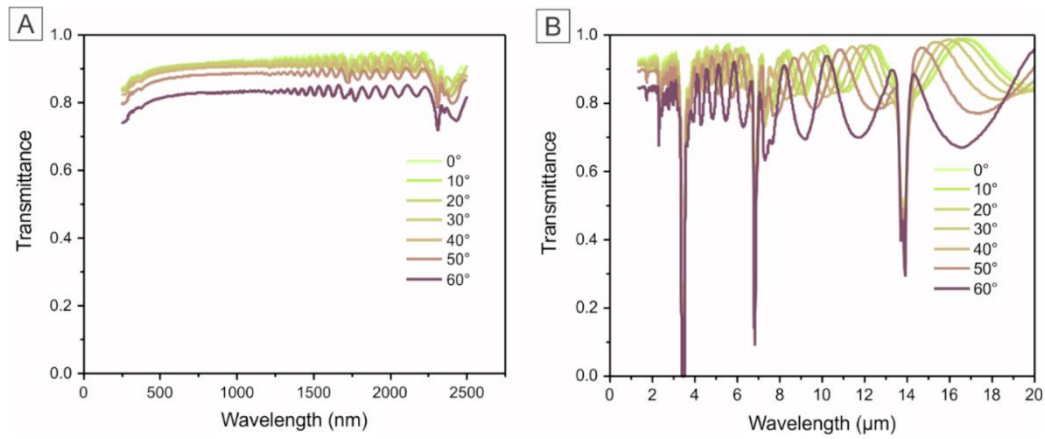


Figure S3. Angle-dependent optical properties in (A) UV/Vis and (B) IR regime for a single, 15 μm thick PE window used in the convection shield. Related to Indoor Setup Design.

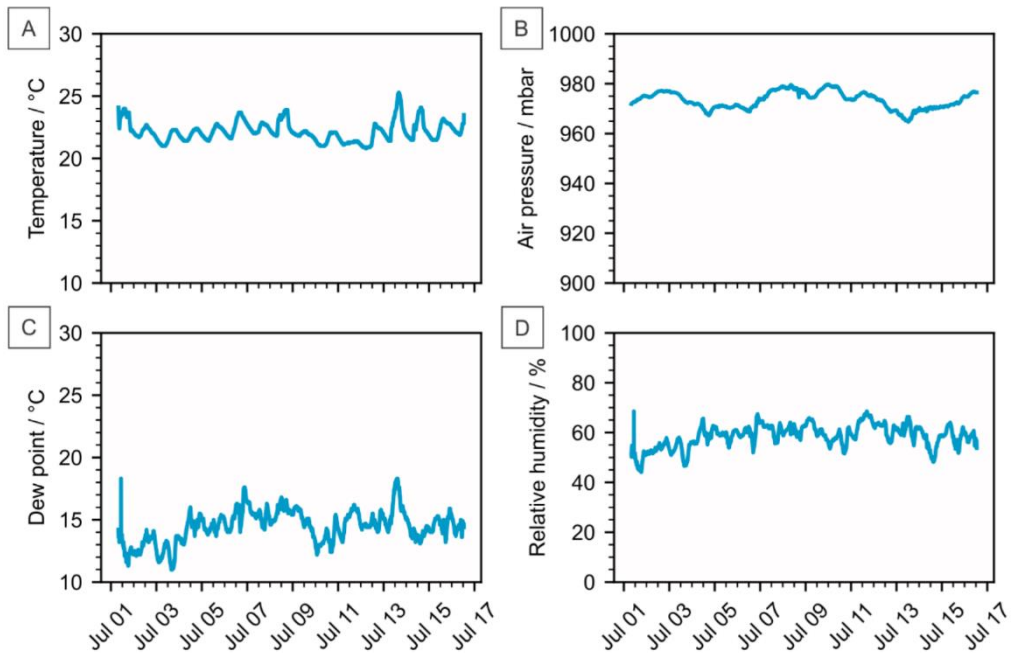


Figure S4. Laboratory conditions. (A) Ambient temperature, (B) air pressure, (C) dew point, and (D) relative humidity in the laboratory over a week. Related to Indoor Setup Design.

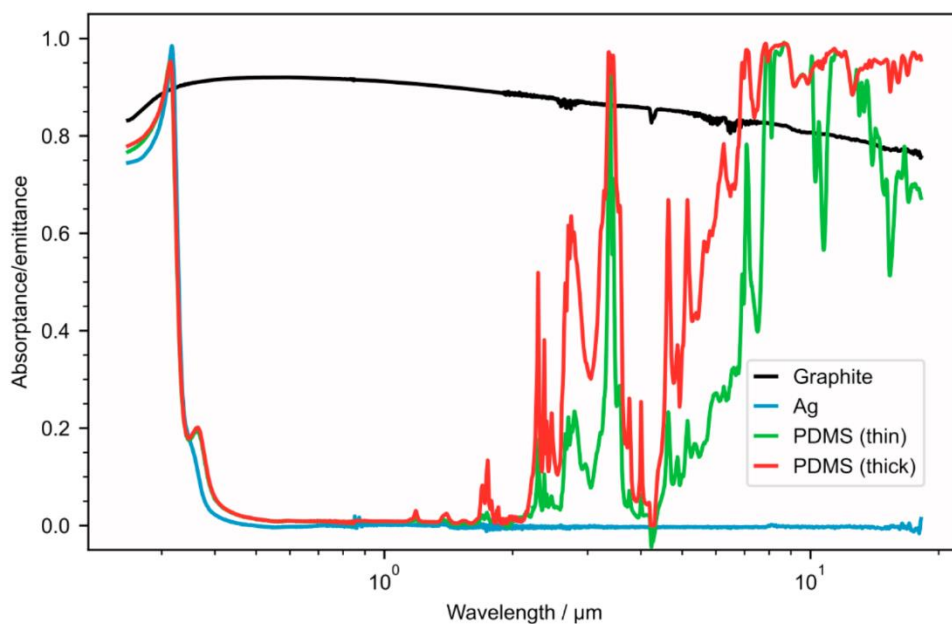


Figure S5. Optical properties of the reference materials used in this work, i.e., PDMS, Ag, and graphite, in the UV/Vis and MIR region. Related to Figure 2 and Performance Assessment.

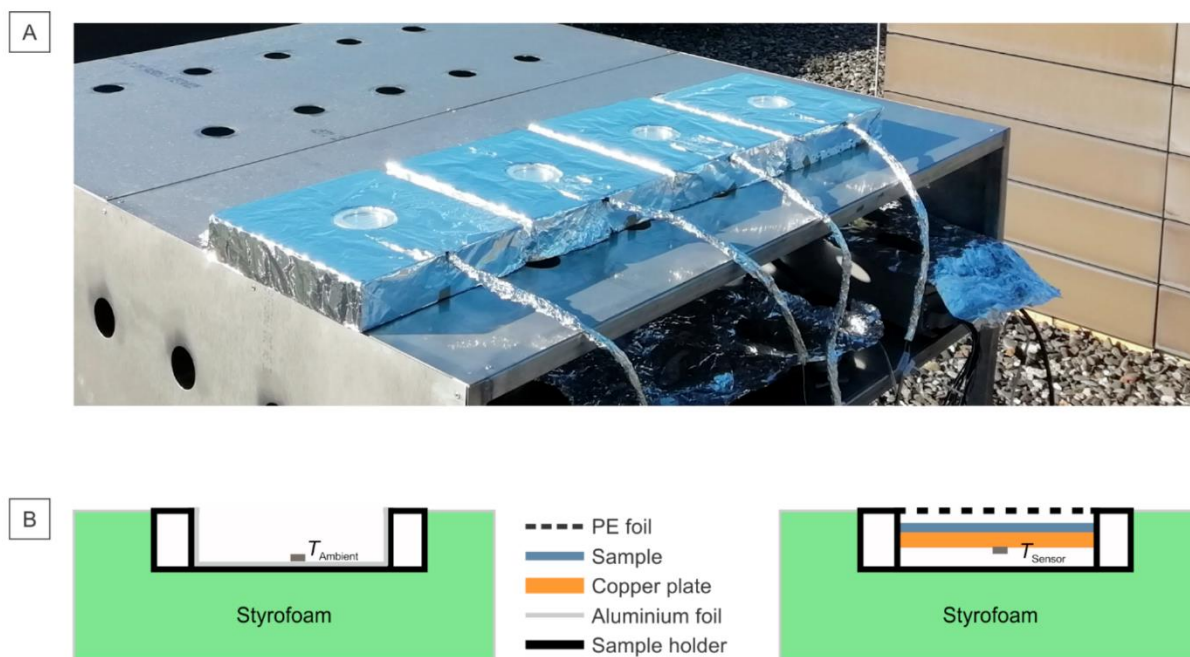


Figure S6. Outdoor setup design. (A) Photograph and (B) schematic of the setup for outdoor measurements. Related to Figure 2 and Performance Assessment.

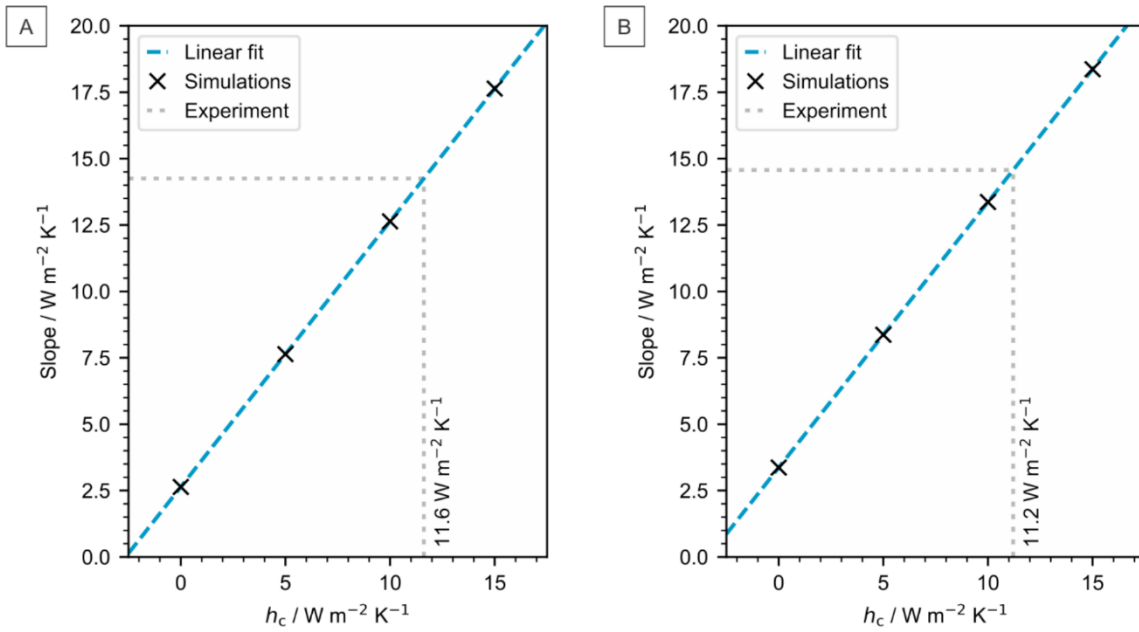


Figure S7. Determination of h_c for the thin (A) and thick (B) PDMS samples in the indoor setup measurement. The linear fit shows how the slope of the simulated cooling power behaves for different values of h_c . Calculating the slope of the experimental cooling powers leads to h_c values of 11.6 and $11.2 W m^{-2} K^{-1}$ for the thin and thick PDMS samples, respectively. Related to Figure 3 and Cooling Power Characterization.

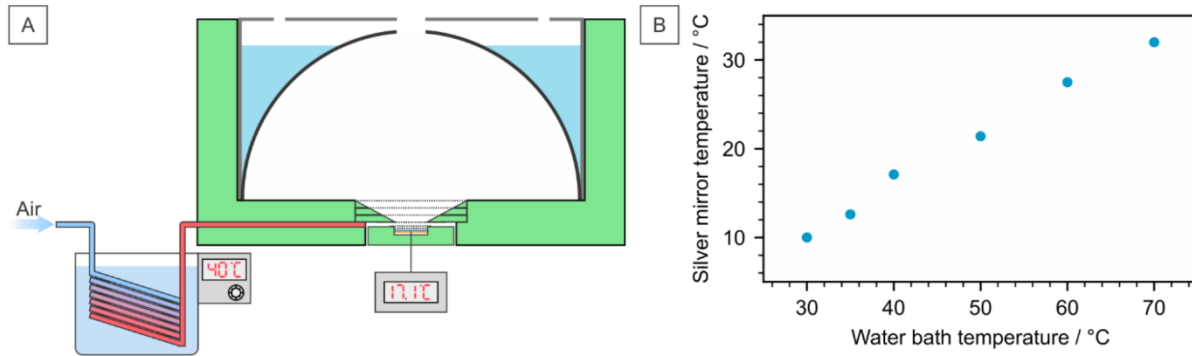


Figure S8. Tunable ambient temperature of the indoor setup. (A) Schematic of a part of the indoor setup. (B) Ambient temperature of the indoor setup as a function of water bath temperature. Related to Figure 4 and Variation of Environmental Parameters.

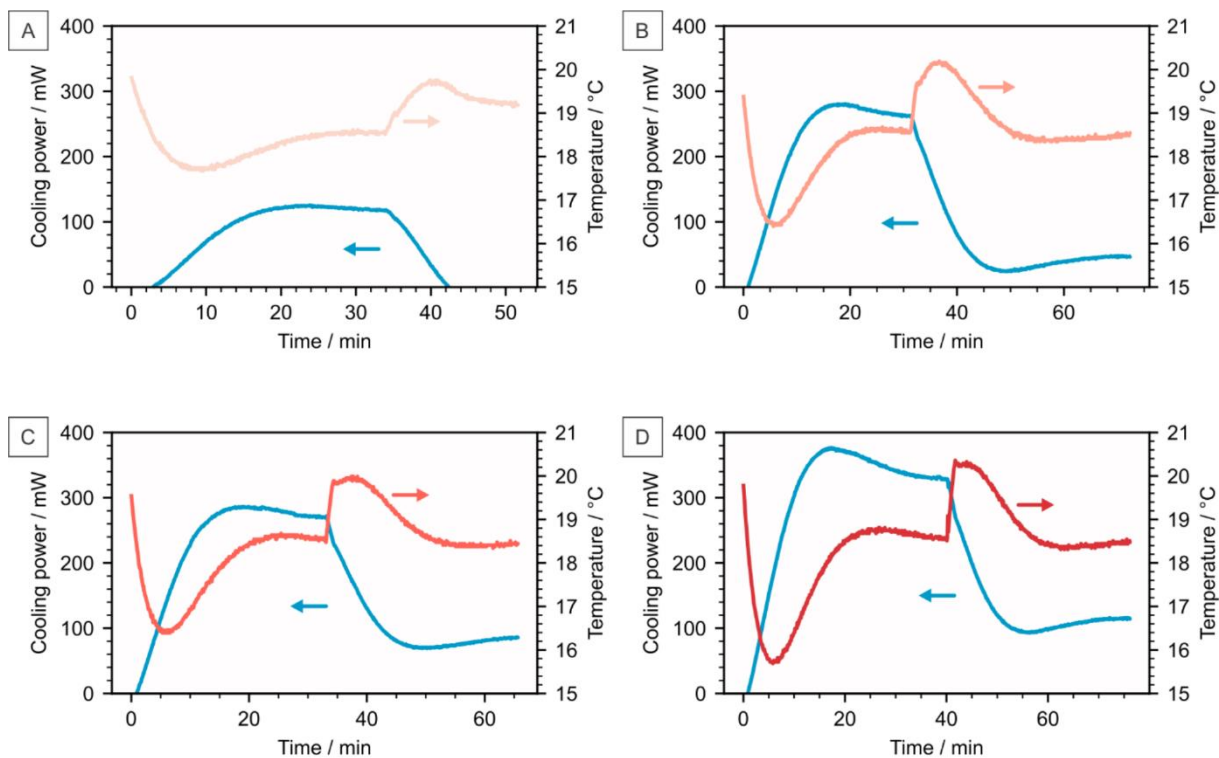


Figure S9. Cooling power measurements with and without a MIR filter for PDMS samples with a thickness of (A) 712 nm, (B) 8.6 μm , (C) 13.1 μm , and (D) 88.4 μm . The MIR filter is inserted into the indoor setup after temperature and cooling power reach a steady state. The insertion of the MIR filter leads to a significant decrease in cooling power for all samples.

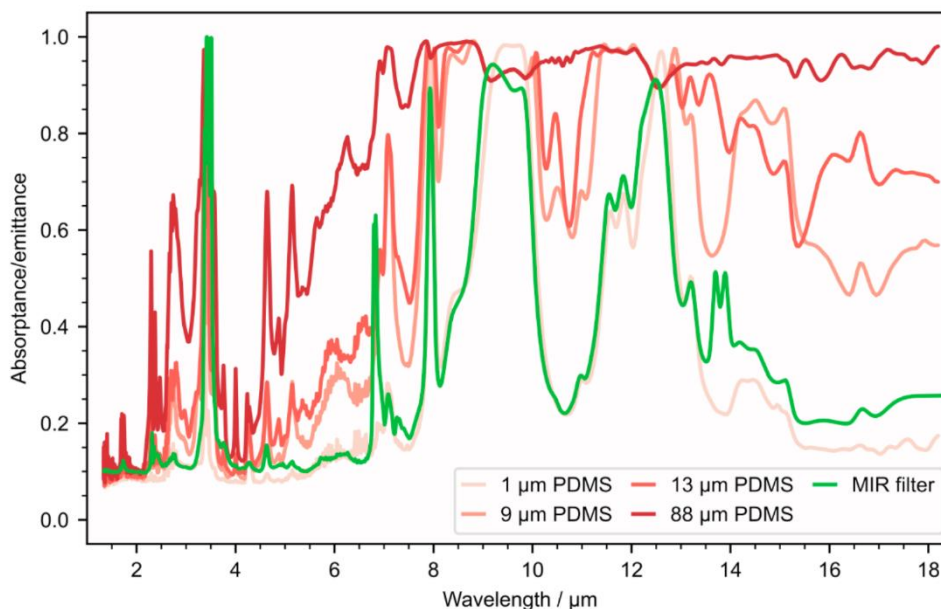


Figure S10. Absorption spectra for PDMS films of different thicknesses and the MIR filter. Decreasing thickness leads to higher emission selectivity.

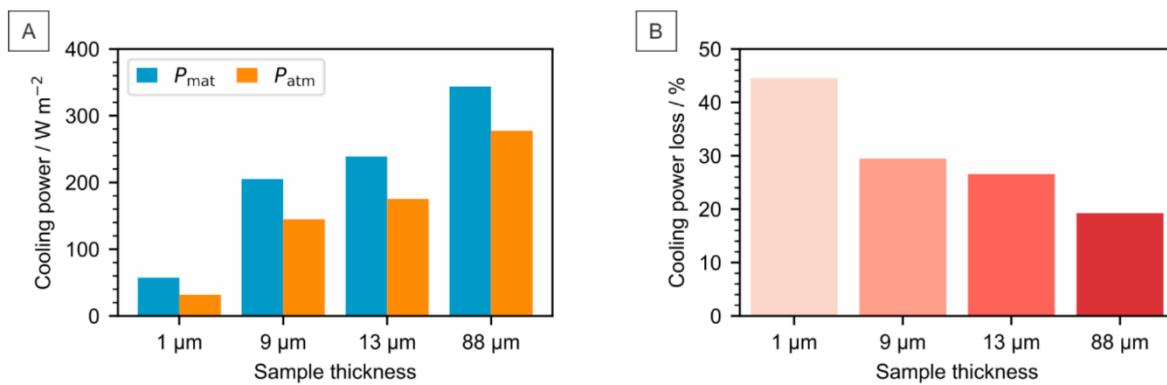
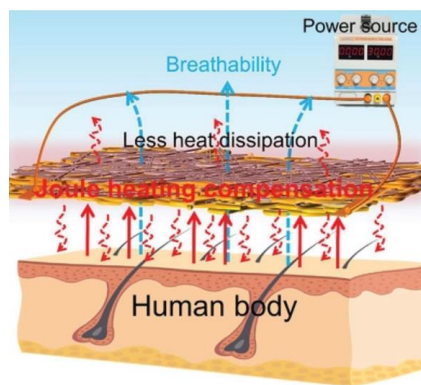


Figure S11. Simulation results for PDMS samples with different thicknesses in outdoor conditions. (A) Absolute contributions to the cooling power. (B) Cooling power loss. The loss is calculated as $(P_{\text{mat}} - P_{\text{atm}}) / P_{\text{mat}}$.

9. Breathable and Flexible Dual-Sided Nonwovens with Adjustable Infrared Optical Performance for Smart Textile



A breathable and flexible dual-sided nonwoven composed of polyimide nanofiber and silver nanowires possesses good electrical conductivity and high infrared reflection performance. A personal thermal management device is constructed of two layers of dual-sided nonwoven containing different amounts of silver nanowires, demonstrating prominent human body warming performance by combining active Joule heating and passive warming via reduced radiative losses.

Breathable and Flexible Dual-Sided Nonwovens with Adjustable Infrared Optical Performances for Smart Textile

Qiang Gao, Tobias Lauster, Bernd A. F. Kopera, Markus Retsch,* Seema Agarwal,* and Andreas Greiner*

Maintaining constant body temperature is the most basic function of textiles. However, traditional fabrics irradiate a massive amount of thermal energy to the ambient environment due to the high emissivity of the materials used for textiles. This phenomenon weakens the thermal function, causing vast thermal energy loss by dissipation as infrared (IR) irradiation. To improve thermal comfort and reduce extra energy consumption, smart thermal management textiles must maintain constant body temperature by regulating IR irradiation from the human body or by compensating heat losses by joule heating. Here, a smart dual-sided nonwovens¹ preparation procedure and properties for use as a textile with this combination of properties are shown. The nonwoven combines a high porosity with high IR reflectance and low IR emittance. The nonwoven is adjustable from reflective to emissive when turned inside out. It is consequently permeable to air and vapor and simultaneously mitigates thermal heat losses with radiation. In addition, low sheet resistance and superior flexibility make it possible to use them in flexible electronics and wearable devices. It can be further equipped with a porous Joule heating layer adding active control to the personal thermal comfort.

1. Introduction

Thousands of years ago, our ancestors used all kinds of plants to cover the body to keep it warm. In recent centuries, silk, cotton, hemp, and other natural materials were applied in the traditional textile field to realize clothing warmer and more comfortable. Textiles are revolutionized by synthetic materials such as polyesters and nylons, and incorporating smart functionalities has become a trend and research objective. The smart functionalities are introduced for monitoring body movements, detection of metabolic indexes, or energy storage.^[1] For instance, solar cell integrated textile is promising for energy storage and charging portable electronic devices.^[2] Initially, the textile's essential function is to keep warm and reduce body energy loss for surviving in the frigid natural environment. Traditional textiles concentrate more on lowering body heat

transfer into the air surrounding via convection and conduction. However, it fails to insulate body thermal emission due to the high emissivity of ordinary cloth. If heating and insulation could be managed based on human requirements, a huge amount of energy could be saved^[3] and personal thermal comfort increased. Hence, personal thermal management devices, wearable like typical textiles and capable of significantly reducing body heat loss or raising the textile temperature according to personal desire, has been developing to improve body thermal comfort control in new strategies and solutions. By regulating heat exchange (infrared (IR) radiation flow) from the human body to its surroundings, developing advanced materials with body thermal irradiation control has attracted considerable attention.^[4] IR transparent radiative,^[5] emissive radiative,^[6] solar-reflecting radiative cooling textiles, and conductive cooling textiles with enhanced thermal conductivity^[7] have been widely reported to keep cool in warm surroundings by heat exchange between human body and environment.^[3] On the contrary, when in cold climate, textiles with warming purpose are highly demanded to significantly reduce heat loss into the surroundings. This is technically achieved by thermal insulating materials, such as porous aerogel fiber,^[8] or IR reflecting materials via incorporating metal particles and metal wires.^[6b,9] To compensate for heat dissipation through IR radiation, textiles with electro heating function are highly desired to realize

Q. Gao, S. Agarwal, A. Greiner
Department of Chemistry
Macromolecular Chemistry II and Bavarian Polymer Institute
University of Bayreuth
Universitätsstrasse 30, 95440 Bayreuth, Germany
E-mail: agarwal@uni-bayreuth.de; greiner@uni-bayreuth.de
T. Lauster, B. A. F. Kopera, M. Retsch
Department of Chemistry
Physical Chemistry I
University of Bayreuth
Universitätsstrasse 30, 95440 Bayreuth, Germany
E-mail: markus.retsch@uni-bayreuth.de
M. Retsch
Bavarian Center for Battery Technology (BayBatt)
Bavarian Polymer Institute, and Bayreuth
Center for Colloids and Interfaces
University of Bayreuth
Universitätsstrasse 30, 95440 Bayreuth, Germany

 The ORCID identification number(s) for the author(s) of this article can be found under <https://doi.org/10.1002/adfm.202108808>.

© 2021 The Authors. Advanced Functional Materials published by Wiley-VCH GmbH. This is an open access article under the terms of the Creative Commons Attribution License, which permits use, distribution and reproduction in any medium, provided the original work is properly cited.

DOI: 10.1002/adfm.202108808

the aims of harvesting energy from the human body to maintain body temperature constant, especially for those people living in harsh regions.^[10]

High-performance polymers like polyimide (PI) have excellent mechanical properties, high chemical resistance and excellent thermal stability. They are often applied as filters, mechanical parts, insulation and passivation films, and medical tubing. Short electrospun fibers constructed polymeric sponge is an excellent thermal insulator with very high thermal resistance thanks to its super-high porosity.^[11] Nevertheless, when some electrically conductive materials such as graphene and carbon nanotube,^[12] electrically conductive polymer,^[13] and metal nanowire^[14] were incorporated, these polymeric materials could change their electrical property from non-conductive to conductive, even highly conductive, which often used to prepare wearable devices, such as sensor and triboelectric nanogenerator.^[15] Recently, silver nanowire (AgNW) has been established as a promising electrically conductive material applied to prepare various kinds of electronic devices such as smart sensors^[16] for monitoring physiological indexes, transparent touch screens,^[17] and nanogenerator for energy-harvesting and storage.^[18] Additionally, AgNW is also known for its ultralow IR emissivity, thanks to the low emissivity of bulk silver (≈ 0.02). A recently developed AgNWs coated textile showed much higher IR reflectance of $\approx 40\%$ compared to uncoated textile ($\approx 1\%$) and provided 21% more thermal insulation due to the reduction of radiation loss.^[9] In comparison, herein, we present the preparation procedure and detailed characterization of an electrically conductive dual-sided PI/AgNW nonwoven with lightweight, highly flexible, air permeable, washable, IR-reflecting, and tailored heating properties. The IR reflecting properties are different on two different sides so that it can be used for multipurpose. The prepared PI/AgNW nonwoven is appropriate for flexible electronics and smart wearable devices and for other applications like for example sensor devices and energy devices for future use.

2. Result and Discussion

The dual-sided nonwovens were prepared, as shown in **Figure 1**. First, the PI electrospun nonwoven (thickness $48.0 \pm 2.5 \mu\text{m}$, area 10 cm^2 , **Figure S1a**, Supporting Information) was placed on a sand core funnel, and then AgNW dispersion (different amounts of 17 g L^{-1} dispersion) was filtered through the PI nonwoven under vacuum assistance. During this process, AgNW networks were formed on top of the PI nonwoven (**Figure S1b**, Supporting Information). The average diameters of PI fibers and AgNWs were 0.30 ± 0.07 and $0.10 \pm 0.03 \mu\text{m}$, respectively (**Figure S1c**, Supporting Information). A thermoplastic polyurethane (TPU) solution was filtered through the PI/AgNW nonwoven network under light vacuum with the intention to bond AgNW networks strongly onto the PI nonwoven by residual TPU acting as glue between the two. The as-prepared nonwovens have dual sides: the AgNW network side (silver gray) and the PI nanofiber layer side (yellow) (**Figure 1b**). The TPU (blue regions in **Figure 1c**) is entangled with AgNWs and attached to the PI nonwoven, as confirmed by energy-dispersive X-ray-scanning electron microscopy (EDX-SEM) (**Figure 1d**). The dual-sided nonwovens are designated as PI/TPU/AgNW-X, where X denotes the volume of AgNW dispersion (17 g L^{-1}) in μL used

for the preparation of nonwovens. PI/TPU/AgNW-25 and PI/TPU/AgNW-500 nonwovens have a thickness of 56.7 ± 1.0 and $57.7 \pm 3.1 \mu\text{m}$ (**Figure S2a**, Supporting Information), respectively. The pore size (**Figure 1e**) of PI/TPU was centered around $1.7 \mu\text{m}$. The dual-sided nonwoven with fewer AgNWs (PI/TPU/AgNW-25) showed a sparse AgNW network, which insignificantly affected the nonwoven's pore size ($\approx 1.7 \mu\text{m}$). However, the sample PI/TPU/AgNW-500 showed a decrease in pore size to $0.7 \mu\text{m}$ due to the denser layer of AgNW networks. All nonwovens were air permeable as the pore structure was retained during the preparation process using a light vacuum for the filtration of TPU and AgNWs (**Figure 1f**). PI/TPU, PI/TPU/AgNW-25 and PI/TPU/AgNW-500 showed air permeability of 5.2 ± 0.5 , 4.3 ± 0.6 , and $2.7 \pm 0.6 \text{ mm s}^{-1}$ respectively, whereas pure PI nonwoven has a permeability of $20.3 \pm 0.5 \text{ mm s}^{-1}$. The nonwovens also presented good moisture permeability (**Figure S2b**, Supporting Information) ($\approx 65 \text{ mg cm}^{-2} \text{ day}^{-1}$ for PI/TPU/AgNW-500), which is close to the value of pure PI electrospun nonwoven ($\approx 82 \text{ mg cm}^{-2} \text{ day}^{-1}$). Both sides of the PI nonwovens were hydrophobic with high contact angles ($\approx 140^\circ$, **Figure S2c**, Supporting Information). Although pure AgNWs are very hydrophilic, the AgNW network side of dual-sided nonwovens also showed very high contact angles (145.5 ± 0.1 and 144.9 ± 0.5 degrees for PI/TPU/AgNW-25 and PI/TPU/AgNW-500, respectively) due to the homogeneously dispersed TPU in the network (**Figure S3**, Supporting Information). The dual-sided nonwovens were as strong as the pristine PI nonwoven (18 MPa in tensile strength, 77% in strain) without any significant effect of TPU or AgNWs (**Figure 1g**).

As both PI nonwoven and TPU are electrically insulating materials, the electrical property of the dual-sided nonwoven is significantly influenced by the amount of AgNW due to the low resistivity ($1.6 \times 10^{-8} \Omega \text{ m}$) of silver. The polymeric nonwovens (PI and PI/TPU) showed very high electrical resistance (sheet resistance: $>10^8 \Omega \text{ sq}^{-1}$). The sheet resistance of the dual-sided nonwovens could be tuned to as low as $0.2 \Omega \text{ sq}^{-1}$ using appropriate amounts of AgNWs. The resistance decreased with the increasing quantity of AgNW (**Figure 2a** and **Table S1**, Supporting Information) with a discontinuous jump between PI/TPU/AgNW-2.5 and PI/TPU/AgNW-5 from $\approx 5 \times 10^8$ to $\approx 10^5 \Omega \text{ sq}^{-1}$. Denser AgNW networks resulting from more AgNWs, as demonstrated by SEM images (**Figure S6**, Supporting Information), contributed to high conductivity, resulting in decreased sheet resistance.

The nonwovens are mechanically flexible. In the circuit with PI/TPU/AgNW-500, there was insignificant variation in luminance of the light-emitting diode (LED) bulb with the nonwoven undergoing bending and twisting deformations (**Figure 2b**) compared to that of the virgin state. These types of bending and twisting deformations are often faced by wearable, flexible devices in everyday life. Additionally, the PI/TPU/AgNW-500 exhibited outstanding electromechanical properties. In particular, the electrical resistance shows a negligible variation ($R/R_0 = 1$, R and R_0 denoting resistance after and before test respectively) even after 100-time repeatable bending (bending angle: $\approx 140^\circ$) (**Figure 2c** and **Figure S7**, Supporting Information), indicating high durability and cyclability to withstand non-tensile deformation. When the sample was stretched to about 65% (**Figure 2d**), there was only a small increase in the resistance of PI/TPU/AgNW-500 from 2 to 40Ω . In contrast, a higher resistance change was observed for dual-sided

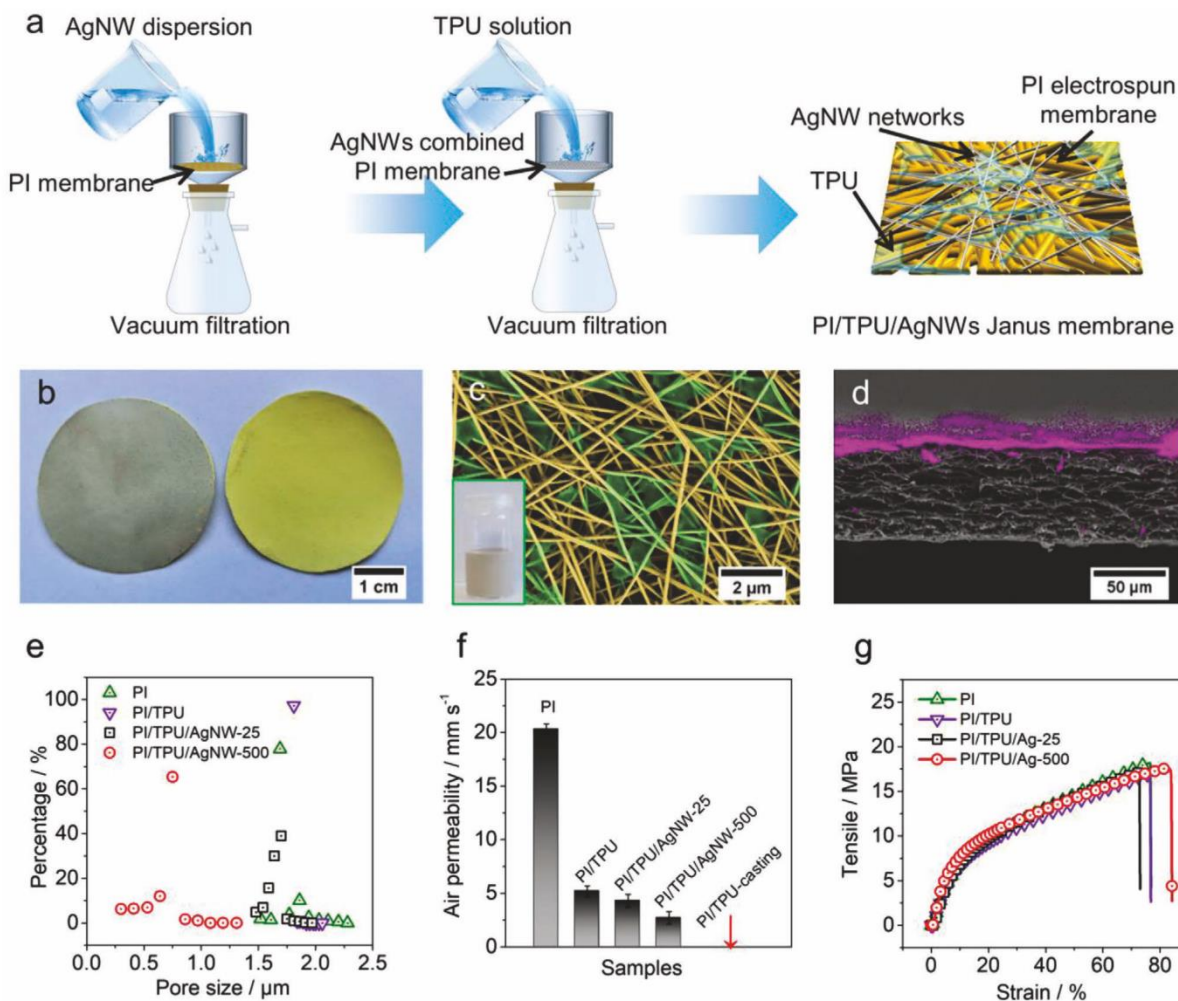


Figure 1. Preparation route a) and b) digital photographs of the dual-sided nonwoven (sliver gray: AgNW networks side, yellow: PI side). c) Photo-shop colored SEM image (original image seen in Figure S4, Supporting Information) of AgNW networks with TPU:TPU colored in green. The digital photograph of the AgNW water suspension is shown in the green frame at the left corner. d) EDX-SEM image of the dual-sided nonwoven PI/TPU/AgNW-500. The purple area presented the AgNW networks. e) Pore size distributions of PI electrospun nonwoven, PI electrospun nonwoven with TPU, PI/TPU/AgNW-25, and PI/TPU/AgNW-500. f) Air permeability of PI electrospun nonwoven, PI electrospun nonwoven with TPU, PI/TPU/AgNW-25, PI/TPU/AgNW-500, and PI/TPU-casting. The sample PI/TPU-casting is prepared by casting 2 mL 8 wt% TPU solution on PI electrospun nonwoven (SEM image in Figure S5, Supporting Information). g) Mechanical properties of PI electrospun nonwoven, PI electrospun nonwoven with TPU, PI/TPU/AgNW-25, and PI/TPU/AgNW-500.

nonwovens with fewer AgNWs (PI/TPU/AgNW-25) under similar conditions. It showed a change from ≈ 700 to $\approx 8000 \Omega$ merely within 10% strain deformation. In PI/TPU/AgNW-25 with fewer AgNWs, stretching just over 10% leads to a break in electrical percolation due to the fracture of AgNW networks leading to the loss of conductivity. The dense network of AgNWs in PI/TPU/AgNW-500 is responsible for tolerating a large deformation without losing performance, despite the network fractures, the electrical connectivity is maintained by interconnected cracked structures. (Figures S8 and S9, Supporting Information).

We also assessed the resistance stability at different temperatures (Figure 2e,f). During the first heat processing, a reduction of resistance with temperature up to 100 °C was observed,

which we attribute to the thermal annealing of AgNWs and the resulting efficient contact of AgNWs at their junctions. In the second heating cycle, the resistance of both dual-sided nonwovens (PI/TPU/AgNW-500 and PI/TPU/AgNW-25) increased linearly with temperature increasing from room temperature to 160 °C, showing the metal-like behavior of electron transport as expected. The dual-sided nonwoven, PI/TPU/AgNW-500 even maintained a stable resistance for 1200 min at 250 °C (Figure 2g). PI/TPU/AgNW-500 also showed an excellent adhesion stability of AgNWs on PI nonwoven as seen in a washing test in soap water at 45 °C for 10 h in total (2 h for five times) (Figure 2h). PI/TPU/AgNW-500 maintained its low resistance after washing.

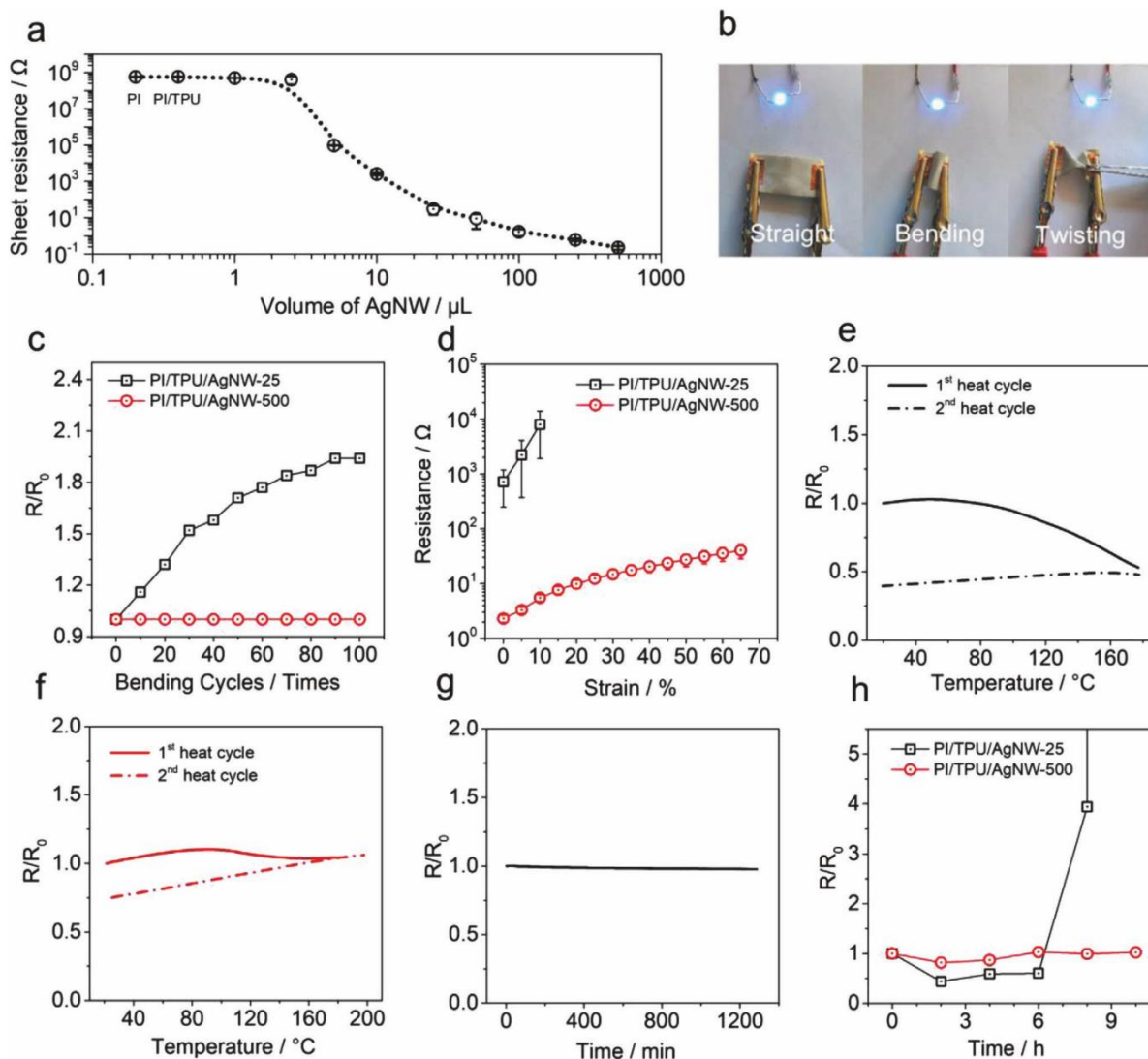


Figure 2. a) Sheet resistance of the dual-sided nonwovens prepared using different volumes of AgNW dispersion (17 g L^{-1}). PI and PI/TPU are labeled on the graphic without AgNWs for comparison. b) The luminance of LED bulb under different deformations of the dual-sided nonwoven. Resistance change of PI/TPU/AgNW-25 and PI/TPU/AgNW-500 on repeated c) bending cycles and d) different strain. e) The change of resistance of PI/TPU/AgNW-25 and f) PI/TPU/AgNW-500 upon temperature change. g) The change of resistance of PI/TPU/AgNW-500 at different time. h) The change of resistance of the dual-sided nonwoven after washing under different washing environments.

The PI/TPU/AgNW-500 demonstrated strong IR reflectance. The IR reflection performance of the samples was investigated by a setup, as depicted in Figure 3a and Figure S10, Supporting Information. The PI/TPU/AgNW-500 acts as a mirror in the mid IR range and, consequently, reflects thermal energy from a hot or cold source. This leads to a significant apparent temperature difference compared to PI (Figure 3b). Note that the exact determination of the absolute surface temperature of highly reflecting surfaces is very hard to conduct. We stress this fundamental issue in thermography by reporting an apparent temperature, which is merely a measure for the temperature of the surrounding environment than of the sample surface itself.

The IR reflectance of the dual-sided nonwoven depends on the AgNW concentration (Figure 3c), whereas the reflectance of PI side is constant at $\approx 30\%$. We then characterized the optical properties of PI/TPU/AgNW-500 and pure PI electrospun nonwovens in more detail, including reflectance, absorptance, and transmittance spectra (Figure 3d,f). The PI/TPU/AgNW-500 show ultralow IR transmittance of 0.2% regardless of their orientation, which is expected to provide passive heating by hindering the thermal exchange between the human body and the ambient environment.^[19] A very significant difference in absorptance and reflectance of the two sides of the nonwovens, AgNW side, and PI side, was observed. The dual-sided

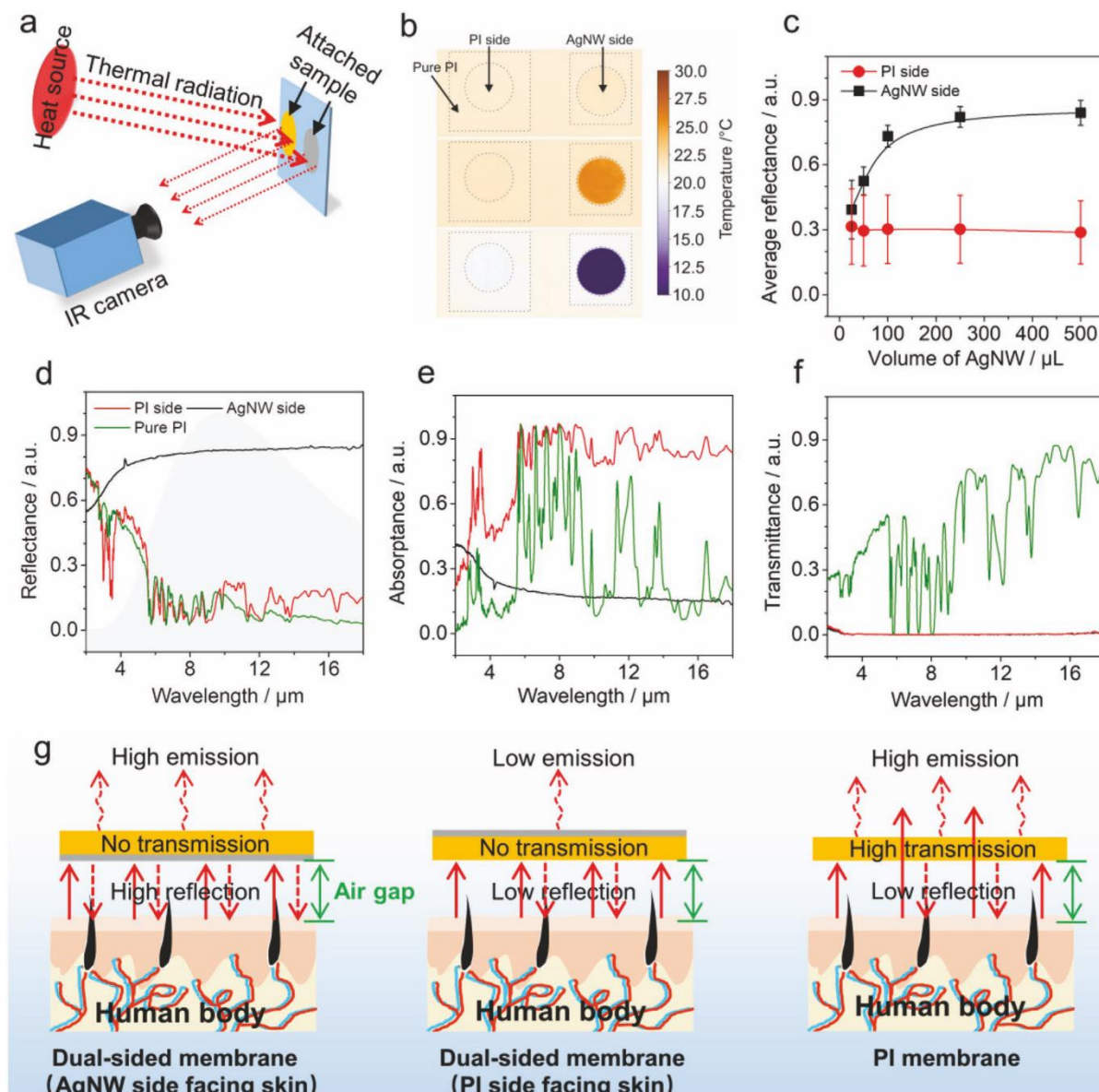


Figure 3. a) The schematic diagram of the setup for the measurement of IR reflection performance. b) Thermal images of IR reflection by dual-sided nonwoven (PI/TPU/AgNW-500). The AgNWs exhibited large apparent temperature difference compared to PI side. The first row: without hot/cold source; the second row: with hot source; the third row: with cold source. (Apparent temperature is defined as the temperature detected by IR camera without any correction) c) Average reflectance of a batch of dual-sided nonwovens with different amounts of AgNWs on the AgNW networks side and PI side. d) IR reflectance, e) absorbance, and f) transmittance of PI/TPU/AgNW-500 from another batch on the AgNW networks side and PI side. Gray area describes the major range of human body radiation. g) A schematic diagram of IR reflection by dual-sided nonwoven.

nonwoven exhibited low absorbance (19.5%) and high reflectance (80.3%) on the AgNWs side, and a high absorbance (78.5%) and low reflectance (21.1%) on the PI side. Compared to other AgNW coated textile, our nonwoven displayed a better IR reflection performance (Table S2, Supporting Information). We attribute this to the preparation procedure and the choice of AgNWs of appropriate length that allowed formation of flat and dense AgNW networks, reflecting most of IR irradiation as specular reflection and a minor portion as diffuse reflection.

On the contrary, PI electrospun nonwovens (reflectance: 17.9%; absorbance: 30.6%; transmittance: 51.5%) and other polymeric materials, such as conventional textile, paper, and polystyrene foam, show poor IR reflectance.^[20]

Continuous IR radiation loss from the human body into the ambient surroundings is the central reason for body heat loss. Materials with high emissivity have been demonstrated to dissipate more heat from objects to the ambient environment.^[21] A textile for on-demand thermal management needs to maintain

the thermal comfort of the body in different environments, regulating temperature as required. The dual-sided nonwoven introduced here, can be worn in two orientations. This will change the mutual radiative energy exchange between skin, fabric, and environment, as the emittance strongly depends on the fabric orientation. According to Kirchhoff's law absorption equals emission. Furthermore, emittance E can be calculated by:

$$E = 1 - R - T \quad (1)$$

where R and T denote reflectance and transmittance, respectively. In the major range of human body radiation, a low emittance ($\approx 20\%$) on the AgNW side was observed (Figure S11, Supporting Information). In contrast, the PI side presented a quite high emittance of $>75\%$ on an average. Figure 3g summarizes the different radiative contributions that will affect the entire system skin, fabric, and environment. One can expect that the AgNW layer will lead to less thermal losses, either since the energy exchange skin-nonwoven (AgNW facing skin) or nonwoven-environment (AgNW facing environment) will be reduced. The optimum orientation will, however, also be influenced by heat conduction at the bottom side and thermal convection at the top surface.

To judge the optimum orientation of the dual-sided nonwoven for a passive warming application, we designed an experiment that closely resembles all contributions (radiative, conductive, and convective) to the heat exchange in this multi-body system. We characterize the overall heat loss of a pure PI electrospun nonwoven compared to PI/TPU/AgNW-500 with a setup as depicted in Figure 4a. A black coated copper plate resembles the high emission of skin and is set to a temperature of 35°C . A small heater controlled and measured the required power until a steady-state temperature was reached as shown in Figure 4b. The nonwoven was loosely placed on the copper plate to mimic wearing of a textile. The surrounding dome acts as the ambient environment with a high emissivity/absorptivity at a temperature of $\approx 22^\circ\text{C}$. The required power for the steady-state condition for the two orientations of the dual-sided nonwoven, the pure PI, and a graphite coated reference are displayed as a function of dome temperature (ambient) in Figure 4c. For both, pure PI samples and the PI side of the PI/TPU/AgNW-500 facing the dome more power is needed to maintain a skin temperature of 35°C compared to the AgNW side facing outward. This indicates that the PI side losses more heat by radiative heat transfer to the environment than the AgNW side. This is in agreement with the collected optical data presented in Figure 3d-f. The pure PI electrospun nonwoven and the PI side of the PI/TPU/AgNW-500 show higher absorptance and are consequently expected to emit more radiation than the AgNW side (Figure 4d). The differences between pure PI and the PI side of PI/TPU/AgNW-500 in the mid IR range ($>10\ \mu\text{m}$) have apparently no significant influence on the overall heat exchange. Furthermore, blocking of direct IR transmission by the AgNW layer facing towards the skin and a concomitant reduced radiative heat exchange between skin and fabric seems to have no measurable effect. The power consumption is the same for pure PI and the dual-sided nonwoven in this configuration. Consequently, for a contribution to passive warming only the dual-sided nonwoven with the

AgNW facing to the outside will have an effect. Additionally, the PI electrospun nonwoven displayed a low thermal effusivity ($88.1\ \text{W s}^{1/2}\ \text{m}^{-2}\ \text{K}^{-1}$), which is comparatively low relative to other normal textiles (Figure 4e). Therefore, upon touching the skin the PI material will feel warm, suggesting that PI side facing towards skin (AgNW side facing towards outside) is the desirable wearing orientation.

A smart textile for thermal management needs to perform two functions: confining and providing heat to the human body for comfort. Thus, electric heating (active heating) usually is a popular and feasible way to offer extra thermal energy for warming a body. We, consequently, characterized the electrical heating performance of our dual-sided nonwovens by applying different direct currents. Electrical power (P) was distributed to the nonwoven by Joule heating according to Equation (2)

$$P = I^2 R \quad (2)$$

where I is applied current, and R is resistance. We used an IR camera to detect the apparent surface temperature of the sample after applying different electrical currents, which is illustrated in Figure 5a. The dual-sided nonwoven PI/TPU/AgNW-25 presented a rapid increase of the apparent surface temperature from room temperature to the equilibrium state within 5 s (Figure 5b and thermal images in Figure S12, Supporting Information). The apparent temperature could even go as high as 230°C (Figure 5b) on increasing the current to 0.37 A. On the other hand, PI/TPU/AgNW-500 merely produced any Joule heat even at high direct current (DC) currents (0.37 A), exhibiting surface temperature close to room temperature. Note, that these apparent temperatures are not corrected to the low emissivity of the AgNW surface and, consequently, should only be taken for a relative estimation of the temperature changes upon electrical heating.

In order to take advantage of both active Joule heating and low radiation losses, we have integrated a nonwoven as a heating electrode (PI/TPU/AgNW-25) and another as a radiation insulator (PI/TPU/AgNW-500) in the form of a double layer (Figure S13, Supporting Information). PI/TPU/AgNW-25 and PI/TPU/AgNW-500 stacked together act as a thermal management device for heat compensation (Figure 5c). The PI side of the double layer was towards the skin. The apparent temperature of the palm was around 37°C . The temperature profile of the as-designed thermal management device is provided in Figure 5d. Already by applying 0.1 A current the apparent temperature loss due to the low emissivity of the AgNW top layer is compensated. As expected, the apparent surface temperature increases even further with a higher DC current. This result indicates our thermal management device has a prominent heating function combining passive heating and active electric heating.

3. Conclusion

In conclusion, we have successfully prepared a breathable and flexible dual-sided nonwoven with tailored electrical and thermal properties that are promising as smart textiles for personal thermal management. The dual-sided nonwoven consisting of PI electrospun nonwoven and AgNW networks,

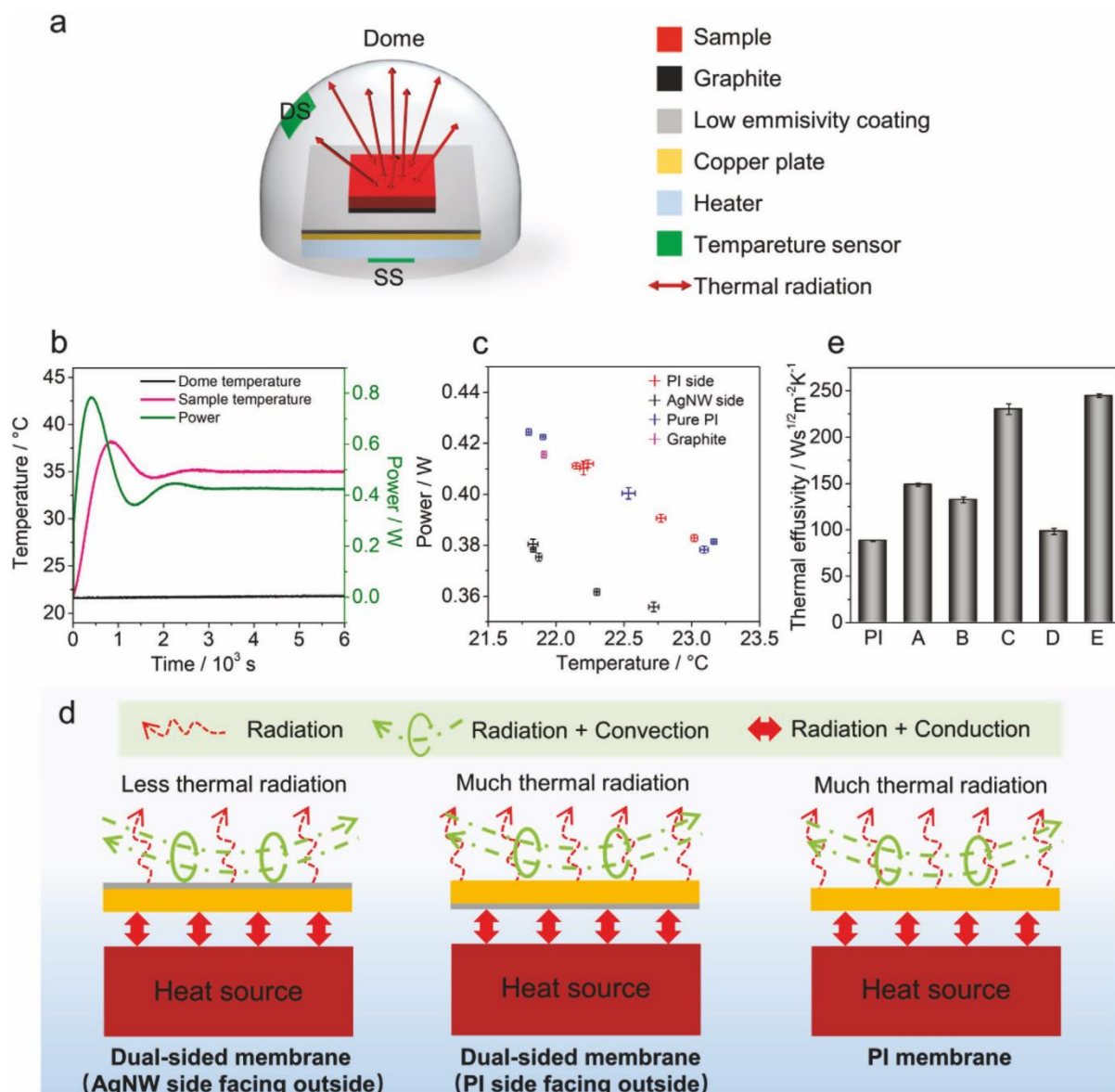


Figure 4. a) A schematic diagram of the setup for measuring radiatively dissipated energy. (SS: system sensor; DS: dome sensor) b) Evolution of dome temperature, sample temperature, and power supplied to the heater over time. c) Radiatively dissipated power for pure PI nonwoven, the respective sides of PI/TPU/AgNW-500, and a graphite reference as function of dome temperature (ambient). d) Schematic diagram of the thermal energy dissipation from PI/TPU/AgNW-500 and pure PI electrospun nonwoven. e) The effusivity of PI electrospun nonwoven and normal fabrics.^[20] (PI: 35 layers of electrospun nonwoven, 10 g m⁻² in each layer; A: 100% polyester, interlock knit fabric, 240 g m⁻²; B: 100% polyester, interlock knit fabric, one side brushed, 255 g m⁻²; C: 100% cotton, woven cotton duck fabric; D: 100% cotton, woven flannel fabric, 122 g m⁻²; E: 100% cotton, woven poplin fabric, 180).

presented significant differences of physical, electrical, and thermal properties on the two sides, which could be tailored by using the amount of AgNW. More AgNW is prone to form dense AgNW networks, which possessed very low electrical resistance of 0.23 Ωsq⁻¹ and excellent IR reflectance of more than 80%, far higher than the normal textiles. The dual-sided nonwoven with the AgNW facing to the outside demonstrated a

desirable effect for a contribution to passive warming. It could be integrated into a thermal management device by applying low current, realizing both functions of reducing heat dissipation to the ambient environment and Joule heating to the human body. Besides, the dual-sided nonwoven showed outstanding flexibility under different deformations as well as washing stability without sacrificing electrical resistance. Such

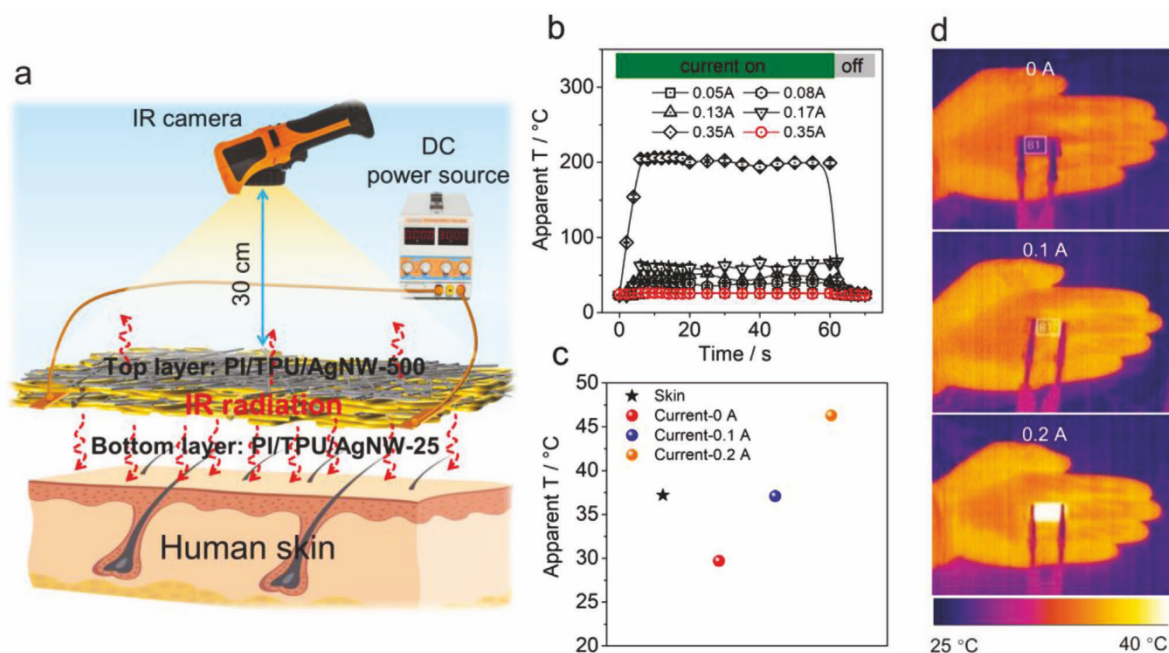


Figure 5. a) Schematic diagram of the smart textile for thermal management. The smart textile is composed of PI/TPU/AgNW-500 (top layer), to reduce thermal emissivity, and PI/TPU/AgNW-25 (bottom layer), to exhibit substantial Joule heating. b) Apparent surface temperature of PI/TPU/AgNW-25 heated by produced Joule heating with different current. (Black and red color represent PI/TPU/AgNW-25 and PI/TPU/AgNW-500 respectively.) c) Apparent surface temperature and d) corresponding thermal images of the thermal management device by the applied different current.

a dual-sided nonwoven can be used as a multifunctional flexible conductor and personal thermal management device to keep warm or smart textile escaping IR detection, which is very promising for next-generation wearable devices.

4. Experimental Section

Materials: PI electrospun nonwoven was kindly provided by Jiangxi Xiancai nanofiber Technology Co., Ltd. TPU (Desmopann DP 2590, Bayer Materials Science, Mn 88 900, Mw 145 000), ethylene glycol (p.a. $\geq 99.5\%$, Fluka), poly(vinylpyrrolidone) (PVP K30, Mw 40 000, Sigma-Aldrich), silver nitrate (AgNO_3 , p.a. 99.9%, Sigma-Aldrich), iron chloride (FeCl_3 , p.a. 98.0%, Sigma-Aldrich), sodium chloride (NaCl, p.a. 99.0%), tetrahydrofuran (THF, distilled) were used as obtained. Other solvents were distilled before use. The AgNWs were synthesized by a solvent thermal method.^[14b,c]

The preparation of dual-sided nonwoven: A piece of PI electrospun nonwoven (5 cm \times 5 cm) was placed on a sand core funnel, followed by filtering AgNW aqueous dispersion through the PI nonwoven under vacuum assistance to obtain the PI/AgNW network. The used amount of AgNW is shown in Table S1, Supporting Information. Next, the dual-sided nonwoven was fabricated by filtering a TPU solution (2 mL, 8 wt%, in THF) through the PI/AgNW network under light vacuum to physically bond AgNWs strongly onto the PI nonwoven. At last, the resulted sample was naturally dried in the fume hood for 24 h. The relevant parameters used during different steps are tabulated in Table S3, Supporting Information.

The scanning electron microscopy (SEM) (Zeiss LEO1530, Jena, Germany) was employed for observing PI nanofibers and AgNW networks. Energy-dispersive X-ray spectroscopy (EDX) was performed by using a Zeiss Ultra Plas (Jena, Germany; 10 kV acceleration voltage).

Pore size distribution measurements were used to investigate pore size of the samples (Tofer as standard test liquid with surface tension of 16.0 mN m^{-1}). The air permeability of the samples was measured by the Air Permeability Tester (FX 3300 LabAir IV, Switzerland) with the test area of 5 cm^2 under the pressure of 98 Pa. Each sample was measured five times at least, and the average value was taken. Tensile tester (Zwick/Roell BTI-FR 0.5TN-D14, Germany) was employed to characterize the mechanical property of samples. The samples (2 cm in length, 2 mm in width) were stretched at a speed of 10 mm min^{-1} (20°C , pretension 0.01 N mm^{-1}). The thickness of samples was determined by a screw micrometer.

The washing test was performed by dipping the samples into 45°C soap water (1 mL Manisoft detergent dissolved into 50 mL DI water) respectively with 100 rpm min^{-1} stirring for washing. The resistance of PI/TPU/AgNW-500 upon temperature and time was conducted with van der Pauw method. Sheet resistance was measured (Four-point measurements) with Keithley 2420 High-Current Source Meter coupled with Signatone SYS-301. Stretching resistance of different strain and cycling bending tests were performed by a tensile tester (Zwick/Roell BTI-FR 0.5TN-D14, Germany) to monitor stretching distance and bending degrees. An EMOS Multimeter (EM391) was connected by a copper conductor to detect the electrical resistance change of samples in different strain and bending cycles.

The IR reflection images were recorded by placing the samples in a cardboard enclosure. Images with a closed box and a hot or cold source above the camera were recorded (VarioCAM HD research 875/30 mm, Infracore) as shown in Figure 3a,b.

FTIR-spectroscopy measurements were conducted with an IR-spectrometer (Vertex 70, Bruker) in combination with a gold-coated integrating sphere accessory (A562, Bruker). The reflectance and transmittance were measured at the respective ports of the sphere. As reference a diffuse gold standard was used. The absorptance/emittance was calculated as Equation (1).

The radiative energy loss of the nonwoven was approximated with a steady-state heat transfer experiment. A circular sample piece with a

diameter of 3 mm was measured in a self-build setup. The sample was placed on a copper plate that was coated with graphite at the sample area and reflective aluminum foil at the outside, respectively. The copper plate was placed on a feedback-controlled heater and the power used to keep the sample at 35 °C (skin temperature) was recorded. The temperature sensor for the feedback control was in contact with the heater to record the sample temperature. The entire heater setup was placed within a block of expanded polystyrene to reduce heat losses by conduction to the surrounding. The heater block was placed below a graphite-coated aluminum dome with a diameter of 75 cm. The dome acts as a heat sink and was kept at ambient temperature during the experiment, which was monitored with a second temperature sensor. For a typical measurement, the sample was placed on the heater and the sample temperature, the dome temperature, and the heater power were monitored every 5 s until a steady state was reached. For each sample, the power and temperature data of 30 min in steady-state were averaged.

The thermal effusivity of the pure PI fabric was determined with a modified transient plane source instrument as described in the ASTM-D7984 standard.^[22] Nonwoven pieces with a size of 5 × 5 cm are stacked to reach a sufficient overall thickness for the measurement. To eliminate the influence of any preferred orientation each layer was positioned with a rotation of 30° with respect to the previous layer. For the measurement, a thermal conductivity analyzer (TCi C-Therm, Canada) with a circular probe area of 1.75 cm² was used. During the measurement, a pressure of 10 N was applied to the stack to ensure good contact.

Different constant electrical currents of 0.05, 0.08, 0.13, 0.17, 0.35, and 0.37 A are applied by a DF-3010 DC power supply to investigate joule heating effect (1 cm × 3 cm, connected with copper cable). A TrueIR camera (Keysight U5856A) was employed to record the temperature of samples, and time-dependent joule heating was depicted by the Origin software.

The detailed preparation procedure of the thermal management device is shown in Figure S13, Supporting Information. The DF-3010 DC power supply was employed to provide constant currents. An IR camera was used to detect surface temperature as shown in Figure 5a.

Supporting Information

Supporting Information is available from the Wiley Online Library or from the author.

Acknowledgements

Q.G. would like to thank the China Scholarship Council for awarding a fellowship for carrying out Ph.D. research in Germany in the lab of Prof. Andreas Greiner. This project has received funding from the European Research Council (ERC) under the European Union's Horizon 2020 research and innovation program (grant agreement no. 714968) and by Deutsche Forschungsgemeinschaft (project no. 431073172). The authors further want to thank Qimeng Song for the help with the heat transfer experiment, Thomas Tran for support with the IR camera images and Ina Klein for the assistance with the thermal effusivity measurements. The authors also would like to acknowledge Bavarian Polymer Institute (BPI) for providing SEM instruments for sample characterizations.

Open access funding enabled and organized by Projekt DEAL.

Conflict of Interest

The authors declare no conflict of interest.

Data Availability Statement

The data that supports the findings of this study are available in the supplementary material of this article.

Keywords

electrospinning, heat management, Janus fabrics, thermal emission, wearable devices

Received: September 1, 2021

Revised: September 27, 2021

Published online: October 20, 2021

- [1] a) W. Weng, P. N. Chen, S. S. He, X. M. Sun, H. S. Peng, *Chem. Int. Ed.* **2016**, *55*, 6140; b) S. Liu, K. Ma, B. Yang, H. Li, X. Tao, *Adv. Funct. Mater.* **2021**, *31*, 2007254.
- [2] a) X. Pu, W. X. Song, M. M. Liu, C. W. Sun, C. H. Du, C. Y. Jiang, X. Huang, D. C. Zou, W. G. Hu, Z. L. Wang, *Adv. Energy Mater.* **2016**, *6*, 1601048; b) C. Li, M. M. Islam, J. Moore, J. Sleppy, C. Morrison, K. Konstantinov, S. X. Dou, C. Renduchintala, J. Thomas, *Nat. Commun.* **2016**, *7*, 13319.
- [3] Y. C. Peng, Y. Cui, *Joule* **2020**, *4*, 724.
- [4] a) R. Hu, Y. D. Liu, S. Shin, S. Y. Huang, X. C. Ren, W. C. Shu, J. J. Cheng, G. M. Tao, W. L. Xu, R. K. Chen, X. B. Luo, *Adv. Energy Mater.* **2020**, *10*, 1903921; b) D. Y. Miao, X. F. Wang, J. Y. Yu, B. Ding, *Adv. Funct. Mater.* **2021**, *31*, 2008705.
- [5] a) P. C. Hsu, A. Y. Song, P. B. Catrysse, C. Liu, Y. C. Peng, J. Xie, S. H. Fan, Y. Cui, *Science* **2016**, *353*, 1019; b) Y. C. Peng, J. Chen, A. Y. Song, P. B. Catrysse, P. C. Hsu, L. L. Cai, B. F. Liu, Y. Y. Zhu, G. M. Zhou, D. S. Wu, H. R. Lee, S. H. Fan, Y. Cui, *Nat. Sustain.* **2018**, *105*.
- [6] a) P. C. Hsu, C. Liu, A. Y. Song, Z. Zhang, Y. C. Peng, J. Xie, K. Liu, C. L. Wu, P. B. Catrysse, L. L. Cai, S. Zhai, A. Majumdar, S. H. Fan, Y. Cui, *Sci. Adv.* **2017**, *3*, 1700895; b) L. L. Cai, A. Y. Song, P. L. Wu, P. C. Hsu, Y. C. Peng, J. Chen, C. Liu, P. B. Catrysse, Y. Y. Liu, A. K. Yang, C. X. Zhou, C. Y. Zhou, S. H. Fan, Y. Cui, *Nat. Commun.* **2017**, *8*, 496.
- [7] Y. Lu, X. D. Xiao, J. Fu, C. M. Huan, S. Qi, Y. J. Zhan, Y. Q. Zhu, G. Xu, *Chem. Eng. J.* **2019**, *355*, 532.
- [8] Y. Cui, H. X. Gong, Y. J. Wang, D. W. Li, H. Bai, *Adv. Mater.* **2018**, *30*, 1706807.
- [9] P. C. Hsu, X. G. Liu, C. Liu, X. Xie, H. R. Lee, A. J. Welch, T. Zhao, Y. Cui, *Nano Lett.* **2015**, *15*, 365.
- [10] A. Hazarika, B. K. Deka, D. Kim, H. E. Jeong, Y. B. Park, H. W. Park, *Nano Lett.* **2018**, *18*, 6731.
- [11] S. H. Jiang, J. Y. Cheong, J. S. Nam, I. D. Kim, S. Agarwal, A. Greiner, *ACS Appl. Mater. Interfaces* **2020**, *12*, 19006.
- [12] a) F. Zhang, Y. Y. Feng, M. M. Qin, L. Gao, Z. Y. Li, F. L. Zhao, Z. X. Zhang, F. Lv, W. Feng, *Adv. Funct. Mater.* **2019**, *29*, 1901383; b) H. L. Li, S. C. Dai, J. Miao, X. Wu, N. Chandrasekharan, H. X. Qiu, J. H. Yang, *Carbon* **2018**, *126*, 319.
- [13] Y. Wang, W. Wang, X. D. Ding, D. Yu, *Chem. Eng. J.* **2020**, *380*, 122553.
- [14] a) S. H. Jiang, S. Reich, B. Uch, P. Hu, S. Agarwal, A. Greiner, *ACS Appl. Mater. Interfaces* **2017**, *9*, 34286; b) Q. Gao, B. A. F. Kopera, J. Zhu, X. J. Liao, C. Gao, M. Retsch, S. Agarwal, A. Greiner, *Adv. Funct. Mater.* **2020**, *30*, 1907555; c) S. Reich, M. Burgard, M. Langner, S. H. Jiang, X. Q. Wang, S. Agarwal, B. Ding, J. Y. Yu, A. Greiner, *npj Flexible Electron.* **2018**, *2*, 5.
- [15] a) J. W. Lee, S. Jung, T. W. Lee, J. Jo, H. Y. Chae, K. Choi, J. J. Kim, J. H. Lee, C. Yang, J. M. Baik, *Adv. Energy Mater.* **2019**, *9*, 1901987; b) L. Dhakar, P. Pitchappa, F. E. H. Tay, C. Lee, *Nano Energy* **2016**, *19*, 532; c) J. Chen, Z. L. Wang, *Joule* **2017**, *1*, 480.
- [16] a) F. C. Li, Y. Liu, X. L. Shi, H. P. Li, C. H. Wang, Q. Zhang, R. J. Ma, J. J. Liang, *Nano Lett.* **2020**, *20*, 6176; b) H. J. Kim, K. Sim, A. Thukral, C. J. Yu, *Sci. Adv.* **2017**, *3*, e1701114; c) J. Kim, M. Kim, M. S. Lee, K. Kim, S. Ji, Y. T. Kim, J. Park, K. Na, K. H. Bae, H. K. Kim, F. Bien, C. Y. Lee, J. U. Park, *Nat. Commun.* **2017**, *8*, 14997; d) S. S. Yao,

- P. Ren, R. Q. Song, Y. X. Liu, Q. J. Huang, J. Y. Dong, B. T. O'Connor, Y. Zhu, *Adv. Mater.* **2020**, *32*, 1902343; e) J. K. Han, J. K. Yang, W. W. Gao, H. Bai, *Adv. Funct. Mater.* **2021**, *31*, 2010155.
- [17] S. Cho, S. Kang, A. Pandya, R. Shanker, Z. Khan, Y. Lee, J. Park, S. L. Craig, H. Ko, *ACS Nano* **2017**, *11*, 4346.
- [18] a) X. W. Liang, T. Zhao, W. Jiang, X. C. Yu, Y. G. Hu, P. L. Zhu, H. R. Zheng, R. Sun, C. P. Wong, *Nano Energy* **2019**, *59*, 508; b) F. Liang, X. J. Zhao, H. Y. Li, Y. J. Fan, J. W. Cao, Z. L. Wang, G. Zhu, *Nano Energy* **2020**, *69*, 104414; c) Z. Li, Q. Zheng, Z. L. Wang, Z. Li, *Research (Wash D C)* **2020**, *2020*, 8710686.
- [19] a) L. L. Cai, A. Y. Song, W. Li, P. C. Hsu, D. C. Lin, P. B. Catrysse, Y. Y. Liu, Y. C. Peng, J. Chen, H. X. Wang, J. W. Xu, A. K. Yang, S. H. Fan, Y. Cui, *Adv. Mater.* **2018**, *30*, 1802152; b) X. A. Zhang, S. Yu, B. Xu, M. Li, Z. Peng, Y. Wang, S. Deng, X. Wu, Z. Wu, M. Ouyang, *Science* **2019**, *363*, 619.
- [20] a) Y. Lian, H. Yu, M. Wang, X. Yang, Z. Li, F. Yang, Y. Wang, H. Tai, Y. Liao, J. Wu, *J. Mater. Chem. C* **2020**, *8*, 8399; b) X. Yue, T. Zhang, D. Yang, F. Qiu, Z. Li, G. Wei, Y. Qiao, *J. Colloid Interface Sci.* **2019**, *535*, 363.
- [21] T. Li, Y. Zhai, S. M. He, W. T. Gan, Z. Y. Wei, M. Heidarinejad, D. Dalgo, R. Y. Mi, X. P. Zhao, J. W. Song, J. Q. Dai, C. J. Chen, A. Aili, A. Vellore, A. Martini, R. G. Yang, J. Srebric, X. B. Yin, L. B. Hu, *Science* **2019**, *364*, 760.
- [22] ASTM D7984-16, *Standard Test Method for Measurement of Thermal Effusivity of Fabrics Using a Modified Transient Plane Source (MTPS) Instrument*, ASTM International, West Conshohocken, PA **2016**.

Supporting Information

for *Adv. Funct. Mater.*, DOI: 10.1002/adfm.202108808

Breathable and Flexible Dual-Sided Nonwovens with
Adjustable Infrared Optical Performances for Smart
Textile

*Qiang Gao, Tobias Lauster, Bernd A. F. Kopera, Markus
Retsch,* Seema Agarwal,* and Andreas Greiner**

Supporting Information

Breathable and flexible dual-sided nonwovens with different infrared optical performances for smart textile

Qiang Gao,¹ Tobias Lauster,² Bernd A. F. Kopera,² Markus Retsch,^{2,3} Seema Agarwal,^{1*} Andreas Greiner^{1*}*

¹Q. Gao, S. Agarwal, A. Greiner

Department of Chemistry, Macromolecular Chemistry II and Bavarian Polymer Institute

University of Bayreuth

Universitätsstrasse 30, 95440 Bayreuth, Germany

E-mail: markus.retsch@uni-bayreuth.de; agarwal@uni-bayreuth.de; greiner@uni-bayreuth.de

² T. Lauster, B. A. F. Kopera, M. Retsch

Department of Chemistry, Physical Chemistry I

University of Bayreuth

Universitätsstrasse 30, 95440 Bayreuth, Germany

³ M. Retsch

Bavarian Center for Battery Technology (BayBatt), Bavarian Polymer Institute, and Bayreuth

Center for Colloids and Interfaces

University of Bayreuth

Universitätsstrasse 30, 95440 Bayreuth, Germany

Supplementary figures:

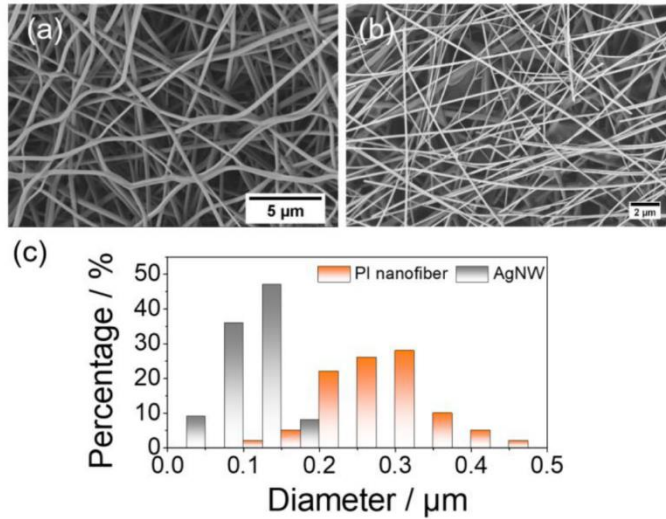


Figure S1 (a) SEM image of PI electrospun nanofiber. (b) SEM image of AgNW mesh prepared by the wet-laid method. (c) Diameter distribution of PI nanofiber and AgNW measured with ImageJ software (100 measurements were selected randomly).

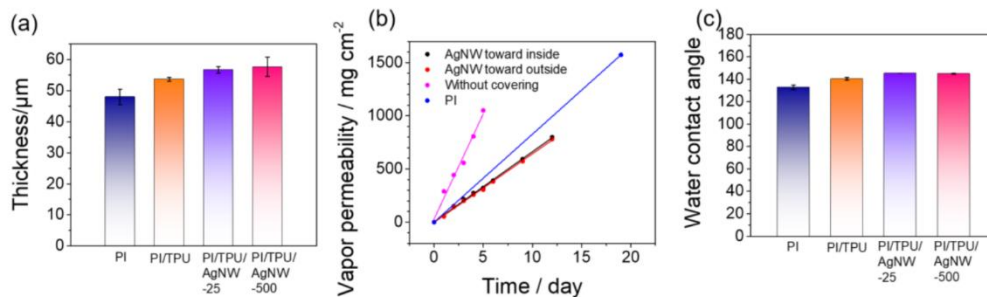


Figure S2 (a) Thickness of PI nonwoven, PI/TPU nonwoven, PI/TPU/AgNW-25, and PI/TPU/AgNW-500. (b) Vapor permeability of the dual-sided nonwoven of PI/TPU/AgNW-500. (c) Water contact angles of PI nonwoven, PI/TPU nonwoven, PI/TPU/AgNW-25, and PI/TPU/AgNW-500.

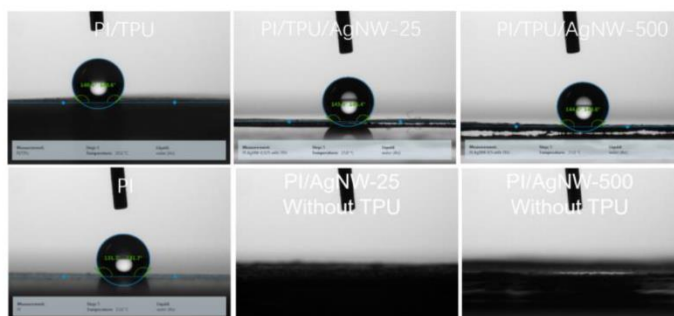


Figure S3 Optical images of water contact angle on nonwovens. PI, PI/TPU, PI/TPU/AgNW-25, and PI/TPU/AgNW-500 were hydrophobic, on which water drop could keep the shape. PI /AgNW-25 and PI /AgNW-500 were hydrophilic, through which water drop could penetrate easily.

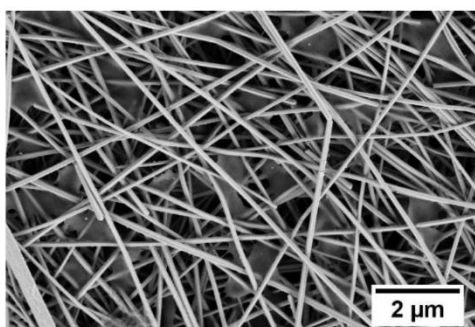


Figure S4 Original SEM image of AgNW networks with TPU.

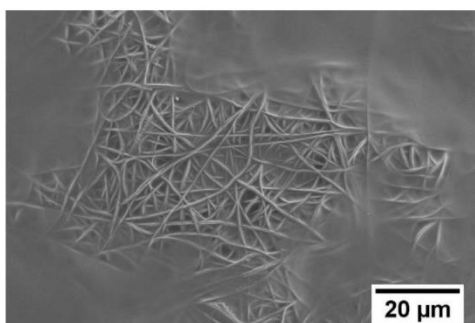


Figure S5 SEM image of TPU casted PI electrospun nonwoven.

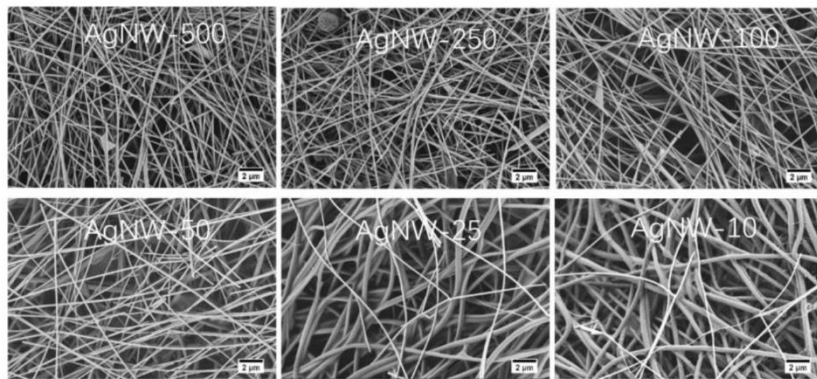


Figure S6 SEM image of the dual-sided nonwoven with different amounts of AgNW.

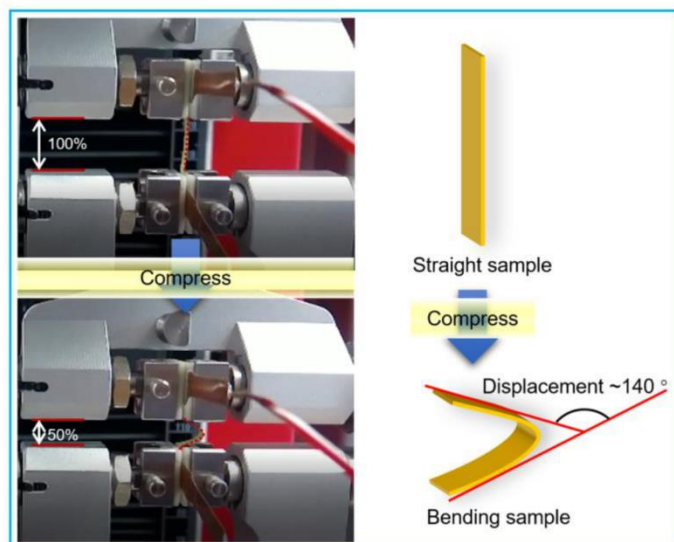


Figure S7 Measurement of 100-time bending test and schematic displacement of dual-sided nonwoven during compressing test.

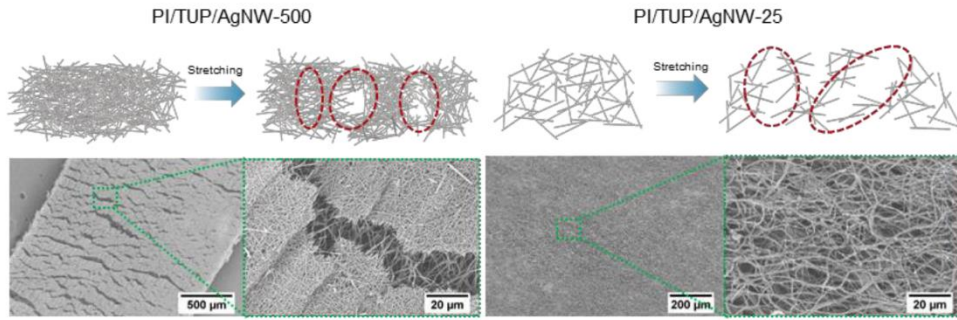


Figure S8 Schematic diagram (up) and SEM image (down) of cracks on AgNW mesh by stretching. Cracks on the AgNW networks of PI/TPU/AgNW-500 appeared by stretching, but AgNW still composed interconnected mesh structure. However, less AgNW cannot maintain the integrated AgNW mesh of PI/TPU/AgNW-25 when stretching, caused to electrical resistance dramatically increase.

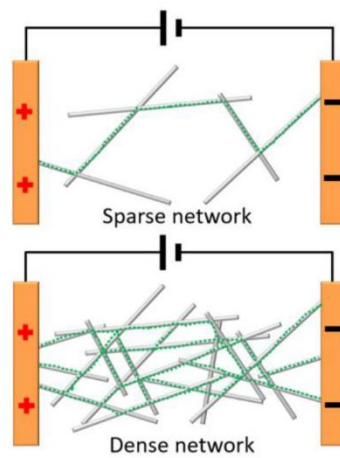


Figure S9 The mechanism of resistance stability of dense AgNW networks.

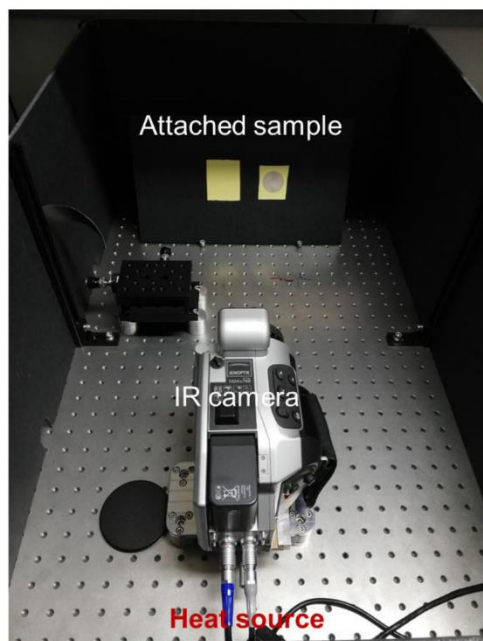


Figure S10 The digital image of the setup for the measurement of IR reflection performance.

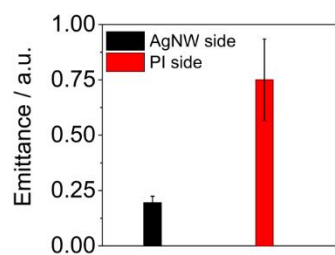


Figure S11 The emittance of PI/TPU/AgNW-500 on AgNW side and PI side.

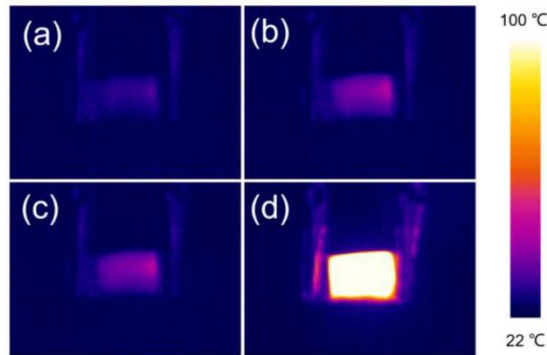


Figure S12 Thermal images of PI/TPU/AgNW-25 with applying different current. (a) 0.05A; (b) 0.13A; (c) 0.17A; (d) 0.35A.

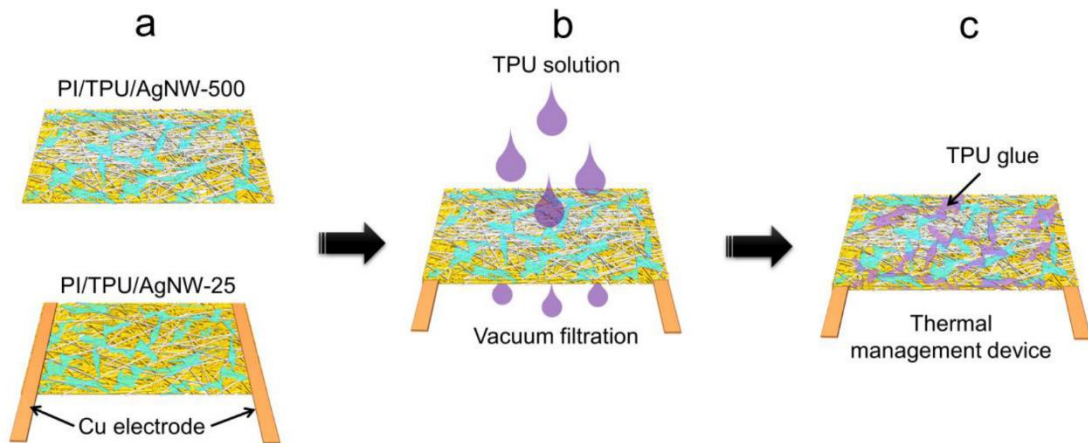


Figure S13 The schematic diagram of the thermal management device. (a) Two dual-sided nonwovens containing different amounts of AgNWs (the top PI/TPU/AgNW-500 for reducing emissivity and the bottom PI/TPU/AgNW-25 for heat compensation) were stacked as shown. Two Cu tapes were used as the electrode, attaching to the AgNW networks of PI/TPU/AgNW-25. (b) Well-stacked PI/TPU/AgNW-500 and PI/TPU/AgNW-25 were filtered 2mL TPU solution under a light vacuum to glue dual nonwovens together in case of delamination. (c) The resulted thermal management device is with tightly bonded double layers of PI/TPU/AgNW-500 and PI/TPU/AgNW-25 after drying.

Supplementary tables:

Table S1 Electrical resistance of dual-sided nonwoven with different amount of AgNW

Sample	Used AgNW(17 g L ⁻¹)	Content of AgNW	Sheet resistance / Ω
	/ μ L	/ (g m ⁻²)	sq ⁻¹
PI	0	-	5.7×10^8
PI/TPU	0	-	5.8×10^8
PI/TPU/AgNW-1	1	0.017	4.9×10^8
PI/TPU/AgNW-2.5	2.5	0.0425	4.8×10^8
PI/TPU/AgNW-5	5	0.085	9.55×10^4
PI/TPU/AgNW-10	10	0.17	2.54×10^3
PI/TPU/AgNW-25	25	0.425	30.7
PI/TPU/AgNW-50	50	0.85	9.1
PI/TPU/AgNW-100	100	1.7	1.7
PI/TPU/AgNW-250	250	4.25	0.6
PI/TPU/AgNW-500	500	8.5	0.2

Table S2. IR reflectance of the dual-sided nonwovens versus previous Ag coated textiles

Sample	Material	Reflectance	ref
Laminated Nanofiber Membrane	Ag/cellulose/carbon nanotube	0.7 (2 - 18 μm)	1
multifunctional E-textile	Cotton/AgNW	0.59 (2 - 16 μm)	2
Metallic nanowire cloth	Cotton/AgNW	0.4 (2 - 15 μm)	3
Normal cloth	Cotton	0.01 (2 - 15 μm)	3
PI nonwoven	PI	0.18 (2 - 18 μm)	This work
PI/TPU/AgNW-500	PI/TPU/AgNW	>0.8 (2 - 18 μm)	This work

Table S3. The relevant parameters of PI nonwoven, TPU solution and AgNW dispersion used for the preparation of dual-sided membrane

	Relevant parameter	Value
PI nonwoven	Fiber diameter / μm	0.30 ± 0.07
	Pore size / μm	1.7
	Thickness / μm	48.0 ± 2.5
	Air permeability / mm s^{-1}	20.3 ± 0.5
	Water contact angle / degree	140
TPU solution	Solvent	THF
	Concentration / wt%	8
	Used amount / mL	2
AgNW aqueous dispersion	Diameter of AgNW / μm	0.10 ± 0.03
	Length of AgNW / μm	20-60
	Concentration of dispersion / g L^{-1}	17
	Used amount / μL	X (See Table S1)

References

1. X. Yue, M. He, T. Zhang, D. Yang, F. Qiu, ACS Appl. Mater. Inter. **2020**, 12, 12285.
2. Y. L. Lian, H. Yu, M. Y. Wang, X. N. Yang, Z. Li, F. Yang, Y. Wang, H. L. Tai, Y. L. Liao, J. Y. Wu, X. R. Wang, Y. D. Jiang, G. M. Tao, J. Mater. Chem. C **2020**, 8, 8399.
3. P. C. Hsu, X. G. Liu, C. Liu, X. Xie, H. R. Lee, A. J. Welch, T. Zhao, Y. Cui, Nano lett. **2015**, 15, 365.

Acknowledgements

The final pages of my dissertation I want to use to thank everyone that made this thesis possible. In case you are reading this to find out whether I included your name or not, I have to disappoint you. My journey up to this point was accompanied by too many people to name them all. Thus I decided not to try.

I want to thank everyone from my research group for their scientific and non-scientific input, their advice, and the good times I had during my time here. I'm grateful that you helped me to overcome the obstacles and difficulties that arose and for the contributions that shaped this thesis.

Next, I want to thank whoever considers themselves my friend, wherever they may be. I am thankful that we have met, whether it was before my time in Bayreuth or here. Thank you for the games we played, the evening program, and the holidays.

I want to thank my flatmates for their patience, for listening, and for the encouragement after a bad day. I also thank you for respecting the core sleeping time and for the coffee.

With the end of this thesis also, my time in Bayreuth will end. I want to thank everyone who made it a good time for me here.

I want to thank my family for their support, both financially and emotionally. I knew that I would always have a place to go to if things went sideways and that you had my back.

Lastly, I want to thank my past self for enduring all of this. The confusion, uncertainty, and frustration that was also part of this journey. And, of course, for writing all of this. I'm currently not looking forward to doing this again. I also don't plan to.

And finally, I want to thank you for reading this. I would be happy if you maybe also read some other part of this thesis because, actually, it was kind of a lot of work, but no pressure. You can also just read it some other time or close it again. Anyway, I will not know.

Wer das liest ist doof.

-unbekannt

Eidesstattliche Versicherungen und Erklärungen

§ 8 Satz 2 Nr. 3 PromO Fakultät für Biologie Chemie und Geowissenschaften

Hiermit versichere ich eidesstattlich, dass ich die Arbeit selbstständig verfasst und keine anderen als die von mir angegebenen Quellen und Hilfsmittel benutzt habe (vgl. Art. 64 Abs. 1 Satz 6 BayHSchG).

§ 8 Satz 2 Nr. 3 PromO Fakultät für Biologie Chemie und Geowissenschaften

Hiermit erkläre ich, dass ich die Dissertation nicht bereits zur Erlangung eines akademischen Grades eingereicht habe und dasss ich nicht bereits diese oder eine gleichartige Doktorprüfung endgültig nicht bestanden habe.

§ 8 Satz 2 Nr. 4 PromO Fakultät für Biologie Chemie und Geowissenschaften

Hiermit erkläre ich, dass ich Hilfe von gewerblichen Promotionsberatern bzw. -vermittlern oder ähnlichen Dienstleistern weder bisher in Anspruch genommen habe noch künftig in Anspruch nehmen werde.

§ 8 Satz 2 Nr. 7 PromO Fakultät für Biologie Chemie und Geowissenschaften

Hiermit erkläre ich mein Einverständnis, dass die elektronische Fassung der Dissertation unter Wahrung meiner Urheberrechte und des Datenschutzes einer gesonderten Überprüfung unterzogen werden kann

§ 8 Satz 2 Nr. 8 PromO Fakultät für Biologie Chemie und Geowissenschaften

Hiermit erkläre ich mein Einverständnis, dass bei Verdacht wissenschaftlichen Fehlverhaltens Ermittlungen durch universitätsinterne Organe der wissenschaftlichen Selbstkontrolle stattfinden können.

Ort, Datum, Unterschrift

Tobias Lauster

Spectroscopic Analysis and Materials Engineering
for Passive Radiative Cooling
Dissertation, Bayreuth 2023

University of Bayreuth

Physical Chemistry I
Faculty of Biology, Chemistry & Earth Sciences
Universitätsstraße 30